ATLAS Levels Up:

Early Searches for Diboson Resonances in Semi-Hadronic Decay Channels at $\sqrt{s} = 13$ TeV Center of Mass Energy

Steve Alkire

Submitted in partial fulfillment of the

requirements for the degree of

Doctor of Philosophy

in the Graduate School of Arts and Sciences

COLUMBIA UNIVERSITY

2017

ABSTRACT

ATLAS Levels Up:

Early Searches for Diboson Resonances in Semi-Hadronic Decay Channels at

$\sqrt{s} = 13$ TeV Center of Mass Energy

Steve Alkire

Searches are made for narrow diboson resonances, ZZ and ZW, in the final states $\ell\ell qq$ and $\nu\nu qq$ at ATLAS, with (13.2 ± 0.4) fb^{-1}data collected from pp-collisions with center of mass energy $\sqrt{s}$=13 TeV during 2015 and 2016, the first two years of Run 2 of the Large Hadron Collider. The hadronic decay products of the vector boson, $V \to qq$, are reconstructed as jets in the electromagnetic and hadronic calorimeters. When the vector boson is sufficiently boosted the decay products are reconstructed as a single anti-k_t $R = 1.0$ jet. Otherwise two anti-k_t $R = 0.4$ jets are matched to identify the vector boson. The Z boson in its leptonic decay is identified by either reconstructing two electrons in the calorimeters, or opposite sign muons in the muon spectrometer. Limits on the production cross section for 3 benchmark signals, a heavy scalar, a spin-1 heavy vector triplet, and a spin-2 graviton are set in the mass range 300 GeV to 5000 GeV.

Contents

List of Tables

List of Figures

For Monique and Dylan.

I owe this work to the generous support of my advisor, Professor Emlyn Hughes;

and to Professor Henry Lubatti for introducing me to the intricate beauty of particle physics.

Chapter 1

Introduction

Particle physics is in the post-Higgs era. The Higgs boson was discovered in 2012 [1, 2] during the first run of the Large Hadron Collider (LHC) at both general purpose experiments, ATLAS (A Toroidal LHC Apparatus) and CMS (Compact Muon Solenoid). The masses of the Z and W bosons can be generated by the mechanism of electroweak symmetry breaking (EWSB) [3, 4] used by the electroweak theory of the Standard Model of Particle Physics (SM). This mechanism, in its simplest implementation predicts an additional field and its quanta, the Higgs boson h, the direct observation of which in 2012 earned Peter Higgs and Francois Englert the Nobel Prize in Physics in 2013. But there is no reason *a priori* to expect that h would be implemented in its simplest possible mathematical form–the history of experimental particle physics in the 20th century has after all served up as many unexpected results as expected. Yet, the SM has been widely–frustratingly–successful at predicting numerous phenomena in the last 50 years, and this latest prediction is the center-most piece of what is looking to be a very complete puzzle. The ATLAS and CMS collaborations at LHC have measured the mass of the Higgs boson to be 125 GeV [5] and the spin, charge, parity, and couplings to be consistent with the minimal implementation of EWSB according to the SM.

Despite the many successes of the CMS and ATLAS collaborations in understanding and constraining the properties of the SM already and especially those related to the Higgs boson, a number of additions to the SM are still well motivated. The related fields of particle physics and cosmology have paid their dues and come up with

great experimental successes with the verification of two long-held theories with back-to-back discoveries: the Higgs boson at LHC and gravitational waves at LIGO [6]. It would not be too much to expect a glimpse of something new, perhaps to inform the connection between these two discoveries. Numerous unanswered problems persist in the theoretical frameworks used in these fields (dark matter, dark energy, the hierarchy problem, naturalness) that will find explanations consistent with and hopefully directly inspired by measurements and searches made with the data being taken right now at the LHC.

This thesis probes many of these questions, in the way that experimental physics does, by way of careful search, documentation, and understanding of the uncertainties of the relevant parameter space. There isn't a single fundamental question to motivate the following search that stands far above the rest. Indeed, it is the objective of the experimental programs at CMS and ATLAS to produce results widely interpretable, and the results of the searches presented below are exemplary in their breadth from a theoretical perspective. Rather, the details involved in the production of a final result from commissioning of a new apparatus, to data simulation and collection, to analysis, to theoretical framework will be presented. The tasks of the experimental particle physicist within an experiment are manifold. The results presented in this thesis are a product of work by the author in the upgrade, operation, and calibration of the ATLAS experiment at the unprecedented $\sqrt{s} = 13$ TeV center of mass energy (CME).

1.1 The Searches

Searches are made for narrow mass resonances in a model independent way using simplified phenomenological models in place of explicit theories. This thesis considers extensions of the SM of 3 general types, each producing a narrow resonance, and for

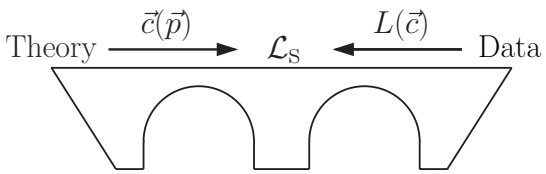

Figure 1.1: The "bridge" method [7].

each there is a benchmark model that is used to set limits on the given type of resonant behavior. Limits are set on the cross section times branching ratio, $\sigma \times \mathrm{BR}$ of the simplified models, which are then readily converted to bounds on parameters of a specific model. To borrow a metaphor used to describe one of the simplified models that is generally applicable to all searches considered in the following, Fig. 1.1 shows how a simplified Lagrangian, $\mathcal{L}_S$ forms the bridge from experimental data to be interpreted in complete theories extending beyond the SM. In this cartoon, the likelihood, L, of the phenomenological model is calculated or confidence limit (CL) curves are produced in terms of the parameters of the phenomenological model, $\vec{c}$. Transfer functions, $\vec{p}(\vec{c})$, can be made for the parameters of a specific theory making the limits set generally applicable to multiple theories current and future. This is generally true modulo some dependence on a non-trivial resonance width.

The models are introduced and briefly motivated below. Theoretical details of each of the extensions will be covered in Chapter 2.

Heavy Scalar The Higgs model employed in the SM is the simplest possible implementation of electroweak symmetry breaking. However, there are many possible models that predict a more extended Higgs sector such as the electroweak-singlet (EWS) model [8] and the two-Higgs-doublet model (2HDM) [9]. For searches relevant to these models a heavy spin-0 neutral CP-even Higgs boson is used with the predicted decay branching from the SM. The signal is generated in the narrow width approximation (NWA) for both the gluon-gluon fusion (ggF) and vector boson fusion

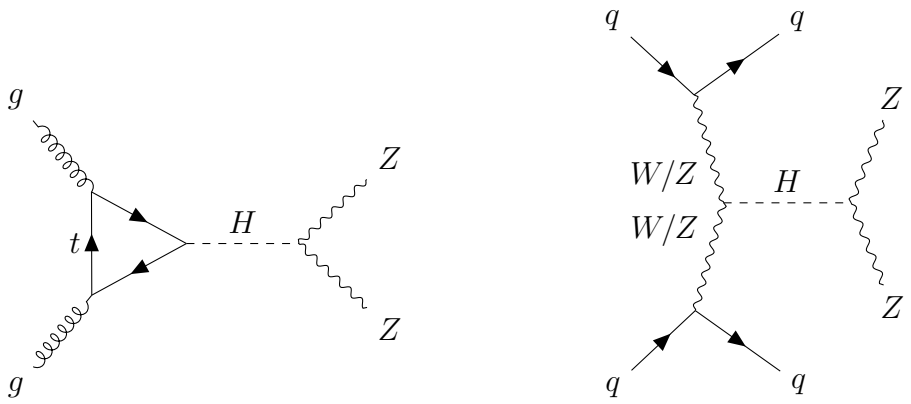

(a) gluon-gluon fusion (b) vector boson fusion

Figure 1.2: Feynman diagrams for the heavy spin-0 extension to the Higgs sector in gluon-gluon fusion (ggF) and vector boson fusion (VBF) production channels.

(VBF) production channels, shown respectively in Figure 1.2. The narrow width approximation assumes a theoretical width of the benchmark signal is only 4 MeV, the width of the SM Higgs according to its decay rate, which is trivial in comparison to the experimental width. In models of these types there are interference effects with the 125 GeV Higgs which has been ignored for these searches but will make for interesting work in the future.

Extended Gauge Models (EGM) with a heavy spin-1 boson This search addresses extensions of the gauge sector in a general way [10] using a simplified phenomenological model with a heavy triplet state of Z and W vector bosons. Figure 1.3 (a) shows the first order Feynman diagrams of the heavy vector triplet, a charged W' that decays to the charged and neutral vector bosons. A broad class of extensions of the SM gauge sector, with varying and rich phenomenologies, can be probed by searches with a spin-1 resonance due to the ubiquity of this additional boson. Technicolor theories are one classic example of an extended gauge sector [11–13]. Gauge extensions often also require the introduction of other fermions and/or additional heavy neutral bosons [14]. For example, Grand Unified Theories (GUT) with this

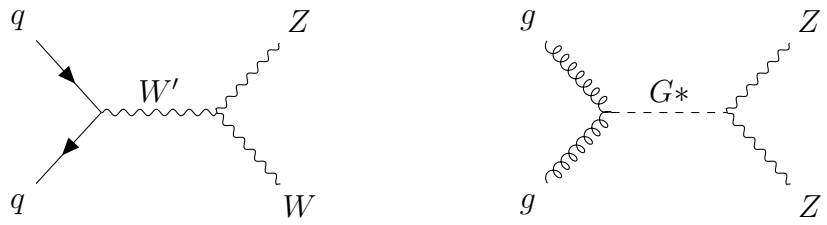

(a) Extended Gauge (b) Graviton

Figure 1.3: Feynman diagrams for the spin-1 W' and spin-2 graviton signals.

formulation [15, 16] in some cases require the existence of SUSY to solve the hierarchy problem, obtaining coupling constant unification.

A spin-2 graviton from models with warped extra dimensions A bulk Randall-Sundrum model [17, 18] is used as the basis for searches for spin-2 gravitons. Models of this type are well motivated theoretically because they can give at least a partial answer to many shortcomings of the SM simultaneously. By adding a single warped dimension to the field theory the hierarchy problem of the Planck and weak scales is reduced to a single order of magnitude from 10^{24}. Simultaneously, the theory provides a quantum field theory solution to the Einstein field equations of general relativity and to electromagnetism as an extension of the Kaluza-Klein model [19], and the bulk allows an explanation for the large variation in the masses of fermions of the SM. Figure 1.3 (b) shows the mode used for our benchmark model in the ggF production channel.

The searches for each of the benchmark models are cut-based (as opposed to optimizing a discriminant) and proceed along a similar course. Except at certain key points each is optimized for the specific signal over the other as will be detailed later in Chapter 6. Common to each analysis is a categorization based on the reconstructed jets in the calorimeters. Both the $\nu\nu qq$ and $\ell\ell qq$ channels require a decay of a vector boson hadronically forming a signature of two jets in the calorimeters. If the boson is significantly *boosted* from the laboratory reference frame then the opening angle

of the jets is small and it is most efficient to reconstruct the detector signature as a single object, the whole boson, in the calorimeters, a "large-R" jet–this is referred to as the *merged* regime. Otherwise, two individual jets are *resolved* and associated with each other to identify the boson. These analysis channels are handled separately, optimizing their own set of cuts. Furthermore, the boosted channel is split based on a jet substructure variable designed to differentiate between the two-pronged jets of a boson decay and the single-pronged jets of a QCD event. The $\ell\ell qq$ channel uses both the resolved and merged regimes whereas the $\nu\nu qq$ channel uses only the merged.

Little is lost from not including the resolved analysis in $\nu\nu qq$ channel since the $\ell\ell qq$ analysis dominates the search in the lower mass range. The two leptons allow the reconstruction of a Z boson mass giving additional discrimination to the $\ell\ell qq$ channel whereas the $\nu\nu qq$ channel relies on high missing transverse momentum ($E_{\mathrm{T}}^{\mathrm{miss}}$) from Z-decay to two neutrinos. The leading SM background of V+jets is larger in the low mass range of the search where the additional discriminating power is necessary to achieve a decent signal to background ratio, $S/\sqrt{B}$. Searches for spin-0 and spin-2 signals further split the resolved regime by identification of jets from the decay of the Z boson to two b-quarks through reconstruction of displaced vertices as the source of the charged particles in the hadron shower. Finally, the scalar search discriminates between ggF and VBF production channels by tagging the two additional jets in the final state of the VBF topology (Fig. 1.2).

For each signal, in each regime, the resonance is searched for with a final discriminating variable of the reconstructed mass. In the resolved $\ell\ell qq$ channel this is the invariant mass of the two reconstructed leptons (either ee or $\mu\bar{\mu}$) and the two reconstructed jets ($m_{\ell\ell jj}$). The merged $\ell\ell qq$ channel uses the invariant mass of the large-R jet and the two leptons ($m_{\ell\ell J}$). For $\nu\nu qq$ channel the transverse mass (M_{T}) constructed from the invariant mass of the missing transverse momentum and the large-R jet limited to the transverse plane. Individual categories within each channel

are combined into a single search.

1.2 Historical Searches

The limits presented are an improvement over those set for narrow resonances previously at the LHC and Tevatron. The ATLAS and CMS collaborations have searched for diboson resonances, ZZ and ZW, at $\sqrt{s} = 7$ and 8 TeV. These analyses offer an improvement in both the range of masses searched and the inclusion of data.

ATLAS has already released 2 analyses with the more limited 2015 data set of 3.2 fb^{-1}. Already an improvement over searches made with 20 fb^{-1}at ATLAS and CMS [20–24] at 8 TeV. One analysis combines searches in the range of 500 to 3000 GeV for a bulk RS graviton and HVT in the $\ell\nu qq$, $qqqq$, $\ell\ell qq$, and $\nu\nu qq$ channels using only a merged analysis [25–27]. A limit of 1100 GeV was set on the bulk RS graviton model and a limit of 2600 GeV was set on the heavy vector triplet. A notably improved confidence limit was set in the lower mass region of the $\ell\ell qq$ channel for a search in the mass range of 300 GeV to 1000 GeV for a heavy Higgs and graviton by improving the efficiency of the analysis and including the resolved analysis, which excludes a bulk RS graviton with mass below 820 GeV [28] in the single channel.

Which channels are dominant in combination depend heavily on the mass range searched and the model used to determine the relative BRs to each of the final states. The important final states to include in a search are determined by the decay products of the bosons and by the expected BRs and their SM backgrounds. The Z and W bosons decay hadronically with approximately twice the width than the leptonic decay. Therefore in the higher mass ranges where QCD background is steeply exponentially suppressed, the fully hadronic channels dominate due to the branching ratios. In a search covering a wide spectrum, the dominant decay channel will shift from $\ell\ell\ell\ell$ to $\ell\ell qq$ to $\nu\nu qq$ to $qqqq$ with increasing mass. $\ell\ell qq$ is most dominant from

500 GeV to 1000 GeV and $\nu\nu qq$ from 1000 GeV to 2000 GeV. Therefore, the channels considered in this thesis are of particular interest at this phase of the LHC experiment, as we reach the moment where the ATLAS experiment collects a sufficient amount of data at the higher Run 2 energy where discovery of a simple resonance from 500 GeV to 2.5 GeV could become statistically obtainable. In other words, at this point we can extend significantly the limits set on these models through the regions where these channels are the most valuable.

This thesis treats the $\ell\ell qq$ and $\nu\nu qq$ channels separately in setting limits. Specific model-dependent combinations of these results are underway, including a search for HVT, G*, and a heavy scalar in WW, ZW, WW, and HH resonances in many decay channels.

1.3 Data Taking

To understand the results of this thesis and the purpose of much of the work that has been done to obtain them it helps to understand the schedule of data-taking at the LHC and in the ATLAS experiment. The results obtained here come from data taken at the beginning of the second run (Run 2) of the LHC, the first year and beginning of the second year after the first long shut down (LS1), see Fig. 1.4. During LS1 the accelerator facilities were upgraded to operate at a CME of $\sqrt{s} = 13$ TeV. Compared to ATLAS at 7 and 8 TeV in Run 1, the ATLAS triggering system was updated to remove one of three stages in evaluating whether to keep or discard a collision event, and the insertable B-layer (IBL) was installed. The IBL is the fourth and innermost layer of pixel detector that allows for improvements to the tracking of charged particles near the interaction point (IP). The purpose of this discussion, however, is to introduce the beginning of the ramp-up of luminosity and corresponding increased rate of interactions at the IP.

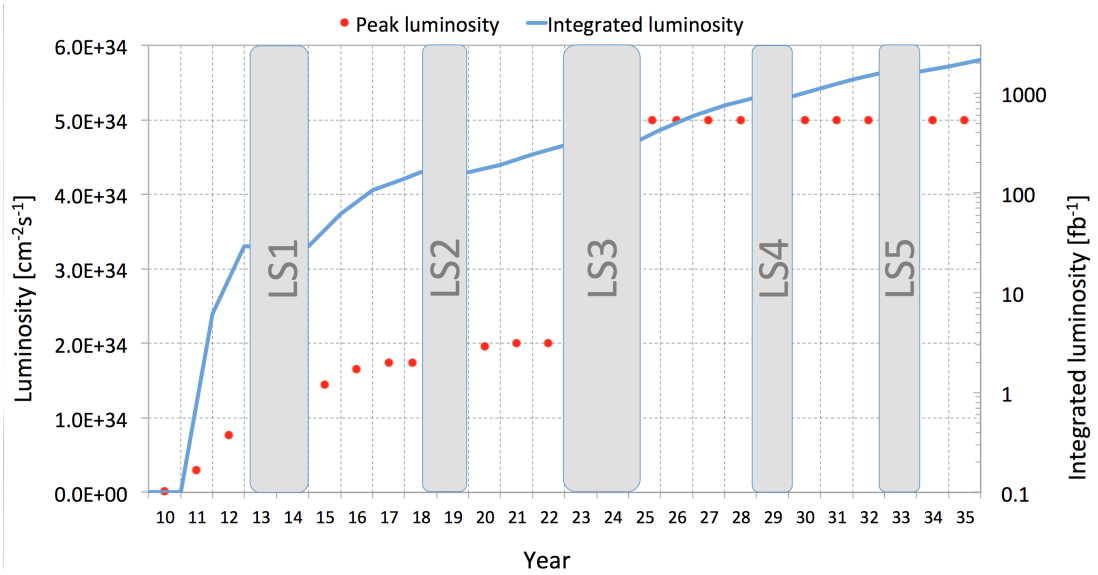

Figure 1.4: LHC schedule of operation through 2035.

In Fig. 1.4 the vertical axis is in inverse $\text{cm}^2\cdot\text{s}$, a unit of cross section per second. The cross section, σ, defines the likelihood of an interaction to occur in a geometric way by allusion to a model like an idealized Rutherford thin gold foil experiment where a particle travels toward a thin target and has a small probability of significant interaction but otherwise passes through without interaction. Dimensionally, there is a number of targets (like gold nuclei in a foil) in a volume (m^{-3}) and there would be an expected number of interactions in a traversed distance (m) through the volume. In this way the cross section is an effective area defining a probability of interaction. The cross section for typical processes of interest in pp-collisions at ATLAS are measured in barns (10^{-24} cm^2), for example at 13 TeV [29] for the three leading backgrounds in these analyses: Z (58.8 nb), W (190.1 nb), and $t\bar{t}$ (818 pb). Cross sections of SM high energy processes depend on the energy of the collision, the basis for exploring the structure of the SM at various and increasing energy. The amount of collision data taken is usually expressed in inverse femtobarns (fb^{-1}) or the number of collisions given (possibly variable) beam conditions in which a single event with a cross section of 1 fb would be expected.

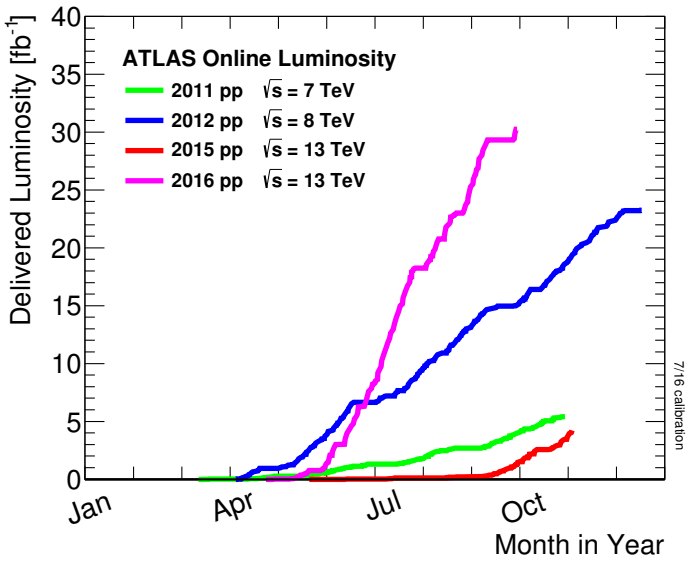

Figure 1.5: Integrated luminosity collected by the ATLAS experiment in 2016. More data has been collected in the last 3 months than in all of Run 1.

ATLAS recorded 3.2 fb^{-1} in 2015, and added 10.0 fb^{-1} in the first few months of data-taking of 2016–this is roughly what Fermilab recorded in its decade of operation and half of what was recorded in all of Run 1. As the instantaneous luminosity (e.g. 10 nb$^{-1}s^{-1}$ = 10^{34} cm$^{-2}s^{-1}$) increases the expected number of interactions per bunch crossing increases proportionally. SM processes are dominated by lower energy quantum chromodynamic (QCD) scattering responsible for a characteristic signature of 2 jets (see Chapter 2) in the detector. On average, more than 20 of these interactions (just strong enough to register in the forward-most parts) in the detector were present in each event in Run 2 conditions corresponding to the day-to-day peak luminosities and total integrated luminosity [30] shown in Figure 1.5. Since the cutoff in mid-July for the public results shared in this thesis, the 2016 data set has tripled.

It is clear from Fig. 1.5 (a) that almost all the data used here was collected in the last month of running the LHC (mid-June through mid-July 2016). With this one month, the results are an improvement over years of data taken at lower CME. By increasing energy the cross section (due to increased available phase space) of higher mass resonances is improved. Additionally, immediate results like these early

searches are valuable, even if the analysis is simple, due to the unprecedented energy, not only for the limits set but for the detailed look into the SM distributions that form the background of a search. Quick feedback to the community is necessary to illuminate the shortcomings in understanding the backgrounds to a search as input for later more sophisticated analyses. It will become clear in Chapter 4 that the simulation of backgrounds in these analyses is not always great and, in the case of backgrounds to the VBF channels in particular, is far off.

In the long term, the LHC plans to deliver 300 times this quantity of data, or 3 inverse attobarns (ab^{-1}) by 2035. To collect this amount of data in a reasonable period of time the luminosity will be increased according to the schedule in Fig. 1.4. After LS3 it will rise to somewhere from 5 to 10 times the current rate; LS3 will be the transition to the high luminosity LHC (HL-LHC) expected to begin operation in 2026. The target luminosity for the HL-LHC is set at $\mathcal{L} = 5 \times 10^{34}$ $cm^{-2}s^{-1}$ but recent work has shown that $\mathcal{L} = 7.5 \times 10^{34}$ $cm^{-2}s^{-1}$ is an achievable goal [31]. At $\mathcal{L} = 5 \times 10^{34}$ $cm^{-2}s^{-1}$ there would be $\mu = 140$ additional min bias interactions per bunch crossing, and at the $\mathcal{L} = 7.5 \times 10^{34}$ $cm^{-2}s^{-1}$ there would be $\mu = 200$. Specific plans for the operations of LHC and ATLAS under HL-LHC conditions are in the process of being made through simulation of these conditions. Plans for various new detectors from calorimeters to inner detector tracking to muon spectrometer upgrades are underway.

The uncertainties in this analysis are driven by jet reconstruction, performance, and resolution within the calorimeters. One of the key tasks in these analyses (and for the whole ATLAS collaboration) has been to provide the calibration of and uncertainties for jets in the calorimeters. This is a unique challenge at varying luminosity conditions, not only in the transition from Run 1 to Run 2 but also in projection to HL-LHC conditions.

1.4 Thesis Outline

The Standard Model of particle physics and the details of its extensions with the simplified models studied are summarized in Chapter 2. The ATLAS detector is outlined in Chapter 3. Chapter 4 introduces the methods of MC simulation used in estimating backgrounds and evaluating uncertainties. Chapter 5 is devoted to a detailed derivation of jets and their uncertainty used in all analyses of Run 2. Chapter 6 describes the details of the searches made. Chapter 7 sets experimental limits on the cross sections of 3 benchmark models for decay to the $\ell\ell qq$ and $\nu\nu qq$ channels.

Chapter 2

Theory

There is evidence for four fundamental forces in nature: the strong, weak, electromagnetic, and gravitational forces. The Standard Model of particle physics (SM) unifies the first three forces in a gauged field theory with symmetries belonging to the group representation SU(3) × SU(2) × U(1). This chapter outlines the SM, elaborating on points relevant to the discussion of its extensions treated in this thesis. The forms of terms in the following discussion are taken from PDG [32] where possible.

2.1 Standard Model

The SM Lagrangian can be written as the sum of the Lagrangian of Quantum Chromodynamics (QCD), the theory of the strong interaction, electroweak physics which combines the weak theory with electromagnetism, and Higgs terms which provide the mechanism for electroweak symmetry breaking (EWSB)[1]

$$\mathcal{L}_{SM} = \mathcal{L}_{QCD} + \mathcal{L}_{EW} + \mathcal{L}_{\text{Higgs}} \tag{2.1}$$

Quantum Chromodynamics

The QCD Lagrangian,

$$\mathcal{L} = \sum_q \bar{\psi}_{q,a}(i\gamma^\mu \partial_\mu \delta_{ab} - g_s \gamma^\mu t^C_{ab} \mathcal{A}^C_\mu - m_q \delta_{ab})\psi_{q,b} - F^A_{\mu\nu} F^{A\ \mu\nu}, \tag{2.2}$$

[1]The following will ignore additional corrective terms necessary to make the quantum field calculations work in various schemes.

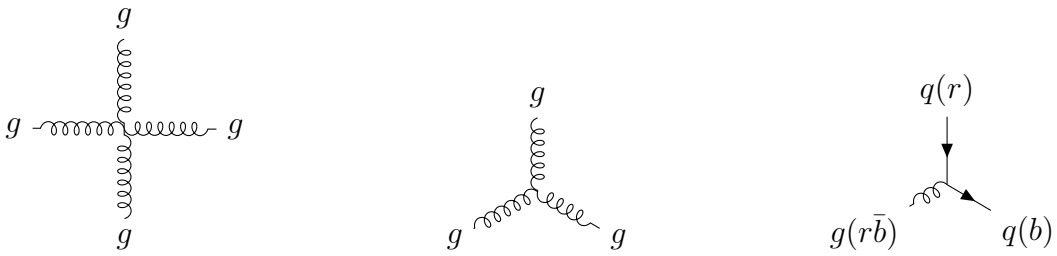

(a) 4-gluon vertex (b) 3-gluon vertex (c) gluon

Figure 2.1: Tree level Feynman diagrams for the interaction terms of the theory of QCD.

where γ are Dirac's matrices and the spinor field carries indices for three quark flavors, q, and three color-indices, a. The group structure of QCD is the SU(3) component of the SM. The $N_c^2 - 1 = 8$ gluon fields, $\mathcal{A}_\mu^C$, encode this structure by way of contracting the index C with the corresponding 3×3 matrices, t_C^{ab} that are the generators of SU(3). Consequently, each interaction of the gluon field with a quark can be understood as performing a rotation in SU(3), or in other words changing its color. g_s is the QCD coupling constant. It is the only fundamental free parameter of QCD other than the experimentally determined quark masses. The last term in the Lagrangian makes use of the field strength tensor,

$$F_{\mu\nu}^A = \partial_\mu \mathcal{A}_\nu^A \partial_\nu \mathcal{A}_\mu^A - g_s f_{ABC} \mathcal{A}_\mu^B \mathcal{A}_\nu^C \qquad [t^A, t^B] = f_{ABC} t^C, \tag{2.3}$$

which encodes the kinetic and self-interacting terms of the gluon fields. The f_{ABC} are the structure constants of the Lie algebra.

There are two key features to the phenomenology of the strong interaction, asymptotic freedom and confinement.

Asymptotic Freedom Asymptotic freedom is a direct result of the self-coupling terms in the Lagrangian. In terms of Feynman diagrams these are the 3 and 4-gluon vertices, Fig. 2.1. For sufficiently high momentum transfer the theory can be treated perturbatively (pQCD). Observables can be expressed in orders of $\alpha_s(\mu_R^2) = \frac{g_s^2(\mu_R^2)}{4\pi}$ where μ_R is the renormalization scale. The coupling constant, g_s, "runs" under renor-

malization, which is to say that it changes depending on the scale of the momentum transfer, Q, in the interaction, i.e. $\alpha_s(\mu_R^2 = Q^2)$ gives the effective interaction strength at that scale. This works in probing small distance measures, or "hard" processes, the coupling becomes small for these terms and thus the perturbation converges quickly for the smallest length scales; hence it is a valid theory for use at arbitrarily high energy.

Confinement While the coupling constant becomes small at short distance and high momenta, it continues to grow linearly for large distance. The consequences of this can be calculated from lattice QCD (iterative computation by discretization of the field theory) and results in hadronization: it is energetically disfavored to find a lone quark and therefore they hadronize, forming groups of 2 (mesons) or 3 (baryons) or more in final decay products. This process pulls quarks from quark-antiquark pairs in the vacuum. Specific hadron masses can be calculated from lattice QCD but so far one cannot calculate directly the evolution of quarks to hadrons across energy scales and only rough models are employed to estimate these processes in the simulation of inelastic scattering.

The LHC collides protons in a process called deep inelastic scattering. The parton theory of hadron collisions is used as the basis for calculations in this energy regime. It was proposed by Feynman [33] prior to understanding that the point particles therein are the quarks and gluons governed by the field theory of Eq. 2.2. It is a simplification that allows the calculation of scattering cross sections from first order pQCD, $\hat{\sigma}_{ij}$, for the hardest processes and absorbs the softer processes, which one could not calculate in perturbation theory, into an experimentally determined probability density functions, known as parton distribution functions (PDFs). The parton model gives the complete cross section of a process,

$$\sigma = \sum_{i,j} \int_0^1 dx_1 \int_0^1 dx_2 f_i(x_1, \mu_F^2) f_j(x_2, \mu_F^2) \hat{\sigma}_{ij}(x1, x2, \mu_R^2, \mu_F^2), \tag{2.4}$$

in terms of longitudinal fractional momentum, x, of the hadron carried by flavor, i, j. The partonic cross section, $\hat{\sigma}_{ij}(x1, x2, \mu_R^2, \mu_F^2)$, and the PDFs $f_i(x_1, \mu_F^2)$ depend on the factorization scale, μ_F, which defines the cutoff between collinear (i.e. soft) interactions absorbed into the PDF, and those harder interactions handled in pQCD. For a given factorization scale the PDFs are meaningful, in that they are transferable from process to process (e.g. from photon emission from an electron to proton - proton collision) and can therefore be built from the aggregate of experimental results. In the limit of infinite momentum transfer, known as the Bjorken limit–the target is Lorentz contracted to 0 and the interaction occurs instantaneously, which means that the PDF becomes a function of x for any interaction, i.e. $f_i(x_1, \mu_F^2, Q^2) \to f_i(x_1, \mu_F^2)$ where Q^2 is the square of the transferred momentum used to indicate the scale of the interaction. For the precision required in ATLAS experiment, this limit is not sufficiently satisfied for all the relevant processes and the PDFs are still parametrized by Q^2. Figure 2.2 shows the PDFs used in much of the MC for the following analyses. The notable dependence on Q^2 for low x is apparent in the different curves at the two different Q^2 shown. Beyond leading order (LO) calculations predict the logarithmic divergences that result in the different curves at different scale.

QCD is a theory that is simply stated in the Lagrangian formalism but happens to be laborious for making calculations. Modern usage of the theory are significantly more complicated than the simplified picture given above. Calculations are made with MC simulation that starts with the initial hard tree-level scattering and then layer many processes and corrections including,

- initial and final state radiation through parton showering ,
- hadronization through additional showering through scales below the applicability of pQCD
- and simulation of the underlying event including the remnants of the proton-proton collision.

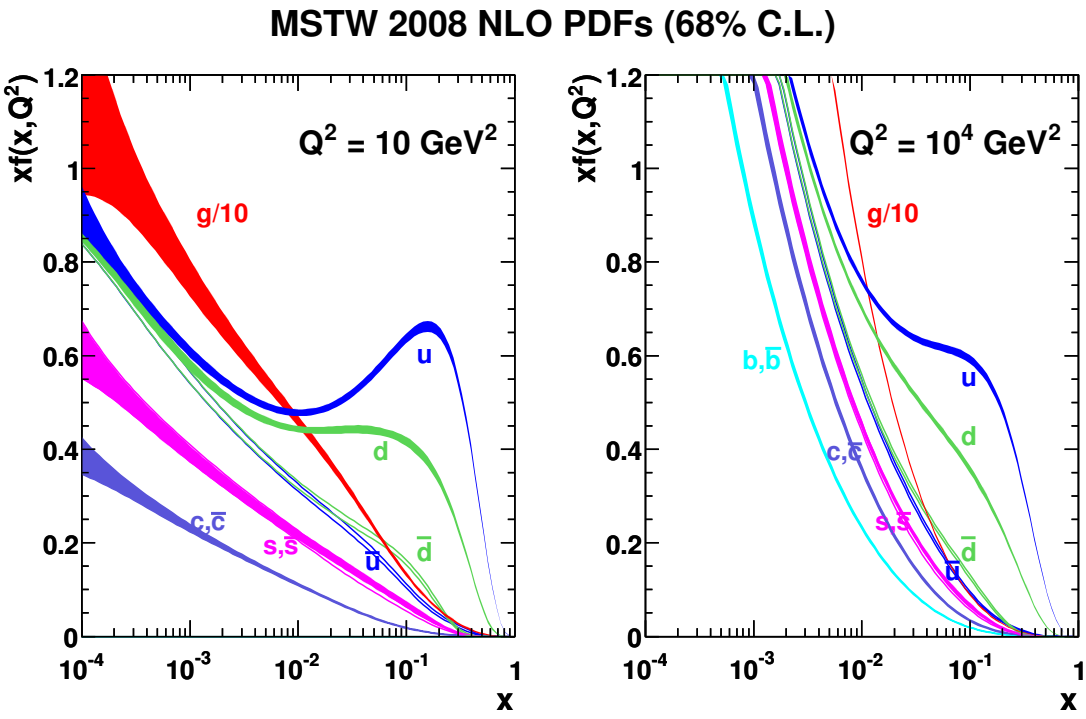

Figure 2.2: PDFs in the MSTW2008 set used in this analysis [34].

All these tools will be discussed in the Simulation Chapter 4 as they apply to the specific MC simulations used in the analysis presented in this thesis.

Electroweak Theory

The electroweak theory of the SM was formulated by Glashow, Weinberg, and Salam in the early 60's in order to explain the precision weak results obtained at the time. The theory explained the apparent charged weak current and predicted the neutral current, which was subsequently observed at CERN in 1973 [35] through the observation of neutral interactions that didn't involve a muon or electron at the Gargamelle experiment. Glashow unified the weak and electromagnetic interactions by suggesting a triplet of vector bosons mediating the weak force in addition to the massless photon [36] mediating the electromagnetic force. He explained in the structure of his field theory the conserved quantities of weak isospin and weak hypercharge with-

out including an explanation for the apparently high mass of the vector bosons that would arise from the experimentally observed short interaction distance of the weak force. Weinberg and Salam utilized the Higgs mechanism of symmetry breaking [3, 4] to impart masses on the 3 vector bosons of Glashow's theory and put the fields in the form currently accepted as the SM [37, 38]. A key prediction of this model is the ratio of masses of the neutral ($m_Z = 91.188 \pm 0.002$ GeV) and charged vector bosons ($m_{W^\pm} = 80.43 \pm 0.04$ GeV) that was confirmed when both were discovered at CERN in the UA1 and UA2 experiments in 1983 [39].

The electroweak theory of the SM is governed by the gauge symmetry $\mathrm{SU}(2)\times\mathrm{U}(1)$ with 3 gauge bosons $W^{1,2,3}$ forming the triplet of SU(2) and the boson, B, the U(1) symmetry. The Lagrangian for the gauge bosons is then,

$$\mathcal{L}_B = -\tfrac{1}{4} W^{i\mu\nu} W^i_{\mu\nu} - \tfrac{1}{4} B^{\mu\nu} B_{\mu\nu}, \tag{2.5}$$

where the covariant field strength tensors for the SU(2) and U(1) gauge freedoms are respectively,

$$\begin{aligned} W^i_{\mu\nu} &= \partial_\mu W^i_\nu - \partial_\nu W^i_\mu - g\epsilon^{ijk} W^j_\mu W^k_\nu, \\ B_{\mu\nu} &= \partial_\mu B_\nu - \partial_\nu B_\mu, \end{aligned} \tag{2.6}$$

where g is the weak coupling constant. There are three families of fermions ($i = 1, 2, 3$ in the following); their properties are summarized in Table 2.1. The weak interaction is a chiral theory where left-handed[2] fermions[3] transform as a doublet, for leptons $\Psi_i = \begin{pmatrix} \nu_i \\ \ell_i^- \end{pmatrix}$ and quarks $\begin{pmatrix} u_i \\ d'_i \end{pmatrix}$. In the second doublet, the Cabibbo-Kobayashi-Maskawa (CKM) mixing matrix is a unitary matrix defining the mixing of down-type quarks, $d'_i \equiv \sum_j V_{ij} d_j$, where only four independent parameters are needed to fully describe it: the 3 Euler angles of a rotation and a single additional phase to

[2]Particle spin is in the same direction as momentum.

[3]And right-handed anti-fermions

Leptons			
family	mass		charge
ν_e electron neutrino	< 2	eV	0
e electron	$0.510998928 \pm 0.000000011$	MeV	$-1e$
ν_μ muon neutrino	< 0.19	MeV	0
μ muon	$105.6583715 \pm 0.0000035$	MeV	$-1e$
ν_τ tau neutrino	< 18.2	MeV	0
τ tau	1776.86 ± 0.12	MeV	$-1e$
Quarks			
flavor	mass		charge
u up	$2.3^{+0.7}_{-0.5}$	MeV	$\frac{2}{3}e$
d down	$4.8^{+0.5}_{-0.3}$	MeV	$\frac{-1}{3}e$
c charm	1.275 ± 0.025	GeV	$\frac{2}{3}e$
s strange	95 ± 5	MeV	$\frac{-1}{3}e$
t top	$173.21 \pm 0.51 \pm 0.71$	GeV	$\frac{2}{3}e$
b bottom	4.18 ± 0.03	GeV	$\frac{-1}{3}e$

Table 2.1: Fermions, the constituents of matter in the SM. Masses are taken from the most recent fits by PDG [32]. All masses are quoted in the modified minimal subtraction [40] scheme, $\overline{\text{MS}}$ except the top which is from direct measurement.

accommodate CP-violation. The standard parametrization is,

$$\begin{bmatrix} \cos\theta_{12}\cos\theta_{13} & \sin\theta_{12}\cos\theta_{13} & \sin\theta_{13}e^{-i\delta_{13}} \\ -\sin\theta_{12}\cos\theta_{23} - \cos\theta_{12}\sin\theta_{23}\sin\theta_{13}e^{i\delta_{13}} & \cos\theta_{12}\cos\theta_{23} - \sin\theta_{12}\sin\theta_{23}\sin\theta_{13}e^{i\delta_{13}} & \sin\theta_{23}\cos\theta_{13} \\ \sin\theta_{12}\sin\theta_{23} - \cos\theta_{12}\cos\theta_{23}\sin\theta_{13}e^{i\delta_{13}} & -\cos\theta_{12}\sin\theta_{23} - \sin\theta_{12}\cos\theta_{23}\sin\theta_{13}e^{i\delta_{13}} & \cos\theta_{23}\cos\theta_{13} \end{bmatrix} \tag{2.7}$$

with $\theta_{12} = 13.04 \pm 0.05°$, $\theta_{13} = 0.201 \pm 0.011°$, $\theta_{23} = 2.38 \pm 0.0°$, and $\delta_{13} = 1.20 \pm 0.08$. The right handed fermion fields on the other hand, transform as singlets under SU(2).

The Lagrangian is most transparently represented *after* spontaneous symmetry breaking by the addition of the Higgs doublet field, which will be described in the following subsection. What remains is a Higgs scalar, h, in the physical particle spectrum, that gets a vacuum expectation value (VEV) $v/\sqrt{2} = 246$ GeV. The Lagrangian

for the fermions, ψ_i, is then written,

$$\begin{aligned}\mathcal{L}_F = &\sum_i \bar{\psi}_i \left(i\partial\!\!\!/ - m_i - \frac{m_i H}{v} \right) \psi_i \\ &- \frac{g}{2\sqrt{2}} \sum_i \bar{\Psi}_i \gamma^\mu (1-\gamma^5)(T^+ W_\mu^+ + T^- W_\mu^-) \Psi_i \\ &- e \sum_i Q_i \bar{\psi}_i \gamma^\mu \psi_i A_\mu \\ &- \frac{g}{2\cos\theta_W} \sum_i \bar{\psi}_i \gamma^\mu (g_V^i - g_A^i \gamma^5) \psi_i Z_\mu\end{aligned} \tag{2.8}$$

The Weinberg angle, θ_W, relates the electric charge $e = g \sin\theta_W$ to the weak coupling constant. θ_W is the angle by which the spontaneous symmetry breaking rotates the plane defined by the uncharged gauge bosons $W^3 - B$–the rotation is apparent in the form of Eq. 2.9 to obtain the familiar massive neutral Z and massless A (γ) bosons. The observable gauge fields in the Lagrangian arise from those defining the initial gauge symmetries:

$$\begin{aligned}\begin{pmatrix} A \\ Z \end{pmatrix} &\equiv \begin{pmatrix} \cos\theta_W & \sin\theta_W \\ -\sin\theta_W & \cos\theta_W \end{pmatrix} \begin{pmatrix} B \\ W^3 \end{pmatrix}, \\ W^\pm &\equiv (W^1 \mp i W^2)/\sqrt{(2)},\end{aligned} \tag{2.9}$$

with their masses from tree level, given as,

$$\begin{aligned}M_W &= \frac{ev}{2\sin\theta_W}, \\ M_Z &= \frac{ev}{2\sin\theta_W \cos\theta_W} = \frac{M_W}{\cos\theta_W}, \\ M_\gamma &= 0.\end{aligned} \tag{2.10}$$

γ is the massless gauge boson arising from the $\mathrm{U}(1)_Y$ gauge symmetry still present in the (Yang-Mills) theory of electromagnetism after EWSB. The first term in Eq. 2.8 is the kinetic term. It is diagonal in flavor, implements the masses of fermions, and defines the coupling of the fermions to Higgs, which consequently defines an incredibly simple relationship between the coupling of the fermions to the Higgs and the masses of the vector bosons and fermions. This is Yukawa coupling which generates the

masses of the fermions through coupling with the Higgs but still adds no additional insight into the wide variation of the couplings.

The weak interactions involving weak isospin transitions, are described by the second term of Eq. 2.8. This term makes use of the T^+ and T^- raising and lowering operators in weak isospin space, defining the couplings as those between upper and lower states of the fermion doublets for interactions with the charged vector bosons. Consequently, W decays to an up and down type pair of weak isospin doublets. One can read from this term at tree level that when considering kinematically allowed decay to leptons and quarks there are 6 options for up-down pairs of quarks–there is no top; it is too heavy–and 3 options for leptons. Therefore the branching is twice that to quarks than leptons. The square of a given CKM matrix element–recall that it is unitary–defines the coupling between each pair of up and down quark.

The third term is the electromagnetic interactions of Quantum Electrodynamics (QED), where Q_i is the electric field charge and A^μ is the electromagnetic four-potential.

The last term covers interactions with the neutral boson, Z, where the vector and axial vector couplings $g_V^i \equiv t_{3L}(i) - 2Q_i \sin^2\theta_W$ and $g_A^i \equiv t_{3L}(i)$, respectively. The $t_{3L}(i)$ is the weak isospin and Q_i the electric charge. The Z boson decays to fermion

	Coupling			
Decay Products	L	R	Vertex Factor	BR
Leptonic				
neutral ($\nu_{e\mu\tau}$)	$1/2$	0	$(1/2)^2$	6.8%
charged ($e\mu\tau$)	$-1/2 + \sin^2\theta_W$	$\sin^2\theta_W$	$(-1/2 + \sin^2\theta_W)^2 + (\sin^2\theta_W)^2$	3.4%
Hadronic				
up-type (uc)	$1/2 - 2/3\sin^2\theta_W$	$1/3\sin^2\theta_W$	$3(1/2 - 2/3\sin^2\theta_W)^2 + 3(-2/3\sin^2\theta_W)^2$	11.8%
down-type (dsb)	$-1/2 + 1/3\sin^2\theta_W$	$-2/3\sin^2\theta_W$	$3(-1/2 + 1/3\sin^2\theta_W)^2 + 3(1/3\sin^2\theta_W)^2$	15.2%

Table 2.2: Z boson decay: couplings and branching ratio to fermions.

and anti-fermion pairs. Playing the same game for the Z as for the W above at tree level, the branching when including right (R) and left (L)-handed fields is given in Table 2.2.

2.2 Electroweak Symmetry Breaking and Higgs Fields

Spontaneous symmetry breaking is the mechanism responsible not only for the large mass of the massive gauge bosons and for the fermions through the Yukawa couplings in the SM but also serves the same function in most of the extensions of the SM. Previously, the Lagrangian for the electroweak theory was shown after symmetry breaking. Here the mechanism of symmetry breaking of the Higgs doublet field is briefly described.

The Higgs complex doublet, can be written explicitly as four scalar fields,

$$\begin{pmatrix} \phi^+ \\ \phi^0 \end{pmatrix} = \begin{pmatrix} \phi_1 + i\phi_3 \\ \phi_2 + i\phi_4 \end{pmatrix}, \tag{2.11}$$

where the up state is electrically charged. The space of the Higgs doublet is then associated with electric charge and the generator of electric charge can be defined,

$$Q \equiv T^3 + Y, \tag{2.12}$$

with T^3 being the generator of weak isospin and Y the generator weak hypercharge (the U(1) symmetry of B). The electric charge generator is defined as the sum of the generators of SU(2) and U(1) rotations of the raw fields W^i and B.

The Higgs Lagrangian is constructed invariant under local SU(2) $\times$ U(1) transformation:

$$\mathcal{L}_{\text{Higgs}} = (\partial^\mu \phi^\dagger + igW_\mu \cdot T\phi - \tfrac{1}{2} ig' B_\mu \phi) - \mathcal{V}(\phi^\dagger \phi). \tag{2.13}$$

The Higgs potential,

$$\mathcal{V}(\phi^\dagger \phi) = \lambda(\phi^\dagger \phi)^2 - \mu^2 \phi^\dagger \phi, \tag{2.14}$$

where the minimum occurs for $\phi \neq 0$ when $\mu^2 > 0$. In the space of the four ϕ scalars, there is a degenerate circle of minima, $|\phi| = \sqrt{\frac{\mu^2}{2\lambda}} \equiv \frac{v}{\sqrt{2}}$. Reparametrizing the field

makes it possible to consider perturbation around the minimum of the potential in the radial direction of the degenerate circle:

$$\phi = U^{-1}(\xi) \begin{pmatrix} 0 \\ (H+v)/\sqrt{(}2) \end{pmatrix} \tag{2.15}$$

$$U(\xi) = \exp(-iT \cdot \xi/v). \tag{2.16}$$

H is the familiar Higgs field introduced in the previous subsection. The other three fields are wrapped up in ξ and become the longitudinal degrees of freedom for the massive gauge bosons after the following gauge transformation:

$$\phi \to U(\xi)\phi \tag{2.17}$$

$$T \cdot W^{\mu} \to UT \cdot W^{\mu}U^{-1} + \frac{i}{g}(\partial^{\mu}U)U^{-1}. \tag{2.18}$$

The reason for this specific transformation is to remove the ξ degrees of freedom from the Higgs Lagrangian altogether. The result is the "eating" of 3 of the 4 Goldstone bosons [41] arising from the gauge degrees of freedom by 3 of the 4 Higgs fields. The Lagrangian restated in the *unitary gauge*–that is fixed in the direction of the vacuum expectation value, X,

$$\begin{aligned} \mathcal{L}_{\text{Higgs}} &= \tfrac{1}{2}\partial_{\mu}H\partial^{\mu}H - \mathcal{V}\Big(\frac{(v+H)^2}{2}\Big) \\ &+ \frac{(v+H)^2}{8}X^{\dagger}(2gT \cdot W_{\mu} + g'B_{\mu})(2gT \cdot W^{\mu} + g'B^{\mu})X, \\ &= \tfrac{1}{2}\partial_{\mu}H\partial^{\mu}H - \mu^2H^2 = \lambda v H^3 - \tfrac{1}{4}\lambda H^4 \\ &+ \frac{(v+H)^2}{8}\Big[(gW^3_{\mu} - g'B_{\mu})(gW^{3\mu} - g'B^{\mu}) + 2g^2W^-_{\mu}W^{+\mu}\Big] \end{aligned} \tag{2.19}$$

The propagator for the B and W^3 fields is not diagonal then. Redefining the fields with a rotation according to the Weinberg angle, θ_W gives the mass terms for the massive gauge bosons in their diagonal and familiar form,

$$\mathcal{L}_{\text{Higgs}} \ni \frac{g^2v^2}{4}W^+_{\mu}W^{-\mu} + \frac{(g^2+g'^2)v^2}{8}Z_{\mu}Z^{\mu} \tag{2.20}$$

The W and Z bosons have acquired mass;

$$M_W = \tfrac{1}{2} = vg = \cos\theta_W M_Z. \tag{2.21}$$

The Higgs mass is still not directly constrained and depends on free parameter λ:

$$M_H = \sqrt{2}\mu \equiv \sqrt{2\lambda}v. \tag{2.22}$$

This is the simplest possible implementation of the Higgs mechanism, the minimal model. The following three sections discuss possible extensions to the SM outlined above, among them are more complicated Higgs sectors.

2.3 Additional Heavy Scalar in the Higgs Sector

Immediately after the Higgs discovery in 2012, the motivation for a heavy scalar or additional heavy Higgs, H, within the Higgs sector was an especially attractive concept for experimental study. Models of this sort are relevant precisely because the scalar would share the branching ratio with the light Higgs, h, through mixing induced by spontaneous symmetry breaking. Measurements on the h cross section, σ_h, and any deviation from the expected value in the SM would indicate the possible presence of an additional heavy scalar in the Higgs sector. The simplest extension of the SM Higgs sector adds an electroweak singlet field (EWS) to the Higgs doublet field. In this model both fields acquire non-zero VEVs through spontaneous symmetry breaking. Consequently there is mixing between the singlet state and the doublet. Both the heavy Higgs, H, and h in this model couple like the SM Higgs. Due to unitarity, the coupling of the light Higgs would be reduced by a factor of κ where κ and κ', the H coupling, would satisfy the following constraint:

$$\kappa^2 + \kappa'^2 = 1. \tag{2.23}$$

This simplest model is no longer well motivated due to σ_h and its couplings being so tightly constrained by measurements in Run 1 from the ATLAS and CMS exper-

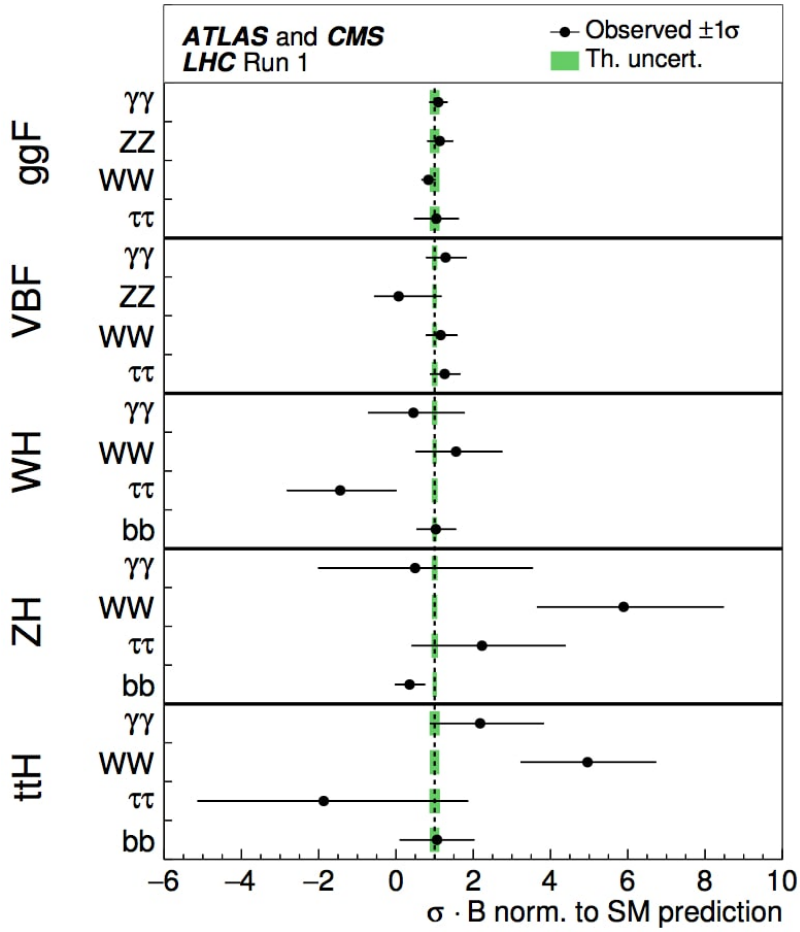

Figure 2.3: Major branching ratio of the Higgs measured at the LHC [5].

iments. For similar reasons the two Higgs doublet models, requiring an additional Higgs doublet, also do not seem to be particularly well motivated any longer as it generally predicts changes in the relative BRs to various decay channels which have not been observed. Figure 2.3 illustrates the high degree to which all the major BRs of the Higgs have been shown to be in agreement with the SM cross section σ_{SM} at the LHC. This result of course does not eliminate the possibility of an extended Higgs sector and certainly does not remove the possibility of a scalar resonance of another type. A scalar benchmark phenomenological model was used for the combination of channels in this 2016 ATLAS search [27]. A search for scalar particles is a fundamental endeavor at the LHC from an experimental perspective and in the following analysis the scalar resonance is treated as if it were a heavy Higgs boson with the

corresponding cross sections and BRs in the narrow width approximation (NWA). A heavy Higgs is CP-even, spin-0, and the narrow width, once convoluted with the experimental resolution, is trivial.

The Higgs signals used in this analysis are produced in two production channels, gluon-gluon fusion (ggF) and vector boson fusion (VBF)–the leading order diagrams are shown in Figs. 1.2 (a) and (b) respectively. The two production modes have distinct event topologies. Specifically, the VBF events are characterized by the presence of the two scattered quark jets in the detector arising from the interacting initial state quarks. This forms the basis for discrimination between the two searches. The relative production rates of the two modes is model specific and therefore the searches are made independently. *A priori* the VBF search is assumed to be a smaller branching ratio and the resulting limits must be set in the presence of the ggF signal.

2.4 Heavy Vector Triplet

The second model used is based on the Heavy Vector Triplet (HVT) phenomenological Lagrangian [7]. It adds a triplet of heavy vector bosons with degenerate mass, shown in the familiar adjoint representation of $\mathrm{SU}(2)_L$ with two electrically charged states and a neutral state:

$$V_\mu^\pm = \frac{V_\mu^1 \mp i V_\mu^2}{\sqrt{2}}, V_\mu^0 = V_\mu^3, \tag{2.24}$$

in terms of the real vectors V_μ^a, $a = 1, 2, 3$. The Lagrangian describes a large class of models where the HVT mixes with the SM heavy gauge bosons:

$$\begin{aligned}\mathcal{L}_V = &-\tfrac{1}{4} D_{[\mu} V_{\nu]}^a D^{[\mu} V^{\nu]a} + \frac{m_V^2}{2} V_\mu^a V^{\mu a} \\ &+ i g_V c_H V_\mu^a H^\dagger \tau^a \overleftrightarrow{D}^\mu H + \frac{g^2}{g_V} c_F V_\mu^a J_F^{\mu a} \\ &+ \frac{g_V}{2} c_{VVV} \epsilon_{abc} V_\mu^a V_\nu^b D^{[\mu} V^{\nu]c} + g_V^2 c_{VVHH} V_\mu^a V^{\mu a} H^\dagger H - \frac{g}{2} c_{VVW} \epsilon_{abc} W^{\mu\nu a} V_\mu^b V_\nu^c,\end{aligned} \tag{2.25}$$

with the covariant derivatives in the first term,

$$D_{[\mu}V^a_{\nu]} = D_\mu V^a_\nu - D_\nu V^a_\mu, \qquad D_\mu V^a_\nu = \partial_\mu V^a_\nu + g\epsilon^{abc} W^b_\mu V_n u^c. \tag{2.26}$$

The g is the SM $\mathrm{SU}(2)_L$ gauge coupling and the g_V coupling (representing the typical strength of V interactions) is allowed to range from *weakly* coupled case, $g_V \sim 1$, to *strongly* coupled case, $g_V \simeq 4\pi$. The V^a_μ aren't mass eigenstates and will mix with the W^a_μ after EWSB and therefore m_V does not coincide with the mass of the resonance. The second line in Eq. 2.25 allows interactions of V with the Higgs current, $iH^\dagger\tau^a \overleftrightarrow{D}^\mu H$[4], and with the left-handed fermionic currents, $J^{\mu a}_F = \sum_f \bar{f}_L \gamma^\mu \tau^a f_L$. The Higgs current term, c_H, leads to vertices with the three unphysical Goldstone bosons eaten in EWSB. From the Equivalence Theorem [42] this therefore defines the coupling with the longitudinal degrees of freedom (DoF) of SM vector bosons W and Z. Likewise, c_F defines the interaction with fermions. The third line contains terms with two or more V and therefore do not contribute directly to V decay; nor do they contribute to the production of V at the LHC. Therefore the factors in the vertices, g_V and $g^2/g_V c_F$ can more-or-less be taken as the fundamental parameters of the general model, and the interpretation of results with respect to them is sufficient to characterize the limits of models within this general framework.

Equation 2.25 is the most general Lagrangian compatible with the SM gauge invariance and the CP symmetry restricted to to operators of energy dimension ≤ 4. In the case of relatively small coupling $g_V \sim 1$ the expected resonances are narrow and are expected in the TeV range. Relying on another argument based on the Equivalence Theorem, the decays to SM gauge bosons in the TeV range are dominated by the longitudinal modes. To first order the branching ratio for the charged modes to SM gauge bosons is,

$$\Gamma_{V^\pm \to W^\pm_L Z_L} \simeq \frac{g_V^2 c_H^2}{192\pi}. \tag{2.27}$$

[4] $\overleftrightarrow{D}^\mu = \overleftarrow{D}^\mu - \overrightarrow{D}^\mu$

Since decay to SM vector bosons is determined entirely by the $g_V c_H$ term, to first order (with respect to finite mass effects) all the branching ratios of the HVT to two bosons are equal, Table 2.3. The neutral diboson states that are not listed in Table 2.3

Partial Decay Width	Relative BR
$\Gamma(V^{\pm} \to W_L^{\pm} Z_L)$	1
$\Gamma(V^{\pm} \to W_L^{\pm} H)$	1
$\Gamma(V^0 \to W_L^{\pm} W_L^{\mp})$	1
$\Gamma(V^0 \to Z_L H)$	1

Table 2.3: Relative BRs of HVT decay to two SM bosons.

are forbidden or suppressed. For example, the $V^0 \to HH$ decay is forbidden by spin considerations and $V^0 \to ZZ$ is missing at dimension 4.

Used for the specific signal in this thesis is "Model A" in the HVT scheme, a model originally considered to potentially allow for gauge bosons of significantly *lower* mass than the SM gauge bosons which had not yet been discovered at the time [43]. It is equally capable of describing a triplet of significantly *heavier* gauge bosons. The HVT emerges from a symmetry breaking, $SU(2)_1 \times SU(2)_2 \times U(1)_Y \to SU(2)_L \times U(1)_Y$ through a linear σ-model. The parameter g_V is set to 1 and constraints from QFT require then that $C_H \sim -g^2/g_V^2$ and $c_F \sim 1$ so the results can be translated directly into two key parameters of the model that are mentioned above. The resulting theoretical width of the resonance across the entire range considered in this analysis in the qq production mode (Fig. 1.3 (a)), $500 - 5000$ GeV, is $\Gamma/M \simeq 2.5\%$.

2.5 Bulk Randall-Sundrum Graviton

The bulk Randall-Sundrum (RS) model is a model with a warped extra dimension used to explain the Planck-weak hierarchy [17, 18]. The original RS model is a simplified model postulating that the 4D spacetime "brane" in which the SM is formulated is a subspace in larger 5-dimensional space along with one other brane, a realm of

hidden physics. The fifth (warped) dimension that separates the two branes is given an exponential factor in the spacetime metric,

$$ds^2 = e^{-2kr_c\phi}\eta_{\mu\nu}dx^\mu dx^\nu + r_c^2 d\phi^2. \tag{2.28}$$

Here k is a scale of the order of the Planck scale, x^μ are the familiar 4D spacetime coordinates. The ϕ-coordinate is periodic and takes a value $-\pi < \phi < \pi$, spanning the extra dimension with spatial size r_c. The visible brane is located at (limited to) $\phi = 0$ and the other hidden brane is located at $\phi = \pi$ and gravitation propagates freely between. The five-dimensional metric G_{MN} with $M, N \in \{\mu, \phi\}$ gives rise to the hidden and visible 4D metrics, which are confined to their respective branes:

$$\begin{aligned} g^{\text{vis}}_{\mu\nu}(x^\mu) &\equiv G_{\mu\nu}(x^\mu, \phi = \pi), \\ g^{\text{hid}}_{\mu\nu}(x^\mu) &\equiv G_{\mu\nu}(x^\mu, \phi = 0). \end{aligned} \tag{2.29}$$

Writing the classical action as the sum of the gravitational action and the action of whatever physics confined to the two branes,

$$S = S_{\text{vis}} + S_{\text{hid}} + S_{\text{gravity}} \tag{2.30}$$

$$= \int d^4x \Big(\sqrt{-g_{\text{vis}}}\{\mathcal{L}_{\text{vis}} - V_{\text{vis}}\} + \sqrt{-g_{\text{hid}}}\{\mathcal{L}_{\text{hid}} - V_{\text{hid}}\} + \int_{-\pi}^{\pi} d\phi \sqrt{-G}\{-\Lambda + 2M^3 R\} \Big) \tag{2.31}$$

Here Λ is the cosmological constant and V_{hid}, V_{vis} are vacuum energies that act as a gravitational source even in the absence of particle excitations. The bulk metric in, Eq. 2.29, is a solution for the Einstein equations with the above action that satisfy Poincaré invariance. Satisfying the Poincaré invariance imposes a fine tuning on the cosmological constant:

$$V_{\text{hid}} = -V_{\text{vis}} = 24M^3 k, \qquad \Lambda = -24M^3 k^2. \tag{2.32}$$

The spacetime in between the branes is a slice of AdS_5 which means that the bulk gravitational dynamics are compatible with a supersymmetric extension.

Randall and Sundrum use a 4D effective field theory on the visible brane to construct the QFT. To see how this geometry works in generating masses on the TeV scale, consider the action of the Higgs field as the example. The coupling of the fields in the two branes is related by Eq. 2.29 defining the metrics. Let $\bar{g}_{\mu\nu} = g_{\mu\nu \text{ hid}}$

$$\begin{aligned} S_{\text{vis}} &\supset \int d^4x\sqrt{-g_{\text{vis}}}\{g^{\mu\nu}_{\text{vis}} D_\mu H^\dagger D_\nu H - \lambda(|H|^2 - v_0^2)^2\} \\ &= \int d^4x\sqrt{-\bar{g}}e^{-4kr_c\pi}\{\bar{g}^{\mu\nu}e^{2kr_c\pi} D_\mu H^\dagger D_\nu H - \lambda(|H|^2 - v_0^2)^2\} \end{aligned} \tag{2.33}$$

After the wave function renormalization, $H \to e^{kr_c\pi}H$,

$$S_{\text{eff}} \supset \int d^4x\sqrt{-\bar{g}}\{\bar{g}^{\mu\nu} D_\mu H^\dagger D_\nu H - \lambda(|H|^2 - e^{-2kr_c\pi}v_0^2)^2\} \tag{2.34}$$

So then the physical scales come from the symmetry-breaking scale,

$$\begin{aligned} v &\equiv e^{-kr_c\pi}v_0 \\ m &\equiv e^{-kr_c\pi}v_0 \end{aligned} \tag{2.35}$$

If the fundamental mass parameters are near the Planck scale, 10^{19} GeV, then the physical mass scales are TeV scale and $kr_c \approx 10$. In this model there are no light Kaluza-Klein modes as in the theory of large extra dimensions, [44]. Rather, the KK gravitons are spin-2 and of the order of TeV and should be observable by their decay products as separated resonances at a hadron collider.

This thesis considers a well-motivated evolution of the original model where the fermions are isolated variously in the warped bulk off of the TeV plane. The fermion fields propagate in the 5D space and their profile is localized by a 5D mass parameter. Thus the same geometry that provides a solution to the weak-Planck hierarchy problem offers a mechanism for generating the fermion masses. The extension of RS gravitons considered allows significant production by gg fusion and decay into longitudinal gauge bosons W_L/Z_L which are localized near the TeV brane along with the Higgs.

The partial decay width, Γ_{ZZ}, to pair of Z_L is,

$$\Gamma(G \to Z_L Z_L) \approx \frac{(cx_n^G)^2 m_n^G}{960\pi}. \tag{2.36}$$

The x_n^G are the 4 widely spaced modes from KK theory. The first one, $x_1^G = 3.83$. The other decays in the model are shown in Table 2.4. Due to the relative purity

Partial Decay Width	Relative BR
$\Gamma(G \to Z_L Z_L)$	1
$\Gamma(G \to W_L^+ W_L^-)$	3
$\Gamma(G \to hh)$	1
$\Gamma(G \to t_R \bar{t}_R)$	3

Table 2.4: Relative BR in bulk RS graviton decay.

$S/\sqrt{B}$ of the ZZ decay mode this makes it the golden channel for discovery.

In a higher dimensional space time with n compact extra dimensions there is a simple formula for the gravitational constant,

$$G^{(4+n)} = G^{(4)} V^{(n)}. \tag{2.37}$$

where $G^{(4)} = G$ is the usual 4D constant of gravitation [45]. Since the Planck mass has the following relation to the gravitational constant,

$$\bar{M}_{\rm Pl} = \sqrt{\frac{\hbar c}{G}} \approx 1.22 \times 10^{19} {\rm GeV}/c^2, \tag{2.38}$$

the relationship between the reduced Planck mass–the one apparent in the TeV brane–and the $4+n$-dimensional Planck mass is,

$$\bar{M}_{\rm Pl}^2 = M^{n+2} V_n, \tag{2.39}$$

It is assumed in the formulation of the theory that the ratio of the compactification scale, k to the Planck scale be order 1. The cross section of the expected signal increases with increased $k/\bar{M}_{\rm Pl}$, but there is an upper bound for the construction of the effective theory:

$$k/\bar{M}_{\rm Pl} < \sqrt{3\pi^3/(5\sqrt{5})} \approx 3. \tag{2.40}$$

This parameter is set to 1 in this analysis and used to interpret the cross sectional limits. The graviton signal used in this analysis, produced in the gg production mode obtains a theoretical width of $\sim 6\%$ over the range of 500-5000 GeV considered.

This page intentionally left blank.

Chapter 3

ATLAS Experiment

This section presents an overview of the structure and operation of the Large Hadron Collider (LHC) and the detector of the general purpose experiment, A Toroidal LHC Apparatus (ATLAS). A couple of topics, beam conditions and calorimetry, are detailed because they are the factors driving the performance of the study through the unprecedented rate of collision data produced in 2016 and through the sophisticated and high-quality performance of the hadronic calibration of the calorimeter systems under these conditions.

3.1 Large Hadron Collider

The LHC is located at CERN (European Organization for Nuclear Research). CERN is a joint venture of 22 member states–the United States, while not a member, is a major contributor to experimental design, detector production and installation, and physics. Founded in 1954, it sits on both sides of the border between Switzerland and France. CERN's primary focus is the operation of seven experiments that analyze particle collisions in the LHC accelerator complex. ATLAS is one of two large, general purpose experiments designed to investigate the largest range of possible physics in proton-proton, proton-ion, and ion-ion collisions along with CMS.

The LHC is a superconducting hadron accelerator and collider that has been installed in the 26.7 km tunnel built for LEP (Large Electron-Positron Collider) in the 80s [46]. It is operated in two phases both as an accelerator of protons and

then essentially as a storage ring for the protons while collisions are being made. It is composed of eight short straight sections ("Points") and eight arcs, forming 8 octants. The straight sections house experiments and utilities. ATLAS and CMS are the two high luminosity general purpose experiments located at Points 1 and 5, respectively. ALICE at Point 2 is a heavy ion experiment and LHC-b at Point 8 studies b-physics. Point 4 houses the radiofrequency (RF) systems responsible for accelerating and grouping the particles into bunches. Point 6 contains a beam dump– the beam can be extracted by rapidly deflection with *kicker* magnets. Beam cleaning occurs at Points 3 and 7. Particles with large momentum offset from the nominal are scattered by a collimator at Point 3 and large betatron motions (deviations from circular orbit) are cleaned at Point 7.

When in operation there are two beams of protons (or lead ions) rotating in opposite directions. For protons, there are four crossings of the beams in four of the eight straight sections. These occur at the interaction points (IP) of the four experiments with laboratory center of mass collisions: ATLAS [47], CMS [48], ALICE [49], and LHC-b [50]. A "two-in-one" superconducting magnet design is used for the bending dipole magnets, meaning that both beams are within the same magnet although not within the same cavity. The LHC is the worlds largest cryogenic device; the superconducting magnets surrounding the vacuum in which the ions circulate are kept around a temperature of 2 kelvin with liquid helium.

Injection Chain

The main LHC storage ring is supplied with protons that are accelerated through the following ladder of energies through the proton accelerator chain at CERN [51]:

50 MeV Linear Accelerator

1.4 GeV Proton Synchrotron Booster

25 GeV Proton Synchrotron

450 GeV Super Proton Synchrotron

In 2015 and 2016 during normal data taking, the beams circulate with 2242 and 2220 bunches, respectively, in trains of 72 bunches with 25 ns bunch spacing in between. Nominally between trains there is a 320 ns gap. This train length of 72 with a larger gap between arises from the filling procedures and the non-trivial rise time of the kicker magnets which redirect the beam. The size of the gap is determined to accommodate the reaction time specifically of the beam dump kicker magnets.

Radio Frequency Systems

Protons are accelerated in the LHC ring by a series of radiofrequency (RF) cavities in the fourth octant. The metal cavities are the optimized to resonate at the first mode when driven at the frequency of 400 MHz. This frequency is 10× higher than the nominal bunch crossing frequency of 40 MHz, so the bunches are tight. Electromagnetic energy is injected from an electron beam source called a klystron through a waveguide and retained by the resonating RF cavity. The resonating electromagnetic field in the cavities and the beam bunches form a phase-locked system. Protons are injected into the LHC storage ring at 450 GeV. They are accelerated and bunched by passage through the RF cavities during the ramp up phase. It takes about 20 minutes to go from 450 GeV to 6.5 TeV, at which point they continue to circulate at that energy. Protons with slightly lower energy (arriving late in the phase) will experience a greater force and accelerate while those arriving early will decelerate traversing the RF cavities. This process forms tight bunches. At collision energy, a proton will lose 7 keV per turn to synchrotron radiation. During the ramp up phase the RF cavities provide a boost of 485 keV/turn.

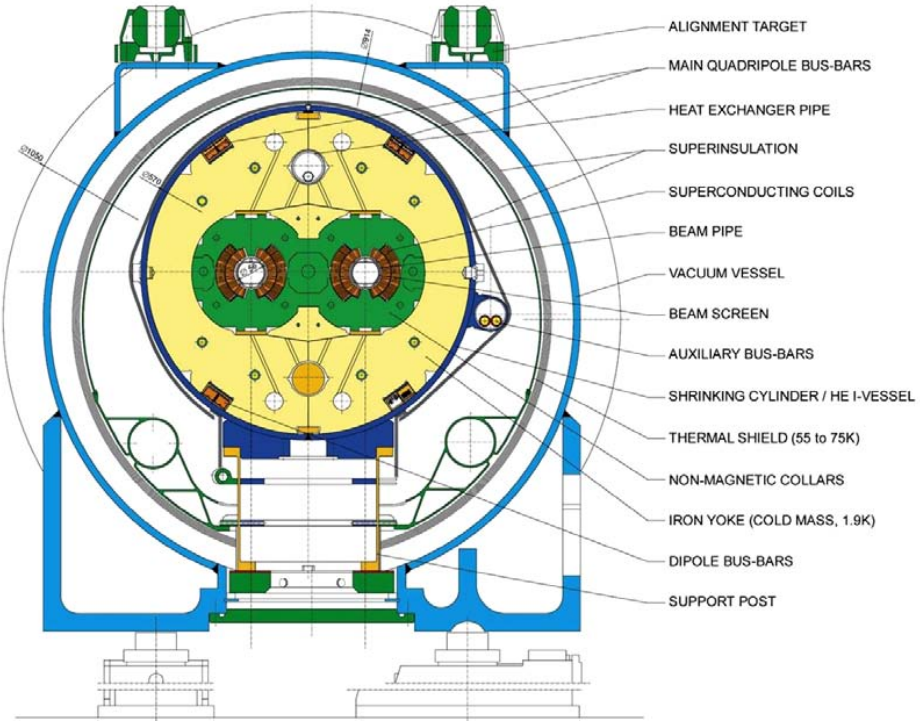

Figure 3.1: Cross-section of the cryodipole magnet. 1232 of these magnets bend confine the LHC beam to its 27 km loop. [47]

Magnets

The LHC has 1232 main dipole magnets which bend the beam around the 27 km loop and numerous (> 800) and various quadrupole magnets to perform the shaping and focusing of the beam [52]. The magnets are NbTi superconducting electromagnets. The main dipoles, a cross-sectional schematic of which is shown in Fig. 3.1, provide an 8.3 T field and are operated at 1.9 K, cooled by superfluid helium. Compared to previous colliders (Tevatron-FNAL, HERA-DESY, RHIC, BNL) this is a lower temperature by a factor of 2, which results in an order of magnitude lower heat capacity. Consequently additional margin is required to reduce the chance of a quench, or the magnet becoming non-superconducting. The margin between the critical point for superconducting NbTi magnet in a 1.9 K liquid helium bath decreases with increasing magnetic field. The cryogenic system must absorb the heat radiated through synchrotron radiation by the circulating beam and this is one of the main limitations in

the number of protons that can be carried by the beam and therefore on the achievable luminosity. There is always a statistical chance of a quench, which depends on the operating temperature, its difference with the superconducting threshold temperature, and the energy radiated by the beam. Such an event did occur during powering tests prior to Run 1 which delayed the turn on of the experiment [53].

3.2 Beam Performance

Record limits were reached for luminosity in Run 2, exceeding the original design of the LHC. This was achieved by pushing the limits in control of the beams in their production and storage and their focal properties at crossing. The luminosity is governed by the following equation:

$$\mathcal{L} = f N_1 N_2 / (4\epsilon\beta^*). \tag{3.1}$$

f is the frequency of colliding bunches and N_1 and N_2 are the bunch populations of the two beams. The denominator is essentially the transverse area for the beams at crossing, but is generally broken up into the following: The transverse beam emittance ϵ is measure of beam quality determined by the injector chain–a low emittance beam will have particles confined to a small distance and with similar momentums. And the amplitude function at the IP β^* indicates the "squeeze" of the beam determined by configuration of the focusing quadrupole magnets and can be defined as the the distance from the IP at which the transverse cross section of the beam doubles. The detailed beam conditions at LHC are shown for design, Run 1 and Run 2 (so far) along with the expected conditions for 2017 in Table 3.1.

In 2015 and 2016 (through August) LHC delivered 26 fb^{-1}and 23 fb^{-1}was recorded by ATLAS with 13.2 fb^{-1}used in the search in this thesis. The delivered luminosity is the luminosity from the start of stable beam operation until a request is made to ATLAS to put the detector in a safe standby mode for a beam dump or further

Parameter	Design	Run 1	2015	2016	*2017*
proton energy [TeV]	7	3.5, 4	6.5	6.5	6.5 or 7
bunch spacing [ns]	25	50	25	25	25
p/bunch [10^{11}]	1.15	1.5-1.7	1.2	1.15	1.25
bunch number	2808	1374	2244	2220	2736
transverse norm. emittance [mm mrad]	3.75	2.5	3.5	2	3.2
stored energy per beam [MJ]	362	140	270	260	
crossing angle [mrad]	142.5	145	145	140	
β^* [cm]	55	60	80	40	40
peak luminosity [10^{34} cm^{-2}s^{-1}]	1.0	0.77	0.5	1.4	1.5
peak pile-up	19	37	16	45	40

Table 3.1: Detailed overview of beam conditions at the LHC (ATLAS experiment) including the prediction for 2017.

beam studies. Data acquisition inefficiencies account for the difference as well as precautions made for the start up of the detectors which are sensitive to the beam conditions. Once the beams are declared stable, the high-voltage is turned on for the tracking detectors followed by the turning on of pixel preamplifiers causing some delay between stable beams and ATLAS recording events.

The ATLAS luminosity is measured by counting the number of interactions at the dedicated detectors in the forward positions along the beam line on both sides of the IP–recall that the optical theorem relates the total scattering cross section to the forward component. The luminosity detectors [54] are the Beam Condition Monitor (BCM) and Cerenkov Luminosity Integrating Detector (LUCID). The relationship between the forward detection and visible luminosity is complicated by the conditions of the beam and their overlap. To calculate the absolute luminosity from the dedicated luminosity detectors the conditions of the beams interaction must be understood. A special van der Meer (vdM) scan is performed [55], which involves varying the separation of the two beams at the collision point in the x and y directions in the transverse plane. The luminosity is determined by the following equation integrating

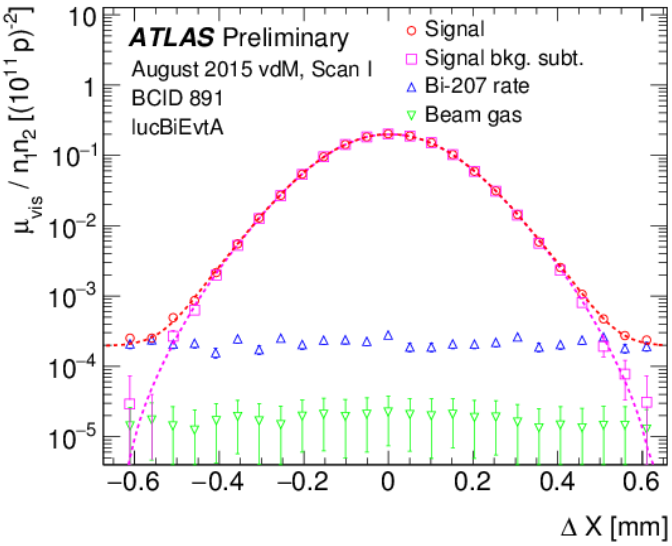

Figure 3.2: Visible interaction rate for the LUCID algorithm [56] that provides the ATLAS luminosity from a horizontal VdM scan made in the August 2015. The background is dominated by random counts from the radioactive Bismuth source used for phototube gain calibration (blue triangles) [30].

the overlap of the normalized particle density functions, ρ_1 and ρ_2, for the two beams:

$$\mathcal{L} = n_b f_r n_1 n_2 \int\int \rho_1(x,y)\rho_2(x,y)dxdy = \frac{n_b f_r n_1 n_2}{2\pi\Sigma_x\Sigma_y}, \tag{3.2}$$

where $\Sigma_x\Sigma_y$ is the convolved beam widths and $n_1 n_2$ is the bunch population product. An x-scan from 2015 is shown in Fig. 3.2, . In practice the visible cross section is calculated as follows:

$$\sigma_{\text{vis}} = \mu_{\text{vis}}^{\text{MAX}} \frac{2\pi\Sigma_x\Sigma_y}{n_1 n_2}. \tag{3.3}$$

From Fig. 3.2, $\mu_{\text{vis}}^{\text{MAX}}$ is the height of the background subtracted peak, $\Sigma_x\Sigma_y$ is the RMS of the distribution, and $n_1 n_2$ is obtained from external LHC beam current measurements [57]. The 2015 and 2016 preliminary luminosity calibration uncertainties are shown by source in Table 3.2.

The uncertainty on the final luminosity is one of the most important uncertainties to minimize for an experiment because it affects every search and measurement and it cannot be creatively mitigated at the analysis level due to its sole dependence on

source	2015	2016
vdM calibration	1.7%	1.9%
calibration transfer	0.9%	0.9%
run-to-run consistency	1.0%	3.0%
Total $\mathcal{L}$ uncertainty	2.1%	3.7%

Table 3.2: Uncertainty on the luminosity calculation broken down by source for 2015 and the combined 2015 and 2016 data sets used in this thesis. The calibration transfer is a correction to the luminosity scale from the low-$\mathcal{L}$ regime where the vdM calculation was made and the high-$\mathcal{L}$ physics runs in which data was recorded extrapolating the result in terms of bunch trains, and adjusted photomultiplier tube (PMT) gains. Variations in closure between various measurements from run to run are considered in the run-to-run consistency term.

the measurement of beam conditions and the democratic effect it has on the quantity of data recorded in any given physics selection.

Pile-up

A consequence of colliding beams with high-luminosity is the presence of additional collisions at the IP along the beam line. These additional collisions are governed by the same interactions of protons in the colliding bunches that govern that of the hard scatter (HS) of interest, but originate from different colliding proton pairs. Consequently, the additional collisions interact with the identical cross sections as the physics governing the primary collision with one notable distinction: that they have not been selected for keeping by the trigger system (discussed in the following section). *Naturally, the selection of events to study introduces bias.* The focus of the LHC is to study hard processes and therefore an event is determined to be interesting (and saved) when sufficiently hard interactions occur, but these are orders of magnitudes less likely to occur than softer so-called minimum bias events which are only just energetic enough to leave a minimal presence in the detector. The total inelastic cross section is dominated by such events but an event is only recorded in data when a sufficiently high momentum transfer takes place in the collision. The interaction

region of colliding beams is narrow in $x - y$ and longer in z, nominally 16 μm and 75 mm respectively. As a consequence, the additional pile-up collisions are distributed widely along the beam line at the IP. The ATLAS detector has been designed to both measure the presence of these additional collisions through measurements of activity with very forward detectors as well as associate charged particle tracks in the main detector volume with great accuracy to their specific point of origin. There are generally thousands of charged particles per bunch crossing with sufficient energy to reach the ATLAS detector volume. The association of tracks to one another to determine their point of origin is called vertexing or vertex finding. The results of running the vertex finding algorithms are a number of "primary vertices".

NPV The number of primary vertices reconstructed per bunch crossing is an important discriminant that is used for analyses in their calibration.

μ The *time-averaged* number of interactions per bunch crossing is the other measure of the amount of pile-up. It comes from the measurements made with the forward luminosity detectors of the inelastic cross section as previously mentioned–it is subject to some calibration dependent on beam conditions.

Figure 3.3 shows the distributions of μ in 2015 and 2016. It is based on a preliminary luminosity measurement:

$$\mu = \mathcal{L}_{\text{bunch}} \times \sigma_{inel} / f_{\text{r}}, \tag{3.4}$$

where $\mathcal{L}_{\text{bunch}}$ is the per-bunch instantaneous luminosity, σ_{inel} is the inelastic cross-section at 13 TeV (which is taken to be 80 mb) and f_{r} is the LHC revolution frequency of 11.245 kHz.

3.3 A Large Toroidal Apparatus (ATLAS)

The ATLAS detector is the large general purpose experiment located at Point 1 of the LHC. It is the largest detector at CERN by dimension. The detector scheme

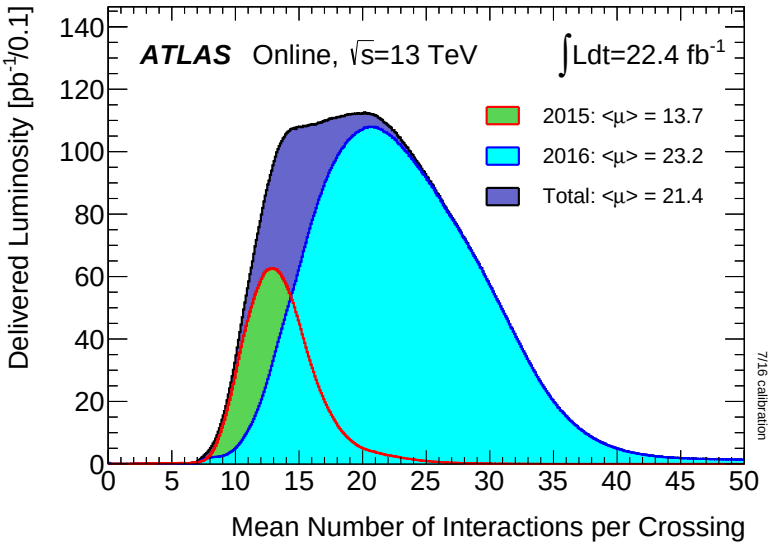

Figure 3.3: The number of inelastic collisions per beam crossing (μ) during stable beams for pp-collisions. The number of interactions shown is averaged over all the the colliding bunch pairs [30].

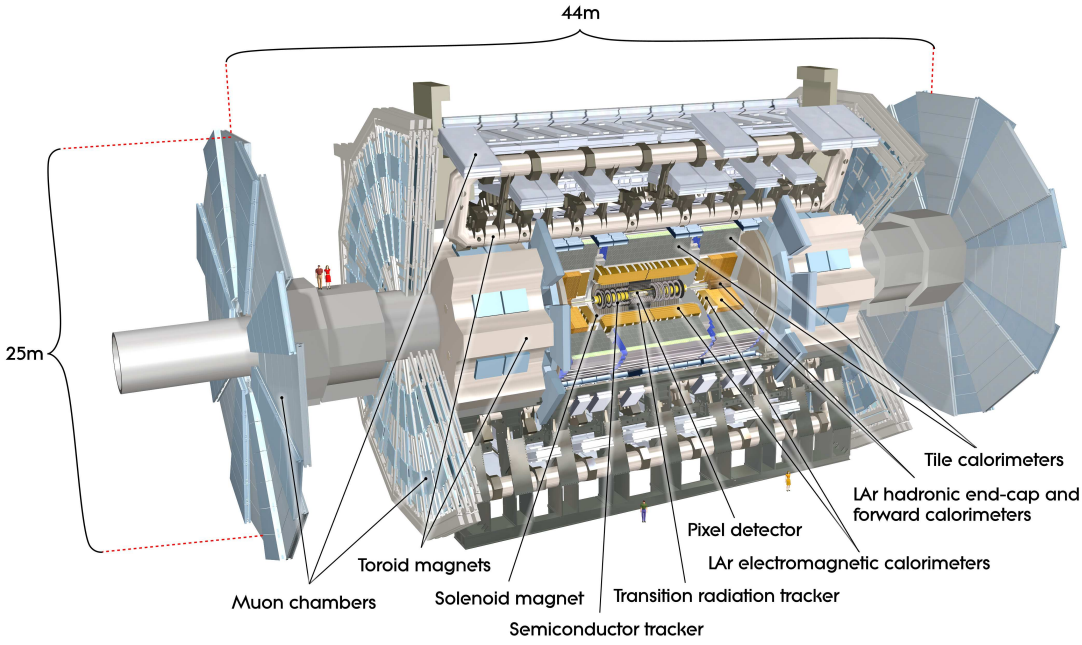

Figure 3.4: Exposed view of the major detector systems in the ATLAS detector.

laid out in a cylindrical form 44 m long and 25 m high, where the detector systems are generally organized in a barrel section and an end-cap section. All together the apparatus weighs 7000 tons. A cutaway schematic is shown in Fig. 3.4.

The ATLAS detector covers nearly the full 4π directional solid angle to detect the outgoing particles from collisions at the IP. There are 2 tiny uncovered portions at high $|\eta|$ [1]along the beamline entering the detector. The detector is nominally forward-backward symmetric in the z-direction while in practice there are small differences present, e.g. in the services to various components of the detector.

The ATLAS detector gets its name from the toroidal magnetic field immersing the muon spectrometer detector generated by 8 embedded superconducting magnetic rings in the barrel and in each of the end-caps [47]. There is a 2 T solenoidal field bathing the inner detector. The magnetic field produced by this complex system of magnets is well-described by careful modeling and monitoring throughout the volume. To illustrate the point, consider the trajectory that a muon would take in the intermediate regions between the barrel and end-cap; it clearly cannot be understood from a back of the envelope calculation.

The mandate of the ATLAS experiment is to provide the following high-quality features for physics analysis at the design energies and luminosities of the LHC:

- Fast, radiation-hard on-detector electronics and sensors with the high detector granularity needed to separate the contributions from PU.
- Full angle ϕ and nearly full angle azimuthal coverage.
- High charged particle path reconstruction efficiency and good momentum reso-

[1]The ATLAS coordinate system is a right-handed system with the x-axis pointing to the center of the LHC ring and the y-axis pointing upwards. The polar angle θ is measured with respect to the LHC beam-line. The azimuthal angle ϕ is measured in the transverse (xy) plane with respect to the z-axis. The pseudorapidity η is an approximation for rapidity y in the high energy limit, and it is related to the polar angle θ as $\eta = -\ln\tan(\frac{\theta}{2})$. The rapidity is defined as $y = 0.5 \times \ln[(E+p_z)/(E-p_z)]$, where E denotes the energy and p_z is the component of the momentum along the beam direction. Transverse momentum and energy are defined as $p_T = p \times \sin(\theta)$ and $E_T = E \times \sin(\theta)$, respectively.

lution as well as the offline tagging of τ-leptons and b-jets which requires vertex detectors very close to the IP to identify secondary vertices.

- Precise electromagnetic calorimetry for the identification of electrons and photons as well as full hadronic calorimeter coverage for a good quality measurement of the missing transverse momentum ($E_{\mathrm{T}}^{\mathrm{miss}}$).
- Good muon resolution to high p_{T} and the determination of muon charge.
- High background rejection on low-p_{T} objects in the trigger system to maintain an acceptable trigger rate in the high-luminosity environment of nominal LHC conditions.

The ATLAS detector is composed of 3 sub-detectors where each in turn is composed of multiple types of fundamental detecting elements designed to capture complementary measurements of the various particles produced in collisions. Working outward from the IP, the inner detector (ID) is designed to track the trajectory of all charged particles through $|\eta| < 2.5$. Next, the electromagnetic and then hadronic calorimeter systems are used to detect and absorb the energy of charged and neutral particles respectively through the full range of $|\eta| < 4.9$. Finally the outermost detector system, the muon spectrometer, fills the vast majority of the overall detector volume up to $|\eta| < 2.7$. A graphical depiction of the tracking and calorimeter information gathered by the ATLAS detector is shown in Fig. 3.5.

ATLAS Trigger System The purpose of the trigger system is to make a decision to keep an event (a snapshot of the detector) for further processing or cast it away. Discarding uninteresting events as early as possible in the chain of data processing is necessary for keeping a manageable volume of computing work and storage. Therefore the ATLAS Run 2 trigger system is structured in two tiers, a level 1 (L1) trigger which must be implemented in hardware–inherently parallel in its design and specific to each detector system–and the high-level trigger (HLT) that is software based [58]. At L1

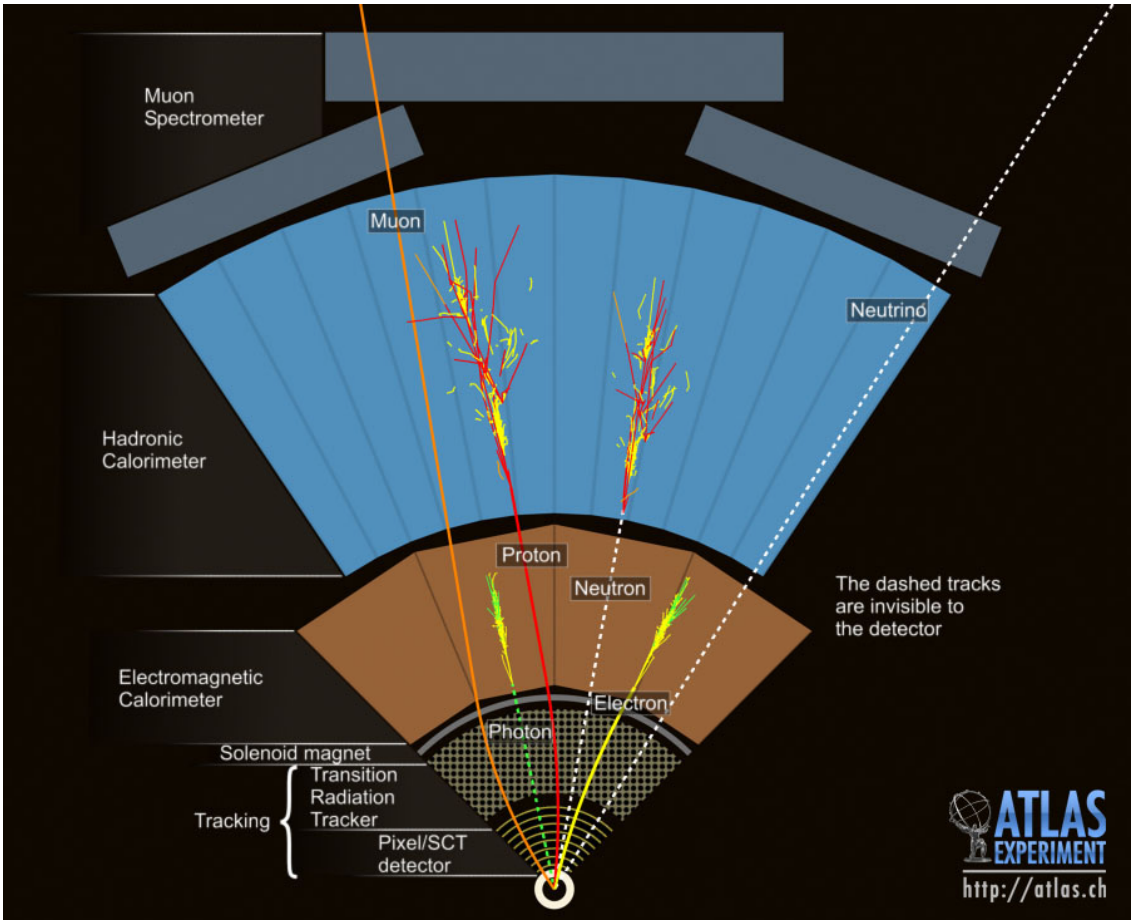

Figure 3.5: Graphic depicting the particles detected and methods of detection within the ATLAS detector. Note the 4 layer scheme of the detector:tracking, EM calorimeter, hadronic calorimeter, and muon spectrometer. The calorimeters act to remove the propagation of particles into the muon spectrometer providing a clean environment for tracking.

the trigger reduces the event rate from the nominal bunch crossing rate of 40 MHz to less than 75 kHz. Then the HLT brings the rate down to a final average recording rate of only a few hundred events per second–given that an event is some 300 MB this still an impressive data rate to disk of ∼100 GB/sec.

The L1 trigger is fed independently by two systems which results in two trigger streams: one in the calorimeter (L1Calo) and separately one from the muon spectrometer (L1Muon). L1 triggers are composed of rather crude measurements with coarse granularity. If an L1 trigger in either stream is passed the event is read from

a buffer by the HLT trigger system. This point introduces the concept that not only the overall rate of the trigger is important but also the rate at which the processing occurs. The buffering systems must be implemented (circularly) in hardware and are limited in capacity. If L1 decision takes too long the data will be over-written and the event lost. ATLAS L1 trigger decisions are made with a latency of no larger than 2.5 μs

The HLT trigger provides a complete event reconstruction (all the physics objects used in analyses), albeit a simpler one than used in final analyses. It combines, in a server farm, the event data from the whole detector and reconstructs tracking within the inner detector and the muon systems as well as improved jet reconstruction in the calorimeters, electrons, photons, taus, and missing transverse energy (MET). For each of these objects there is a chain of triggers whose order is determined to most efficiently reject the most events using the least processing time before considering the event for the next triggers which would select a subset of the events. Triggers with a high rate (e.g. those only requiring the presence of a low-p_{T} jet) are pre-scaled by factor which may change during the course of data taking as the beam conditions permit. This means that the event is only written out a fraction of the time that the trigger is satisfied. Note that for any given event if another trigger is satisfied then the event may be written out anyway.

Inner Detector

The inner detector [59] comprises four tracking sub-detectors that work together to provide positional information to charged particles at multiple points in $R - \phi - z$ (although not all 3 dimensions for all measured points). All tracking detectors experience a 2 T magnetic field in the z-direction (ideally).

Paths of charged particles therefore follow helical trajectories oriented in the z-direction. The detecting elements have been designed to make measurements with

fine granularity and high redundancy. This allows for the precise reconstruction of hit position and a robustness to a large multiplicity of tracks. With good precision comes the reduction of the overhead for the algorithms that identify and follow potential particle paths, which is a task combinatorial in nature. In Run 2 this task takes about 200 ms to perform, and is the most computationally expensive task in the high level trigger (HLT) system. To solve this problem the FTK (Fast Tracker) [60] is being installed during Run 2, which brings the task of track reconstruction into a hardware system with massively parallel processing capable of providing 100 μs track reconstruction times in HL-LHC conditions. Tracking is made from tracks from hits in the 3 innermost sub-detectors of the inner detector, the Insertable B-Layer (IBL), Pixel Detector, and the Semiconductor Tracker (SCT). The last and outermost sub-detector is the Transition Radiation Tracker (TRT). A schematic of the inner detector barrel and end-cap geometry is shown in Fig. 3.6. The inner detector is designed to track well the traversal of charged particles above 500 MeV and measure well the p_{T} of particles below 150 GeV. The lower bound is the nominal limit defined by the radius of curvature of a 500 MeV particle in a 2 T magnetic field reaching all layers of the inner detector. In practice tracks are easily reconstructed down to 250 MeV with hits from the inner layers. The upper limit is due to the granularity and limited curvature of a very energetic particle. The inner detector provides "continuous" tracking with an average of 37 hits per track and electron identification complementing the EM calorimeters.

Pixel Detector The pixel detector [61, 62] is composed of 3 layers of silicon sensor modules in the barrel and 3 layers for each end-cap, as shown in Fig. 3.6. Each charged track is expected to make 3 hits in the pixel detector. The detector is composed of 1744 semiconductor modules, each with 16 (FEI3) front-end chips with 2880 pixels for a total of 47,232 pixels per module. There are 80.4 million readout channels total.

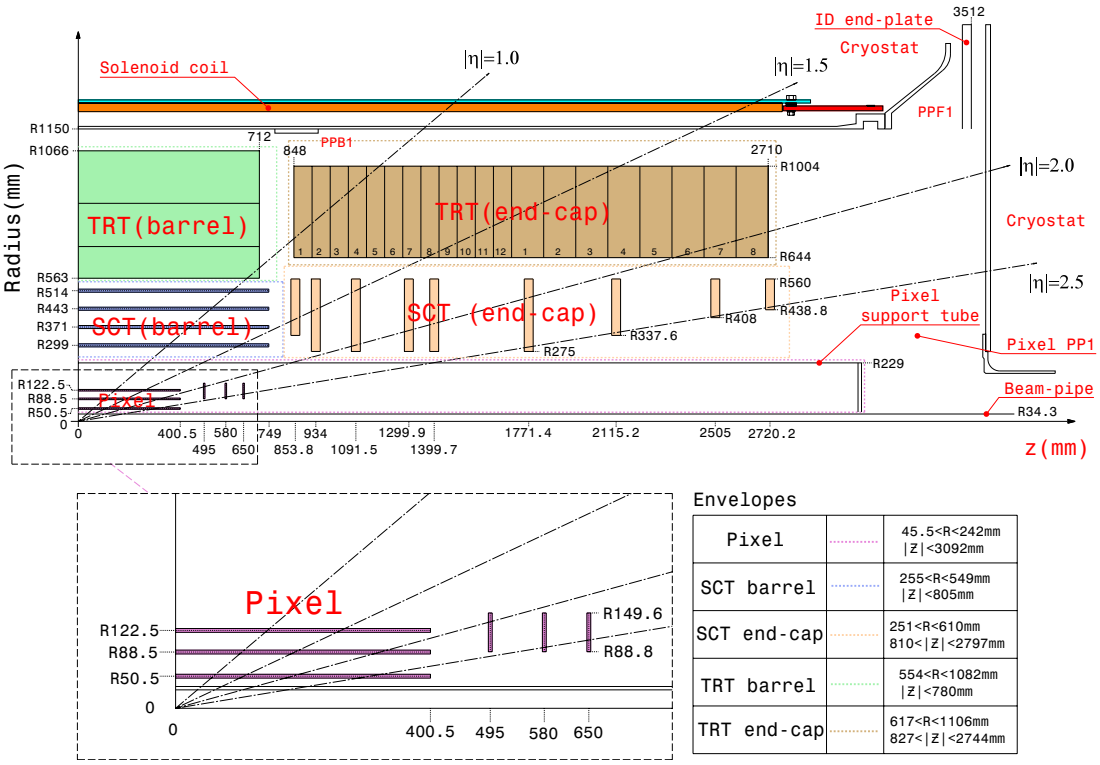

Figure 3.6: Schematic of a quarter-section of the ATLAS inner detector geometry showing each of the major detector elements–notably excepting the IBL which is not shown [47].

Pixel areas are 50 μm $\times$400 μm, and the intrinsic accuracy of the barrel measurement is 10 μm ($R\phi$) and 115μm (z).

The layer closest to the beam pipe is called the B-layer. In Run 1 it was critical for precise tracking to the IP and therefore the precise reconstruction of vertices and inputs to b-tagging algorithms. The harshness of the radiation environment increases rapidly in proximity to the IP. The B-layer will be the first to begin to fail to operate due to the effects of radiation damage depleting the silicon wafer. The expected lifetime of the B-layer is 300 fb^{-1}.

Insertable B-layer The Insertable B-Layer (IBL) [63] provides a fourth layer of pixels inside the B-layer closest to the beam pipe. The installation of the IBL occurred in 2014 during LS1 (long shut down one) just prior to the commencement of Run 2.

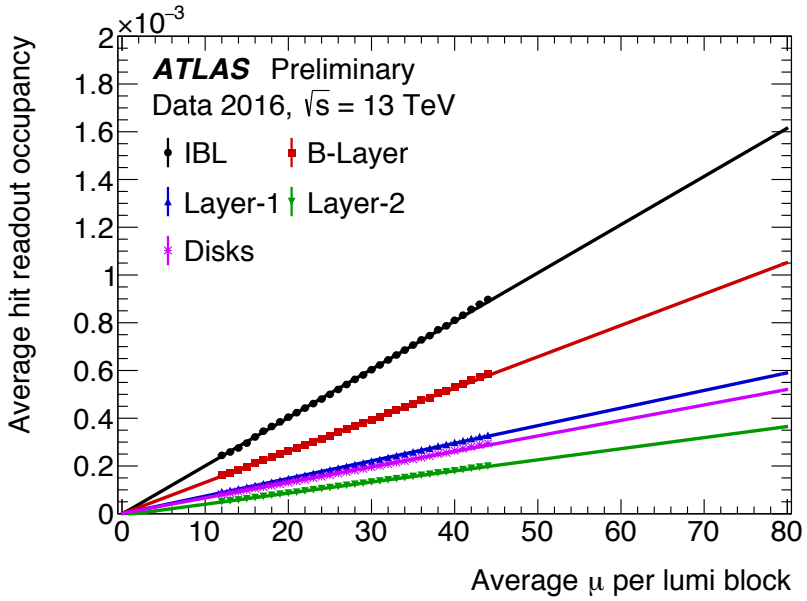

Figure 3.7: The average hit readout occupancy (the average number of hits per pixel per event) for the IBL(black), B-Layer(red), Layer-1(blue), and Layer-2(green) of the 4-layer pixel detector as well as the Disks (purple) for events collected in 2016 [64].

This involved the removal of the beam pipe to free up room and its replacement with one that is 4 mm narrower. The IBL brings the nearest inner detector tracking layer from a radius of 5.05 cm to 3.27 cm. The IBL was the answer to the limited lifetime of the B-layer in a high-radiation environment and its installation extended the capabilities of tracking near the IP, adds redundancy to the pixel tracking, and ensures the longevity of the 4-layer pixel detector in the expected case of B-layer failures. The IBL sensors are significantly more radiation hard than the pixel detector and should last until HL-LHC without replacement.

The IBL comprises 14 long staves oriented around the beam-pipe, each made of 32 (FEI4b) upgraded front end sensors with smaller pixels (50 μm $\times$ 250 μm). In total there are 12 million channels. The hit occupancy of the IBL is much higher than the pixel layers and the IBL has been designed with an improved readout system to handle the higher data rate. The hit occupancy of the 4 layers of the combined pixel detector is shown in Fig. 3.7. Extrapolating the data gives a y-intercept of $\sim$0; the true y-intercept is the average number of hits from the hard scatter process of

interest, which is quite tiny. The IBL is designed to operate well below its data-rate threshold throughout its lifetime whereas the B-Layer will require upgrading of the data acquisition to avoid saturation at projected higher luminosities.

Semiconductor Tracker The semiconductor tracker (SCT) is an additional four layers (of pairs) of silicon microstrip sensors which make 8 precision measurements per track in the $R\phi$ (17 μm) and z (580 μ)-directions. Each detector is 6.4 cm $\times$ 6.4 cm, segmented into 780 strips. In the barrel each detector is 2 pairs of sensors mounted with a rotation at small angle (40 mrad) with respect to each other within the same plane perpendicular to beam pipe. This geometry allows for precise measurements in the z-direction from strips. In addition there are 9 disks on the ends of the detector designed in a similar way but oriented radially.

Transition Radiation Tracker The transition radiation tracker (TRT) [65] is the outermost layer of the inner detector, composed of ∼300,000 drift tubes ("straw tubes"). Each tube is 4 mm in diameter, filled with Ar gas, with a single gold-plated tungsten wire run down the center and a high negative voltage applied to the walls. A cascade of charged electrons instigated by 5-6 primary ionizations from the passage of a charged particle through the Xe-Ar gas mixture produces a measurable signal. Only the radius of the traversal is determined from the characteristic drift velocity of the electrons in the gas. In the barrel, straws are oriented parallel to the beam and in the end-caps, radially. Hit information is therefore 2-dimensional only, with no information along the length of the tube.

The straw tubes are relatively inexpensive and have aided in the continuous tracking concept of charged particles employed by ATLAS by providing the majority of hits from the inner detector particle tracking. The 2D nature of the measurements makes them particularly susceptible to increased luminosity, and the TRT is expected to be replaced by silicon detectors for the HL-LHC. However, the great value of the

TRT is in its combined ability as a tracker and in its use for particle identification based on transition photon radiation produced by the many transitions between the heavy Xe environments in the detector. For a given energy the lighter particles will radiate more heavily. The electromagnetic calorimeters pick this up and use it as a discriminant. In Run 2 a neural network was trained for the purposes of electron identification on the combination of tracking and electromagnetic calorimeter measurements.

Calorimetry

The calorimeters in ATLAS are all sampling calorimeters which means that they are composed of layers of absorber and active material. The calorimetry is split into two types, electromagnetic (EM) calorimeters and hadronic calorimeters. Both the EM calorimeters and the hadronic calorimeters have a barrel region, an extended barrel region, and end-caps. When including forward calorimeter (FCal) the calorimeter coverage provides continuous electromagnetic and hadronic calorimetry through $|\eta| < 4.9$. All calorimeters in ATLAS are non-compensating which means that energy lost to absorber material or leaked is not corrected for. The path of particles from the IP always reaches the EM calorimeter first in which electrons and photons interact and should be fully absorbed. A detailed summary of the ATLAS calorimeters–their material design, granularity, and layers–is shown in Table 3.3.

The structure of the electromagnetic and hadronic (tile) calorimeter modules is shown in Fig. 3.8. Figure 3.8 (a) also shows the granularity of the L1Calo trigger which sums all energy in an $\eta - \phi$ tower called a trigger tower.

Electromagnetic Calorimeters EM calorimeters collect ionized electrons that drift to electrodes in the liquid argon (LAr) active medium, created from the interaction of high energy charged particles. LAr is used for its high linearity and radiation

Layers	Absorber	Active Medium	Granularity
Electromagnetic barrel calorimeter			
barrel: $\|\eta\| < 1.0$ extended barrel: $0.8 < \|\eta\| < 1.7$			
Presampler	(none)	LAr	$\Delta\eta = 0.0031$, $\Delta\phi = 0.1$
EM1	lead	LAr	$\Delta\eta = 0.025$, $\Delta\phi = 0.025$
EM2	lead	LAr	$\Delta\eta = 0.025$, $\Delta\phi = 0.025$
EM3	lead	LAr	$\Delta\eta = 0.05$, $\Delta\phi = 0.025$
Tile barrel calorimeter			
barrel: $\|\eta\| < 1.0$ extended barrel: $0.8 < \|\eta\| < 1.7$			
Tile1	steel	scintillator	$\Delta\eta = 0.1$, $\Delta\phi = 0.1$
Tile2	steel	scintillator	$\Delta\eta = 0.1$, $\Delta\phi = 0.1$
Tile3	steel	scintillator	$\Delta\eta = 0.2$, $\Delta\phi = 0.2$
Electromagnetic end-cap calorimeter			
$1.5 < \|\eta\| < 3.2$			
EMEC1	lead	LAr	$\Delta\eta < 0.1$, $\Delta\phi = 0.1$
EMEC2	lead	LAr	$\Delta\eta = 0.025$, $\Delta\phi = 0.025$
EMEC3	lead	LAr	$\Delta\eta = 0.050$, $\Delta\phi = 0.025$
Hadronic end-cap calorimeter			
$1.5 < \|\eta\| < 3.2$			
HEC1	copper	LAr	For all:
HEC2	copper	LAr	$\Delta\eta \times \Delta\phi = 0.1 \times 0.1$
HEC3	copper	LAr	$(\|\eta\| > 2.5 \Delta\eta \times \Delta\phi = 0.2 \times 0.2)$
HEC4	copper	LAr	
Forward calorimeter			
$3.1 < \|\eta\| < 4.9$			
FCal1	copper	LAr	$\Delta x = 3.0\ cm$, $\Delta y = 2.6\ cm$
FCal2	tungsten	LAr	$\Delta x = 3.3\ cm$, $\Delta y = 4.2\ cm$
FCal3	tungsten	LAr	$\Delta x = 5.4\ cm$, $\Delta y = 4.7\ cm$

Table 3.3: Summary of the sampling calorimeters of ATLAS.

hardness. The absorber interacts with photons producing pairs of electrons which generally re-radiate photons in showers within the alternating calorimeter materials. Showering is often started with the Brehmsstrahlung of electrons, is propagated through Compton scattering, $e^+ - e^-$ pair production, and further Brehmsstrahlung, and so on until the electrons are of low-enough energy to propagate to the electrodes. The EM calorimeters use an accordion geometry, to provide full homogeneous coverage in ϕ without any cracks. The first layer of the barrel EM calorimeter, the presampler, is a separate, thin sampling layer with extremely fine η-segmentation. It is used to obtain a precise position measurement of particles entering the calorimeters and to collect the energy lost prior to entering the calorimeter in the TRT. The EM calorimeter is 20+ radiation lengths (X_0) throughout its volume with a notable

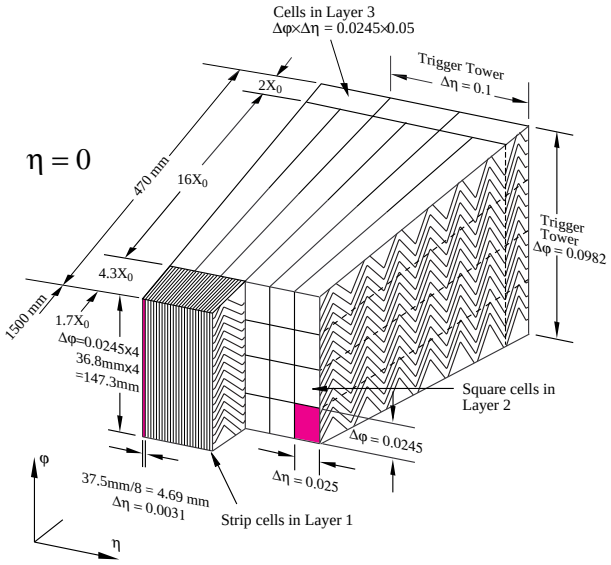

(a) Barrel electromagnetic calorimeter module with the different layers and radiation lengths of a minimum ionizing particle (MIP) shown. Note the extremely fine $\Delta\eta$ granularity of the strip cells of Layer 1.

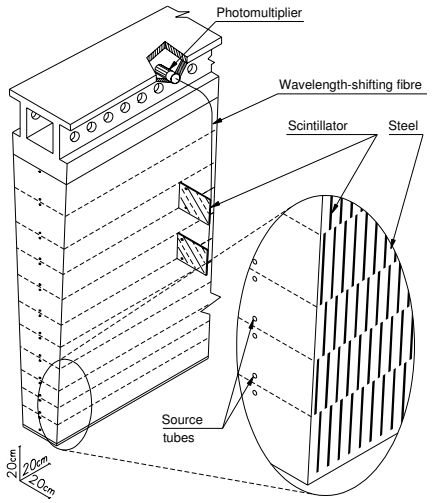

(b) Barrel tile calorimeter module showing the optical readout, structure of the scintillating tiles, fibers, and photomultipliers.

Figure 3.8: Schematic layouts of individual electromagnetic (a) and tile (b) barrel calorimeter modules [47].

exception around $|\eta| = 1.4$. Its fine granularity of $\Delta\eta \times \Delta\phi = 0.025 \times 0.025$ provides the possibility to understand the shape evolution of showers within its volume.

A critical feature of the EM calorimeter performance in pile-up conditions is the bi-polar pulse shaping (roughly a differentiator circuit) by the front end electronics. The result of this signal processing step is shown in Fig. 3.9 for an injected triangular pulse, which has been shown to be a good representation of the actual signal. The 25 ns intervals are shown on the curve to show the points of the curve that are digitally sampled and also serves to illustrate how the signal runs over 24 bunch crossings. The pulse shaping has a very important purpose: to ensure that the calorimeter signal integrates to 0 in time. The most important consequence of which is that the trigger thresholds are less sensitive to the luminosity and the specific number of additional collisions that occur within a given bunch crossing. When multiple signals in a single calorimeter cell are summed (due to the presence of multiple shower sources)

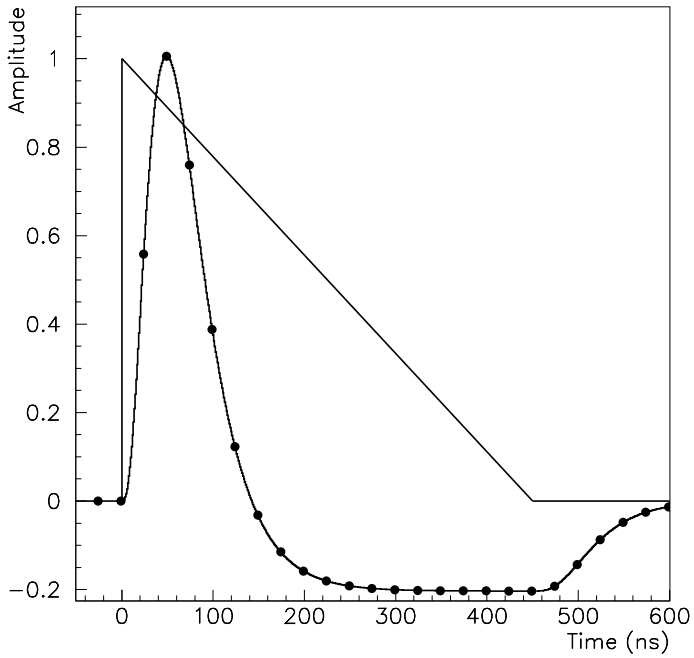

Figure 3.9: The amplitude of the signal resulting from an injected triangular pulse of current into the front end board after bi-polar shaping. Indicated are the 25 sampling points of the curve every 25 ns.

the opposing effects on the resulting measurement depend on whether they have originated from the same bunch crossing or from a previous bunch crossing. This creates two distinct effects from pile-up (PU) in the calorimeters at ATLAS:

In-time pile-up In-time PU results in an *overestimate* of energy deposited by the hard scattered (HS) jet of interest by the addition of energy whose source are the pile-up collisions within the same event. This effect is noise-like: it is subject to a Poisson-distributed chance of additional activity overlapping in the same cell.

Out-of-time pile-up Out-of-time PU results in an *underestimate* of energy deposited from particles originating from the HS vertex. This effect is not very noise-like because (in sufficient PU conditions) it is time-averaged by the long flat tail of the negative response of many previous signals. Rather it is an offset to the measured energy more dependent on the time-averaged beam conditions.

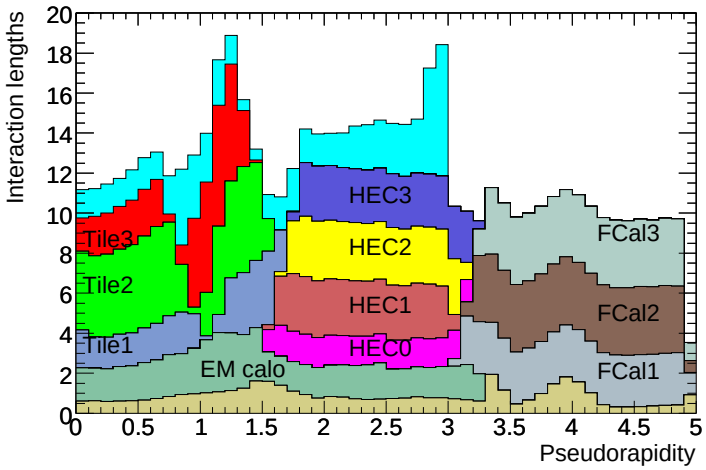

Figure 3.10: Cumulative material by sub-detector layer in the EM and hadronic calorimeters as well as the material distribution prior to calorimetry. Also shown is the total amount of material in front of the muon spectrometer (MS).

These two measures of event activity, NPV and μ, form the parameter space over which to understand PU on the calorimeter measurements. The first, NPV, is purely track-based and is dependent on measurements made from particles that were created in the bunch crossing. While the second, μ, is inherently *time-averaged*, reflecting the overall beam conditions and luminosity at the time of data-taking. The effect of the luminosity on measurements can be understood through studying the dependence of measured jet energies on these parameters and their associated uncertainties.

Hadronic Calorimeters The hadronic calorimeters are designed to interact with particles containing quarks through their interactions with atomic nuclei. The degree of hadronic interaction of a material is measured in interaction lengths (λ), which for most materials are much longer than radiation lengths. The distribution of hadronic calorimeter material is shown in Fig. 3.10. The hadronic calorimeter is not as efficient in recovering energy as the electromagnetic calorimeter, and lost signal in the absorber is significant. The gap at $|\eta| \approx 1.5$ between the extended barrel section of the calorimeters and the end-cap sections (visible in the material distribution), is filled with additional scintillator.

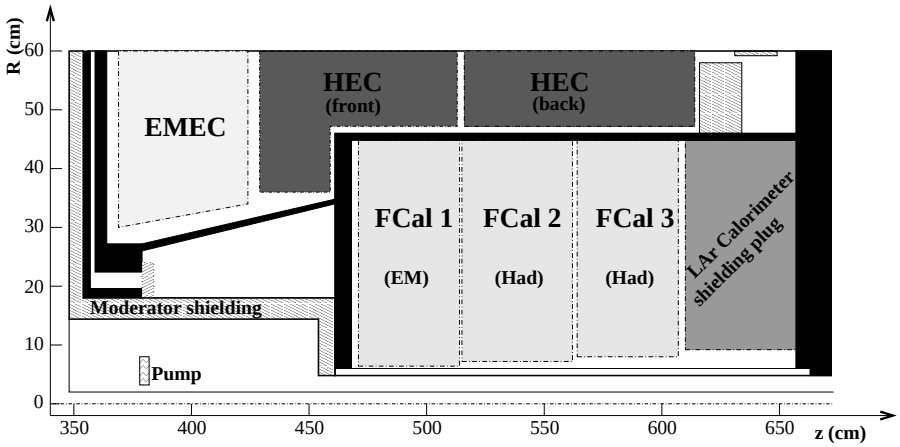

Figure 3.11: Schematic of the FCal modules composing the ATLAS forward calorimeter in the range $3.1 < |\eta| < 4.9$. The black regions are structural components of the cryostat. Note the exaggerated vertical scale–this is a very forward detector.

Forward Calorimeter The forward calorimeter (FCal), shown in Fig. 3.11 is a special detector designed for the high radiation flux in in the forward direction. It is a LAr end-cap detector in three wheels around the beam pipe made from copper tubing with a copper rod insert in the first layer (chosen for its radiation hardness) and tungsten rod in the second and third layers. The thin gap between the rod and the tubes is filled with LAr. The first layer consists of 28 radiation lengths of absorber and together the 3 wheels are 10 interaction lengths which is sufficient for calorimetry. The detector has special cooling needs to handle the large radiation flux without boiling the LAr. It is expected to operate very close to its limit under HL-LHC conditions of $\mu = 200$. A proposal to upgrade it for HL-LHC (a project with major contributions from the author) with new cooling services, higher granularity, and thinner gaps was just rejected (due to the risk of the replacement and studies suggesting an acceptable amount of degradation from radiation damage).

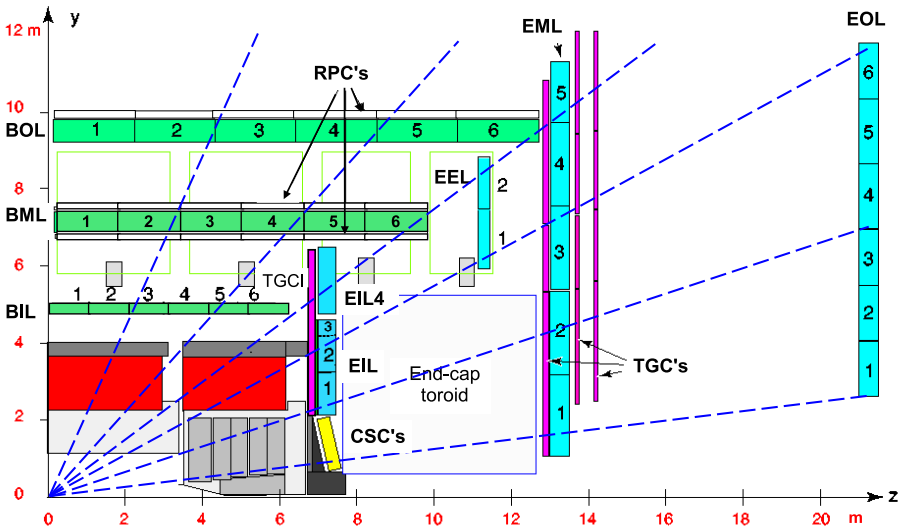

Figure 3.12: Cross-sectional quarter view of the ATLAS muon spectrometer. Note that this is the bending plane produced by the toroidal magnet system. Infinite-momentum muons propagate along the dotted lines. Barrel MDTs (green), and end-cap MDTs (blue).

Muon Spectrometer

The final and outermost detector of ATLAS is the muon spectrometer. It provides at least 3 measurements of position and direction to a muon coming from the IP up to $|\eta| < 2.7$. In the barrel region ($|\eta| < 1.4$) the 3 layers are arranged in concentric cylinders and in the end-cap region there are 3 layers in the plane transverse to the beam axis. The muon trigger system and the detectors providing the precision measurements are two separate systems in ATLAS. Muon p_T is determined by the curvature of the path in the magnetic field provided by the large air-core toroidal magnets.

The precision measurements are made with monitored drift tubes (MDT) in the precision-tracking chambers. At large pseudorapidity ($2 < |\eta| < 2.7$), a higher granularity measurement is provided by multiwire proportional chambers called Cathode Strip Chambers (CSC). The CSC is used to provide robustness against a higher rate of background that it will record due to its forward position, seen in yellow in

Fig. 3.12. The trigger detectors sandwich the precision tracking chambers. In the barrel they are composed of Resistive Plate Chambers (RPC) and in the forward Thin Gap Chambers (TGC) are used. The trigger detectors serve a threefold purpose: they provide bunch-crossing identification, implement well-defined p_T thresholds, and provide a measurement in the coordinate orthogonal to that determined by the precision-tracking chambers. Hall sensors distributed throughout the spectrometer volume allow for the reconstruction of the bending power of the B-field to a precision of a few parts per thousand.

ATLAS Performance

The data acquisition of each of sub detectors performed with high efficiency in 2016. Table 3.4 shows the percent of time each sub detector was fully functioning. The data acquisition system carries flags for the detector operation in short time periods of data taking over which a luminosity measurement is made called lumi-blocks (usually ∼1 min). Periods of the simultaneous good performance of all detector systems (relevant to a given analysis) are tabulated as "good runs lists" used in the analysis. This ensures that the result of an analysis has been made with data that has been approved by experts in the ATLAS system monitoring. Due to the use of muons in

Pixel	SCT	TRT	LAr	Tile	MDT	RPC	CSC	TGC	Solenoid	Toroid
98.9	99.9	100	99.8	100	99.6	99.8	99.8	99.8	99.7	93.5
Good for physics: 91-98% (10.1-10.7 fb^{-1})										

Table 3.4: Luminosity weighted-relative detector up-time and good data quality efficiencies [%] during stable beam in pp-collisions with 25 ns bunch spacing at $\sqrt{s} = 13$ TeV between 28 April and 10 July 2016, corresponding to the 2016 data set used in this analysis.

this analysis, the quantity of 2016 data used here is the lower value of 10.1 fb^{-1}; the toroidal electromagnet system, hardest hit by loss of up-time in 2016, was required to be fully operational for this analysis.

Chapter 4

Monte Carlo Event Generation and Detector Simulation

Simulation of QCD events is an integral part of the calibration, analysis, and interpretation of data taken at ATLAS. It plays a key role in the understanding of the hypothetical signal in a search, the constraint of SM parameters integral in the understanding of backgrounds, and the key technology through which one can understand the capabilities and refine the design of proposed future experiments.

The final states of deep inelastic hadron-hadron collisions are complicated, often involving hundreds of particles whose energy spans a few orders of magnitude. Each individual hard collision involves many of the SM particles and the relevant matrix elements in a given process quickly become unmanageable once one is beyond the first couple orders of perturbation theory. Consequently, predictions at the LHC start with perturbative QCD calculations at leading order (LO), next-to-leading order (NLO), or even next-to-next-to leading order (NNLO). Matrix elements (ME) are calculated in an approximation of the underlying theory of QCD. To handle the divergences that are inherent arising from confinement at low-energy, approximations must be used in place of actual theoretical calculation. Because of this and the extremely large phase space of final states, Monte Carlo (MC) sampling is the standard procedure for generating precise theoretical predictions to be compared with data.

Since steps in calculating QCD final states in hadron collisions require approximations, there are several MC generators in use by the experimental community, each employing different techniques. There are trade-offs between them, and there is an active feed back between the phenomenological community and the results coming

from experiment. This section will introduce the MC simulations used in the generation of the signal and leading backgrounds in the diboson search as well as those used in the calibration of jets.

Generally, the MC event generation is broken into 4 steps. The chain begins with the scatter defined by the MEs of the hardest process, proceeds through an iterative scale evolution down to a lower cutoff energy scale, then undergoes a non-perturbative hadronization into the final state hadrons, and finally the interaction of the final state particles with the detector is modeled. At hadron collider energies the hard scattered partons emit gluons and quark-antiquark pairs which then re-radiate themselves and so on, creating a cycle that repeats at lower energy. Following this process iteratively for both the incoming and outgoing participants of the hard scatter is known as parton showering (PS). The end result is a collimated shower of final state particles with a non-trivial width known as jets. Showering takes place down to order of 1 GeV at which point QCD is strongly interacting and hadronization occurs. Soft interactions play an important role in the evolution of the shower and hadronization but can not be calculated from pQCD, but rather only through QCD-inspired estimates with tunable parameters. Secondary interactions from the primary hard scatter result in some additional detectable final state particles in the interaction and are grouped together in what is known as the underlying event (UE). These aspects of a complete event generation are summarized in Fig. 4.1 showing how each stage evolves for a typical hadron collider event.

4.1 Event Generation

General purpose generators like those used at ATLAS provide at least LO matrix element generation for $2 \to 1, 2$ or 3 final states. Many can interface with other matrix element/phase-space generators for the generation of higher multiplicity final states,

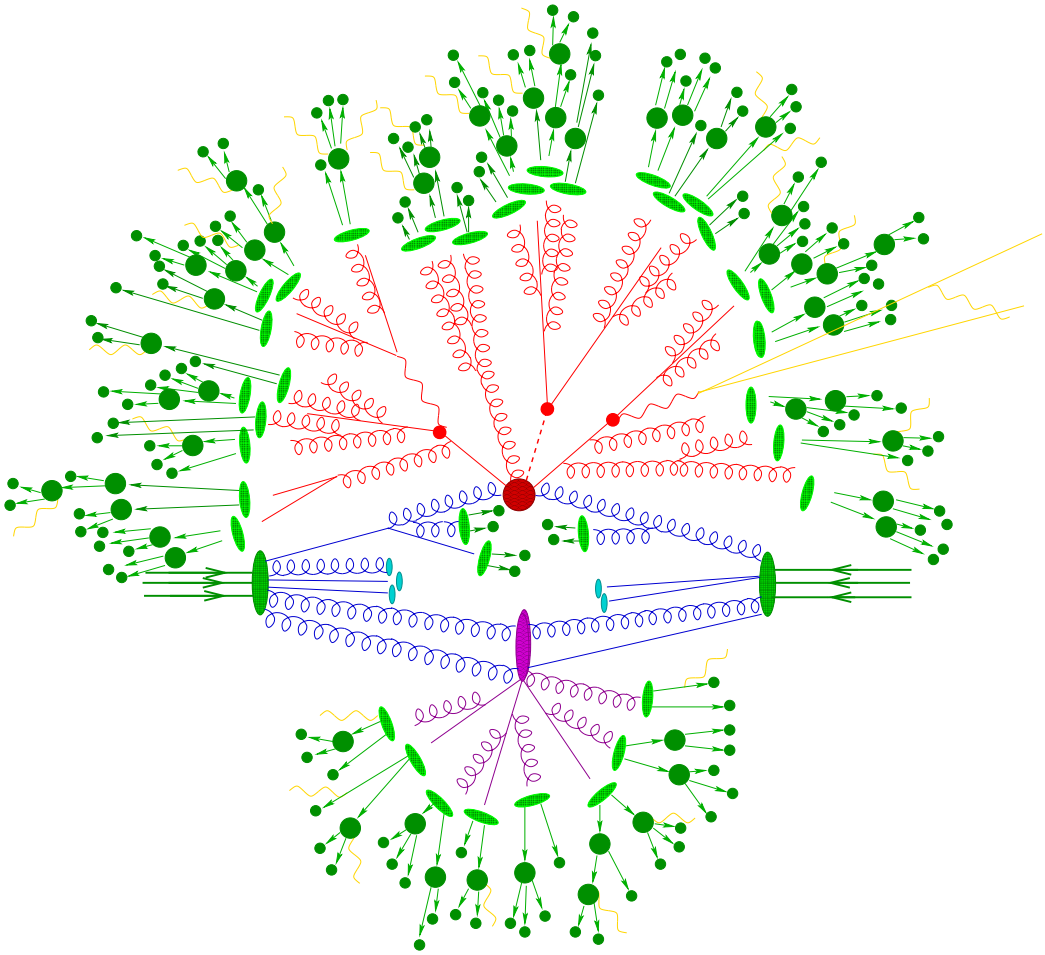

Figure 4.1: Cartoon of a pp-collision simulated by MC generator at LHC energies. It includes the steps used in the complete MC simulation chain discussed. The initial protons are represented by the three horizontal green lines and the squished dark green blobs. The large red spot is the LO collision decay to final state products (red) which undergo parton showering still in the red. The products of the parton shower hadronize (light green blobs). A secondary QCD interaction is shown in the purple. The light green squished blobs show the hadronization. The dark green final products are hadrons which have in some cases undergone further decay. The yellow curves indicate final state radiation (FSR).

like Comix [66], OpenLoops [67], Madgraph [68]. Special tools are used because the number of Feynman diagrams required to represent a state increases roughly factorially with the number of final state particles. Computation simply using the textbook squaring of amplitudes becomes prohibitive for final-state multiplicities from a final state multiplicity of four.

Picking up from the QCD discussion in the theory section, a factorization formula is used to calculate cross sections at LHC. To make the calculation one integrates over the phase space, for given set of matrix elements, with parton distribution functions in hand. Rewriting the the factorization equation 2.4 from Chapter 2 in a little more detail [69]:

$$\begin{aligned}\sigma &= \sum_{a,b} \int_0^1 \mathrm{d}x_a \mathrm{d}x_b \int f_a^{h_1}(x_a,\mu_F) f_b^{h_2}(x_b,\mu_F) \mathrm{d}\hat{\sigma}_{ab\to n}(\mu_F,\mu_R) \\ &= \sum_{a,b} \int_0^1 \mathrm{d}x_a \mathrm{d}x_b \int \mathrm{d}\Phi_n f_a^{h_1}(x_a,\mu_F) f_b^{h_2}(x_b,\mu_F) \times \frac{1}{2\hat{s}} |\mathcal{M}_{ab\to n}|^2(\Phi_n;\mu_F,\mu_R),\end{aligned} \tag{4.1}$$

The PDFs, $f_a^h(x,\mu_F)$, are functions of light cone momentum fraction x and the factorization scale μ_F used. Each parton a is labeled with its parent hadron h. The parton level production cross section $\hat{\sigma}_{ab\to n}$ for final state n from initial partons a and b depends on the momenta of the final-state phase space Φ_n. The differential parton-level cross section is given by the product of the PDFs with the square of the matrix element $|\mathcal{M}_{ab\to n}|^2$ and the parton flux $1/2\hat{s} = 1/(2x_a x_b s)$, where $\sqrt{s}$ is the usual CME. The matrix element $\mathcal{M}_{ab\to n}$ can be interpreted as the sum over Feynman diagrams, although in practice there are some subtleties. The sum over quantum numbers helicity and color can come out of the following square term,

$$|\mathcal{M}_{ab\to n}|^2(\Phi_n;\mu_F,\mu_R) = \sum_{h_i;c_j} |\mathcal{M}^{\{ij\}}_{ab\to n}|^2(\Phi_n,\{h_i\},\{c_j\};\mu_F,\mu_R) \tag{4.2}$$

Therefore, helicity and color configurations can be sampled to form the starting conditions for showering. The differential phase space element,

$$\mathrm{d}\Phi_n = \prod_{i=1}^{n} \frac{\mathrm{d}^3 p_i}{(2\pi)^3 2E_i} \cdot (2\pi)^4 \delta^{(4)}(x_a P_a + x_b P_b - \sum_{i=1}^{n} p_i), \tag{4.3}$$

where $x_a P_a$ and $x_b P_b$ are the initial state momentum fractions of these partons. This equation is generally applicable to all orders of perturbation theory. Typically, one hard scale $\mu_F = \mu_R = Q^2$ is used to set the renormalization and factorization scales as well as the starting scale for the initial and final state parton showering. Each generator utilizes a default PDF set with tunes made for the parton showering, hadronization and underlying event. At leading order the shapes of distributions are well-described, but it is common for the overall normalization to be accurate to only a factor of 2 or so. To make distributions useful, an overall normalization or k-factor is determined from a designated study to compensate for this inaccuracy.

Parton Showers The effects of higher order corrections are simulated through parton shower algorithms. These are implemented by a recursive branching of momentum down from higher scales associated with the hard process to an order of 1 GeV, where confinement requires further description of the evolution as hadrons.

The critical structure in the theory of QCD that allows for the idea of a shower to accurately represent higher multiplicity states is the proportionality of production cross section to that with additional gluon final states: e.g. the production cross section for $q\bar{q} \propto q\bar{q}g$. The interpretation for the process as the emission of a gluon is valid and an iterative algorithm will suffice to describe this process. The point is completely general so starting with any hard process the showering algorithm can be applied to generate a collinear splitting. The splitting can then be treated as the new hard process for collinear splitting to be reapplied down to the showering cutoff, Q_0. Like radioactive decay, the probability of non-branching to cut-off value q^2, $\Delta_i(Q^2, q^2)$, is given by the exponent of the instantaneous branching probability.

The non-branching probability is known as the Sudakov form factor. Its first derivative is the probability for the first branching. To go through the process recursively it is necessary to introduce an ordering variable. The choice of ordering

variable is one of the key differences between generators. This type of algorithm lends itself naturally to straight forward MC evaluation: A random number ρ from 0 to 1 is generated, and then the equation $\Delta_i(Q^2, q^2) = \rho$ is solved for q^2. If q^2 is less than the cutoff Q_0^2 the branching terminates, otherwise it continues.

When considering all soft emissions together however, it is clear that many diagrams will contribute and the treatment of interference will be an unavoidable part of a good description. This seemingly invalidates the model of the independent evolution of partons and suggests that soft gluons must be considered to be emitted by the whole scattering process. The method used by HERWIG [70] ensures the correct handling of soft gluon color interference at the cost of not ensuring the conservation of momentum.

The discussion has so far assumed radiation is from outgoing partons (FSR), but the same construction applies to radiation from the initial state (ISR). To shower from the initial state, event generators start from the hard process and proceed by backward evolution, dressing it with an additional radiated gluon. Using the DGLAP equations, the probability distribution for a parton with given momentum fraction and scale is determined to come from higher momentum fraction and lower scales. This process is iterated until the scale reaches the infrared cutoff. In this process the Sudakov form factor $\Delta_i(Q^2, q^2)$, giving the probability that a final state parton does not radiate between the scales Q^2 and q^2, is replaced by the non-emission probability. Since PDFs decrease exponentially with x the non-emission probability is close to one, and it is generally more probable that the parton has come straight out of the hadron. Of course the distinction between ISR and FSR is not a physical one and all soft emissions can interfere with one another. The specific treatment of ISR with FSR in generators is yet another point of specialization among generators.

One last area of subtlety in the interface between parton-level matrix elements and parton shower is the possibility of double counting. A sufficiently hard emission in

showering from an outgoing product can result, by recoil of the parent, in an identical state as that of a harder process producing a soft emission. In all cases the showering algorithms have been developed in the soft and collinear limit, which indicates that the later case is prioritized in cases of double counting.

Hadronization

Hadronization refers to the model used in event generation to transition from the parton-level description of a final state to the actual hadronic final state products. There are two classes of hadronization model in use, string and cluster models. The string model turns a system of partons directly into hadrons, whereas the cluster model uses an intermediate stage of cluster objects with a typical mass scale of a few GeV. To go into detail about how these models work is well beyond the scope of this thesis, however a short summary is worth some discussion in order to understand how the MC is used in experiment to determine systematic uncertainties.

String model The string model [71] is based on the linear increase of the QCD potential at large distance, leading to confinement. As the partons move apart, a color flux tube, represented as a 1-D string, is stretched between quark pairs with the linear potential $V(r) = \kappa r$. The energy per unit length is known to be about $\kappa \approx 1$ GeV/fm. Gluons form kinks in the string while quarks form end points. A break in the string produces quark-antiquark pairs where each forms part of its own hadron. The emission of a soft or collinear gluon disturbs little the string motion and fragmentation–this is referred to as collinear and infrared safety, a key feature discussed in more detail in Chapter 5. Consequently, the choice of parton shower cutoff scale does not affect the resulting distribution of hadrons. The string model provides a predictive framework for space-time evolution of hadrons and momentum and energy distributions of the products. There are several tunable parameters used

in string models to obtain the correct distributions of hadrons from string breaks. A typical leangth of breaking string is from 1 to 5 fm apart in the $q\bar{q}$ rest frame. A potential drawback to the string model, comes from the formulation of each string in isolation to the rest of the event. After showering, the string configuration is assigned to the parton-level products in the event, and each string evolves in isolation. Since color effects can be felt from the event as a whole in hadronization of a given parton this is a shortcoming of the model, but it may only be significant for busy events–this mis-modeled effect should certainly be significant for heavy ion collisions and trivial in clean e^+e^- collisions.

Cluster model The cluster hadronization model works from the preconfinement property [72] of parton showers. A consequence of the property is the formation of color singlet clusters of partons with a universal mass distribution around the scale of a few GeV. In the model gluons are split into $q\bar{q}$ pairs and clusters are formed from those that are color-connected. Decaying each cluster according to the available two-body phase space determines the production rates of various hadrons. The multiplicities are determined by flavors, spins, and available kinematic phase space. Suppression of heavy flavor and the expression of the limited transverse momenta of heavy hadrons are a direct result of the limited distribution of cluster mass. The basic cluster model for hadronization has been shown to represent the distributions observed in data well using relatively few tuned parameters compared to the string model, primarily requiring only the tuning of the shower cut-off scale. The clusters evolve individually like the strings in the string model.

After excited hadrons are formed either through cluster or string model there is the final step of their decay. Both models simplify non-trivial effects arising from a busy hadronic environment.

It is standard procedure for experimentalists to estimate the sensitivity of an

observable to the hadronization model used and/or showering by simply generating MC with multiple schemes and comparing observables. This strategy is used in the calibration of jets to determine systematic uncertainties as well as in the search presented in this thesis to cover systematic uncertainties in the fits associated with generator modeling.

Underlying event

The underlying event (UE) refers to various physics processes that contribute to the total observed activity in hadron collisions. The source of additional activity can mainly be understood as the interaction from more than one pair of partons from the colliding hadron pair. This encapsulates all activity from the leading hadron pair interaction not directly associated with the leading parton pair interaction. For example it excludes ISR from the leading parton-parton collision. The additional interactions are relatively soft and are not frequently hard enough to directly produce jets above the minimum thresholds for reconstruction. However, events have numerous soft interactions below the cutoff for jet reconstruction that can affect the color flow in the event since color is exchanged between all participants in the scattering. In turn this has an outsized effect on the final-state activity increasing the sum of transverse energy, particle multiplicity, and beam remnant interactions resulting typically in greater activity in the forward region as well as central.

The UE is influenced by the hard interaction and is more than the sum of individually treated soft interactions of the remaining partons in the colliding hadrons. A harder leading parton-parton interaction indicates a greater chance of secondary interactions and so a cut on the transverse momentum of leading products biases upward the contribution of the UE.

The *event tune* is a generator-specific tuning of the free parameters in the models used for description of the UE model, the model used for hadronization and hadron

decay. Typical parameters that require tuning include: α_s/Λ_{QCD}, hadron shower cutoffs, string tension, fragmentation function parameters, cluster momentum smearing functions, flavor enhancement and suppression in hadronization, and parameters for models of multiple parton interaction (MPI). The specifics of treatment of UE is unique to each of the generators.

Generally tuning uses event data from as many hadron collider experiments as possible. New event tunes are used in Run 2 incorporating the constraints of studies made on Run 1 LHC data.

Specific Generators

Matrix elements (MEs) are typically generated to NLO and combined with the parton shower. The combination of fixed order MEs with parton showers is a sophisticated task that requires a careful stitching together of the results from parton showering and ME calculation. One reason this is a challenge is that parton showers give results correct to all order of strong coupling α_s for a fixed number of parton emissions, and ME calculations give results only correct to fixed order in α_s but for any number of parton emissions. The accuracy of parton shower calculations diverges for large angle, and hard emissions and the accuracy of ME calculations is limited in softer and collinear emissions. The use of NLO ME calculations improves the agreement between data and simulations because the first (hardest) emission is often poorly treated in a parton shower framework and calculations using MEs are more accurate. The POWHEG [73, 74] and MC@NLO [75–77] tools correct the parton shower for the first emission in distribution and cross section. For a good simulation of higher jet topologies, a different approach is taken used in CKKW [78] and CKKW-L [79] that introduces a merging scale above which the second and *higher* emissions of the parton shower are corrected to the MEs. This strategy essentially simulates the jet multiplicity by ME calculation and then applies parton showering to each jet. This

introduces a tunable scale separating the ME calculation from the parton shower.

To eliminate double counting from PS and ME merging in NLO calculations terms are subtracted. A byproduct of the experimental use of these techniques is that for a limited MC sampling (or fine enough binning) negative weights result in locally negative final distributions which are unphysical. Care is taken not to choose binning too fine in the statistical procedures for searches, but inevitably the sub-leading backgrounds have areas in the analysis that are statistically limited without detriment to the analysis. Distributions are forced to be positive definite in such cases to make them more physical and ensure a good fit.

Pythia 8 Pythia incorporates a LO ME generator with a highly tunable parton showering based on the dipole approximation [80]. Hadronization uses the Lund string fragmentation framework [81]. Ordering in the event evolves globally in p_{T} including multiple parton interactions and parton showering. Pythia interfaces with NLO tools like Powheg for the generation of multiple parton final states. Stand alone Pythia QCD dijet simulation is the standard for the development of jet calibrations where the focus is on the simulation of individual jets and the overall event topology is less important.

Sherpa 2.2 Sherpa 2.2 [82] is a general MC event generator that performs both ME generation as well as the parton shower, using the ME+PS@NLO prescription [83]. In this analysis it is used to generate W/Z+jets samples, the dominant backgrounds in both $\ell\ell qq$ and $\nu\nu qq$ channels. Matrix elements for W/Z+0,1,2 jets processes are generated at NLO and W/Z + 3,4 jets processes to LO using the Comix [84] and OpenLoops [67] programs. Sherpa 2.2 uses the CKKW-L matching and merging procedure. Massless b and c-quarks are used in the MEs but are massive in the parton shower. A refined tuning is used improving the description of LHC data over previous Sherpa 2.1 used. The PDFs are NNLO using NNPDF 3.0 [85]. Sherpa uses dipole showering based

on the Catani-Seymour factorization formalism. A cluster-based model is used for hadronization with flavor-dependent scales between clusters and hadrons.

Herwig++ HERWIG (Hadron Emission Reactions With Interfering Gluons) [70] is distinct in its use of an angular ordering (instead of p_{T}) in the evolution of parton showering and underlying event simulation. This strategy better represents aspects of color coherence in the parton shower but sacrifices local conservation of momentum and requires corrections. HERWIG uses a cluster-based approach to hadronization. Consequently HERWIG is a favorite alternate for gauging the dependence of a process on the simulation of PS and UE.

4.2 Simulation of pile-up

Proton-proton collisions occur outside of the hard scatter of interest which creates an additional source of signal within the detectors. There are five sources of pile-up in ATLAS events. The most important source are the additional pp-collisions near the IP both in time with the bunch crossing and out-of-time during previous bunch crossings at 25 ns intervals. In and out-of-time PU are simulated by overlay of of minimum bias events according to the nominal bunch chain structured. MC for 2016 is generated with the expected distribution of μ around 30 for data taken in 2016.

There are additional PU effects which are not included in the simulation either because they are very efficiently selected against and do not scale with luminosity or because their simulation is very expensive:

Cavern background A gas of neutrons and photons within the cavern during LHC runs. The kinetic energies of particles in the background are on the order of 1 MeV.

Beam halo Protons interact with the upstream collimator which results in sprays of muons running roughly parallel to the beam-axis. An example of this type

of event is shown in Chapter 5 on jets in Fig. 5.15.

Beam gas Scattered protons from residual gas in the beam-pipe resulting in an off-center interaction with the detector.

4.3 Geant4

MC generated events are run through a full simulation of the ATLAS detector [86] utilizing the GEANT4 framework [87]. GEANT4 interfaces with the stable particles from MC generators and is used to complete the simulation. It implements the simulated detector, propagates the particles, models the interactions and decays in the presence of detector materials, and generates response signals in the sensitive detector elements. From there the L1 trigger is interfaced. GEANT4 contains a comprehensive and sufficient list of physics models covering the behavior of photons, electrons, muons, ions, and hadrons in the energy range 250 eV to PeV. The processes simulated include ionization, bremsstrahlung, multiple scattering, photo-electric effect, pair conversion, annihilation, synchrotron and transition radiation, scintillation, refraction, reflection, absorption and Cherenkov effect. Differences manifest themselves between simulation and experiment which are corrected for by hadronic calibration, discussed in the following chapter.

Processing proceeds in three steps: simulation, hits, and digitization. Simulation advances the paths of final state particles through magnetic fields and through detector matter. A hit is a short record of physical interactions of particle tracks with a sensitive detector element. Digitization turns hits into the detector output, digital or trigger signal. The stages are run in succession to allow the overlay of multiple events to recreate PU conditions.

4.4 Diboson Resonance Search MC Summary

A number of generators are used for generating all the contributing backgrounds to the searches. The main background sources are Z and W bosons produced in association with jets (Z+jets and W+jets), followed by top-quark production (both $t\bar{t}$ pair and single-top) and non-resonant vector-boson pair production (ZZ, WZ and WW). A full summary of MCs used in the diboson resonance searches is in Table 4.1.

Flavor labeling Jets in MC simulation are labeled according to the flavors of hadrons with $p_{\mathrm{T}} > 5$ GeV found within a cone of $\Delta R < 0.4$ around the jet axis. If a b-hadron is found, the jet is labeled a b-jet. Otherwise, if a charm hadron is found, the jet is labeled as a c-jet. If neither is found, the jet is labeled as a light flavor (a u-, d-,s-quark, or gluon) jet. The labeling of Z+jet events according to the flavor of identified hadrons in $Z \to qq$ decays are then $Z + bb$, $Z + bc$, $Z + bj$, $Z + cc$, $Z + cj$, and $Z + jj$–indicating the truth-level flavor content of the individual hadronic decay products of the Z.

Process	ME Generator	ME PDF	Fragmentation	UE Tune	XS Order
		Signal			
$H \to ZZ$	POWHEG-BOX v1 [73, 74, 88]	CTEQ6L1 [89]	PYTHIA 6 [90]		AZNLO [91]
$W' \to ZW$	MADGRAPH 5 2.2.2	NNPDF23LO	PYTHIA 8 [92]	A14 [93]	N/A
$G^* \to ZZ$	MADGRAPH 5 2.2.2	NNPDF23LO	PYTHIA 8	A14	N/A
		Background			
Z+jets	SHERPA 2.2	CT10 [94]	SHERPA	Default	NNLO [66, 67, 95]
W+jets	SHERPA 2.2	CT10	SHERPA	Default	NNLO (NLO 4 LO)
$t\bar{t}$	POWHEG-BOX v2	CT10	PYTHIA 6	P2012 [96]	NNLO+NNLL [97–102]
Single top (Wt, s)	POWHEG-BOX v1 [103, 104]	CT10	PYTHIA 6	P2012	NNLO+NNLL [105, 106]
EW single top (t)	POWHEG-BOX v1 [107]	CT10 [94]	PYTHIA 6	P2012	NNLO+NNLL
ZZ, ZW, WW	SHERPA 2.1.1	CT10	SHERPA	Default	NLO (4 LO)

Table 4.1: Overview of the key MC distributions used in this analysis.

4.5 MC Comparison

The agreement of different generators is not sufficient to show that that distributions are well modeled. However, when generators agree and they have used different methods for ME matching, showering, and different event tunes it is a strong validation and differences can indicate regions to pay special attention to. The current choice of the SHERPA 2.2 generator used for Z/W+jet production comes after some comparison studies at both CMEs $\sqrt{s} = 7$ TeV and $\sqrt{s} = 13$ TeV and tuning of SHERPA 2.2 to ATLAS Run 1 data. In addition to the SHERPA 2.2 sample a well-tuned Madgraph 5.1 sample (MG) has been used as a cross check in this analysis. This sample uses MadGraph5@MCNLO [108] v2.2.2 for generation of MEs at LO interfaced with PYTHIA 8 for the modeling of the parton shower. It also uses CKKW-L for the merging procedure. Comparison has shown a good agreement with data and between these two generators over a number of observables [109].

A comparison between SHERPA and MADGRAPH in the m_{llqq} distributions used in the searches in the $\ell\ell qq$ channel is made in Fig. 4.2. A full description of the selection criteria and analysis signal and control regions is found in Chapter 6 but isn't necessary here to compare the MC description of some critical regions. It is sufficient for the discussion here to understand that the analysis is split between resolved and merged regimes for low and high mass resonance searches respectively, and also that the signal region (SR) contains two mass window cuts around each pair of Z decay products ($M_{Z\to\ell\ell}$ and $M_{Z\to qq}$) while the Z control region (ZCR) inverts the $M_{Z\to qq}$ mass window cut.

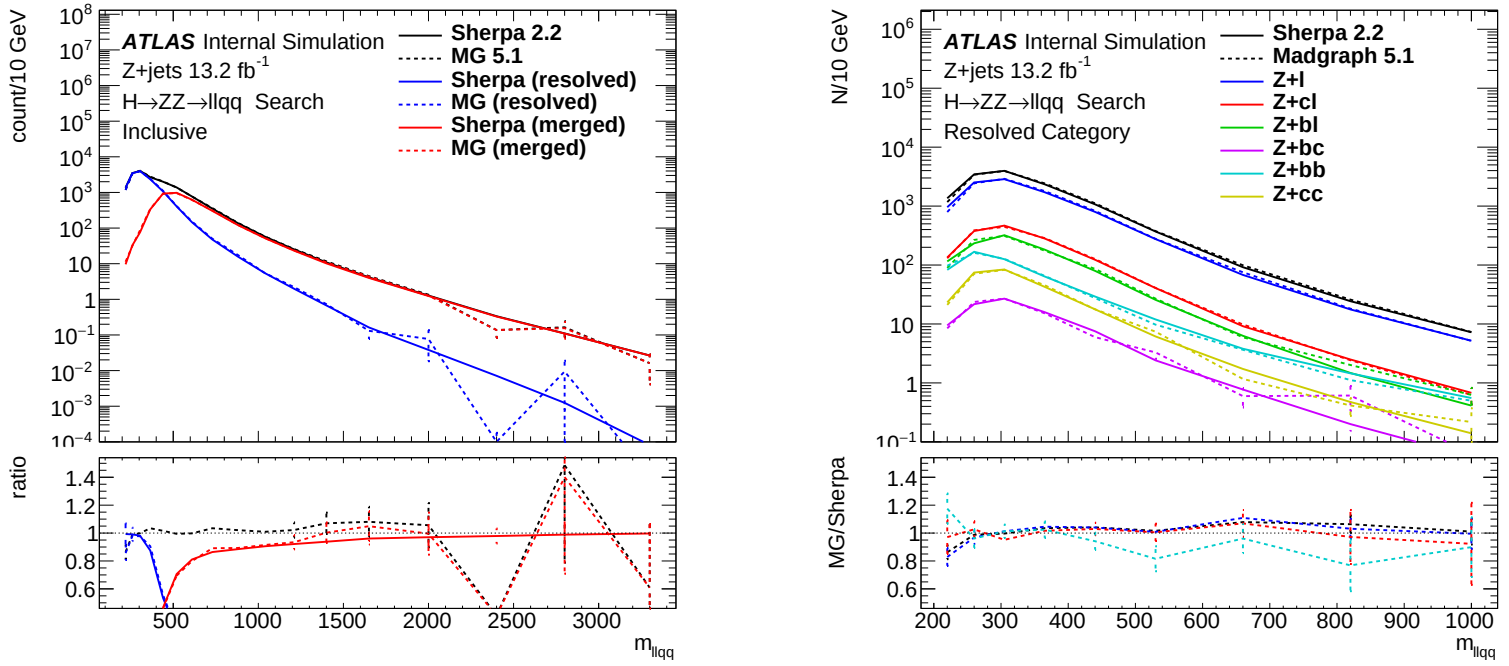

Figure 4.2: Comparison between the nominal SHERPA sample and a well-tuned MADGRAPH sample. Differences could indicate regions not well modeled by the nominal SHERPA sample. The inclusive distributions (SR+ZCR) are shown for the resolved and merged categories of the $\ell\ell qq$ analysis in (a) and for the flavor distributions of Z decay products in the resolved analysis (b).

The excellent agreement between the MadGraph sample and nominal Sherpa sample in Fig. 4.2 (a) indicates in particular that Z+jet angular and p_{T} jet distributions are well-modeled in the region through the transition from the resolved analysis to the merged analysis. Good agreement here suggests that the analysis is not highly sensitive to the specifics of the treatment of NLO matching and correction procedures nor to the specifics of the PS. The good agreement in Fig. 4.2 (b) for the various flavor combinations suggests good modeling of flavor as well. The small but significant deviation in $Z \rightarrow \ bb$ distribution could indicate some mis-modeling in Sherpa. This interpretation is supported somewhat by the observation in previous diboson resonance searches at ATLAS that the predicted overall cross section in this channel may be as much as 20% low. The present search is insensitive to this, but it indicates an avenue for future study.

Chapter 5

Jets

Jets, the collimated showers of hadrons resulting from the hadronization of scattered partons, are the key final state objects to the analyses in this thesis. Grouping the reconstructed particles and energy deposited by the hadrons in a way that correctly identifies the underlying topology of the scattering at parton level and is robust to the effects of the specific treatment of reconstruction, non-perturbative effects, and underlying event contamination is the aim of jet definitions, which will be discussed in Sec. 5.1. The reconstruction of jets from energy deposited within the various calorimeters as well as other available information within the ATLAS detector is addressed in Sec. 5.2. The calibration of jets is addressed in and the determination of systematic uncertainty is outlined in Sec. 5.3. The quality criteria used to reject jets not originating from collisions at the IP are introduced in Sec. 5.4 The reconstruction, calibration, and systematic uncertainties for "large-R" jets, designed to contain two or more distinct scattering products in a single object are covered in Sec. 5.5.

5.1 Jet Definition

Jets are reconstructed with the anti-k_t algorithm [110, 111] at ATLAS. There are generally two classes of jet algorithms, iterative cone-based algorithms [112] and sequential recombination algorithms [113, 114] that are parametrized by the energy scale with a distance measure. Iterative cone algorithms start with seeds and iteratively find stable configurations of cones with fixed radius R, summing the p_{T} of

the particles within the cone. The direction of the cones are adjusted to reflect the direction of the sum of the particles falling within, which consequently results in a different set of particles within the new cone direction. This process iterates until a stable configuration is achieved. In sequential recombination (the method used in ATLAS) with a distance measure, d_{ij} between particles i and j, the clustering proceeds by combining the entities with the smallest distance and proceeding with the new (smaller) set of particles. The distance measure is weighted by a function of transverse momentum, k_t (meaning p_T). A general form to write it in is,

$$d_{ij} = \min(k_{ti}^{2p}, k_{tj}^{2p}) \frac{\Delta_{ij}^2}{R^2}, \tag{5.1}$$

where $\Delta_{ij}^2 = (y_i - y_j)^2 + (\phi_i - \phi_j)^2$ and k_{ti}, y_i, and ϕ_i are respectively the transverse momentum, rapidity, and azimuth of particle i. A special distance cutoff representing the distance between i and the beam,

$$d_{iB} = k_{ti}^{2p}, \tag{5.2}$$

is used to stop the recombination of a given particle and define it as a jet. In these the two equations the p is a parameter used to govern the dependence of the ordering of recombination on the geometric distance and the energy between to particles. Two popular jet algorithms of this type, k_t [115] and Cambridge/Aachen [116], respectively take p to be 1 and 0. The anti-k_t algorithm takes p to be -1. The resulting jet shapes arising from the use of these three different algorithms (and an advanced cone algorithm) on a single simulated event at parton level with a typical soft background of PU and UE are compared in Fig. 5.1.

Collinear and Infrared Safe A usable jet algorithm must determine jets in a way that is *collinear and infrared safe*. Collinear safety ensures that replacing a parton with any collinear set of partons with equal momentum produces the same result. This is a necessary condition in practice for the jet topology of an event at parton

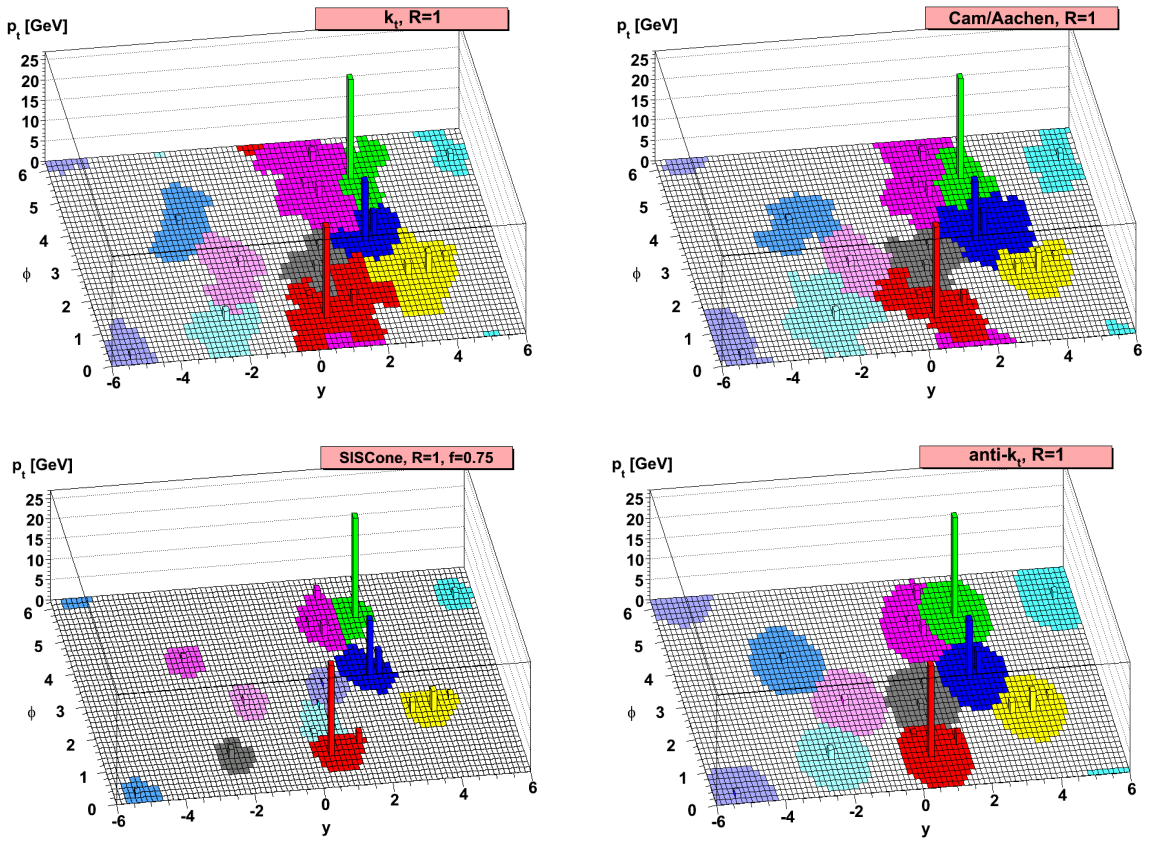

Figure 5.1: A sample parton-level event with a soft background clustered with four different jet algorithms: k_t (upper left), Cambridge-Aachen (upper right), SIScone (an improved cone algorithm, lower left), and anti-k_t (lower right). The colored areas show the catchment areas [117] of the resulting hard jets. The areas of the jets for Cambridge/Aachen and k_t are determined by the specific soft background used and change when the background is replaced with equivalent but different set.

level to match that reconstructed from energy deposits in calorimeters, which are only sensitive to the sum of energy deposited. An infrared safe algorithm reconstructs jets whose properties are insensitive to soft emissions. This property allows jet cross sections to be finite at any perturbative order and non-perturbative corrections to be suppressed by powers of jet momentum. Jets from hard collisions are then well described at the parton level. Infamously, simple cone algorithms fail these two conditions. For example, in the case of 3 particles in a line in ϕ direction, where the central particle has seeded the cone algorithm which has covered them, splitting the central central particle into two can result in two cones being seeded from the outer 2

particles instead. This results in two different stable event topologies for the measured and (simulated) parton-level jets respectively. Furthermore, an infinitesimal radiation between two otherwise stable cones can cause them to converge into one.

The jet definitions shown in Fig. 5.1 all satisfy these two conditions. However, the anti-k_t algorithm is the superior choice of jet definition due to the consistent circular boundary shape that is insensitive to the presence of soft radiation. Jets formed from a hard scatter (HS) particle in the anti-k_t definition obtain a catchment area of πR^2. Soft jets have more complex shapes–when near to a harder jet the overlapping circular area is clustered into the harder jet for example. The stability of the catchment area around a hard jet in the presence of soft emission is a desirable feature for the calibration of jets in the detector. The area of k_t and Cambridge-Aachen jets is heavily dependent on the presence of soft emission and acquire an "anomalous dimension" in their area's dependence on perturbative soft particles. The anomalous dimension of anti-k_t jets is 0. A stable jet boundary is even more important for meaningful evaluation of jet mass.

These properties when taken together allow a very powerful strategy for the calibration of jets in ATLAS. One is able to match one-to-one the sequentially combined detector-level objects to those determined from true (or parton-level) final state particles in a given event. The one-to-one relationship between the so-called calo jets and truth jets is used to compare the reconstructed calorimeter energy of a jet to its true value determined by the combination of truth-level final state particles. Calorimeter jet energies are calibrated by a factor determined from the ratio of the matched jets. And differential QCD cross sections can be determined with little intermediate translation from calorimeter level measurements to final parton-level results.

5.2 Reconstruction

The reconstruction of jets begins with the three-dimensional topological clustering of cells within the calorimeters [118]. The cluster formation is based on a pattern of the significance of positive signals of topologically-connected calorimeter cells aimed at capturing the energy of a shower within the calorimeter. The method is a natural way to suppress noise in the reconstruction of jets by excluding cells that fail to have a significant reconstructed energy over the expected level of noise. Topological cell clusters (topoclusters) obtain both a shape and location information. A method of weighting local clusters called calorimeters *local cluster-weighting* (LCW) is used to compensate at the cluster level for ATLAS non-compensating [1] and energy lost in gaps of coverage.

Topological cluster formation

The formation of topological clusters in ATLAS works through the 3-step process of seeding, growth, and addition of boundary energy. For each cell the noise is calculated as the sum quadrature of electronic noise and noise from pile-up sources:

$$\sigma_{\text{noise}} = \sqrt{(\sigma_{\text{noise}}^{\text{electronic}})^2 + (\sigma_{\text{noise}}^{\text{pile-up}})^2}. \tag{5.3}$$

The value of σ_{noise} for each cell is determined prior to data-taking based on an estimate of the average running conditions for the upcoming year. This is necessary for the fast reconstruction of collected data. An extensive internal study is usually made to evaluate the full effects from final jet reconstruction to missing transverse energy reconstruction from a scan of estimated noise levels–e.g. in 2016 one was made to determine the optimal choice of noise threshold for the continued data-taking in Run

[1] Calorimeter non-compensation means that no attempt is made to compensate for the differing response to different types of particles.

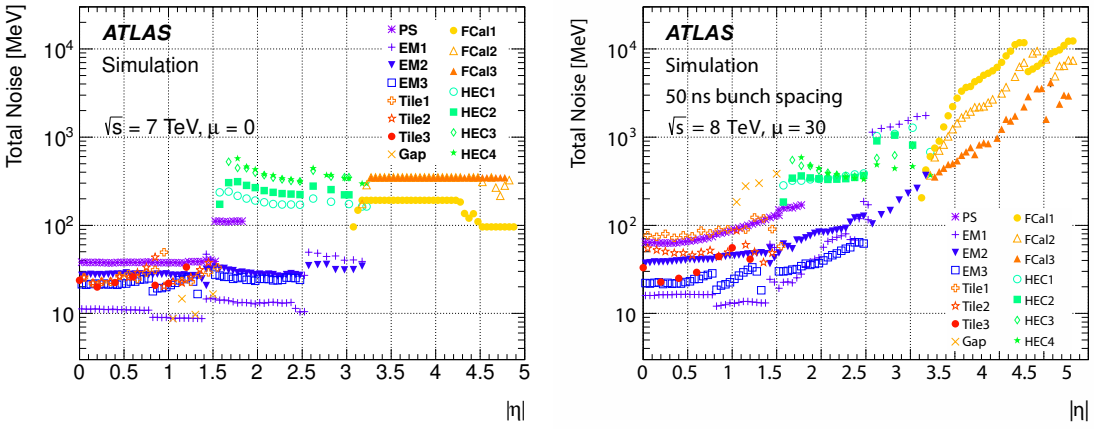

(a) No pile-up (b) $\langle\mu\rangle = 30$

Figure 5.2: The cell noise (in equivalent units of energy) in the ATLAS calorimeters at the EM scale as a function of $|\eta|$ location [118].

2 [119]. The energy equivalent cell noise in the ATLAS calorimeters is shown in Fig. 5.2 for pile-up conditions expected in 2016.

The values are only optimal for a central point of the instantaneous luminosity for a given run, before which there will be an excess of noise and after which it will have sub-optimally reduced sensitivity to small calorimeter signals.

The significance of cell energy deposits are calculated from the ratio of measured cell energy to the cell noise,

$$\zeta_{\text{cell}}^{\text{EM}} = \frac{E_{\text{cell}}^{\text{EM}}}{\sigma_{\text{noise,cell}}^{\text{EM}}}. \tag{5.4}$$

Cell significance forms the input to the 3-step formation of topoclusters. There are three thresholds (S, N, P) in this parameter corresponding to the three phases of cluster formation:

$$\begin{aligned}
&|E_{\text{cell}}^{\text{EM}}| > S\sigma_{\text{noise,cell}}^{\text{EM}} \Rightarrow |\zeta_{\text{cell}}^{\text{EM}}| > S = 4 && \text{(primary seed threshold)} \\
&|E_{\text{cell}}^{\text{EM}}| > N\sigma_{\text{noise,cell}}^{\text{EM}} \Rightarrow |\zeta_{\text{cell}}^{\text{EM}}| > N = 2 && \text{(threshold for growth control)} \\
&|E_{\text{cell}}^{\text{EM}}| > P\sigma_{\text{noise,cell}}^{\text{EM}} \Rightarrow |\zeta_{\text{cell}}^{\text{EM}}| > P = 0 && \text{(principal cell filter)}
\end{aligned} \tag{5.5}$$

The algorithm starts by identifying seed cells which exceed a significance of S. Each seed is grown into a proto-cluster with adjacent cells (overlapping in $\eta - \phi$ between

layers or adjacent within a layer) that exceed a significance of N. And then the volume is covered by a surface layer of cells exceeding a significance of P. Cells are allowed to belong to 2 proto-clusters with weighting. Negative energy cells arising from out-of-time pile-up signals can contribute since the absolute value of the significance is used. The absolute value of cell energy is also used as the weights when constructing the final $\eta - \phi$ direction of the cluster. Perhaps counterintuitively, this turns out to be a best choice for how to handle the negative energy cells because it eliminates bias that occurs in cluster direction and energy when ignoring negative energy cells. The values of $S = 4$, $N = 2$, and $P = 0$ have been found to be optimal from the response of the relative energy resolution for charged pions in test-beam experiments on ATLAS calorimeter prototypes [120].

Local hadronic cell-weighting A better energy measurement of a cluster can be made beyond simply summing deposited energy in the clustered cells (referred to as EM scale). A method of local hadronic cell-weighting (LCW or LC scale) is used in ATLAS to correct for a number of sources of calorimeter inefficiency in signal reconstruction. In this thesis it is used for large-R jets but not regular jets which are reconstructed at EM scale. Information from cluster shape, energy density, and detector location are exploited to compensate for the following sources of inefficiency:

Calorimeter non-compensation The signal in the ATLAS calorimeters is not corrected for differing response to electrons/photons from that of hadrons. This is a consequence of the deeper penetrating depth of the hadrons in the calorimeters and therefore differences in interaction with the calorimeter materials and consequently the deposition of energy in different layers of the calorimeters.

Signal losses from clustering Especially with increased estimate of noise due to pile-up, a significant fraction of the energy of a shower may not be captured in the clustering procedure.

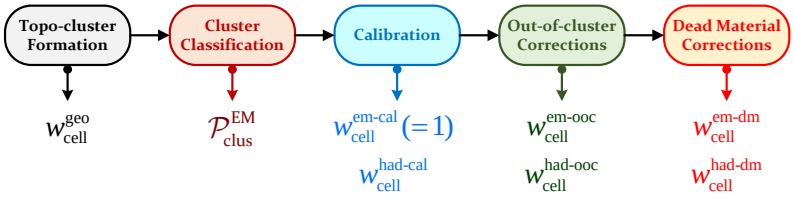

Figure 5.3: : Overview of the local hadronic cell-weighting (LCW) calibration scheme for topo-clusters. Following the topo-cluster formation, the likelihood for a cluster to be generated by electromagnetic energy deposit $\mathcal{P}_{\text{clus}}^{\text{EM}}$ is calculated. After this, cluster weights are determined for EM and HAD-like clusters and two additional corrections to the weights are added. The out-of-cluster correction is based on a search for significant energy deposits near to the cluster but separated topologically. The dead material correction adds an estimate of the energy lost in dead material in front of the calorimeter.

Energy lost in inactive material This correction accounts for energy that has been lost in inactive material in front of, between, and inside the calorimeter modules.

The weighting is termed "local" because it is made locally in cluster energy and pseudorapidity. A classification is made to determine the likelihood ($\mathcal{P}_{\text{clus}}^{\text{EM}}$) that a cluster is generated from an electromagnetic energy deposit or from hadronic energy deposits, and then used to apply different weights respectively:

$$w_{\text{cell}}^{\text{cal}} = \mathcal{P}_{\text{clus}}^{\text{EM}} \cdot w_{\text{cell}}^{\text{em-cal}} + (1 - \mathcal{P}_{\text{clus}}^{\text{EM}}) \cdot w_{\text{cell}}^{\text{had-cal}}. \tag{5.6}$$

The process of hadronic calibration of clusters is outlined in Fig. 5.3. It aims to improve the energy resolution of clusters through the identification of a the source of cluster energy as hadronic or electromagnetic. For each type a specialized calibration is applied. While the LCW procedure is expected to improve the resolution of jet energies after final calibration, as of this writing, little improvement has been demonstrated across the range of jet energies in ATLAS compared to using EM-scale.

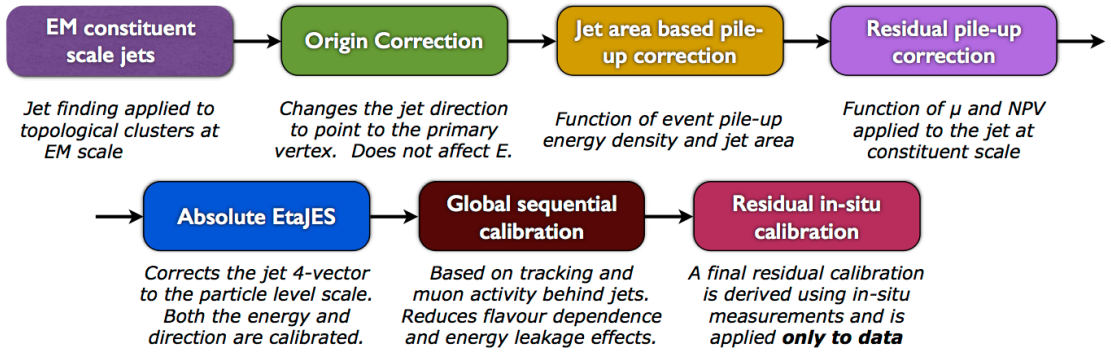

Figure 5.4: Calibration stages for EM-scale jets.

5.3 Calibration

The calibration of jets is made on MC first, and then a correction to the calibration is made by MC-data comparison in balance studies that exploit conservation of momentum transverse to the beamline. The initial calibration is made by comparing the response of jets reconstructed from truth particles in simulation to jets composed of calorimeter topoclusters in the same simulation. The response is initially corrected for the effects of pile-up before the jet calorimeter response is evaluated. Following the evaluation of the jet energy response a number of sequential corrections are applied based on specific information in the tracking, calorimeter layers, and the muon spectrometer.

A summary of the steps of jet calibration is shown in Fig. 5.4. Application of the complete jet calibration restores on average the energy and direction of jets of true particles reconstructed with the same jet definition. After the initial formation of jets from topoclusters, the origin correction recalculates the direction of the topocluster 4-momentum by adjusting the origin from the nominal $(0, 0, 0)$ to the location of the reconstructed hard-scatter primary vertex that is based on track reconstruction of charged particles in the inner detector. Next, the pile-up corrections remove the dependence of reconstructed jet energy on the measured pile-up in the event. The

reconstructed energy is then multiplied by a factor derived from MC comparison of true and reconstructed jet energy, referred to as the jet energy scale (JES). Further improvements are made to the precision of reconstructed jet energies by correcting for the dependence of jet energy on calorimeter, track, and muon spectrometer (MS) variables known as the global sequential calibration (GSC). The last step is the *in situ* calibration determined from the comparison of the p_{T}-balance of several physics selections against a jet in both data and MC.

Pile-up Correction

Final state particles originating from pile-up vertices affect the reconstructed jet energies of hard scatter (HS) jets in two ways. One, in the case that they cause showers that overlap cells in clusters originating from the HS, the calorimeter signals at the front end board are more-or-less linearly summed. Two, in the case that calorimeter showers from PU don't overlap significantly energy deposited by the HS, they can cause the seeding of additional clusters which are included in the formation of jets. The calorimeter signal of a given cell is sampled 4 times with optimal filtering coefficients (OFCs) [121], which are a (lossy) linear combination of the 24 signal samplings that occur at 25 ns intervals over the course of a calorimeter impulse (Fig. 3.9). The use of only four values, optimally determined, to evaluate the signal curve is required by the read out bandwidth of the calorimeters. The complete effects of the compression in the presence of high PU are not fully understood and may not completely retain linearity of signal.

The PU corrections are composed of two steps: area-based subtraction of the average jet energy density contribution attributable to PU, and then a correction for any residual reconstructed jet energy dependence on the two variables indicating the level of in and out-of-time PU, N_{PV} and μ respectively [122]. The corrections are

made to the reconstructed p_{T}, $p_{\mathrm{T}}^{\mathrm{const}}$:

$$p_{\mathrm{T}}^{\mathrm{corr}} = p_{\mathrm{T}}^{\mathrm{const}} - \rho \times A - \alpha \times \left(\mathrm{NPV} - \mathrm{NPV}^{\mathrm{ref}} - 1\right) - \beta \times (\mu - \mu^{\mathrm{ref}}), \tag{5.7}$$

where ρ is an event-by-event calculation of the transverse momentum density, A is the catchment area attributed to the jet, α and β are the residual p_{T}-dependency on N_{PV} and μ respectively. The reference values $\mathrm{NPV}^{\mathrm{ref}}$ and μ^{ref} are determined from the average values in the run. Due to the long calorimeter signal time and the differential signaling of the LAr calorimeters (Fig. 3.9) the timing of the overlap, whether it is within the given bunch crossing or in previous bunch crossings, determines whether the overlap results respectively in an increase or decrease of the strength of the calorimeter signal.

Area-based subtraction Positive average contributions to jet energy from in-time PU vary event by event about an average value determined by the average out-of-time PU. The specific number of interactions in an event is distributed according to the Poisson distribution. Random positive fluctuations to jet energy occur from the overlap of many low-p_{T} minimum bias QCD jets from the additional vertices accordingly. The positive statistical variation occurs on top of a negative shift to measured energy in the calorimeter cells from the long flat negative cell signal which acts to produce a constant negative shift dependent only on the time-averaged conditions prior to the bunch crossing.

For reasonable jet definitions [123] the effect on jet p_{T} due to PU is,

$$\Delta p_{\mathrm{T}} = A\rho \pm \sigma\sqrt{A} - \mathcal{O}(\alpha_{\mathrm{s}} \cdot A\rho \ln \tfrac{p_{\mathrm{T}}}{A\rho}) \ , \tag{5.8}$$

where ρ is the amount of transverse momentum added to the event per unit area and σ is the standard deviation of the resulting noise measured in regions of unit area. This equation essentially states that the average contribution of PU to the measured jet energy can be subtracted out event by event, that there will be an unavoidable

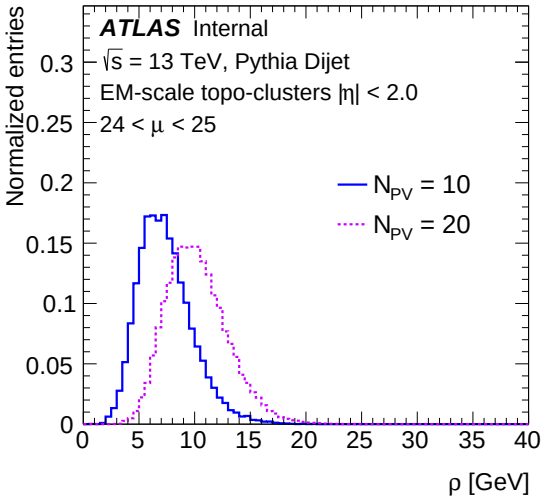

Figure 5.5: Per-event p_{T} density, ρ, at NPV of 10 (solid) and 20 (dotted) for $24 < \mu < 25$.

random fluctuation on top of that, and other effects will be suppressed by an order of strong coupling. This recipe turns out to be quite effective in practice; the first term corresponds to the first term subtracted in Eq. 5.7. The area A is calculated by adding an even array of infinitesimal particles (called *ghosts* spread evenly in the $\eta - \phi$ plane along with the clusters. The ghosts combined with the jet after use of the anti-k_t algorithm determine the catchment area of the jet. The transverse momentum density ρ is determined by clustering the event with the Cambridge-Aachen algorithm–because its jets cover the space instead of having a roughly fixed radius–with positive energy clusters. The median of the p_{T} density of the resulting jets (including any 0 density space) is taken to represent the average p_{T} density in the event. Figure 5.5 shows the distribution of ρ for the MC simulation used to determine the calibration of jets in 2016. The areas of jets are insensitive to the clustering noise thresholds, but ρ is almost perfectly sensitive to the choice of noise threshold used in the (4-2-0) cluster making algorithm. It has been shown that after the area subtraction procedure any significant effect on the variation of noise thresholds has been removed after area-based subtraction [119].

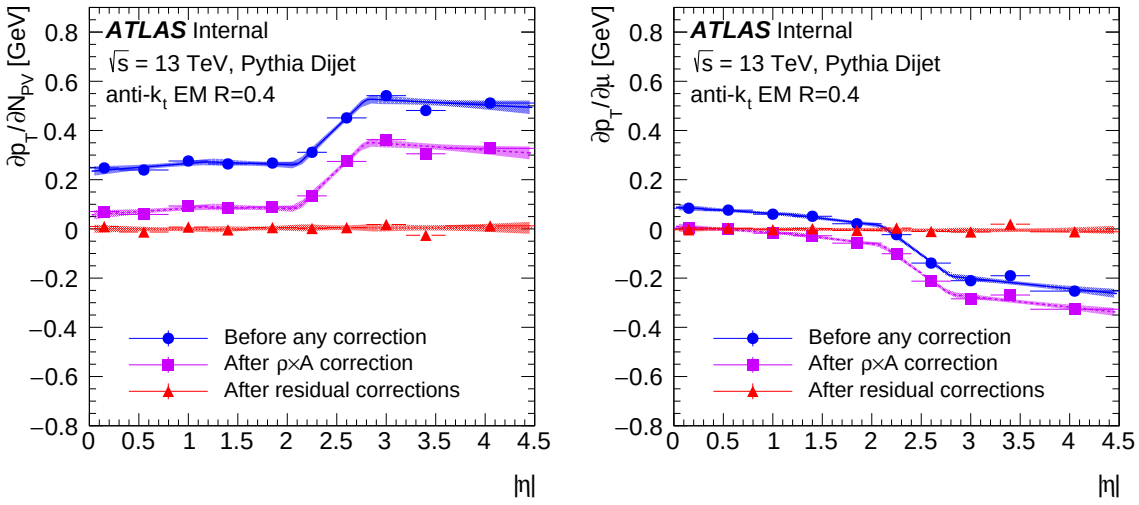

(a) In-time pile-up dependence

(b) Out-of-time pile-up dependence

Figure 5.6: Dependence of EM-scale anti-kt jet p_{T} on in-time pile-up (NPV averaged over μ) and out-of-time pile-up (μ averaged over NPV) as a function of $|\eta|$. The dependence is shown before pile-up corrections (circle), after area subtraction (square), and after the fitted residual correction (triangle). The dependence on in-time (out-of-time) pile-up after the area correction is taken as the residual correction factor α (β).

There is some residual dependence of the JES on in and out-of-time PU, $\frac{\partial p_{\mathrm{T}}}{\partial N_{\mathrm{PV}}}$ and $\frac{\partial p_{\mathrm{T}}}{\partial \langle\mu\rangle}$. This dependence is fit in MC simulation and removed with terms 2 and 3 of the correction in Eq. 5.7. The dependence of the JES on $N_{\mathrm{PV}}$and μ is highly anti-correlated. Additionally, the magnitude of the JES dependence changes with jet-p_{T}. Consequently the fitting is performed in the 4D space of $\{\mu, N_{\mathrm{PV}}, p_{\mathrm{T}}, \eta\}$.

The correction for the residual dependence of the JES on the in-time pile-up (N_{PV}) is shown in Fig. 5.6 (a) and on the out-of-time pile-up (μ) in Fig. 5.6 (b). The closure–the dependence re-evaluated after the application of the corrections–is also shown in red in the same figures. The p_{T}-dependence of the residual corrections is fit logarithmically, which turns out to be small and the corrections are well-made constant in p_{T}. This means that the effect of PU dominates low-p_{T} jets and becomes trivial at high-p_{T}. Consequently, to evaluate the corrections the p_{T} dependence curve is sampled at the lower end of the usable jet energy range, a value of $p_{\mathrm{T}} = 25$ GeV. The

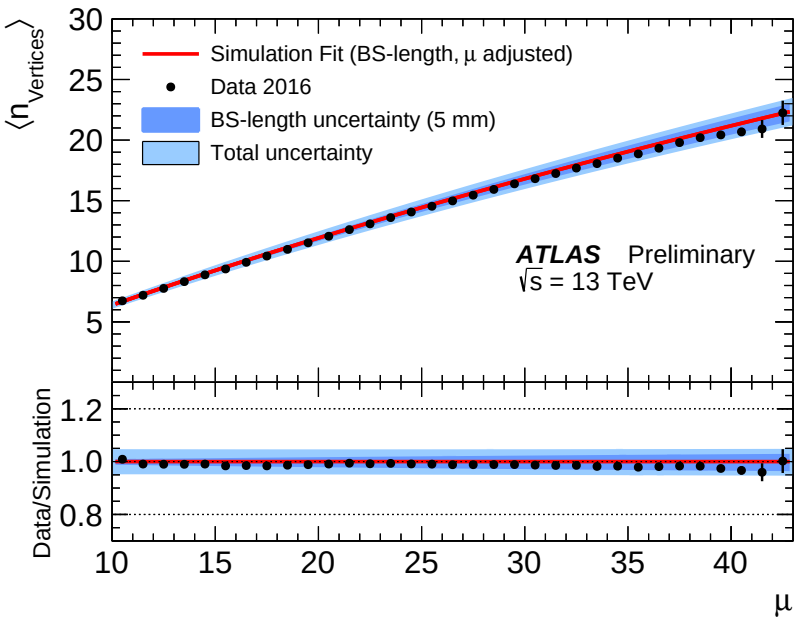

Figure 5.7: Distribution of the average number of reconstructed vertices as a function of μ. The curve represents the result of a fit to the simulation of minimum-bias events, while dots are a representative subset of zero-bias data collected in 2016. Simulation is corrected for the difference in beamspot length (BS-length) with respect to data as well as to match the inelastic cross section value measured in $\sqrt{s} = 13$ TeV data (μ-adjusted) [30].

lowest used jet p_{T} in ATLAS is 20 GeV, below which inefficiencies in jet reconstruction are poorly understood and there is little capability to separate HS jets from those from PU.

Inevitably the beam conditions prepared in sample simulation are different than those realized during data-taking. The length of the beamspot (in z) determines the relationship between N_{PV} and μ. Since the PU corrections are parametrized by N_{PV} and μ, derived from MC, and applied to data this difference must be accounted for. It is sufficient to apply a single scale factor to μ measured in data to make the correction–in 2015 this was 1.16. Figure 5.7 shows the comparison between data and MC after the correction has been applied. After the PU corrections to the JES, average jet energies are no longer dependent on the PU conditions (within a wide range) present during the taking of the data. Naturally, there remains some increase

of the jet energy resolution (JER) with the increased presence of PU.

There are four uncertainties used to capture systematic uncertainties related to PU in the JES, joining the complete list of jet uncertainties summarized in Table 5.1. A complete description of the derivation of PU systematics uncertainties is available [122]. The first uncertainty is the aforementioned logarithmic dependence of the residual corrections. The systematic uncertainty on the jet-p_{T} dependence on N_{PV} and μ is determined by data-MC comparison made with a selection of Z+jet events where a Z candidate decays to $\mu\mu$ and balances well a jet, such that they are "back-to-back" in ϕ. Conservation of transverse momentum ensures that p_{T} of $\mu\mu$ system balances the p_{T} of the jet. In the same studies a match between calorimeter jets and track jets is made[2]. This can only be done for $|\eta| < 2.1$, the limit of the inner detector where tracks are reconstructed, but the result is extended to the forward regions. The dependence of Δp_{T}, the difference between the reconstructed jet p_{T} and the reference object being used (either track jet or Z), on N_{PV} and μ is determined. The closure between data and MC and between data and 0 and the statistical uncertainty from the study in evaluating them are all taken together as sources of uncertainty. Furthermore, the forward jets have an additional uncertainty that arises from bias occurring from the use of only the Z+jets study, which does not have sufficient statistics to exclusively bin in N_{PV} and μ and cannot completely resolve the anti-correlated effects of in and out-of-time PU. The envelope of these closures is taken to be an (slightly conservative) estimate of the uncertainty on residual PU corrections to N_{PV} and μ, respectively $\Delta\left(\frac{\partial p_{\mathrm{T}}}{\partial N_{\mathrm{PV}}}\right)$ and $\Delta\left(\frac{\partial p_{\mathrm{T}}}{\partial \langle\mu\rangle}\right)$. The uncertainty grows linearly from the reference values of μ and N_{PV} used in the data set used to

[2]Track jets are defined using the anti-k_t algorithm but using charged-particle tracks from the inner detector instead of calorimeter topoclusters

determine them μ^{ref} and $N_{\text{PV}}^{\text{ref}}$:

$$\begin{aligned}\Delta_{p\text{T}}^{N_{\text{PV}}} &= \pm\Delta\left(\frac{\partial p_{\text{T}}}{\partial N_{\text{PV}}}\right) \times (N_{\text{PV}} - N_{\text{PV}}^{\text{ref}}) \\ \Delta_{p\text{T}}^{\langle\mu\rangle} &= \pm\Delta\left(\frac{\partial p_{\text{T}}}{\partial \langle\mu\rangle}\right) \times (\langle\mu\rangle - \langle\mu\rangle^{\text{ref}})\end{aligned} \tag{5.9}$$

The fourth and last PU uncertainty is meant to cover the dependence of ρ on the energy from the UE. It is derived from the comparison of the difference in ρ between differing event topologies in data and MC. This strategy results in an over estimate and a more careful study should be performed in the future to get a precise knowledge of the real dependence of ρ and jet-p_{T} on the UE. The combined uncertainty from PU is shown on the uncertainty summary plot, Fig. 5.12.

Jet Energy Scale and η calibration

The jet energy scale corrects, on average, the reconstructed particle-level jet energy by applying a factor derived from QCD dijet MC.

The jet energy scale (JES) is the inverse of the jet energy response to truth jets in the calorimeters: JES $= 1/R = E^{\text{true}}/E^{\text{reco}}$[3]. Truth jets and reco jets are geometrically matched with $\Delta R < 0.3$ in MC–ΔR is many times larger than the precision and accuracy of reconstructed jet directions in ATLAS so the precise ΔR has negligible effect on the result. The truth response R^{true} is evaluated as $\langle E^{\text{reco}}\rangle/E^{\text{true}}$ in bins of E_{true} and then fit with a log polynomial of up to degree 8. This results in a function that maps E^{true} to E^{reco} when jets are binned in E^{true}, but in data we do not have E^{true} of a jet so this form is not yet useful. Therefore what is needed

[3] Throughout this chapter, the average calorimeter response to jets, or average jet p_{T} response, for a given population of calorimeter jets is defined as $R = \langle p_{\text{T}}^{\text{jet}}/p_{\text{T}}^{\text{true}}\rangle$, where $p_{\text{T}}^{\text{jet}}$ is the calorimeter jet p_{T} and $p_{\text{T}}^{\text{true}}$ is the p_{T} of the matched truth jet. The mean is taken from a Gaussian fit to the $p_{\text{T}}^{\text{jet}}/p_{\text{T}}^{\text{true}}$ distribution within a range of 1.6σ from its mean value. The same prescription is used for fitting of the jet *energy response*, using the energies instead of the transverse momenta. The jet resolution, σ_R, is defined by the standard deviation of the Gaussian fit to the jet response distribution. The fractional jet resolution ($\sigma_R/R = \sigma_{p_{\text{T}}}/p_{\text{T}}$) is used to determine the size of the fluctuations in the jet p_{T} reconstruction.

is a mapping solely from E^{reco} to $\langle E^{\text{true}} \rangle$. The response curve R^{true} that is already in hand provides the needed mapping to translate the reconstructed energy into its expected truth energy for application of the JES:

$$E_i^{\text{true}} = R^{\text{true}^{-1}} E_i^{\text{reco}}, \tag{5.10}$$

where the index i refers to a specific measurement. The result is the *stretching* of R^{true} to get the final calorimeter response curve $R(E^{\text{reco}}) = 1/\text{JES}$. This process is known as *numerical inversion* and most importantly results in an unbiased energy scale no matter the distribution of jets in the MC sample used to derive it. The JES is applied simply as $\text{JES}(E^{\text{true}}) \times E^{\text{true}}$ in exclusive η_{det} bins after the step of the PU corrections.

An inclusive selection of jets is used for determining the jet calibration [4] as opposed to, say, a leading jet calibration only.

Simultaneously, using the same methodology a correction to the η-direction of jets is derived. Average bias in jet directions comes from transitions of granularity within and gaps between calorimeters. The JES and η-corrections are shown in Fig. 5.8. Gaps between calorimeters are clearly visible in the distributions, for example at $|\eta| = 1.5$ and $|\eta| = 3.3$.

Global sequential calibration

Longitudinal and transverse features of calorimeter jets and the distributions of charged and neutral particles affect the reconstructed energies in the calorimeters. Differences in the measured energies arise both from the statistical nature of the evo-

[4] It is made with the following prescription: Reconstructed calorimeter jets are matched geometrically to truth jets within $\Delta R = \sqrt{(\eta_{\text{calo}} - \eta_{\text{true}})^2 + (\phi_{\text{calo}} - \phi_{\text{true}})^2} < 0.3$. Only "isolated" jets are used to avoid any ambiguities in the matching of calorimeter jets to truth jets. The isolation requirement for calorimeter jets is that there should be no other calorimeter jet of $p_{\text{T}} > 5$GeV (at the scale obtained after $\rho \times A$ subtraction) within $\Delta R = 1.0$, and only one truth jet with $p_{\text{T}}^{\text{true}} > 7$GeV within a cone of $\Delta R = 0.6$.

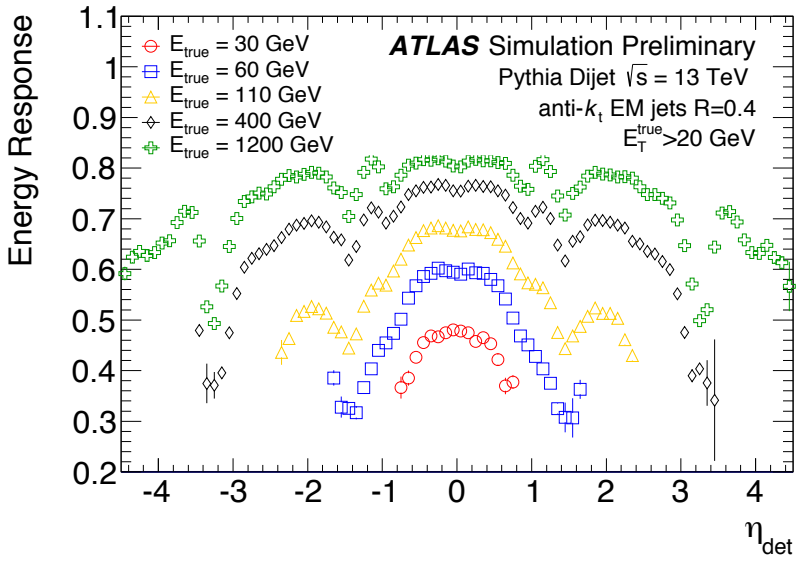

Figure 5.8: Energy response as a function of η_{det} for jets of a truth energy of 30, 60, 110, 400, and 1200 GeV. The energy response is evaluated after origin and pile-up corrections have been applied.

lution of jet showers within the detectors and from the variation in the composition of jets–for example from quark and gluon-initiated jets which have different fractions of charged particles on average. Five observables are identified to correlate with reconstructed jet energy. Corrections to these five variables are applied sequentially in a global sequential calibration (GSC)–this can be done because they are mostly uncorrelated. Corrections are made in a way that preserves the JES previously derived. The five stages of the GSC fit the dependence of jet energy linearly and then correct for it on the following variables:

$\boldsymbol{f_{\text{Tile0}}}$ the fraction of energy deposited in the first layer of the Tile calorimeter ($|\eta| < 1.7$).

$\boldsymbol{f_{\text{LAr3}}}$ the fraction of energy deposited in the third layer of the electromagnetic LAr calorimeter ($|\eta| < 3.5$).

$\mathbf{width_{trk}}$ the p_{T}-weighted average transverse distance between the jet four-momentum and all tracks with $p_{\text{T}} > 1$ GeV associated to the jet ($|\eta| < 2.5$).

$\mathbf{n_{trk}}$ the number of tracks with $p_{\text{T}} > 1$ GeV associated to the jet ($|\eta| < 2.5$).

$\boldsymbol{N_{\text{segments}}}$ the number of muon segments associated with the jet ($|\eta| < 2.7$)

The dependence of jet energies on the variables used in the GSC has been studied between data and MC and found to be in excellent agreement [124].

In situ Calibration

After the complete MC calibration of jets comes a final correction based on comparison of the p_{T}-balance of a reference object against a jet. The *in situ* correction accounts for differences to jet p_{T} reconstructed in MC and data that arise mainly from inaccuracies in the detector description, modeling of interactions in the calorimeters, and the physics of jet formation.

The η-inter-calibration evaluates the relative response of forward jets by comparison to the better-measured central jets using dijet events. After this initial relative geometric calibration, three types of p_{T}-balanced events are used to determine the absolute response of jets over the wide range of jet p_{T} to a reference object: Z boson, photon, and a system of 2 or more lower p_{T} jets. For each, the ratio of the p_{T} of the reference object in both data and MC $\mathcal{R}_{\text{in-situ}}$ is evaluated and then the ratio is again taken between data and MC:

$$c = \frac{\mathcal{R}^{\text{data}}_{\text{in-situ}}}{\mathcal{R}^{\text{MC}}_{\text{in-situ}}}. \tag{5.11}$$

The "double ratio" c is taken to be an unbiased estimator of the ratio between the jet energy scale in data and MC. The *in situ* calibrations are derived and applied in sequence, evaluating systematic uncertainties along the way. Systematic uncertainties arise from the mis-modeling of physics effects, measurements of the kinematics of the reference object, and the event selections in obtaining the balance samples.

η-inter-calibration

The purpose of the η-inter-calibration is to bring the well-studied jet response in the central region ($|\eta| < 0.8$, often referred to as the "fiducial region") to provide a precise

calibration of more forward jets and take the the ratio between data and MC at each η over the full range of jet p_{T} [125].

The η-inter-calibration finds the ratio $\mathcal{R}_{ijk}$ of relative calorimeter response between back-to-back jets, where each lies in different η-regions i and j of the detector, and their average p_{T} is in bin k. It is derived in data and POWHEG+PYTHIA MC and a comparison to the SHERPA generator provides a systematic modeling uncertainty. A bit of linear algebra yields the best fit for the relative response of each region i of η to the fiducial region c_{ik} for given p_{T} range. A least squares strategy is used to fit the best response to each of the N η-bins simultaneously by minimizing S:

$$S(c_{1k},\ldots,c_{Nk}) = \sum_{j=1}^{N}\sum_{i}^{j-1} = 1\Big(\frac{1}{\Delta\langle\mathcal{R}_{ijk}\rangle}(c_{ik}\langle\mathcal{R}_{ijk}\rangle - c_{jk})\Big)^2, \tag{5.12}$$

where $\langle R\rangle$ and $\Delta\langle R\rangle$ here are the measured relative responses between regions and their statistical uncertainty, respectively. This strategy utilizes the full statistical power of the data taken compared to only balancing each region directly with the central region, which is still used as a cross check to ensure a good fit.

Figure 5.9 shows slices in p_{T} and η of the relative jet response obtained in MC and data. There is generally a bit higher response in data in the forward regions and there is no observed statistically significant difference in $\pm\eta$ response. Systematic uncertainty is taken as an envelope of the MC comparison and a variation made in each of PU, a jet veto cut, and a $\Delta\phi_{ij}$ cut used in the analysis. The ratio of MC to data forms the *in situ* correction to data, shown in Fig. 5.10.

In situ calibration balance studies

The central region, $|\eta| < 0.8$, is then calibrated by the balance of a well-measured object to a jet. The following three studies extend the *in situ* calibration to different jet p_{T} ranges sequentially:

1. ***Z*-jet balance** Both the $Z \to e^+e^-$ and $Z \to \mu^+\mu^-$ channels are used for the reconstruction of the Z boson. The electrons (or muons) are precisely measured

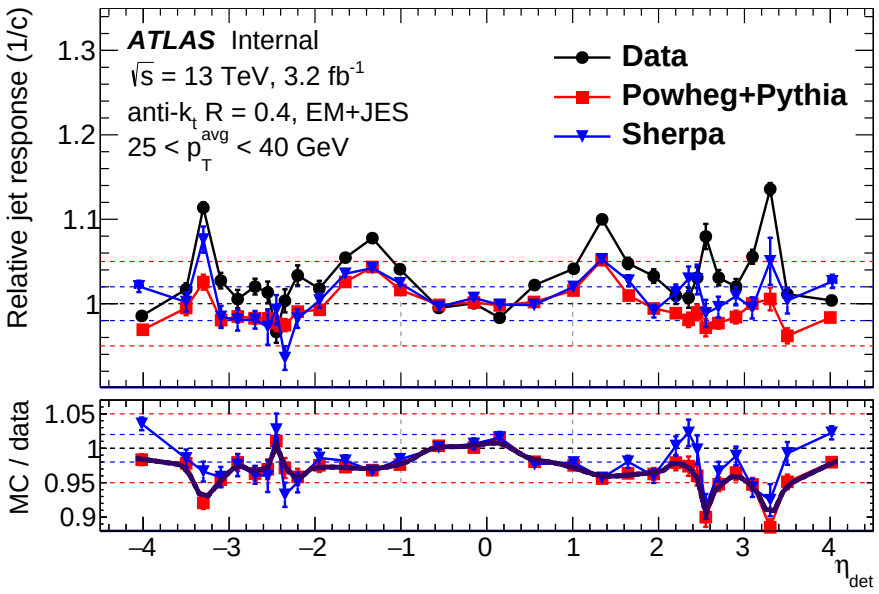

Figure 5.9: Relative jet response of forward regions with respect to the *fiducial* central region of the ATLAS calorimeters. Response is evaluated in two MC simulations and in data. The ratio of MC/data defines the relative *insitu* calibration in η.

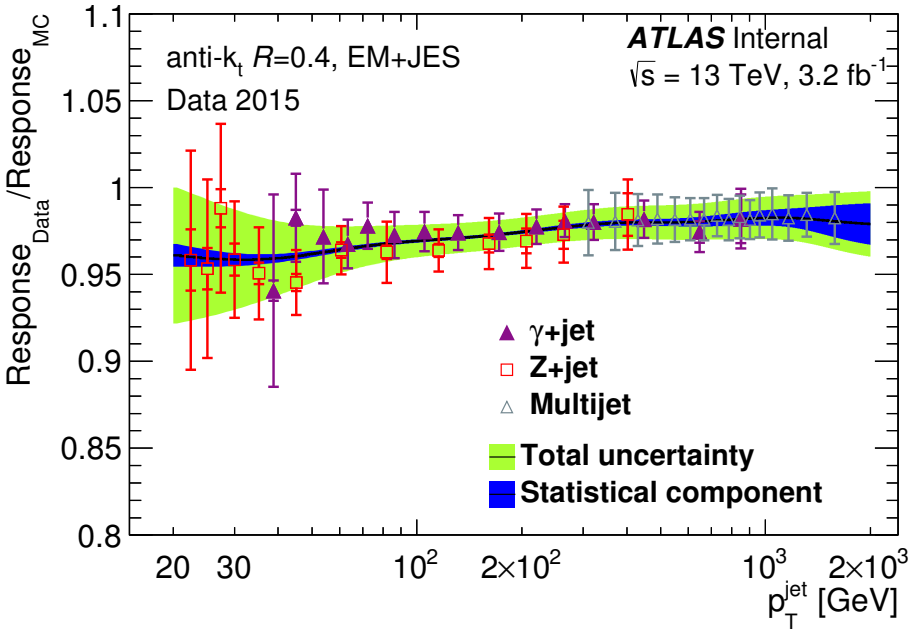

Figure 5.10: Ratio of EM-scale jet response in data to the nominal MC generator as a function of jet p_{T} for γ-jet, Z-jet, and multijet *in situ* calibrations. The final derived correction (black line) and its statistical and total uncertainty bands are also shown.

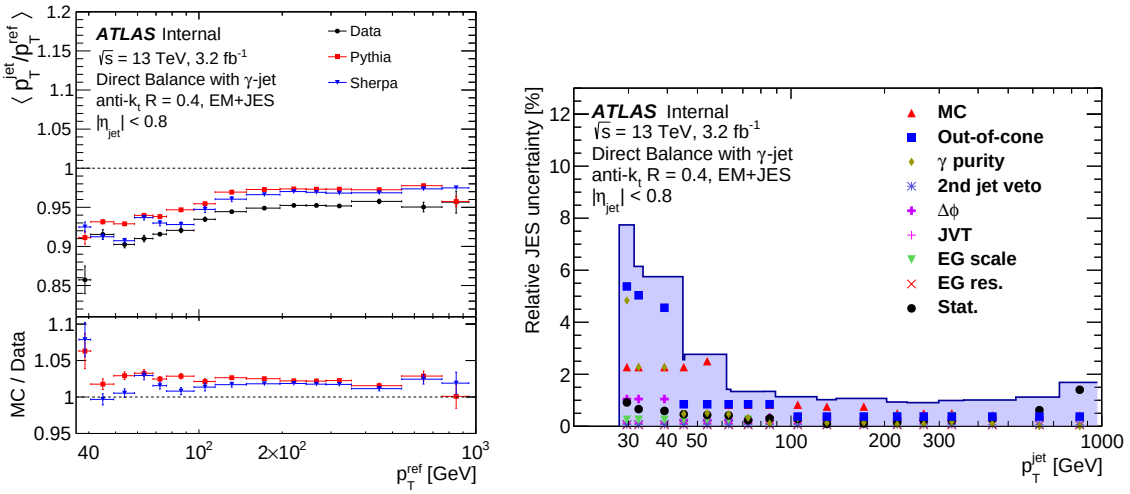

Figure 5.11: Average direct p_{T}-balance (a) and uncertainty (b) of jets after η-inter-calibration in data and MC as a function of jet p_{T} for γ-jet events.

from the electromagnetic calorimeter (muon spectrometer). The range of applicability is limited by the statically significant range from data collected in 2015, between $20 < p_{\mathrm{T}} < 506$ GeV. The complete hadronic recoil of the event is used instead of a direct balance between the jet and the reconstructed Z boson. Lower-p_{T} jets are more susceptible to the (poorly modeled) out-of-cone radiation that can fall outside the $R = 0.4$ jet cone from fragmentation processes. By using the full hadronic recoil rather than just the jet, it is insensitive to the jet definition, the radiation falling outside the jet cone, and the PU activity (which is ϕ-symmetric). The calorimeter response to the hadronic recoil (missing projection fraction or MPF) is a function of the missing transverse momentum $E_{\mathrm{T}}^{\mathrm{miss}}$ and $E_{\mathrm{T}}^{\mathrm{ref}}$ the transverse energy of the reconstructed reference object (Z here) and its direction $\hat{n}_{\mathrm{ref}}$:

$$R_{\mathrm{MPF}} = 1 + \frac{\hat{n}_{\mathrm{ref}} \cdot E_{\mathrm{T}}^{\mathrm{miss}}}{\hat{n}_{\mathrm{ref}}}. \tag{5.13}$$

. The R_{MPF} in MC in data and its ratio is shown in Fig. 5.11 (a).

2. **γ-jet balance** The photon reference p_{T} is constructed from transverse momen-

tum perpendicular to the jet axis,

$$p_{\mathrm{T}}^{\mathrm{ref}} = p_{\mathrm{T}}^{\gamma} \times |\cos(\Delta\phi)|, \tag{5.14}$$

where $\Delta\phi$ is the azimuthal angle between γ and the jet. The direct balance between the reference object and the jet is taken in MC and data. The γ-jet balance has significant statistics for jet transverse momentum in the range $36 < p_{\mathrm{T}} < 944$ GeV. In the Z/γ-jet balances studies the uncertainties from electrons [126], photons [126], and muons [127] are propagated into the measurement. The $\Delta\phi$, 2nd jet veto, and JVT uncertainties are all determined by variation of selection criteria around their chosen point. The out-of-cone uncertainty addresses systematic bias in the balance caused by particles falling outside the jet cone.

3. **Multi-jet balance** The final stage of the *in situ* calibration extends the calibration to the higher p_{T} range covering jet transverse momentum by balancing the recoil of 2 or more jets against the highest energy jet in the event for the central $|\eta| < 1.2$ region. This step can be applied multiple times updating the uncertainties each time–in 2015 it was done twice.

A summary of uncertainties entering the *in situ* balance studies by source is provided in Table 5.1.

Combination of uncertainty

The *in situ* studies are combined with a weighted minimum χ^2 fit to evaluate the *in situ* calibration curve and the combined uncertainty. The *in situ* calibration curve is shown in Fig. 5.10 showing the combination of overlapping regions. The final JES calibration includes 80 uncertainty terms. In addition to the 67 *in situ* uncertainties there are the 4 PU uncertainties, 3 jet flavor uncertainties from MC studies. The punch-through uncertainty covers the 5th GSC correction. There is a fast simulation

Source	Description
Z-jet	e/μ scale and resolution, JVT, kinematic selection, out-of-cone particles, stats, and MC
γ-jet	γ scale, res. and purity, JVT, kinematic selection, out-of-cone particles, stats, and MC
Multijet balance	kinematic selection, MC, and stats
η-inter-calibration	
Physics mis-modeling	Envelope of the MC, pile-up, and event topology variations
Non-closure	Non-closure of the method in the $2.0 < \lvert\eta_{\text{det}}\rvert < 2.6$ region
Statistical component	Statistical uncertainty
Pile-up	μ and NPV dependence, ρ-dependence on UE p_{T}-dependence of PU corrections
Jet flavor	quark-gluon composition, gluon and b-quark response
Punch-through	GSC punch-through correction
AFII non-closure	Different scale in ATLAS Fast Simulation II
Single hadron response	High-p_{T} only, from single-particle and test-beam measurements

Table 5.1: Summary of the systematic uncertainties in the jet energy scale calibration propagated from electron, photon, and muon energy scale calibrations.

(AFII) used for large or expensive MC productions [128] which makes approximations in showering and tracking in place of a complete simulation. In this analysis it is used for the generation of 50 million $t\bar{t}$ samples. The non-closure between the MC calibration generated with AFII and the nominal calibration is taken as an uncertainty on these samples. Finally, for very high-p_{T} jets where there is not ample statistics in data to make an *in situ* calibration a method based on the response to single hadrons is extrapolated to full jets based on the MC distribution of hadrons in jets [129]. The final JES uncertainty from the combination of channels is shown in Fig. 5.12. The uncertainty over the full p_{T} range in the central region is dominated by the absolute *in situ* JES and in the forward calorimeters by the relative *in situ* JES. Uncertainties are shown under the assumption of no knowledge of flavor composition in the analysis. This is an important point in interpretation of the uncertainty curve, considering a significant response difference between gluons and quark jets. This thesis makes no attempt to reduce this uncertainty through determination of the quark-gluon composition of the jets used in the analysis. The (green) "pre-recommendation" uncertainties were derived from an analysis made by the au-

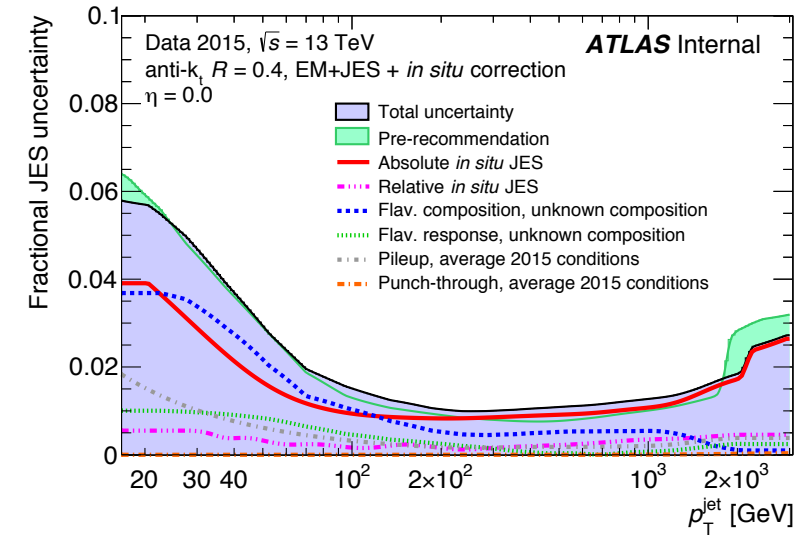

(a)

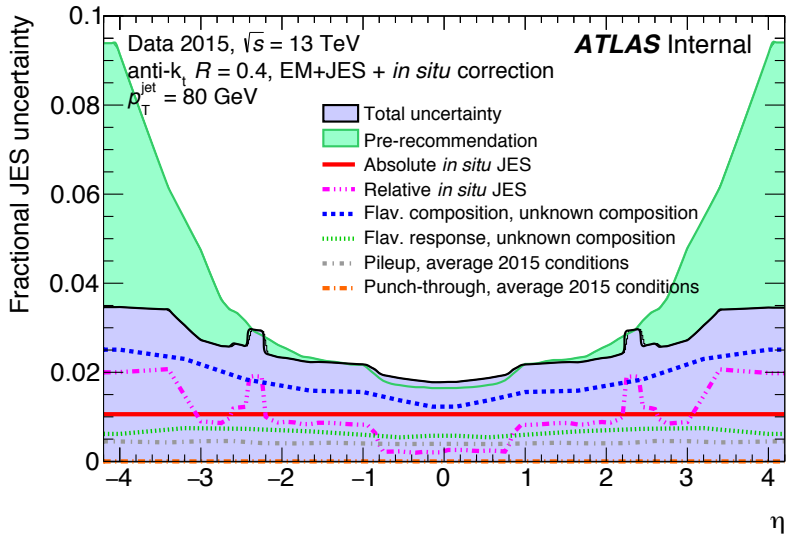

(b)

Figure 5.12: Combined uncertainties on the jet energy scale as a function of jet p_{T} at η=0 and η at $p_{\mathrm{T}} = 80$ GeV. Systematic components include pile-up, punch-through, and uncertainties propagated from the Z/γ-jet and MJB (absolute *in situ* JES) and η-inter-calibration (relative *in situ* JES). The flavor composition and response uncertainties are taken from Monte Carlo and simulate an unknown composition by assuming a 50/50 composition of quark- and gluon-initiated jets with a conservative 100% uncertainty.

thor converting the *in situ* calibration from 2012 data at $\sqrt{s} = 8$ TeV to 2015 at $\sqrt{s} = 13$ TeV [130]. It was in use for over a year until the *in situ* Run 2 correction was completed in August 2016.

Uncertainties are communicated to analyses with ***nuisance parameters*** (NP) expressed as $\pm 1\sigma$ up and down variations of the jet-p_{T} calibration. The carrying of 80 such variations through to analyses is a bit excessive when many of the variations are similar and sub-dominant to the leading NPs. To reduce the load on analyses an eigenvalue reduction is performed on the complete *in situ* NP set that projects 67 NPs on to an optimal 5 and then summing quadratically the remaining 62 NPs to produce a 6th NP. The loss of correlation from 67 to 6 NPs is shown to be on the percent level. When combined with an additional 13 NPs on jet scale there are a total of 19 NPs after this "weak" reduction. A further reduction to just 3 NPs from 19 is used for analyses that are insensitive to further loss of correlation such as the ones presented in this thesis. This is referred to as a "strong" reduction of NPs and results in certain areas of phase space in as high as 15% loss of correlation. The loss generally occurs between high and low-p_{T} jet pairs and therefore does not strongly affect this analysis which is composed of events with two jets that are no more unbalanced than the mass of their parent Z-boson allows them kinematically. A comparison of the use of weakly reduced 19 NPs to 3 strongly reduced NPs as it affects the $\ell\ell qq$ channel diboson resonance search is made in Fig. 5.13.

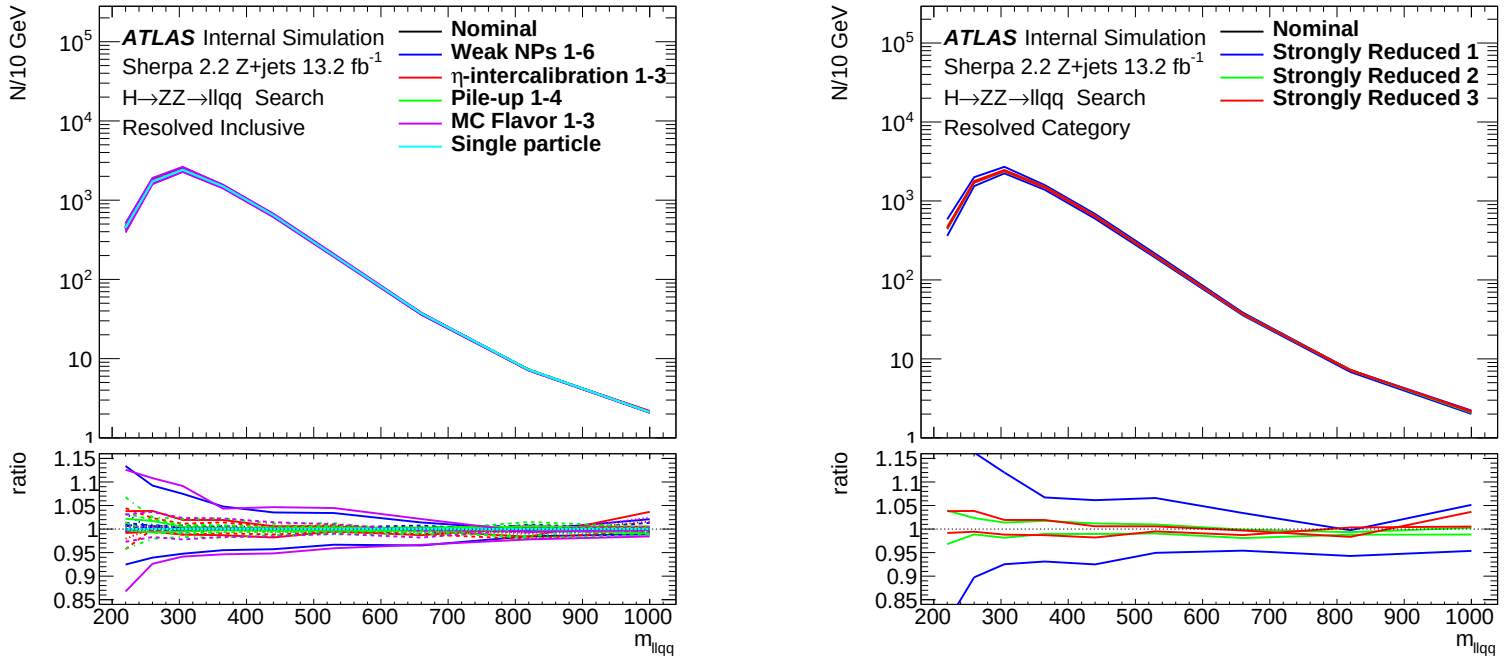

Figure 5.13: One-sigma up/down variations for weakly (a) and strongly (b) reduced small-R jet NP sets in the inclusive (SR+ZCR) resolved (small-R) analysis. The weakly reduced NP set is dominated by only a few NPs and most have very similar shape distributions. Lines are colored by subset according to source and different lines styles indicate different NP in each subset. The strong reduction has almost no effect on this analysis.

Jet Resolution

Ensuring that the comparison between data and MC is a good one depends not only on the understanding and validation of the JES but also that of the jet energy resolution (JER). The JER in data and MC is determined with the same direct balance techniques used in evaluating the *in situ* JES correction. The resolution of a jet in the direct balance is evaluated by subtracting in quadrature a known (or simultaneously measured) resolution of the reconstructed balanced object (Z, γ, other jet) in both MC and data. The full description of the methods for obtaining the resolutions would be lengthy; the calculation in the jet-jet balance channel can be found here [131]. The remaining width of the distribution is attributable to the jets. The resolution studies have similar sources of uncertainty as the JES. The final fit to the evaluated resolution in the three channels is parametrized as a function of three terms [132, 133]:

$$\frac{\sigma(p_{\mathrm{T}})}{p_{\mathrm{T}}} = \frac{N}{p_{\mathrm{T}}} \oplus \frac{S}{\sqrt{p_{\mathrm{T}}}} \oplus C. \tag{5.15}$$

The N parametrizes the electronic noise and PU noise, S parametrizes the stochastic contribution arising from the sampling nature of the calorimeters, and C is p_{T} independent component. There is little constraint on N from the balance studies so additional studies of noise are used to constrain this term. One can get a good measure of the N term by using term 2 from Eq. 5.8 which has already been calculated simultaneously event-by-event along with ρ. The value of N obtained this way matches a value obtained by simply checking the balance of the energy measured in two randomly placed (in η) back-to-back cones in ϕ.The two methods produce a consistent value of N in the central region and the second is used to determine N for forward jets.

The combined fit to the resolution measured in the three channels is shown in Fig. 5.14. For the analysis in this thesis the JER uncertainty is distilled into a single NP. For an analysis, the difference in the jet p_{T} resolution in MC and data is corrected

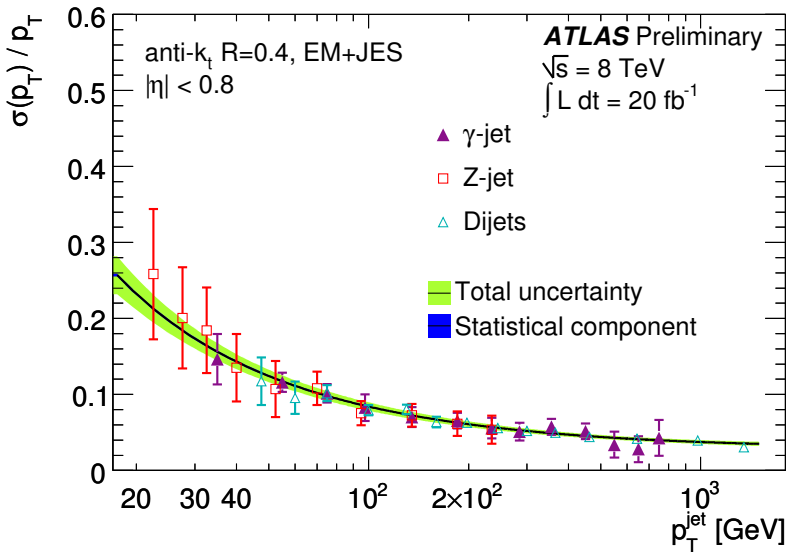

Figure 5.14: Jet p_{T} resolution in the central region. The three *in situ* measurements show excellent agreement.

for by "smearing" the smaller resolution in either data or MC with the addition of a random p_{T} determined by the difference in quadrature of the resolutions. The systematic uncertainty on the resolution is propagated into an analysis by smearing the resolution in both data and MC. The green band in Fig. 5.14 shows the range of uncertainty on the final fit.

5.4 Jet Quality Selection

Jets are sometimes reconstructed from calorimeter energy deposits arising from non-collision backgrounds. These undesirable jets are due to three main sources:

1. Beam induced background from protons ejected from the beamline at a shallow angle. This occurs from interactions of the beam with gas in the incomplete vacuum and also from diffuse loss from the tails of the beam distribution. Protons lost from the beam can introduce secondary interactions that shower muons which intersect the various ATLAS sub detectors at fixed ϕ and often at relatively fixed radius. Energy deposited from Brehmsstrahlung within the

calorimeters can result in the reconstruction of at jet. An event display of such an event from data taken without quality selection applied is shown in Fig. 5.15 [134].

Evidence of the muon's traversal in this case is left in a line passing through the muon drift tubes in the muon spectrometer end caps and within a single layer of the hadronic barrel calorimeter. The large energy deposit in the hadronic calorimeter comes from a Brehmsstrahlung on the lead scintillator.

2. Cosmic-ray showers produced in the atmosphere that overlap with collision events. Typically only muons reach the depth of the experiment and come from the vertical direction.
3. Additionally, the LAr calorimeters in ATLAS are noisy. The calorimeters are susceptible to both isolated pathological cells and large scale coherent noise. Identified noisy cells are masked both in jet reconstruction and MET reconstruction either on an event-by-event basis, permanently, or in data quality inspection.

A number of simple variables are used to discriminate against non-collision backgrounds. They come in 3 categories: signal pulse shape in the LAr calorimeters, ratio of energies in the calorimeters, and track-based variables that connect jets to the interaction point through the association of tracks to jets. A common selection of 6 cuts is used for many analyses at ATLAS [133, 135] and results in a reduction of non-collision backgrounds to negligible level with an equally negligible effect on signal acceptance. A full description of the list and the good comparison between 2015 data and MC is available [136].

Jet Vertex Tagger In some cases, PU interactions are sufficiently hard to produce a jet in the central region with sufficient energy that it is reconstructed. In higher PU conditions the overlap of energy attributable to multiple PU vertices increases

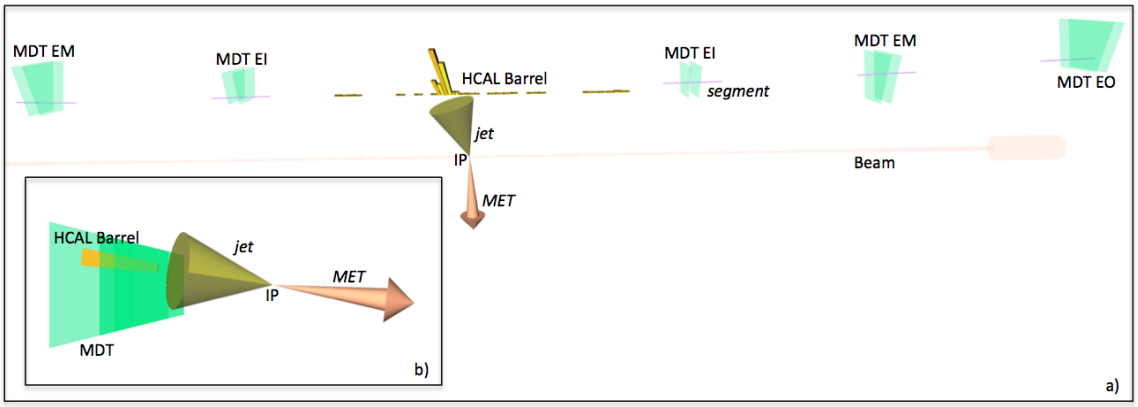

Figure 5.15: Recorded ATLAS event from 2010 without L1 and HLT jet quality criteria. The Brehmsstrahlung of a muon from beam gas on the tile calorimeter causes an oddly shaped jet in the tile calorimeter as well as leaving muon segments in both muon end-caps. The resulting naive interpretation is a mono-jet event topology with a hard jet and missing transverse energy.

this chance significantly. It is easy to remove these jets in the central region by associating charged particle tracks to each jet and ensuring that they come from the HS vertex. An evolution and combination of multiple techniques based on this concept has resulted in a robust tool for this. The jet vertex tagger (JVT) is a likelihood-based discriminant $\mathcal{L}(\text{jet}^{\text{HS}}|\{\text{tracks}\})$ covering the space of two discriminants, corrJVF and R_{pT} [137]. The corrected vertex fraction CorrJVF is the ratio of the p_{T}-weighted sum of tracks in the jet attributable to the HS primary vertex to the p_{T}-weighted sum of all tracks in the jet. The corrected part refers to a further linear correction removing the dependence of the discriminant to the total number of PU vertices in the event. The R_{pT} discriminant is similarly the ratio p_{T}-weighted sum of tracks to the jet p_{T}. JVT is trained on MC with simulated PU to produce a 2D likelihood map from each discriminant. Both the *in situ* calibration of jets and the analysis in this thesis utilize JVT to reject PU jets for jet p_{T} up to 50 GeV, above which the presence of PU jets is negligible.

5.5 Large-R jets

Large-radius jets, like regular jets, are formed with the anti-k_t [138] algorithm, but with a larger distance parameter $R = 1.0$. They are then trimmed [139] by clustering the the constituents of the jets again with the k_t algorithm with a distance parameter $R_{\text{sub}} = 0.2$. Subjets with transverse momentum of less than 5% of the original jet p_{T} are removed. Trimming significantly limits the presence of PU in the measurement of jet energy while keeping enough of the structure to meaningfully evaluate jet mass. Large-R jets are made from clusters with local hadronic cell weighting (LCW).

Using large-R jets for the identification of hadronic decay products means that in the case of the Z/W boson both decay products are constructed within the same large-R jet for a sufficiently boosted boson. Roughly, the ΔR separation of jets is $2M_{Z/W}/p_{\text{T}}$. Guaranteeing the capture of the decay products within a single jet allows for a systematic way to process the substructure of the reconstructed jet to identify the parent particle. The following subsection discusses the use of substructure techniques to identify boosted bosons.

Large-R jet energy and η are calibrated in the same way as the regular jets. Following the calibration of energy and pseudorapidity is a calibration of mass.

W/Z tagging

The use of substructure techniques to identify boosted W bosons was extensively studied in Run 1 [140]. Over 500 combinations of jet trimming [141]/pruning [142, 143]/split-filtering [144] algorithm and jet substructure variables were tested. The purpose of such algorithms is to preserve information of the hadronic decay and discriminate between processes while suppressing the effects of PU. The best combinations were identified for achieving discrimination between QCD multijets and W bosons at a benchmark of 50% boson efficiency. The best performing combination

from this study informed the choice to use jets trimmed with the following combination of parameters:

- jets are constructed from LCW topoclusters using the anti-k_t algorithm with radius parameter $R = 1.0$,
- then trimmed with subjet radius of $R_{\text{subjet}} = 0.2$,
- using a momentum fraction, the ratio of subjet to full jet momentum, of $f_{\text{cut}} = 0.05$ to define the threshold for inclusion of the subjet in the final reconstructed jet. Subjets failing to contain 5% of the total jet momentum are excluded.

The best performing combination also informs the choice of substructure variable, energy correlation ratio $D_2^{(\beta=1)}$, that is used to discriminate between QCD jets and hadronic boson decay in this analysis.

Energy correlation functions The D_2 substructure discriminant is analytically determined to distinguish between 1-pronged jets (like QCD) and 2-pronged jets like the boosted hadronically decaying Z boson [145]. It is based on the ratio of n-point energy correlation functions, which are infrared and collinear safe observables sensitive to the n-prong structure in a jet. The 2- and 3- point correlation functions are a convenient basis for identifying decays to 2 particles in particular, respectively,

$$e_2^{(\beta)} = \frac{1}{p_{\text{T}J}^2} \sum_{1 \le i \le j \le n_J} p_{\text{T}i} p_{\text{T}j} \Delta R_{ij}^{\beta}, \tag{5.16}$$

$$e_3^{(\beta)} = \frac{1}{p_{\text{T}J}^3} \sum_{1 \le i \le j \le k \le n_J} p_{\text{T}i} p_{\text{T}j} p_{\text{T}k} \Delta R_{ij}^{\beta} \Delta R_{ik}^{\beta} \Delta R_{jk}^{\beta}, \tag{5.17}$$

where $p_{\text{T}J}$ is the transverse momentum of the jet, $p_{\text{T}i}$ that of particle i, and ΔR_{ij}^{β} is the distance measure parametrized by β–so ΔR_{ij}^2 is the usual euclidean distance in the azimuthal-rapidity plane (or in experiment $\eta - \phi$).

For a value of $e_2^{(\beta)} << 1$ the particles in a jet must all have small $p_{\text{T}i}$ or small R_{ij}^{β}, or in other words be dominated by soft and collinear emissions. A large value of $e_2^{(\beta)}$ would indicate a hard perturbative splitting. For QCD jets this is suppressed by a

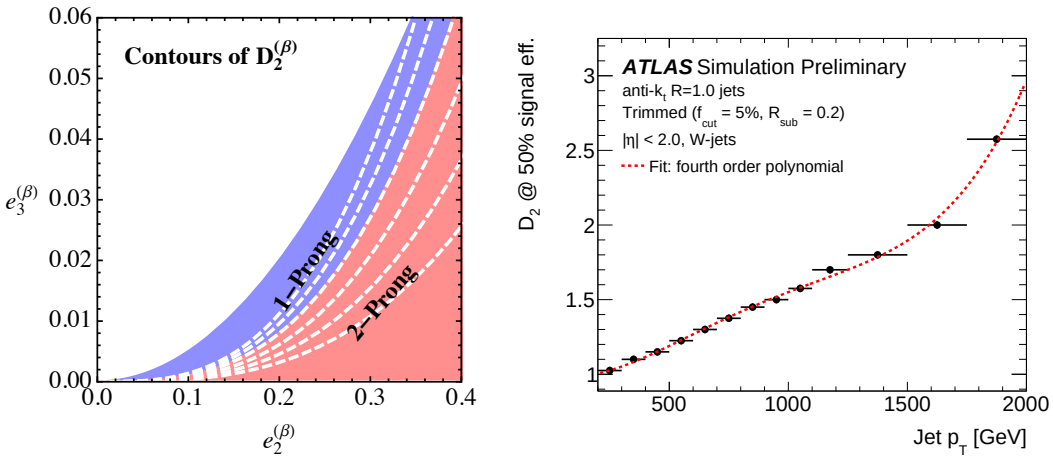

(a) (b)

Figure 5.16: 1- and 2-prong regions of phase space with constant contours of $D_2^{(\beta=1)}$ (a). The D_2 cut yielding a 50% signal efficiency when combined with a window on the calibrated boson mass(b).

factor of α_s. Likewise, a large value of $e_3^{(\beta)}$ indicates strong 2 or 3 prong structure. An analytic study of the (e_2, e_3) phase space [146] for QCD jets and Z boson decays has indicated that there is a clear separation in the population of 1- and 2-prong jets in this space. Contours of,

$$D_2^{(\beta)} \equiv \frac{e_3^{(\beta)}}{\left(e_2^{(\beta)}\right)^3}, \tag{5.18}$$

optimally separate the populations. Constant contours of $D_2^{(\beta)}$ are shown in Fig. 5.16 (a) superimposed on the schematic representation of the two populations. D_2 is boost invariant which makes it a convenient variable for use at hadron colliders. The choice of $\beta = 1$ and $\beta = 2$ was examined in run 1 [140] and $\beta = 1$ was found to be optimal. With a rate of 50% efficiency (in combination with a mass-window cut) the background rejection of QCD jets for 2015 conditions in ATLAS was found for W and Z jets with $200 < p_{\mathrm{T}}^{\mathrm{true}} < 350 (1500 < p_{\mathrm{T}}^{\mathrm{true}} < 2000)$ to be respectively 55.3(40.9) and 47.8(50.5) [147]. The mass window used for W/Z-tagging is $\langle M \rangle \pm 15$ GeV. The window is made on the calibrated large-R jet mass, addressed in the following section. The D_2 cut parametrized by jet p_{T} for the identification of $Z \rightarrow$jets is shown in Fig. 5.16 (b) resulting in 50% efficiency at given jet p_{T}.

Jet energy and jet mass calibration

The large-R JES is determined by an identical application of numerical inversion as with small-R jets [148]. This is done without an explicit step for PU subtraction; the method of trimming sufficiently reduces the effects of PU on the JES that it is unnecessary. Large-R jets are used in the high-p_{T} regime, which is proportionally less affected by the constant-scale energy contribution of PU anyway. Following the JES is a calibration of jet mass scale (JMS), applied in the same way as JES, a scale factor c_{mass}:

$$m = c_{\mathrm{mass}}(E, \eta_{\mathrm{det}}) \times m^{\mathrm{LCW}} = c_{\mathrm{mass}}(E, \eta_{\mathrm{det}}) \times \sqrt{\Big(\sum_{i \in J} E_i\Big)^2 - \Big(\sum_{i \in J} \vec{p}_i\Big)^2} \tag{5.19}$$

Here E_i is the energy of cluster i belonging to jet J and $\vec{p}_i$ is the vector in the direction of the cluster energy with magnitude E_i. The calibration of jet mass is again made by numerical inversion, but within the space containing the additional dimension of the already calibrated jet energy. This provides a calibration parametrized by jet energy as well as η.

Large-R Jet Uncertainties

The large-R jet uncertainties must be determined through a different approach than the small-R jet p_{T} uncertainties. In the case of jet mass there is no conservation law that can be readily exploited for direct balance. Instead, a completely different approach is taken to obtain a measure of the systematic uncertainties on large-R jet observables that begins with the matching of track jets to the hadronically reconstructed jets. The ratio of jet observable $o \in \{p_{\mathrm{T}}, m, D_2\}$ calculated from the calorimeter jet is compared to that calculated from a ΔR-matched track jet : $r^{o}_{\mathrm{track}} = o^{\mathrm{calo}}/o^{\mathrm{track}}$. For an inclusive QCD dijet selection, the average value r^{o}_{track} is proportional to the jet o scale. The divergence of the ratio of the average values measured in data and

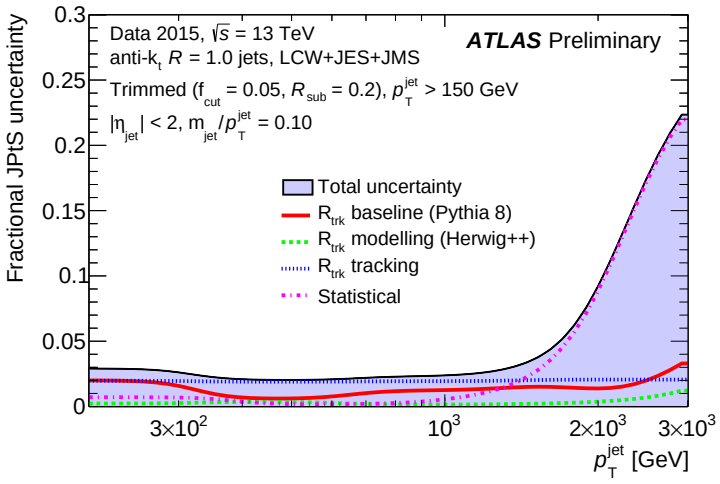

Figure 5.17: Fractional systematic uncertainty on calibrated jet-p_{T} for anti-k_t $R = 1.0$ trimmed jets with $f_{\mathrm{cut}} = 5\%$ and $R_{\mathrm{sub}} = 0.2$. The uncertainty is shown for jets with $p_{\mathrm{T}} > 150$ GeV, $|\eta| < 2.0$ and $m_{\mathrm{jet}}/p_{\mathrm{T}}^{\mathrm{jet}} = 0.1$. Uncertainties were derived on the full 2015 data set. The baseline uncertainty corresponds to the the difference between data and Pythia 8 MC in the R_{trk} double ratio. A modeling uncertainty is estimated with the difference between Pythia 8 and Herwig. Uncertainties from track reconstruction efficiency, impact parameter resolution, track momentum calibration, and fake tracks are combined in the tracking component. The statistical precision in data is a limiting factor in the combination at high-p_{T} [149].

MC from 1 is taken as the measure of the scale uncertainty:

$$1 - \langle r^{o}_{\mathrm{track}} \rangle_{\mathrm{data}} / \langle r^{o}_{\mathrm{track}} \rangle_{\mathrm{MC}}. \tag{5.20}$$

Track modeling and fragmentation modeling introduce changes into this value, and therefore must be included as additional sources of uncertainty. The resulting systematic uncertainty for jet-p_{T} is shown in Fig. 5.17. The systematic uncertainty for D_2 and m are of similar magnitude, shape, and source.

The resolution cannot be calculated with this method because r^{o}_{track} resolution is dominated by the fluctuation in the distribution of charged and neutral tracks in jets. Instead, for jet mass resolution (JMR) the uncertainty was evaluated with a selection of $t\bar{t}$ by exploiting the $t \to Wb \to qqb$ decay chain [148]. The distribution of reconstructed W mass is examined between truth and reconstructed mass in MC and the reconstructed mass in data. A fit is made parametrizing the mapping from

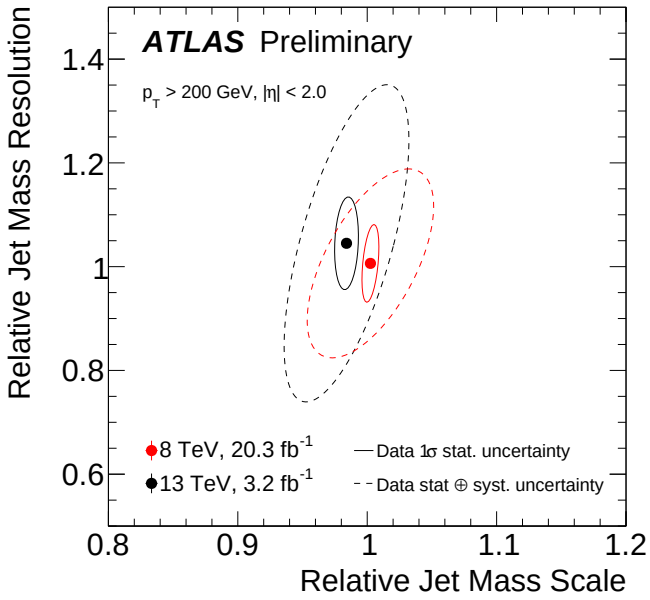

Figure 5.18: Relative jet mass scale and resolution, best fit from the reconstruction of the $W \to qq$ peak in sample of $t\bar{t}$ in $\sqrt{s} = 8$ TeV ($R_{\text{sub}} = 0.3$)) and $\sqrt{s} = 13$ TeV ($R_{\text{sub}} = 0.2$) [148].

the distribution of truth-level mass to the reco-level mass by a scale s and resolution smearing r. In this parametrization, with $s = r = 1$ one recovers the MC reco distribution and with $s = 1, r = 0$ one recovers the MC truth distribution. The values of s and r are scanned evaluating the χ^2 between the resulting distribution and data. The minimum value and 1σ error curves obtained are shown in Fig. 5.18. This results in 20% uncertainty on mass resolution. For mass, p_{T}, and $D_2^{(\beta=1)}$ the scale and resolution evaluated in MC are consistent with data.

This chapter covered the methods by which the various jet objects used in the following analyses have been convstructed and their uncertainties understood. Both small-R and large-R jets are used directly in the search. Jets also dominate the uncertainty in the determination of the missing transverse momentum ($E_{\text{T}}^{\text{miss}}$), which is the other primary observable used in the analyses. The response of the ATLAS calorimeters to QCD physics has been well understood, optimized, and calibrated for the following study.

This page intentionally left blank.

Chapter 6

Analysis

The following describes the search for diboson resonances in ATLAS of the form $ZZ \to \ell\ell qq$, $ZZ \to \nu\nu qq$, $ZW \to \ell\ell qq$, and $ZW \to \nu\nu qq$. The $ZZ \to \ell\ell qq$ and $ZZ \to \nu\nu qq$ resonance analyses are considered for a spin-0 narrow width Higgs and a spin-2 Randall-Sundrum graviton models. The $ZW \to \ell\ell qq$, and $ZW \to \nu\nu qq$ analyses are designed around a heavy vector triplet model, capturing a spin-1 resonance. The theoretical details are found in Chapter 2 and the setting of limits on the cross section and limited theoretical interpretation are given in the following Chapter 7. This chapter motivates and defines the analysis strategy used in the searches. Section 6.1 presents an overview of the physics objects used in the analysis. Section 6.2 motivates and describes the regions used in the analysis. Section 6.3 describes the signal distributions obtained from the benchmark models, uncertainties associated with signal modeling, and methods used for narrowing the experimental resonances. Sections 6.5 and 6.6 outline the selection used in obtaining the signal regions, control regions, and validation regions in the $\ell\ell qq$ and $\nu\nu qq$ channels, respectively. This analysis has been published in conference proceedings August 2016 by ATLAS [150] in its exact form as well as in a more preliminary state [28] in March 2016 at Moriond. Additionally, two of the following analyses are the subject of two ATLAS papers in progress in a nearly identical form. Most of the following plots and discussion can be found in these public documents and associated internal documents. It is understood that individual citations are used in the following only in the case of the inclusion of work from sources other than the above mentioned.

6.1 Reconstruction and Object Definitions

Most important to these analyses are the reconstruction of jets in ATLAS, which has been detailed extensively in Chapter 5. The other important reconstructed final state objects used in these channels are electrons and muons. The $\nu\nu qq$ channel makes critical use of *missing transverse momentum* ($E_{\mathrm{T}}^{\mathrm{miss}}$), the transverse sum of all calibrated reconstructed objects in an event and a soft term accumulating remaining soft radiation. These three sets of objects will be discussed in detail. Remaining products in ATLAS collisions like taus and photons enter into the event selection trivially and are excluded from further discussion.

Basic event quality criteria To enter the analysis, an event must satisfy some basic criteria designed to ensure that a hard scatter has occurred at the IP, and recorded hard scattered objects are not the result of erratic detector behavior, beam backgrounds, or cosmic background. Events must first belong to good runs lists (GRLs) which have been validated to ensure that all detectors were operating nominally during data-taking. Detectors in 2016 were highly efficient; see Chapter 3. Events require a reconstructed vertex with at least three associated tracks. Finally, to eliminate any potential presence of beam and cosmic backgrounds, events with any jet failing the minimal jet cleaning criteria (see Chapter 5) are rejected.

Initial jet selection To avoid any potential mis-modeling from low-p_{T} jets and restrict the analysis to the region for which the Sherpa 2.2 MC used for the leading backgrounds has been tuned and recommended, small-R jets are considered starting with a $p_{\mathrm{T}} > 30$ GeV. Jets from 20-30 GeV are fully calibrated and recommended for use but the JES uncertainty does increase significantly in this lowest range. Little phase space is lost in this search since signal jets are the decay products of a Z/W boson. Additionally, signal jets are restricted to the barrel and extended barrel

calorimeters $|\eta| < 2.5$ and required to pass the JVT > 0.59 for $p_{\mathrm{T}} < 60$ GeV. Forward jets of $2.5 < |\eta| < 4.5$ are added only for selection criteria in the VBF channel.

Large-R jets are required to have $p_{\mathrm{T}} > 200$ GeV and $|\eta| < 2.0$ for consideration in the $\ell\ell qq$ or $\nu\nu qq$ channels. The summary of minimum jet selection criteria is given in Table 6.1.

Missing transverse energy/momentum Missing transverse momentum ($E_{\mathrm{T}}^{\mathrm{miss}}$) is a calculation of transverse momentum lost in an event to particles not interacting significantly with the ATLAS detector, which in the SM is limited to neutrinos. $E_{\mathrm{T}}^{\mathrm{miss}}$ is determined to be the additive inverse of the vectorial sum of the transverse momenta of calibrated objects (electrons, muons, τs, photons, small-R jets) and a soft term composed of tracks outside of the calibrated objects associated with the primary vertex:

$$E_{\mathrm{T}}^{\mathrm{miss}} = -\sum_{\{o \in e,\mu,\tau,\gamma,\mathrm{jets,soft}\}} p_{\mathrm{T}}^{o} \tag{6.1}$$

The tracking soft term captures energy from the underlying event and soft and wide-angle radiation not captured by the calibrated objects [151–153]. Also used is the track-based missing transverse momentum $p_{\mathrm{T}}^{\mathrm{miss}}$, defined as the negative vectorial sum of the transverse momenta of all good-quality tracks reconstructed in the ATLAS inner detector. Events are required to have $E_{\mathrm{T}}^{\mathrm{miss}} > 250$ as the starting point for selection in the $\nu\nu qq$ channel.

Electrons Electrons are reconstructed from clusters in the EM calorimeter that are matched to ID tracks. A likelihood-based discriminant [154] is used to distinguish the prompt production of electrons from other electrons coming from the conversion of photons, semi-leptonic decay of heavy-flavor, and mis-identified hadrons. In the first two cases there is an actual electron present. Identification is based on the matching of the ID track to calorimeter cluster in $\{\eta, \phi, p_{\mathrm{T}}\}$. The transition radiation

Selection	**Large-R jets**
Kinematic	$p_{\mathrm{T}} > 200$ GeV $\|\eta\| < 2.0$
Type	anti-k_T R =1.0 LCTopo Trimmed ($R_{\text{subjet}} = 0.2$, $f_{\text{cut}} = 5\%$)
Isolation	From leptons ΔR ¿1.0
	Small-R jets
Kinematic	p_T >30 GeV if $\|\eta\| < 2.5$ p_T >35 GeV if $\|\eta\| = [2.5, 4.5]$
Type	anti-k_T R =0.4 EMTopo
Quality	JVT >0.59 if p_T <60 GeV,$\|\eta\| < 2.4$
	Missing transverse momentum
Kinematic	$E_{\mathrm{T}}^{\mathrm{miss}} > 250$ GeV
Type	tracking soft term

Table 6.1: Table of minimal criteria defining jets and $E_{\mathrm{T}}^{\mathrm{miss}}$ in the analyses.

tracker (TRT) and the first (fine granularity) layer of the EM calorimeter are valuable in identifying the conversion of photons. A *loose* criteria (loose-$\mathcal{L}$) is used as the minimum criteria for all electrons in the analysis, with a reconstruction efficiency of $\sim 96\%$. Additional, tighter criteria provide medium and tight working points with $\sim 90\%$ and $\sim 80\%$ efficiency respectively and are used in the trigger and final selections. The efficiency of the *reconstruction*, *identification*, *isolation*, and *trigger* have been studied. Corrections for each of the efficiencies in data and MC are applied as scale factors $\mathrm{SF} = e^{\mathrm{data}}/e^{\mathrm{MC}}$ where e is the efficiency determined through designated tag and probe studies of $Z \to ee$ decay in Z+jets selections. Individual scale factors are applied to MC:

$$\mathrm{SF}^{\mathrm{total}} = \mathrm{SF}^{\mathrm{reconstruction}} \times \mathrm{SF}^{\mathrm{identification}} \times \mathrm{SF}^{\mathrm{isolation}} \times \mathrm{SF}^{\mathrm{trigger}}. \tag{6.2}$$

Scale factors are determined in exclusive η and E_{T} regions correcting for differences in mis-modeling of tracking and showering in different subdetectors. Systematic uncertainty from the determination of each of the scale factors enters the searches.

Selection	**Electrons**
Kinematic	$p_{\mathrm{T}} > 7$ GeV $\lvert\eta\rvert < 2.5$
Identification	loose likelihood-based discriminant all silicon: 7 hits (IBL hit + 2 pixel hits)
Isolation	loose track isolation
Impact Parameter	$\lvert d_0/\sigma(d_0)\rvert < 5$ $\lvert z_0 * \sin\theta\rvert < 0.5$ mm
	Muons
Kinematic	$p_{\mathrm{T}} > 7$ GeV $\lvert\eta\rvert < 2.5$
Identification	loose quality criteria
Isolation	loose track isolation
Impact Parameter	$\lvert d_0/\sigma(d_0)\rvert < 3$ $\lvert z_0 * \sin\theta\rvert < 0.5$ mm

Table 6.2: Table of minimal criteria defining leptons in the analyses. Triggers used in these analyses and signal leptons can have tighter selection criteria.

Muons Muons are reconstructed by fitting inner detector (ID) tracks to muon spectrometer (MS) tracks. Muons pass identification quality requirements based on the number if hits in the various detector layers and the significance of the difference of the ratio of charge q to measured momentum in the ID and MS $|q/p_{\mathrm{MS}} - q/p_{\mathrm{ID}}|$ [155]. All muons considered in the analyses pass a minimum *loose* quality and isolation criteria [156] each with a $> 99\%$ efficiency. Like electrons, muon event selections are corrected for different efficiencies in reconstruction, identification, isolation, and trigger in bins of transverse momentum and rapidity by the use of corrective scale factors applied to MC. Corrective scale factors are similarly determined from designated tag and probe studies for all the commonly used quality, isolation, identification, and trigger criteria used in these analyses.

Electrons and muons are required to be isolated from other tracks using $\sum p_{\mathrm{T}}$ of other tracks within a variable sized cone as the discriminant. The isolation criteria are tuned in exclusive regions in the $\eta - \phi$ plane to produce a 99% efficiency for the loose working point in the isolation criteria from designated studies in Z+jets events of the $Z \to \ell\ell$ decay.

Leptons are determined to originate from the primary vertex by two constraints:

On (1) the longitudinal impact parameter z_0, $|z_0 \sin(\theta)| < 0.5$ mm, where θ is the polar angle of the track. And (2) on the significance of the transverse impact parameter $d_0/\sigma_{d_0} < 3(5)$ for electrons (muons), where d_0 is the impact parameter in the transverse plane and σ_{d_0} is its uncertainty. A good lepton is defined by passing all the above minimal selection criteria.

Flavor Tagging A multivariate discriminate trained on ATLAS MC and validated with data is used to discriminate between b-jets [157] originating from the decay of b-quark from jets arising from light and charm hadrons. Training of the discriminant utilizes the truth-level labeling of jets in association with a W or Z (Chapter 4). Flavor tagging in Run 2 uses a boosted decision tree (BDT) [158][1] to combine the discriminatory power of 3 pre-trained discriminants:

IP3D Based on the longer lifetime of hadrons containing a b-quark ~ 450 μm utilizes the transverse d_0 and longitudinal $z_0 \sin\theta$ impact parameters of tracks associated with the jet[2]. The longer lifetime of b-hadrons produces measurably larger impact parameters than light hadrons which are prompt in comparison and the association of multiple tracks can define the location of a secondary vertex. The location of the associated secondary vertex in front of the jet is used for discrimination against background. The discriminant is based on a log-likelihood ratio obtained from the product of likelihoods determined from distributions of individual tracks associated with light and b-jets in a space associated with the impact parameters and their significance.

[1]The BDT technique simply results in an optimized set of many weighted cut-based spaces in the parameter space of the multiple discriminating variables. In general this approach is superior to a single region defined as the Cartesian product of intervals in each variable typical of a cut-based approach.

[2]The transverse impact parameter d_0 is defined as the distance of closest approach in the $r-\phi$ plane. The longitudinal impact parameter $z_0 \sin\theta$ is defined as the distance of the track to the primary vertex in the longitudinal plane at the point of closest approach in the $r-\phi$ plane.

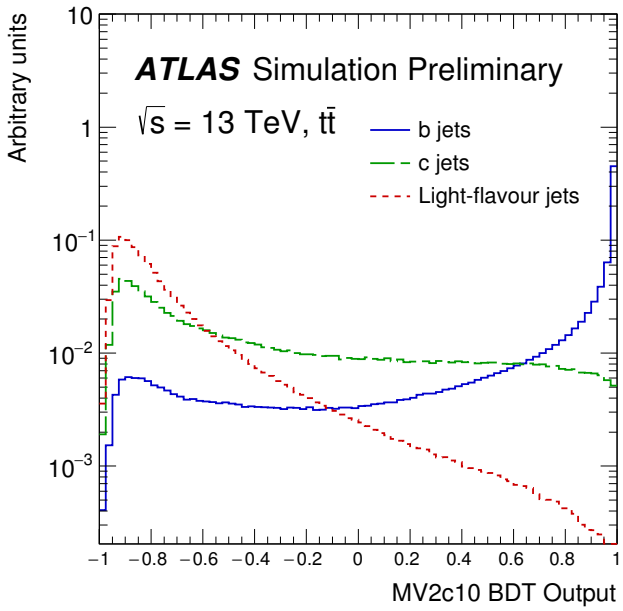

Figure 6.1: Distribution of the w discriminant (MV2C10) for MC truth flavor-tagged jets [157].

Secondary Vertex Finding Algorithm This algorithm identifies possible secondary vertices from all possible combinations of two tracks associated with a jet [159]. The algorithm iteratively associates the remaining tracks with the best candidate, producing a number of observables based on the decay length, track multiplicity, track energies, and track mass.

JetFitter The fragmentation of b-hadrons often involves a decay to one or multiple c-hadrons. This results in tertiary vertices which tend to lie along the flight path of the b-hadron. The JetFitter algorithm [160] provides information about the structure of the hadron decay and attempts to reconstruct the whole hadron decay chain.

The MV2 multivariate classifier is trained on $t\bar{t}$ events with b-jets as signal, and a 2-to-1 mix of light and c-jets as background. The 70% b-jet efficiency point is used in all the following analyses. It provides a high level of discrimination, with a light-jet rejection factor of 310 and charm rejection factor of 12.

The distribution of the final trained discriminant w (known as MV2c10) is shown in Fig. 6.1. Jets with higher w are more likely to be b-jets and less likely to be a light or c-jets. The entire w distribution is calibrated to match the b-tagging efficiency in MC to that in data. The calibration of the continuous distribution allows for the use of flavor tagging outside of the single 70% working point which is exploited in this analysis in a *truth tagging* method (see next Sec. 6.5) to bypass the statistical limitations introduced by the high rejection factor of the b-tagging discriminant.

Overlap removal

The last step in the selection of physics objects used in the analysis is a removal of overlapping reconstructed objects of different types. This is done when two reconstructed objects are believed to represent the same final state particle. Both small-R and large-R jets are removed when overlapping electrons or muons. Small-R jets are removed by a standard procedure widely used in ATLAS analyses in a ΔR=0.6 cone around leptons. Large-R jets are removed within a cone of ΔR=1.0 around selected loose leptons or if two electrons are matched to it.

6.2 Design

The searches are made in 2 categories in the $\nu\nu qq$ final state and from 3 to 7 categories in the $\ell\ell qq$ final state depending on which of the three benchmark models are used. The $\nu\nu qq$ channel to a lesser degree and $\ell\ell qq$ searches in particular have been designed to exploit features unique to the three benchmark models. Consequently, there are three separate analyses made to optimize the search for each of the benchmark signals. The trigger and preliminary cuts are identical for all three; small differences in optimized cuts and the selection of regions are specialized for each. This section will describe the different regions for each of the analyses and the rest of the chapter will

treat them together mentioning only where they differ.

The structure of the analyses follows from two principles:

1. The MC simulation of backgrounds provides reliable shapes of the relevant kinematic distributions. No such assumption is made about the total cross section of backgrounds. State of the art NLO MC techniques have been used in the generation of backgrounds and signals (Chapter 4). While MC generated at NLO is known to reliably model the shapes of distributions, this is sometimes at the expense of the accuracy in the overall normalization. So while in some cases, the MC discussed here have cross sections generated to NNLO, resolving much of the total cross sectional mis-modeling, the analysis has been explicitly designed not to require high accuracy. The final fits (outlined in Chapter 7) indicate that all the MC cross sections used have normalizations already determined with 10% accuracy. As a rule of thumb one gets roughly 50% accuracy from LO calculations.
2. For each significant background process entering a given signal region (SR) there is a corresponding control region CR for the process (ZCR,WCR, or TopCR) with a similar but complementary phase space targeted at isolating the process (Z+jets, W+jets, or $t\bar{t}$ respectively) and minimizing signal contamination. The control regions provide a data-driven approach to determine normalization scale factors for each of the leading processes. Details of the scheme using these normalization scale factors in the fit will be covered in Chapter 7.

The second point is the unifying principle in the design of the analyses. *It is followed for every background in every SR in every channel in all searches presented.* Understanding the search strategy then requires two steps: One, motivate the choice of SRs. Two, identify the major backgrounds present in each and provide designated CRs for their correct normalization.

The topology of the final state in the $\ell\ell qq$ channel is composed of a $Z \to \ell\ell$ and

a $V \to qq$ decay, back-to-back in the azimuthal angle between the two bosons $\Delta\phi_{ZV}$. From special relativity it is clear that when sufficiently boosted, the hadronic decay products of one W/Z are collimated so that the preferred jet width by ATLAS for anti-k_t jets of $\Delta R = 0.4$ will be a poor choice for the individual resolution of two jets in the mass range covered in the search, because the typical separation will place the jets on the $\Delta R = 0.4$ threshold. This motivates the use of Large-R jets with jet substructure techniques used to distinguish between the two-pronged structure of the vector boson decay from the single-pronged structure of QCD jets. As discussed in Chapter 5 the choice of jet algorithm was arrived at after extensive studies of various configurations of jet pile-up suppression techniques and substructure variables in Run 1. The ratio of two and three pronged energy correlation functions $D_2^{(\beta=1)}$ was shown to be the most effective discriminant considered and is used through the following analyses. A 50% efficiency working point, when taken in combination with a $\pm$15 GeV mass window cut is used to define the *high-purity* region. But even failing the substructure cut, the mass window alone is a strong discriminant against the background of Z+jets and is therefore a useful channel, which defines the *low-purity* region.

For less massive resonances the Z hadronic decay products are well-separated and are likely to form well-resolved small-R jets–this defines the *resolved* category. One can exploit the Z boson's enhanced decay width to $b\bar{b}$ with respect to a predominantly light-flavored background of jets arising from the Z+jets process. The 70% working point for the MV2C10 b-tagging discriminant is used to tag *both* resolved jets–this defines the *tagged* region. The presence of only one or no b-tags defines the *untagged* region. This strategy is based on a ZZ resonance, since the leptonic decay products must come from a Z. For a ZW resonance this leaves the hadronic decay products coming from the W. In that case, the mass window on $W \to qq'$ is shifted accordingly and the b-tagging is not a useful discriminant. The W boson does not have enhanced

decay to bs. For the HVT W' resonance search then, there is only a resolved category without splitting.

The topology of the final state in the $\nu\nu qq$ channel is the hadronic $W/Z \rightarrow \ qq$ decay in the direction opposite in ϕ to large missing energy attributable to the decay of $Z \rightarrow \nu\nu$. This channel is highly sub-dominant to the $\ell\ell qq$ channel for low mass signals (200-500 GeV) for at least three reasons:

1. They lack reconstructible Z-mass window around $Z \rightarrow \nu\nu$ decay;
2. There is relatively poor resolution of the $E_{\mathrm{T}}^{\mathrm{miss}}$ observable entering the transverse mass final discriminant;
3. There are large modeling uncertainties present in the low-$E_{\mathrm{T}}^{\mathrm{miss}}$ phase space.

For these reasons, only a merged analysis in the $\nu\nu qq$ channel is considered in these studies.

Backgrounds and Control Regions

Figures 6.2 and 6.3 shows the expected backgrounds present in the spin-0 analysis in the $\ell\ell qq$ and $\nu\nu qq$ channels, respectively.

The leading background present in all signal regions of both the merged and resolved regimes of the $\ell\ell qq$ analysis is Z+jets, with $t\bar{t}$ also playing a significant role in the resolved analysis. Therefore, for each SR there is a dedicated ZCR to constrain the overall cross section of the Z+jets process. And to constrain the $t\bar{t}$ cross section in the resolved analysis there is a single TopCR. The structure of all regions entering the spin-0 $\ell\ell qq$ analysis is summarized in Fig. 6.4. The spin-0 analysis is divided by an additional set of criteria on 2 additional jets present in the event in order to separate the event topology of the vector boson fusion (VBF) production channel from that of the glue-glue fusion (ggF) channel. The tagged and untagged categories of the resolved analysis are combined for events passing the VBF selection criteria due to lack of sufficient background in the VBF tagged ZCR to adequately confine the

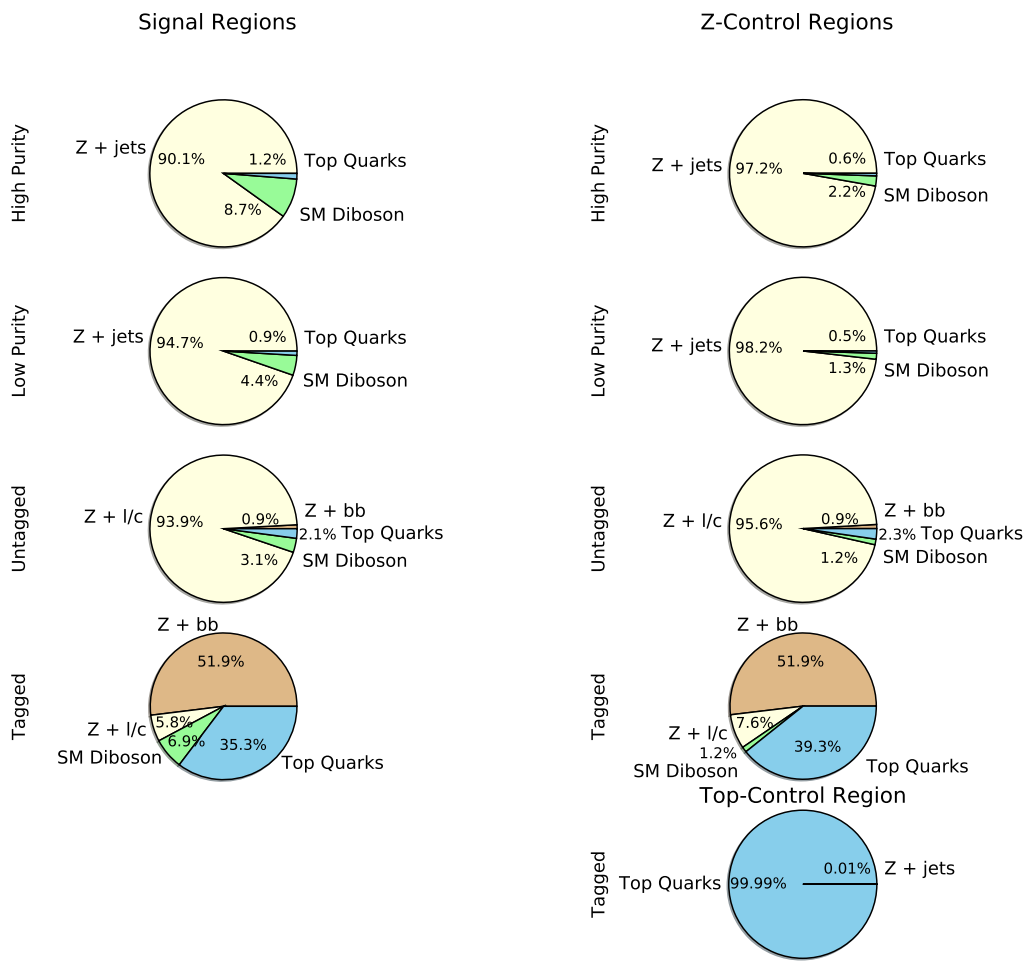

Figure 6.2: Background in the regions of the $H \to ZZ$ analysis for the $\ell\ell qq$ channel. Background in the SRs motivates the choice for CRs.

background in the SR from MC. The VBF regions mirror those in the ggF analysis. The spin-2 analysis summarized in Appendix Fig. 1 is structured as the spin-0 analysis only without separation into ggF and VBF categories. The spin-1 analysis, capturing the hadronic decay of the W boson, is structured as the spin-2 analysis but without the splitting of the resolved regime into tagged and untagged categories. Appendix Fig. 5 summarizes the structure of the spin-1 analysis.

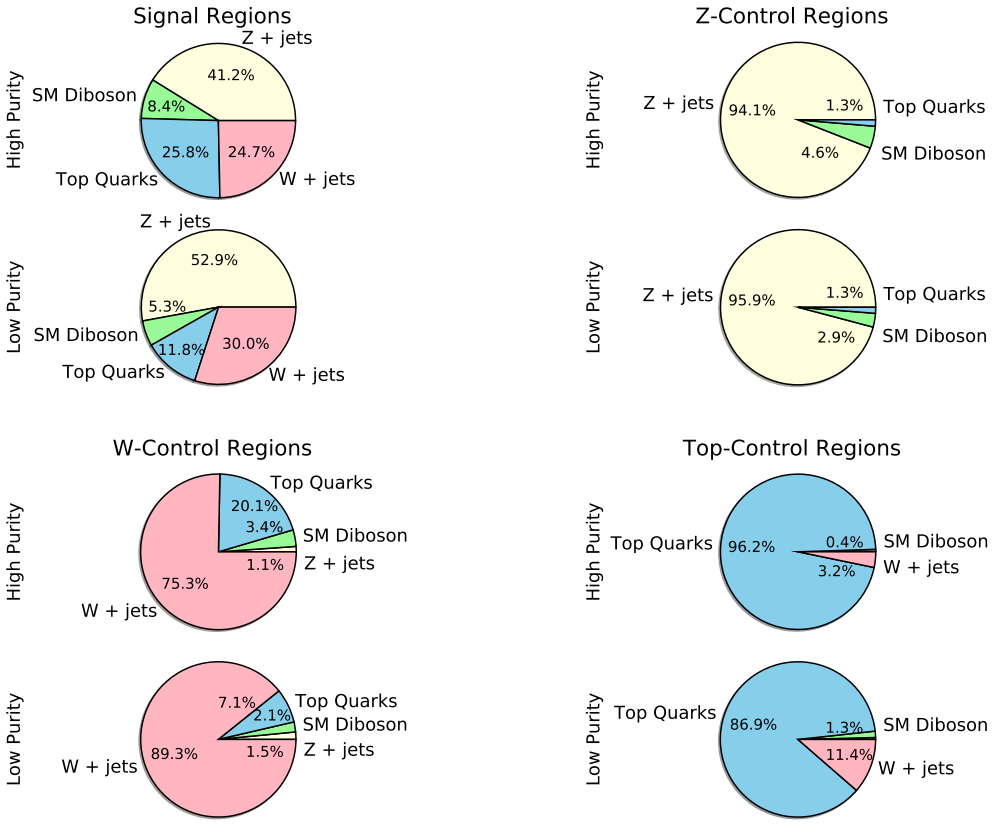

Figure 6.3: Background in the regions of the $H \to ZZ$ analysis for the $\nu\nu qq$ channel. Background in the SRs motivates the choice for CRs.

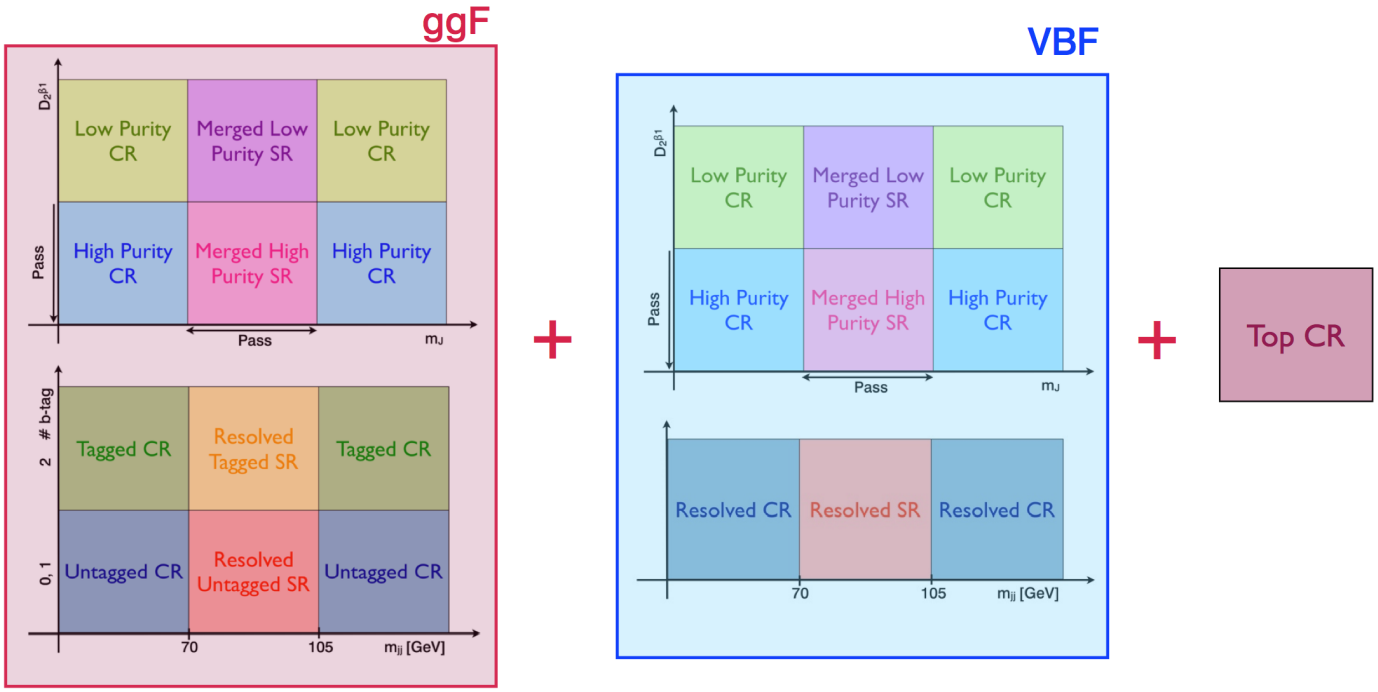

Figure 6.4: Event categories entering the spin-0 analysis. Events are separated into the ggF and VBF production channels. The ggF channel has 8 regions: the high and low-purity merged signal regions, corresponding high and low-purity Z-control regions, the untagged and tagged resolved signal regions, and the untagged and tagged resolved Z-control regions. The VBF channel has 6 regions: the high and low-purity merged signal regions, corresponding high and low-purity Z-control regions, the resolved signal region, and the resolved Z-control regions . There is one resolved top control region. Events entering the SR (Pass) the m_J mass window around the Z/W-mass.

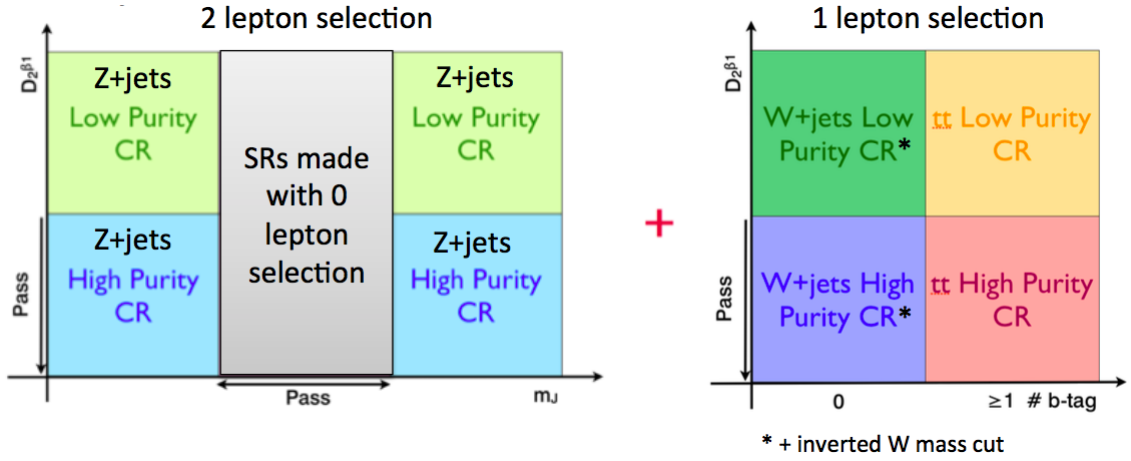

Figure 6.5: Event categories entering the spin-0,1 and 2 analyses in the $\nu\nu qq$ channel. There are 8 regions in the merged regime: high and low-purity signal regions, high and low purity Z-control regions requiring 2 leptons, high and low-purity W-control regions requiring 1 lepton, and high and low-purity Top-control regions requiring 1 lepton and at least one b-tagged jet. Events entering the SR (Pass) the m_J mass window around the Z/W-mass and have 0 leptons.

Standard model diboson processes (ZZ and to a small extent ZW) enter this analysis. The SM continuous ZZ-process is irreducible and naturally satisfies the decay structure selected for in the analysis $ZZ \to llqq$. It cannot be selected against and provides a continuous background on which the mass-resonance is searched for. It is sub-dominant to the Z+jets background through search range. Single top processes are simulated and included in the analysis but only enter the SRs in trace amounts. The lepton selection is sufficient to completely reject any QCD dijet background well beyond any detectable level.

Like the $\ell\ell qq$ channel, the leading background in the $\nu\nu qq$ channel are Z+jets processes, but it also contains strong contamination from the W+jets and $t\bar{t}$ backgrounds. A CR for each in both the low and high-purity categories is used (WCR and TopCRs, respectively). A complete summary of the regions in the $\nu\nu qq$ analysis is shown in Fig. 6.5.

The continuous diboson backgrounds (ZZ,ZW,WW) all make a non-trivial presence in the analysis. All three channels naturally satisfy the selection on the signal

final state. Generously large uncertainties on the cross sections of diboson processes are used in these analyses with little effect on the strength of the statistical analysis because of their relatively low cross section with respect to V+jets and the similarity in shape in the final discriminants.

Specific cuts are used to suppress the QCD dijet background, which would otherwise be present despite the high-$E_{\mathrm{T}}^{\mathrm{miss}}$ requirement $\ell\ell qq$ in the analysis selection. After the so-called "anti-QCD" cuts this background can be neglected. Single-top backgrounds have low cross sections compared to $t\bar{t}$ in the final selection. They are included in the analysis simulation but treated as sub-dominant to $t\bar{t}$ in all cases.

6.3 Benchmark Signals

The benchmark signals: spin-0 heavy Higgs signal in the narrow width approximation, spin-1 heavy vector triplet, and spin-2 graviton benchmark signals are all relatively narrow resonances. The simulated widths of each of the resonances before convolution with experimental resolutions is roughly 0, 0.025, and 0.06 of the resonance mass, with only the last having somewhat increasing relative width. The best reconstruction of the resonance mass available in each of the channels is used as the final discriminant, since the backgrounds have no such resonant behavior and provide a relatively smooth background to identify the resonance on.

The $\nu\nu qq$ channel utilizes the *transverse mass* defined from the invariant mass of the the missing transverse energy and the large-R jet projected on the transverse plane, since it is not possible to fully reconstruct the invariant mass of the ZZ/ZW resonance due to the presence of neutrinos. The transverse mass is defined,

$$m_{\mathrm{T}} = \sqrt{(E_{\mathrm{T},J} + E_{\mathrm{T}}^{\mathrm{miss}})^2 - (\vec{p}_{\mathrm{T},J} + \vec{E}_{\mathrm{T}}^{\mathrm{miss}})^2}, \tag{6.3}$$

where $E_{\mathrm{T},J} = \sqrt{m_J^2 + p_{\mathrm{T},J}^2}$. Figure 6.6 shows the 3 benchmark signals with a mass of 2000 GeV. The asymmetrical shape is similar to the so-called Jacobian peak fa-

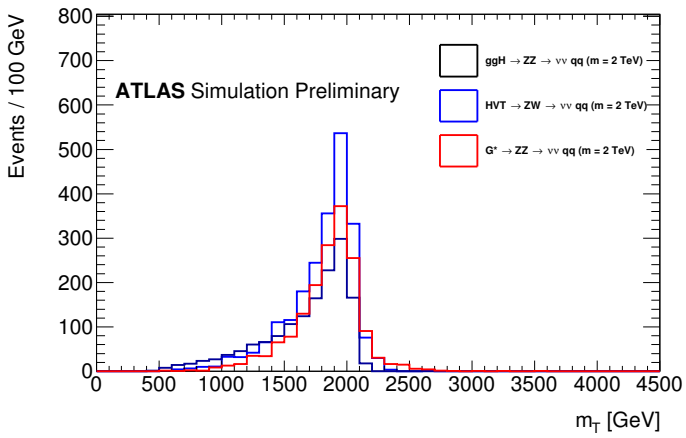

Figure 6.6: Transverse mass distributions of benchmark signals: heavy Higgs boson, for HVT W', and RS $G*$ at 2000 GeV.

miliar in W-decay due to broadening from the inability to resolve the polar angle θ-information of the neutrinos. This is partially responsible for the broadness of the resonance in M_T with the remaining width due to the use of $E_{\mathrm{T}}^{\mathrm{miss}}$ in construction of M_T. The experimental width of all three signals is roughly 25% to 30% of signal mass. The resolution of the $E_{\mathrm{T}}^{\mathrm{miss}}$ observable is limited by the sum of the resolutions of the reconstructed objects entering it as well as by the distribution of unreconstructed low-p_{T} neutral particles not attributable to calibrated objects and falling outside the TST. The $\ell\ell qq$ channel uses the 3-body mass $m_{\ell\ell J}$ from the large-R jet and two leptons in the merged regime and 4-body mass $m_{\ell\ell jj}$ composed of 2 small-R jets and two leptons in the resolved regime. Figure 6.7 shows the width for the 3 benchmark signals in the $\ell\ell qq$ analysis over the relevant mass ranges. The RS graviton search and HVT W' searches are made for signal masses from 500 GeV to 5000 GeV. The heavy scalar search is made for signal masses from 300 GeV to 3000 GeV. The experimental width of the heavy Higgs and HVT W' signals are between 3-4% in the full mass range considered. The width of the graviton increases from 5% at 500 GeV to 7% at 5000 GeV. Experimental broadening is sub-dominant to the intrinsic width of the signal for the graviton with the increase in width coming from the intrinsic width of the signal.

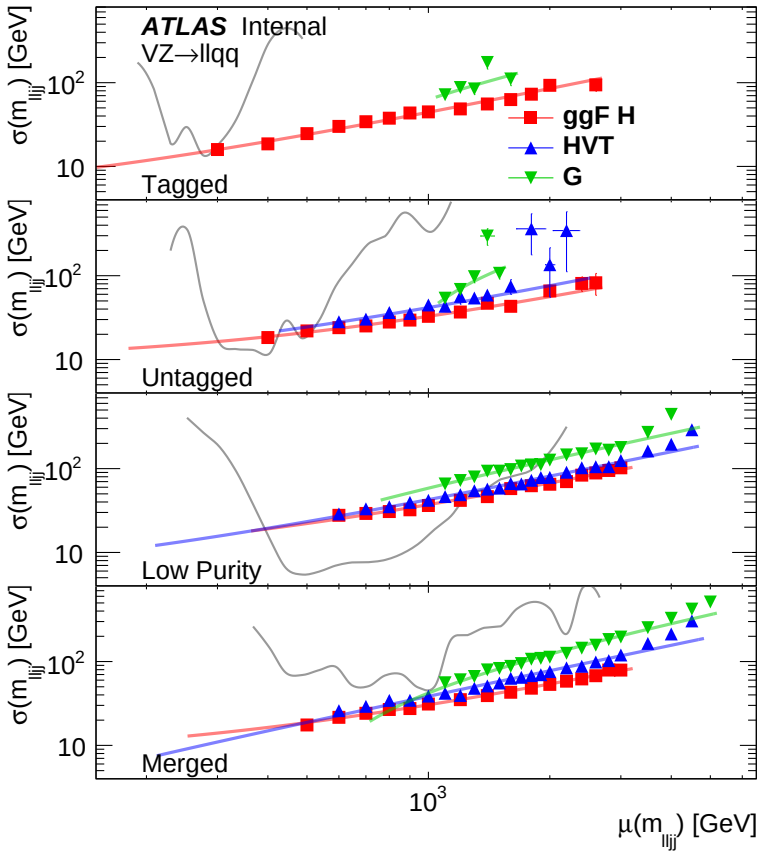

Figure 6.7: Signal resolutions evaluated with 1.7σ trimmed Gaussian fit in the ggF category. Also shown is the estimated bin width to achieve 5% statistical uncertainty on the MC.

Mass constraint

The resolution of the reconstructed signal in the 3 and 4-body mass benefits from some clever compensation for sources of experimental broadening. For the signal, the deviation from the ideal vector boson mass in reconstructed $Z \to \ell\ell$ and $Z \to jj (Z \to J)$ decays is primarily due to experimental sources. The correlation of the mass and energy measurements can be exploited to correct a given deviation in the jet energy measurement used to construct the final 3 or 4-body mass. One corrects the mass of the reconstructed boson $m_{1,2}$ to the nominal PDG mass m_Z^{nominal} in the final discriminant, where the indices $1, 2$ refer either to the two lepton or jet decay products

of the W/Z. The mass constraint on the two W/Z-decay products is therefore:

$$p_{\mathrm{T}W/Z}^{\mathrm{constrained}} = \frac{m_Z^{\mathrm{nominal}}}{m_{1,2}} * p_{\mathrm{T}1,2}.$$

It is not immediately obvious that this strategy would improve the resolution of the 4-body mass $m_{\ell\ell qq}$. In fact the benefit depends on the specific topology and source of experimental uncertainty. On the boosted $Z \to \mu^-\mu^+$ the muon spectrometer has a diminished ability to resolve the p_{T} of individual muons but ample angular resolution to determine their direction. The direction of high-energy muons is tightly resolved but they will follow nearly straight line paths at high-p_{T}, making a precise measurement of their curvature difficult to obtain. The p_{T}-resolution of muons drops off at high-p_{T} and becomes the dominant source of uncertainty in determining $m_{Z\to\mu\mu}$. However, for a high mass resonance the muon decay products are collimated and variation in the p_{T} dominates over angle in the 3 and 4-body mass calculation. Therefore correcting the Z-mass in the final discriminant significantly reduces the experimental resolution. This effect is most evident in the boosted regimes, Fig. 6.8.

The energy resolution of the calorimeter is good and angular resolution relatively poorer and therefore no benefit is seen for the application to the ee decay products. Benefit from the constraint on the W/Z hadronic decay products is clear in the Tagged region for lower mass and has been applied to the resolved selection. In all analyses for the $\ell\ell qq$ channel $Z \to \mu\mu$ is corrected to PDG mass of the Z boson in the final discriminant. In ZZ the resonance analyses $Z \to qq$ is corrected to the PDG mass of the Z, and in the ZW resonance analysis $Z \to qq$ is corrected to the PDG W mass. The resolutions of the reconstructed ggF H signal mass in the $\mu\mu$ and ee channels are almost the same after the correction. After the application of the mass constraint the reconstructed signal mass widths in the $\mu\mu J$ and eeJ final states are comparable.

The application of the mass constraint improves the resonance mass resolution in the dimuon final state by 36% for a resonance at 1600 GeV. When combined with the dielectron events the improvement is still 5%.

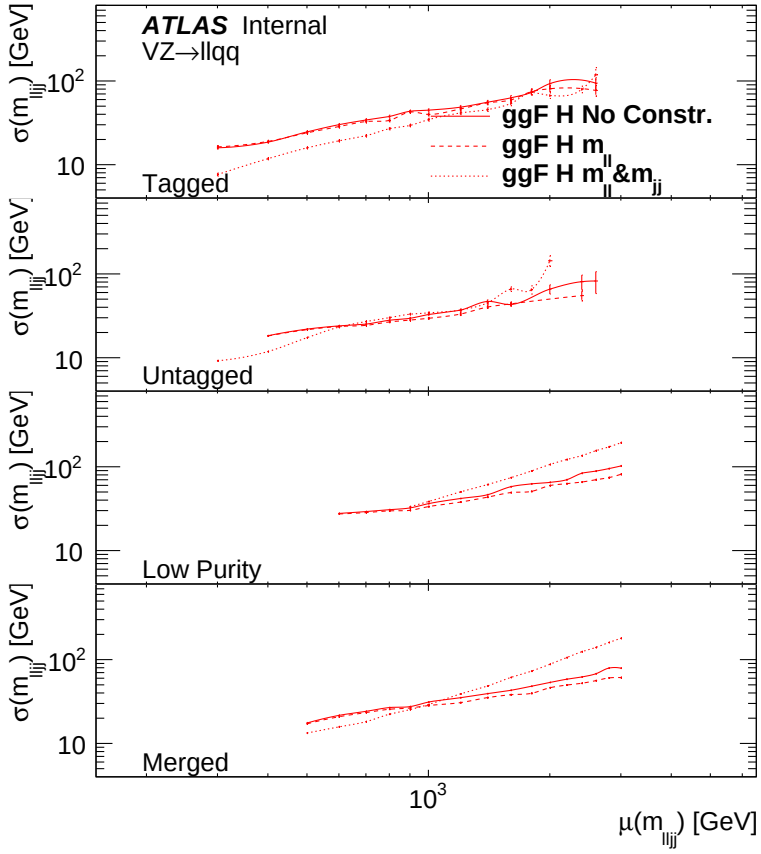

Figure 6.8: Resolution of the narrow width heavy Higgs signal by mass with no constraint, $\mu\mu$-constraint, and both $\mu\mu$ and jj-constraint. The $\mu\mu$-mass constraint is applied throughout the $\ell\ell qq$ signal regions. The jj-mass constraint is applied in the tagged category of the resolved regime only.

6.4 Triggers

Events used in the $ZV \to \ell\ell qq$ search were recorded with a combination of multiple single-electron or single-muon triggers with varying E_{T} (electron) and p_{T} (muon), quality, and isolation requirements. The minimum E_{T}-threshold for electrons is 24 GeV, while the minimum p_{T}-threshold for muons is 20 GeV. These triggers are complemented by triggers with higher thresholds with no isolation requirement (60 GeV or 120 GeV for electrons and 50 GeV for muons). Events belonging to the $ZV \to \nu\nu qq$ channel are recorded using an $E_{\mathrm{T}}^{\mathrm{miss}}$ trigger with an online threshold of 80 GeV for 2015 data and of 100 GeV for 2016 data.

$\ell\ell qq$				
Period	Electron triggers		Muon triggers	
	p_{T}	quality	p_{T}	isolation
2015	24 GeV (L1: 20 GeV)	medium-$\mathcal{L}$	20 GeV (L1: 15 GeV)	loose
2016, A	24 GeV	tight-$\mathcal{L}$	24 GeV	loose
2016, B	24 GeV	tight–$\mathcal{L}$	24 GeV	medium

$\nu\nu qq$	
Period	$E_{\mathrm{T}}^{\mathrm{miss}}$ triggers
2015	80 GeV
2016	100 GeV

Table 6.3: Lowest-p_{T} ($E_{\mathrm{T}}^{\mathrm{miss}}$) high-level triggers used for the $\ell\ell qq$ and $\nu\nu qq$ channels. The lowest-p_{T} triggers are combined with higher-p_{T} triggers with looser identification and isolation criteria to increase efficiency in the high-p_{T} range where there is reduced fake rate.

Single lepton triggers are used in the $\ell\ell qq$ channel even though 2 lepton triggers are available. Muon trigger event rates are just low enough at 2016 luminosities for this analysis to proceed without any special consideration for trigger efficiencies or need for more complex triggers.

Table 6.3 provides a list of the lowest un-prescaled lepton triggers–all are used in logical OR as the starting point for data selection. The near constant, maximum efficiency over the full range of utilized selection in the analysis is referred to as being on the "trigger plateau". In such cases a careful analysis of the combination of prescaled triggers or precise understanding of the trigger turn on curve are not necessary. The $\ell\ell qq$ and $\nu\nu qq$ channels are on their trigger plateaus, at or very near full efficiency. A comparison was made between the trigger efficiency of the 2015 and 2016 lists in reprocessed MC which indicated there was no significant change. It is therefore possible to combine 2015 and 2016 data sets.

6.5 $\ell\ell qq$ Analysis

The $ZV \to \ell\ell qq$ event selection starts with events with exactly two leptons passing the minimal (signal) lepton selection criteria. Both leptons are required to have the

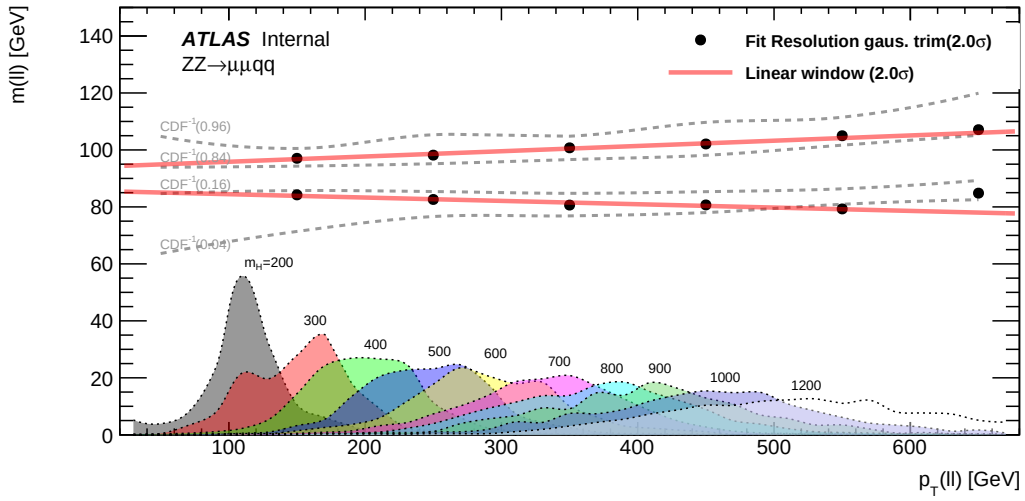

Figure 6.9: 2σ bound of fit to dimuon mass for H signal forming the SR cut window. Signal PDFs are shown at bottom in the $p_{\mathrm{T}}(ll)$ distribution to show the correlation between signal $p_{\mathrm{T}}(ll)$ and signal mass.

same flavor, and one must be of medium quality. Opposite charges are required for muons, but not for electrons, which are much more likely to have poorly measured charge due to confinement of tracking to the inner detector only for electrons and from the higher cross-sections for Brehmsstrahlung which results in more conversions in the inner detector. A window around the Z-mass is used to identify the $Z \to \ell\ell$ decay. Selected dielectron pairs have $m_{\ell\ell}$ between $83 - 99$ GeV. For muon pairs a mass window dependent on the dilepton transverse momentum ${p_{\mathrm{T}}}^{\ell\ell}$ is used:

$$85.63 - 0.00117{p_{\mathrm{T}}}^{\ell\ell} < m_{\ell\ell} < 94.00 + 0.0185{p_{\mathrm{T}}}^{\ell\ell} \tag{6.4}$$

The linearly varying window accounts for the diminished p_{T}-resolution of muons at high p_{T}. The loss of detector resolution for high-p_{T} muons is evident in the $Z \to \ell\ell$ mass resolution shown in Fig. 6.9. The window (in red) is determined from fitting a 2σ-acceptance window on the aggregate heavy Higgs samples from $m_H = 200 - 1200$ GeV. The window shown is defined by a trimmed Gaussian fit to the peaks and compared against the cumulative density function for validation. The uptick at high-${p_{\mathrm{T}}}^{\ell\ell}$ is an effect of the correlation between $m_{\ell\ell}$ and ${p_{\mathrm{T}}}^{\ell\ell}$ and the

high-p_{T} tail of the last sample. The $m_{\ell\ell}$ resolution for electron pairs on the other hand is consistent over the range of the study. Events with ≥ 3 loose leptons are vetoed in all regions of the analyses.

The definition of signal and Z-control regions then proceeds on the basis of jet selection. Events entering the merged regime $\ell\ell J$ have at least one large-R jet. Large-R jets are only reconstructed in the central region with $|\eta| < 2.0$. If more than one large-R jet is present then the one with highest-p_{T} is associated with the $V \to qq$ decay. Jet selection in the resolved regime, used for the reconstruction of the $V \to qq$ decay, uses the leading and subleading small-R jets.

A topological cut (topo $\angle$) is used to reject additional Z+jets background:

$$\frac{\min({p_{\mathrm{T}}}^{\ell\ell}, {p_{\mathrm{T}}}^{J})}{m_{\ell\ell J}} > 0.3\ (0.35), \qquad \text{(merged)} \tag{6.5}$$

$$\frac{\sqrt{p_{\mathrm{T}}^2(\ell\ell) + p_{\mathrm{T}}^2(jj)}}{m_{\ell\ell jj}} > 0.4\ (0.5). \qquad \text{(resolved)} \tag{6.6}$$

The looser cuts are for the $H \to ZZ$ search and tighter cuts in parentheses for the $W' \to ZW$ and $H/G^* \to ZZ$ searches. Although expressed in terms ${p_{\mathrm{T}}}^{\ell\ell}$, ${p_{\mathrm{T}}}^{J}$, and $m_{\ell\ell J}$ these cuts are essentially an angular cut reflecting the more central distribution of the signal compared to the Z+jet background. The values used retain high efficiency for the signal over the full signal search range, but still improve significance $S/\sqrt{B}$ especially at high $m_{\ell\ell J}$. The spin-1 and spin-2 distributions are more central, allowing for the tighter cut of 0.35 in the merged regime and 0.5 in the resolved regime.

The m_J and m_{jj} distributions for the Z+jets background are broadly distributed, while signal $V \to qq$ decay is tightly peaked around the vector boson mass. Excellent agreement in the m_J and m_{jj} distributions is seen between data and MC simulation prior to any fitting, as shown in Fig. 6.10.

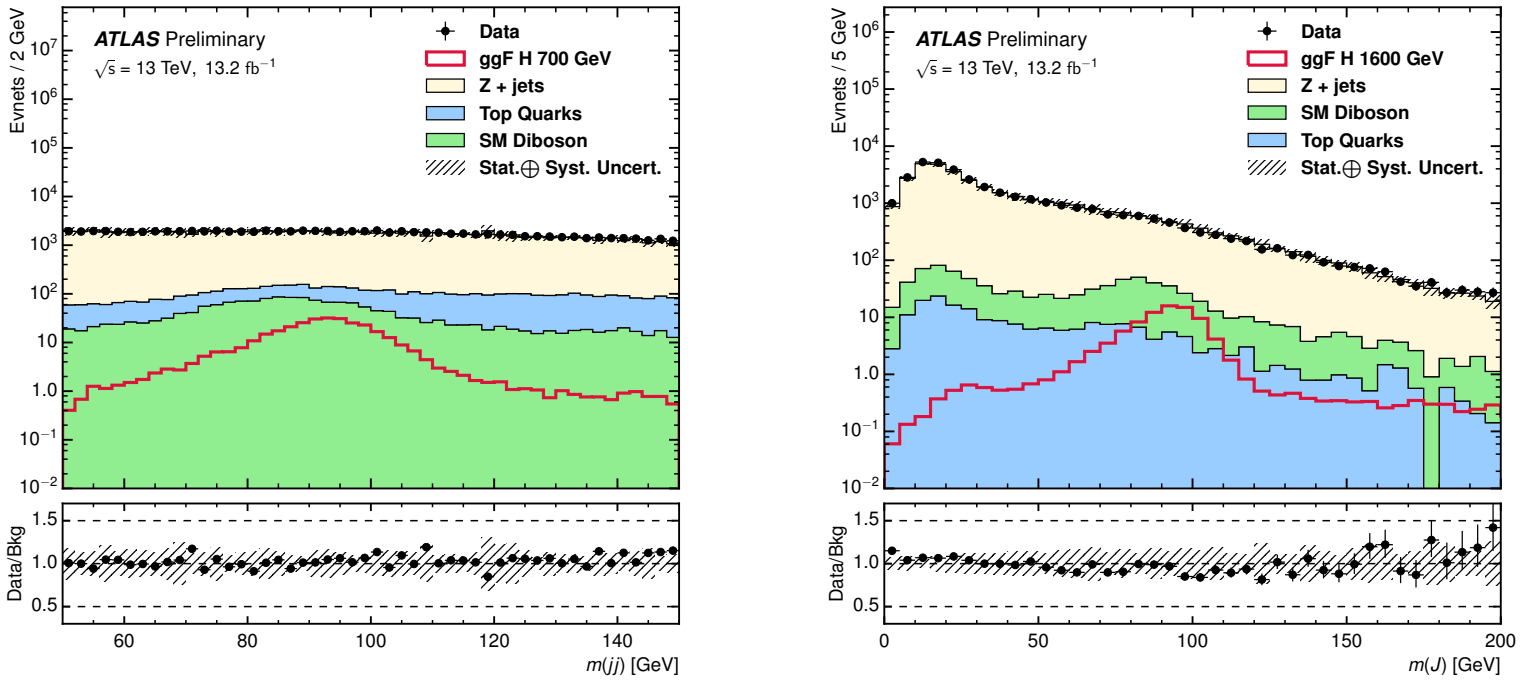

Figure 6.10: Comparison of data and MC in the (a) the resolved dijet mass m_{jj} and (b) the large-R jet mass m_J in the merged channel. Distributions are inclusive selections in the resolved and merged regimes. Signal distributions shown in (red) are from a Higgs boson with mass $m_H = 700$ GeV for the resolved analysis and at $m_H = 1600$ GeV for the merged analysis. Signals are shown with a cross section of $\sigma \times$ BR$(H \to ZZ) = 100$ fb at 700 GeV and 10 fb at 1600 GeV.

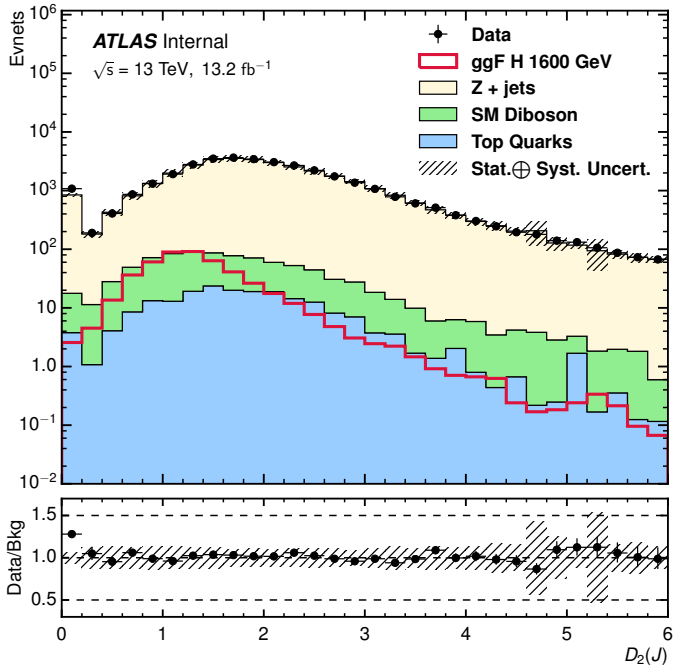

Figure 6.11: Comparison of data and MC in the $D_2^{(\beta=1)}$ distribution in the $\ell\ell qq$ channel. Shown is the inclusive selection in the merged regime. Signal distributions shown in (red) are from a Higgs boson with mass $m_H = 1600$ GeV and a cross section of $\sigma \times$ BR$(H \rightarrow ZZ) = 10$ fb at 1600 GeV.

Merged analysis

The merged analysis proceeds with the presence of the large-R jet passing the minimal selection criteria. A mass window of $m_V \pm 15$ is used in the merged regime to define the signal regions. It captures the mass peak of the hadronic boson decay loosely over the mass range searched. An example of the $Z \rightarrow q\bar{q}$ mass peak for a signal of 1600 GeV was shown in Fig. 6.10 (b). To gain discriminatory power the $D_2^{(\beta=1)}$ jet substructure discriminant (discussed extensively in Chapter 5) is used. The distribution of $D_2^{(\beta=1)}$ in the $\ell\ell qq$ analysis is shown in Fig. 6.11. Large-R jets passing the 50% efficiency cut enter the *high purity* category and those failing enter the *low purity*.

The Z-control regions are formed from the complement of the union of the SR mass-windows for the W and Z-decays in the $m_J$distribution: $m_J < 65$ GeV, $m_J > 106$ GeV. The Z+jets contribution to the merged SRs is constrained by a simultaneous

fit to control regions and signal regions.

Resolved analysis

In the spin-0 and spin-2 ZZ resonance searches the hadronic decay comes from a Z boson. About 1/5 of hadronic Zs decay to $b\bar{b}$ pairs (see Table 2.2). The dominant Z+jets background has a much smaller relative cross section to $Z + bb'$s–the ratio of production for heavy flavor of additional jets in association with the Z is $\sigma(Z + b)/\sigma(Z + j) \approx 0.1$. This motivates the split of the resolved analysis into *tagged* and *untagged* categories, with the former requiring two b-tagged jets and the latter having either one or zero. Events with more than two b-tags are rejected because they increase the presence of $t\bar{t}$ background. In the tagged category the two b-tagged jets are assumed to be associated with the $Z \to qq$ decay. In events with one b-tagged jet the b-jet and leading jet are assumed to be from $Z \to qq$ decay. The leading jet associated with $V \to qq$ decay is required to have $p_{\mathrm{T}} > 60$ GeV in all cases. The topological cut is removed in the tagged category to make it insensitive to the angular distribution of the selected jets which may be affected to small degree in MC simulation in the application of the *truth tagging* technique discussed later in this section.

A dijet invariant mass window $70 < m_{jj} < 105$ GeV is used to identify the signal region in the $H/G^* \to ZZ$ searches and a window of $62 < m_{jj} < 97$ GeV used in the $W' \to ZW$ search.

Sidebands around the union of the two signal regions in the m_{jj} distribution are used to define the Z-control region. The best modeling from MC excludes a wider range in this variable so the bands $50 < m_{jj} < 62\ GeV$ or $105 < m_{jj} < 150$ are used.

Top-quark production is a dominant background in the tagged category of the resolved analysis. Therefore, a designated $t\bar{t}$ control region is used to normalize the contribution from top processes in the SR. The TopCR is defined by requiring one μ

and one e in the tagged category instead of same-flavor leptons. The invariant mass of the lepton pair $e\mu$ is required to be within $76 - 106$ GeV and the b-tagged jet pair in the range $50 - 150$ GeV. This selection yields a high-purity top-quark region with $> 99\%$ $t\bar{t}$ and single-top processes. It is used for both the tagged and untagged categories but isn't necessary for the merged regime because the $m_{\ell\ell qq}$ invariant mass spectrum for $t\bar{t}$ is quite low.

Truth Tagging

Directly determining the background in the tagged category of the resolved analysis would be a highly wasteful strategy to generate binned distributions with sufficient statistical power due to the requirement for 2 b-tagged jets. Since the rejection factor for the b-tagging discriminant is > 300 for light jets only one in $\sim$10,000 background events would pass this cut alone. Simulation at ATLAS is an expensive part of the operation of the experiment and therefore an alternate approach of *truth tagging* is used that exploits the knowledge of the efficiency distribution of light, c, and b jets in passing the w working point. Instead of generating the MC background distribution by requiring w of both jets in a given background event to pass the 70% working point a scale factor based on the efficiency ϵ of the MC-determined truth flavor of each jet to pass the working point is used. Flavor specific efficiency maps (b, c, and light jet) are used for independently evaluated $t\bar{t}$ and Z+jet samples. The *truth tagging* methodology assigns a random w to each jet by sampling the distribution above the working point, which by definition will then pass the w cut in the analysis. Then a scale factor SF$= 1/\epsilon$ is applied for each candidate jet in the event.

This strategy allows the tails of the tagged category to be evaluated to reasonable precision. Any correlation between the tagging efficiency of multiple jets in a single event is lost. However, no evidence of significant correlation has been found and the statistically limited data taken so far in Run 2 in the high-mass tail of the tagged

category suggests any fuss about bias arising in the tails won't be relevant until more data is taken. Figure 6.12 compares the 4-body mass distribution obtained in the tagged selection. The improvement in the description of the high-mass tail is evident in most distributions, as is the agreement between the methods of direct tagging and truth tagging. Some disagreement in distributions containing c in the ZCR (especially in $Z + cc$) has been noted and calls for exploration in the future. It is not apparent in the SR shown, presumably because kinematic differences arise from the larger mass of the c, which enter in the sideband but not for events passing the Z mass constraint. The differences are not explicitly corrected in these analyses because they contribute minimally. Very large uncertainties are applied to the normalization of these backgrounds (with little effect) in the fit as there is little constraint on them.

VBF analysis

The vector-boson fusion production channel $qq' \to H \to ZZ \to \ell\ell qq$ is searched in addition to the ggF production channel in the spin-0 analysis. It is a well-motivated production process in many models that results in the presence of two additional jets (referred to as VBF-tag jets here) in the event topology coming from the scattering of the initial quarks in the interaction. The VBF-tag jets typically have a large dijet invariant mass and a large separation in pseudorapidity. The VBF-tagged jets are selected from small-R jets passing the minimal selection criteria. In the merged regime they are required to have a pseudorapidity separation of $|\Delta\eta| > 1.5$ from the leading large-R jet. In the resolved regime, VBF-tag jets are selected from those not already associated with the $V \to qq$ decay.

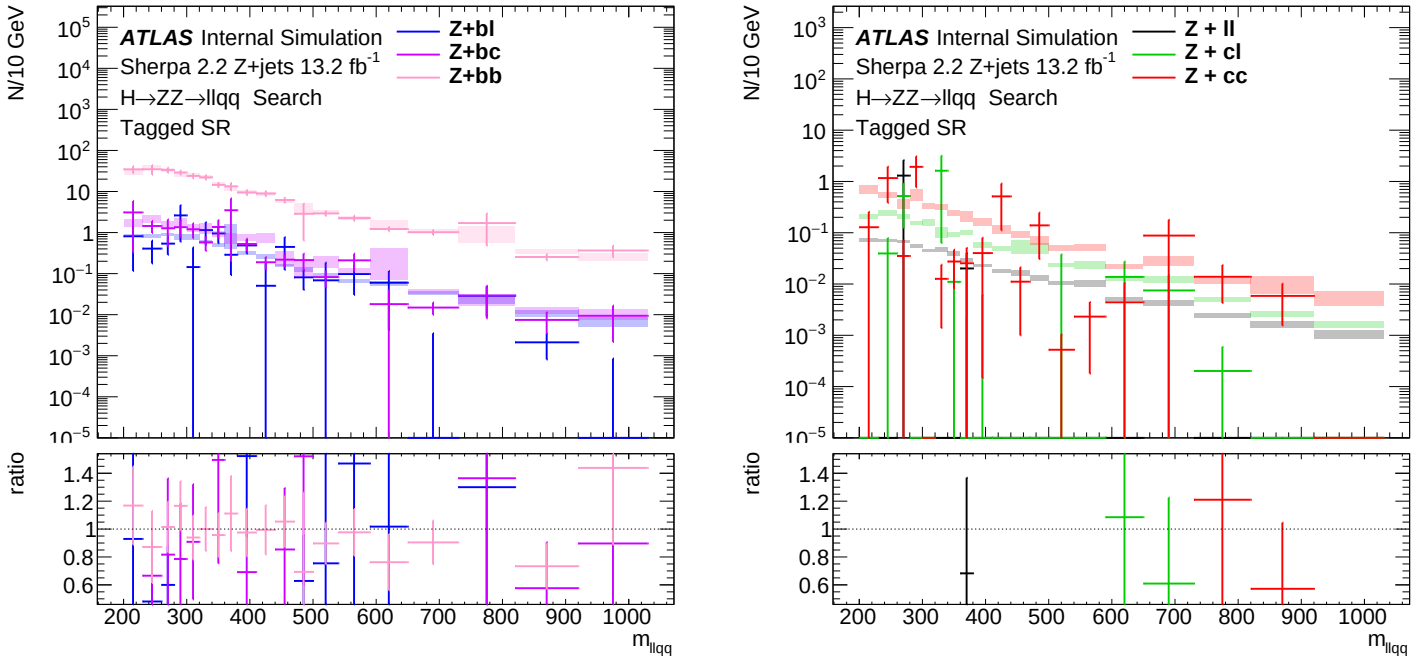

Figure 6.12: Comparison of direct tagging and truth tagging methods in the SR, used for determining the Z+jets background in the tagged category of the resolved regime. (Points) show the distributions from direct tagging and (boxes) the resulting distribution from truth tagging. Some distributions (in particular $Z + l$ cannot be resolved with direct tagging due to the high rejection factor of b-tagging discriminant.

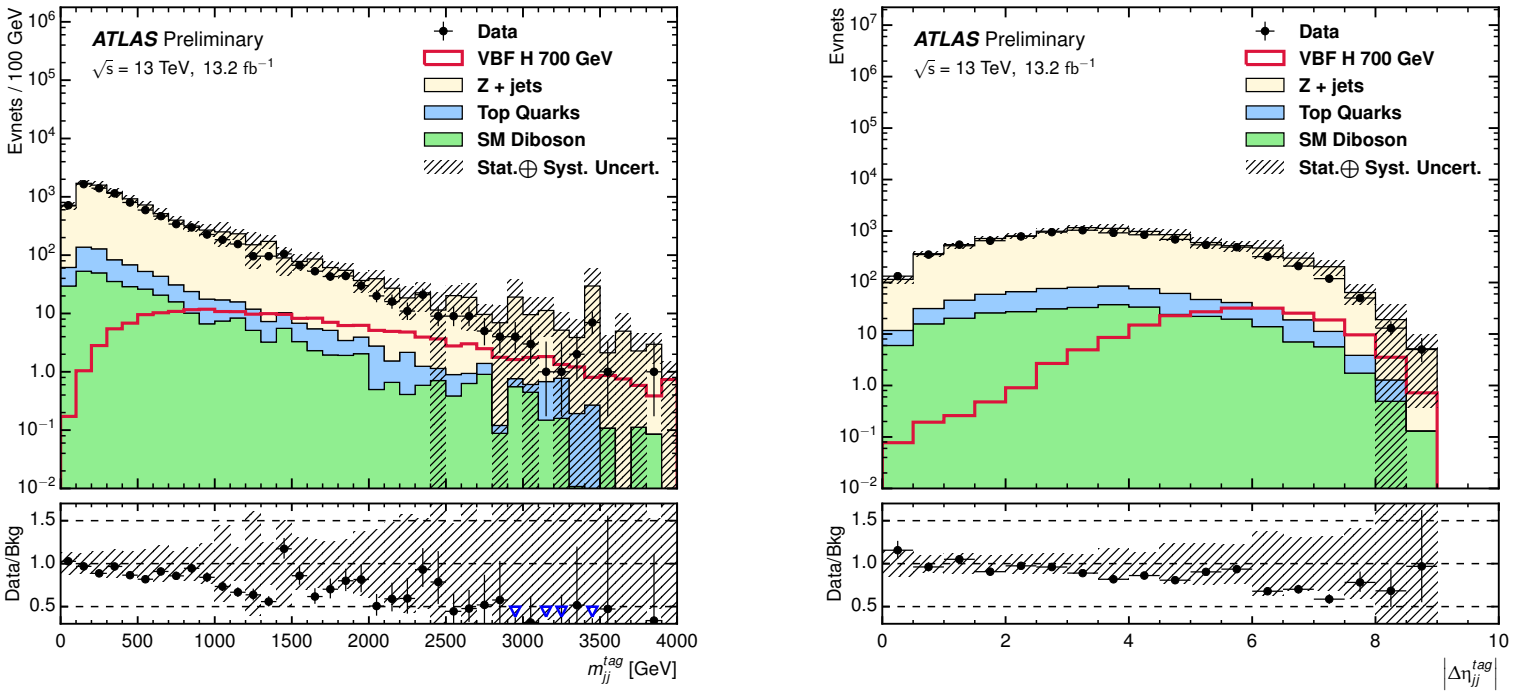

Figure 6.13: Comparison of data and MC in the (a) the resolved dijet mass m_{jj} and (b) the large-R jet mass m_J in the $\ell\ell qq$ channel. Distributions are inclusive selections in the resolved and merged regimes. Signal distributions shown in (red) are from a Higgs boson with mass $m_H = 700$ GeV for the resolved analysis and at $m_H = 1600$ GeV for the merged analysis. Signals are shown with a cross section of $\sigma \times$ BR$(H \rightarrow ZZ) = 100$ fb at 700 GeV and 10 fb at 1600 GeV.

Figure 6.13 shows the distributions of the dijet invariant mass m_{jj}^{tag} and pseudo-rapidity separation $|\Delta\eta_{jj}^{\text{tag}}|$ of the two tag jets, shown inclusively in the merged and resolved regimes. These two variables are not perfectly modeled. Consequently, cuts on them lead to differences between data and MC in overall normalization in kinematic distributions involving the signal jets and leptons. This effect is compensated for in the fit design discussed in Chapter 7. Events entering the VBF analysis are selected by requiring $m_{jj}^{\text{tag}} > 600$ GeV and $|\Delta\eta_{jj}^{\text{tag}}| > 3.1$. These cuts were arrived at from an optimization of significance $S/\sqrt{B}$ in MC simulation. Both cuts have been placed on the inclusive end of broad minima to maximize the number of potential signal events entering the VBF analysis. Events in $H \to ZZ$ analysis failing the VBF criteria enter the ggF analysis. There is almost no contamination of the ggF signal in VBF regions and vice versa, however contamination is allowed modeled in the fit.

The best association of individual jets in the categorization of an event as either ggF or VBF has been studied. It is found to be optimal to associate the two leading-p_{T} jets to the $Z \to q\bar{q}$ decay. The remaining jets with the largest invariant mass are taken to be the VBF-tag jets. An added benefit of this approach is the selection of VBF-tag jets second allows for the $Z \to q\bar{q}$ selection to be consistent for all signal types (including those without VBF production channel).

Event Prioritization and Recycling

For events which satisfy both the small-R jet criteria for the resolved regime and the large-R jet criteria for the merged regime the following is used to classify events with respect to jet regime, region, and signal category. When an event fails a given selection, it is tested against the next criteria according to its priority; this is termed "recycling". Only upon failing all selections is an event discarded. The order of selections is as follows:

- Merged SR

- Low Purity SR
- Resolved SR
- Merged ZCR
- Low Purity ZCR
- Resolved ZCR

The phase space considered in this search where the recycling strategy is most important is roughly in the transition region from $400 \leq m_H \leq 800$ GeV . Above and below these signal masses hadronic decays $Z \to q\bar{q}$ are reconstructed primarily as either merged or resolved, respectively, but small differences in signal to background significance are found over the full mass range. The recycling strategy is superior to a fixed cut strategy because it saves signal events, no matter the cut optimization. The placing of merged prior to resolved was determined by studies using signal to background optimization, and confirmed with the expected limits of the analysis with 2015 data presented at Moriond [28].

For the scalar signal benchmark in the spin-0 analysis, events passing the VBF selection enter the VBF regions and otherwise enter the ggF regions. The order of selection inside each of the VBF and ggF regions follows the same order described above.

Event Selection Summary

The complete event selection for the $\ell\ell qq$ channel has been discussed in the proceeding subsections and is summarized in Table 6.4. In determining the optimal cuts throughout, an effort has been made for the inclusiveness and retaining of the greatest possible efficiency of the benchmark signals. This philosophy has led to wide topological, mass cuts, VBF-tag cuts, and the recycling strategy with hardly any loss of signal significance that tighter cuts might bring at the cost of greater exclusivity. Figure 6.14 shows the efficiency for each of the benchmark signal types. The resolved

Common	
	Criteria
Preselection	Exactly 2 loose leptons ≥ 1 medium lepton
$Z \to \ell\ell$	$83 < m_{ee} < 99$ GeV $-0.01170 {p_{\mathrm{T}}}^{\ell\ell} + 85.63 < m_{\mu\mu} < 0.01850 {p_{\mathrm{T}}}^{\ell\ell} + 94.00$ GeV
Lepton charge	$Z \to \mu^+\mu^-$ No requirement $Z \to ee$
Merged Regime	
Signal jet	≥ 1 large-R jet Leading large-R jet $p_{\mathrm{T}} > 200$ GeV
topo $\angle$	$\min[{p_{\mathrm{T}}}^{\ell\ell}, {p_{\mathrm{T}}}^{J}]/m_{\ell\ell J} > 0.3$ (0.35) for spin-0 (1 or 2)
mass window $Z \to q\bar{q}$ $W \to qq'$	 $75 < m_J < 105$ GeV $66 < m_J < 96$ GeV ZCR: $50 < m_{jj} < 66$ GeV or $105 < m_{jj} < 150$ GeV
boson tag	$D_2^{(\beta=1)}(Z)$ spin-0 or 2 $D_2^{(\beta=1)}(W)$ spin-1
Resolved Regime	
Signal jets	≥ 2 small-R jets $\lvert\eta\rvert < 2.5$ Leading jet $p_{\mathrm{T}} > 60$ GeV Subleading jet $p_{\mathrm{T}} > 30$ GeV
topo $\angle$	$\sqrt{\left({p_{\mathrm{T}}}^{\ell\ell}\right)^2 + \left({p_{\mathrm{T}}}^{jj}\right)^2} > 0.4$ (0.5) for spin-0 (1 or 2) in untagged regions
mass window $Z \to q\bar{q}$ $W \to qq'$	 $70 < m_{jj} < 105$ GeV $62 < m_{jj} < 97$ GeV ZCR: $50 < m_{jj} < 62$ GeV or $105 < m_{jj} < 150$ GeV
flavor tag (ZZ analyses only)	*tagged*: exactly 2 b-jets *untagged*: 0 or 1 b-jet

Table 6.4: Event selection summary for the $\ell\ell qq$ channel.

analysis has limited acceptance but dominates the selection efficiency at low mass. The merged analysis becomes highly efficient at high mass. The transition between resolved and merged analyses occurs quickly in the mass range from 400 to 800 GeV. The low transition mass range is due to the prioritization in event recycling of the merged regimes over the resolved, which has been shown to be optimal–although the effect is not large.

A fit is performed simultaneously to all regions of $\ell\ell qq$ analysis. The Z-control regions and $t\bar{t}$-control regions constrain the normalization of the major backgrounds in the fit. The predicted background counts for each of the control regions, taking

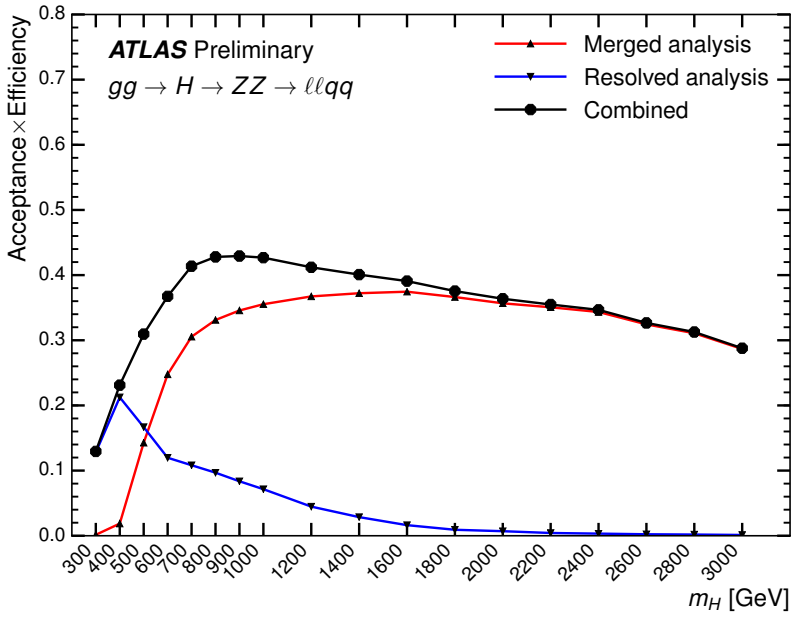

Figure 6.14: Selection efficiencies of $ZV \to \ell\ell qq$ signals from MC simulations as functions of the resonance mass for both merged and resolved analyses.

into account the constraining power of the fit in the presence of all systematic uncertainties, are shown in Table 6.5. The most important pieces of information to read from the table are the consistency between data and MC in all the control regions. This indicates that within the statistics of the MC samples and the systematic uncertainties proposed the model is a sufficient description of the data.

The fit in many cases has the power to constrain the sum of several backgrounds better than an individual background. This happens when backgrounds have similar shapes–notably in the untagged category in the case of Z,Zl, and Zcl. The lack of constraint on Zcl is the leading source of uncertainty on the normalization of Zl even though the data tightly constrains the sum of all flavors (Z). In the current configuration there is little power to constrain the contribution of individual flavors in the Z+jets background. The author has shown that the analysis has the power to constrain individual flavors tightly by switching the ZCR discriminant to a function of w the b-tagging discriminant of the two leading jets. However, a derivation

	Hi P.	Low P.	VBF HP	VBF LP	Untagged	VBF Res.	Tagged
Top	3.5 ± 0.7	5.9 ± 1.0	0.11 ± 0.04	0.02 ± 0.04	290 ± 30	8.8 ± 1.8	131 ± 6
Diboson	49 ± 7	51 ± 4	1.3 ± 0.4	3.1 ± 0.9	670 ± 40	13.9 ± 1.3	54 ± 6
Z	580 ± 20	1230 ± 30	18 ± 2	54 ± 7	19900 ± 140	230 ± 15	409 ± 18
Zl	–	–	–	–	15100 ± 600	–	0.8 ± 0.2
Zbb	–	–	–	–	170 ± 30	–	360 ± 20
Zbc	–	–	–	–	117 ± 17	–	21 ± 4
Zbl	–	–	–	–	1600 ± 200	–	24 ± 12
Zcc	–	–	–	–	390 ± 120	–	6 ± 3
Zcl	–	–	–	–	2500 ± 600	–	1.2 ± 1.3
Total	630 ± 20	1290 ± 30	20 ± 2	57 ± 7	20860 ± 140	253 ± 15	594 ± 18
Data	606	1270	25	59	20857	246	608

Table 6.5: Best-fit values of the global yields for the Standard Model backgrounds from the background-only ($\mu = 0$) fit, as well as the total number of data candidates in all Z-control regions.

of systematic uncertainty on the continuous w distribution has not been made at ATLAS. This limits use of w to the fully-studied efficiency working points (e.g. 70% used here). The discriminant used in the control regions instead is the 3 and 4-body mass–this excludes any mass constraints used in the SRs.

Figure 6.16 shows the ZCRs of the resolved regime as they are fit in the analysis. The normalization of each of the MC backgrounds has been set by the fit. The gray bands show the uncertainty on the MC fit, which takes into account MC statistics and all systematic uncertainties. The pink dotted line shows the MC-predicted background prior to any fitting, nearly identical in this case. The agreement between data and MC is excellent over the full spectrum, the lowest bin starting at 280 GeV through the highest observed data, not exceeding 2000 GeV. The $t\bar{t}$ background makes an outsize appearance in the first $\sim$ 200 GeV of the tagged ZCR Fig. 6.16 (a), which requires the use of its own control region if a good understanding of background is to be made for signal with 4-body mass in the range 300 GeV to 500 GeV . Differences in the data-MC agreement of $t\bar{t}$ distribution in the μe channel and $\mu\mu$ or ee channels is limited to experimental sources of uncertainty related to the efficiency of lepton reconstruction, which are small in these analyses.

Figure 6.17 shows the ZCRs of the merged regime. The ZCRs in the merged regime

also show excellent agreement between data and MC. Very little change is observed between pre-fit and post-fit backgrounds. Notice the order of magnitude reduction in background achieved by the use of $D_2^{(\beta=1)}$ between the high and low-purity regions.

Figure 6.15 shows the ZCR in the resolved regime of the spin-0 VBF analysis. The SHERPA 2.2 samples generate Z+2 jets to NLO with NNLO cross sections but only LO calculations are made for Z+4 jets. The cross sections for LO processes are not expected to be particularly accurate; it is no surprise that the pre and post-fit normalization on the Z+jets background in the VBF categories with the additional requirement of 2 VBF-tagged jets is different from the MC simulation. The normalization of the Z+jets background away from 1 is expected and accommodated in the fit design. The agreement excellent after the fit shown, although there are large systematic uncertainties in this region. Larger bin widths and the combining of the tagged and untagged categories brings systematic uncertainty associated with limited MC statistics in the region to satisfactorily constrain the Z+jets normalization in the VBF categories. The systematic uncertainty is shown in the shaded region. Figure 6.17 shows the ZCR in the merged regime of the spin-0 VBF analysis. Initial agreement in the higher-mass region of Figs. 6.15 and 6.17 is better than in the low mass region visible in the resolved ZCR. The difference is capably covered by systematic uncertainties resulting in good agreement after the fit.

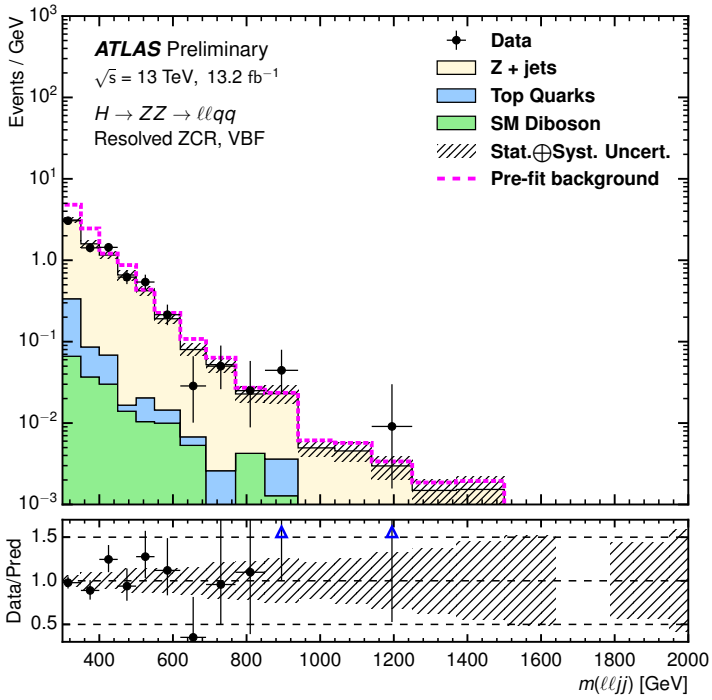

Figure 6.15: Data and MC comparison of the $m_{\ell\ell jj}$ distribution in the Z+jets control region of the VBF production channel of the resolved regime in the spin-0 analysis. This distribution controls the the normalization of Z+jets in the VBF signal regions.

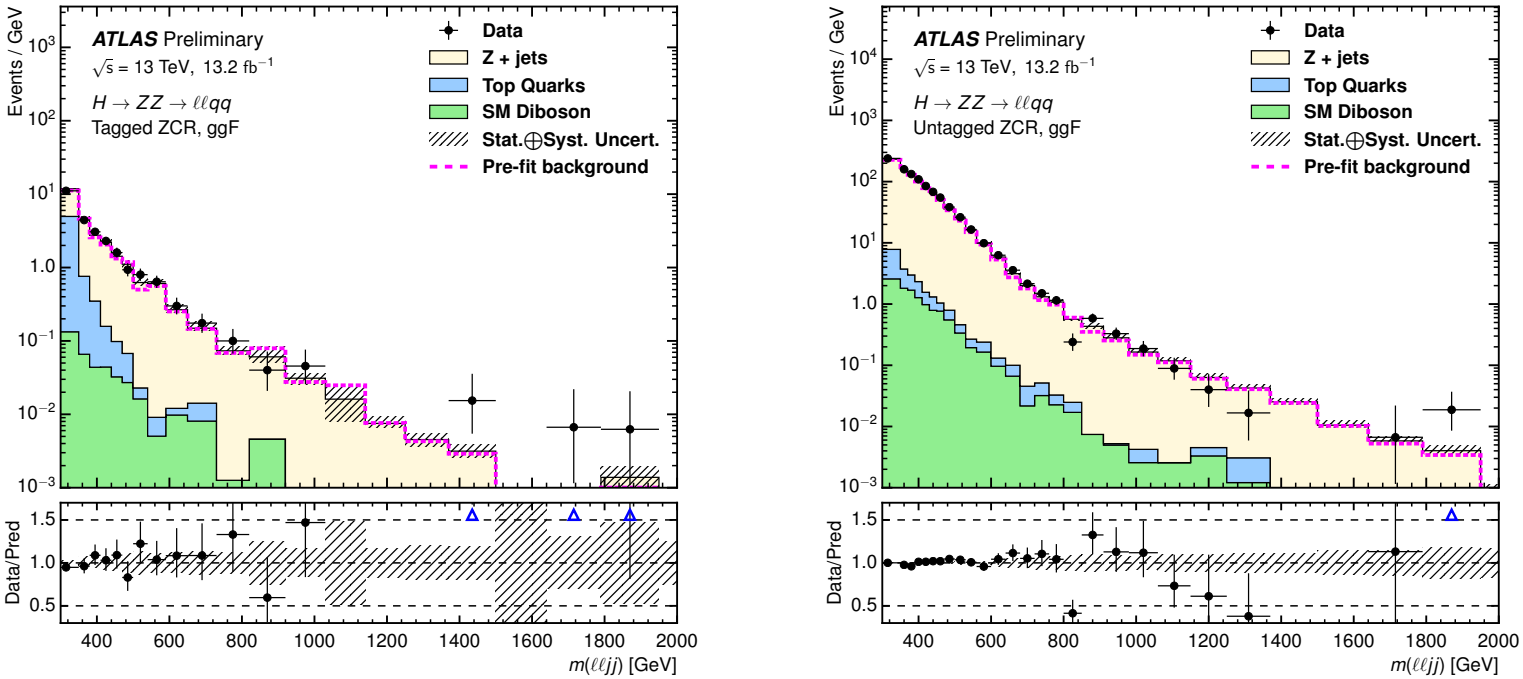

Figure 6.16: Data and MC comparison of the $m_{\ell\ell jj}$ distribution in the Z+jets control regions of the ggF production channel of the resolved regime in the spin-0 analysis for (a) the tagged and (b) untagged categories. These distributions are used to constrain the Z+jets normalization in the resolved signal regions.

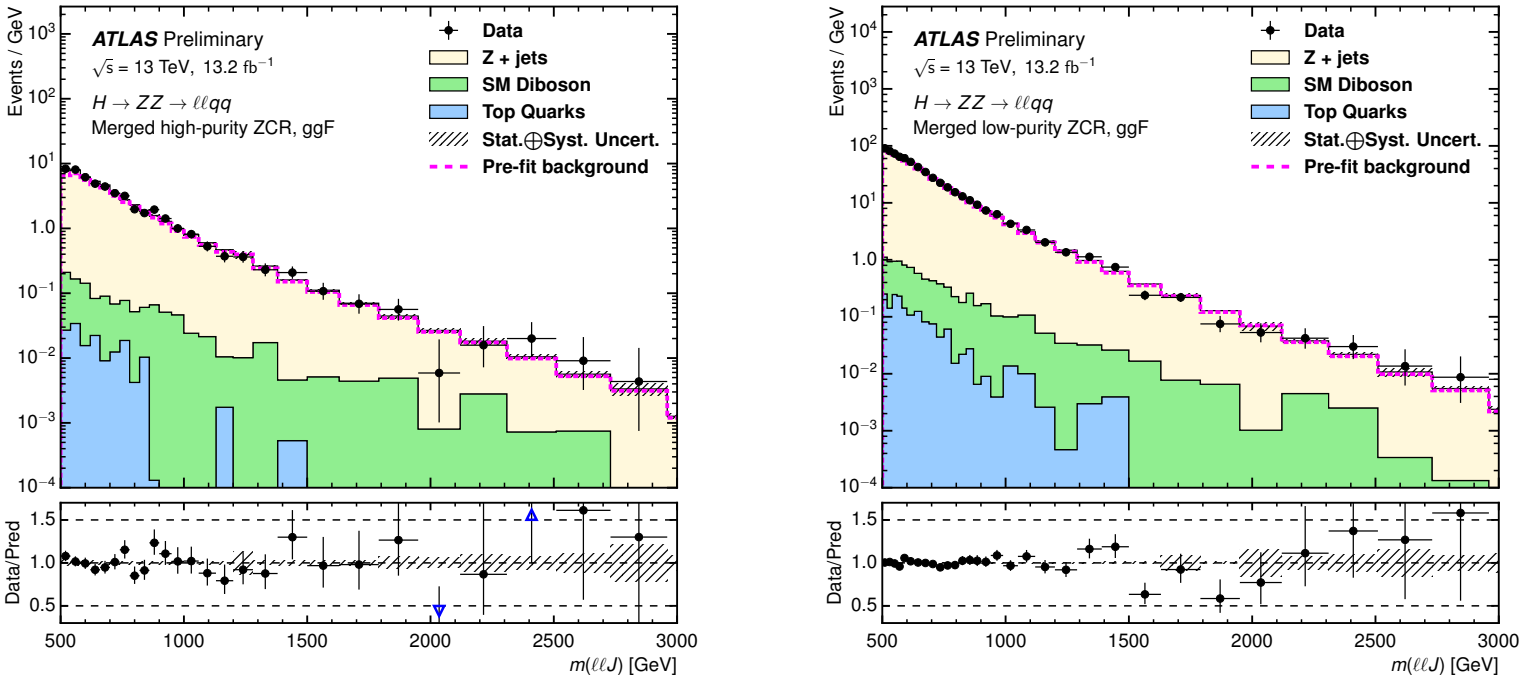

Figure 6.17: Data and MC comparison of the $m_{\ell\ell jj}$ distribution in the Z+jets control regions of the ggF production channel of the resolved regime in the spin-0 analysis for the merged analysis for (a) the high-purity and (b) low-purity categories. These distributions are used to control the Z+jets normalization in the merged signal regions.

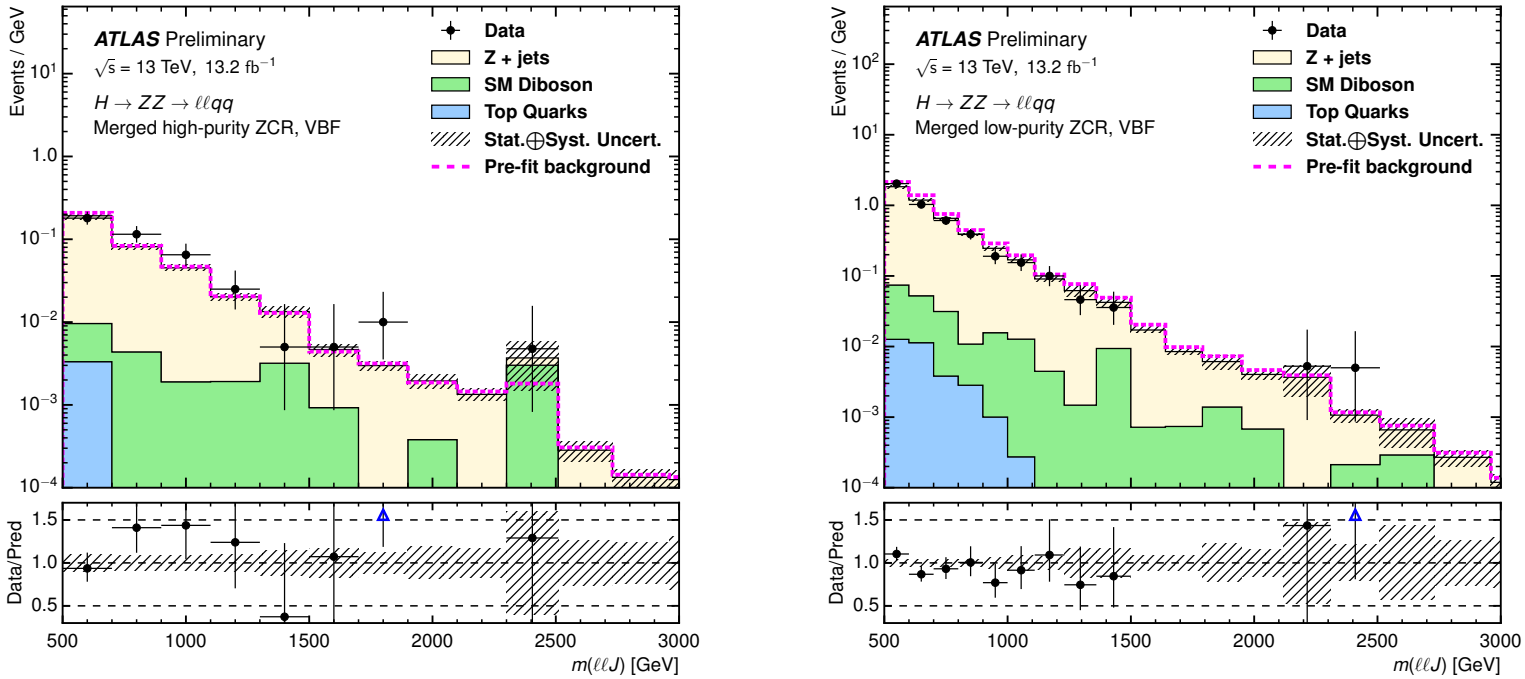

Figure 6.18: Data and MC comparison of the $m_{\ell\ell jj}$ distribution in the Z+jets control regions of the VBF production channel of the merged regime in the spin-0 analysis in the (a) high-purity and (b) low-purity categories. This distribution controls the the normalization of Z+jets in the VBF signal regions.

6.6 $\nu\nu qq$ analysis

Event selection in the $ZV \rightarrow \nu\nu qq$ channel begins with a large $E_{\mathrm{T}}^{\mathrm{miss}} > 250$ GeV cut to identify events containing the boosted $Z \rightarrow \nu\nu$ decay of the signal back-to-back in ϕ with the boosted $V \rightarrow qq$ decay. This cut alone reduces drastically most SM backgrounds, especially QCD multijet events which have no intrinsic missing transverse momentum. A significant number of QCD dijet events still obtain large $E_{\mathrm{T}}^{\mathrm{miss}}$, either through terrible mis-measurement of a jet or through non-collision background. Any analysis not requiring the presence of leptons explicitly is subject to the presence of these type of events due to the large cross section of the QCD dijet process.

A set of *anti-QCD* cuts are employed to get rid of QCD events with the presence of erratic measurements. To eliminate high-$E_{\mathrm{T}}^{\mathrm{miss}}$ events arising from spurious measurement isolated to the calorimeters an alternate measurement of missing transverse momentum composed only of all good tracks of charged particles $p_{\mathrm{T}}^{\mathrm{miss}}$is used. Two cuts are made utilizing $p_{\mathrm{T}}^{\mathrm{miss}}$:

1. A much lower cut of $p_{\mathrm{T}}^{\mathrm{miss}} > 50$ GeV is used as a calorimeter independent measure. It is just high enough to reject the vast majority of remaing dijet events even given the distribution of charged fraction of particles in a jet. Yet it is also low enough to efficiently accept signals with mass starting at 500 GeV, since a very small fraction of jets have a charged fraction below 10%.
2. $\Delta\Phi(E_{\mathrm{T}}^{\mathrm{miss}}, p_{\mathrm{T}}^{\mathrm{miss}}) < 1$ Events with real $E_{\mathrm{T}}^{\mathrm{miss}}$ will have reconstructed track-based missing transverse momentum in a similar direction as $E_{\mathrm{T}}^{\mathrm{miss}}$. In the case of a dijet event associated with a poorly measured calorimeter jet there will be little correlation.

Finally, the requirement $\Delta\Phi(E_{\mathrm{T}}^{\mathrm{miss}}$,small-R jets)$> 0.4$ is used to specifically reject the event topology of a single mis-measured jet (passing the minimal selection) in a dijet event. In this case $E_{\mathrm{T}}^{\mathrm{miss}}$ will point in the ϕ-direction of one of the two jets. The signal event topology should not have such a jet in the $E_{\mathrm{T}}^{\mathrm{miss}}$ direction except possibly

arising from initial state radiation.

The $\nu\nu qq$ channel proceeds only with a merged selection. The hadronic boson decay is identified requiring that the leading (highest p_{T}) large-R jet in the event has a mass consistent with the W or Z boson mass. The $\nu\nu qq$ analysis mirrors the $\ell\ell qq$ analysis in the treatment of large-R jets. The m_J mass window of $V \pm 15$ GeV is used to identify the SR. And again, a 50% efficient cut of $D_2^{(\beta=1)}$ is used to separate the high purity region from the low purity region. The pre-fit distribution of the mass of the leading-R jet distribution and the $D_2^{(\beta=1)}$ are shown in Fig. 6.19.

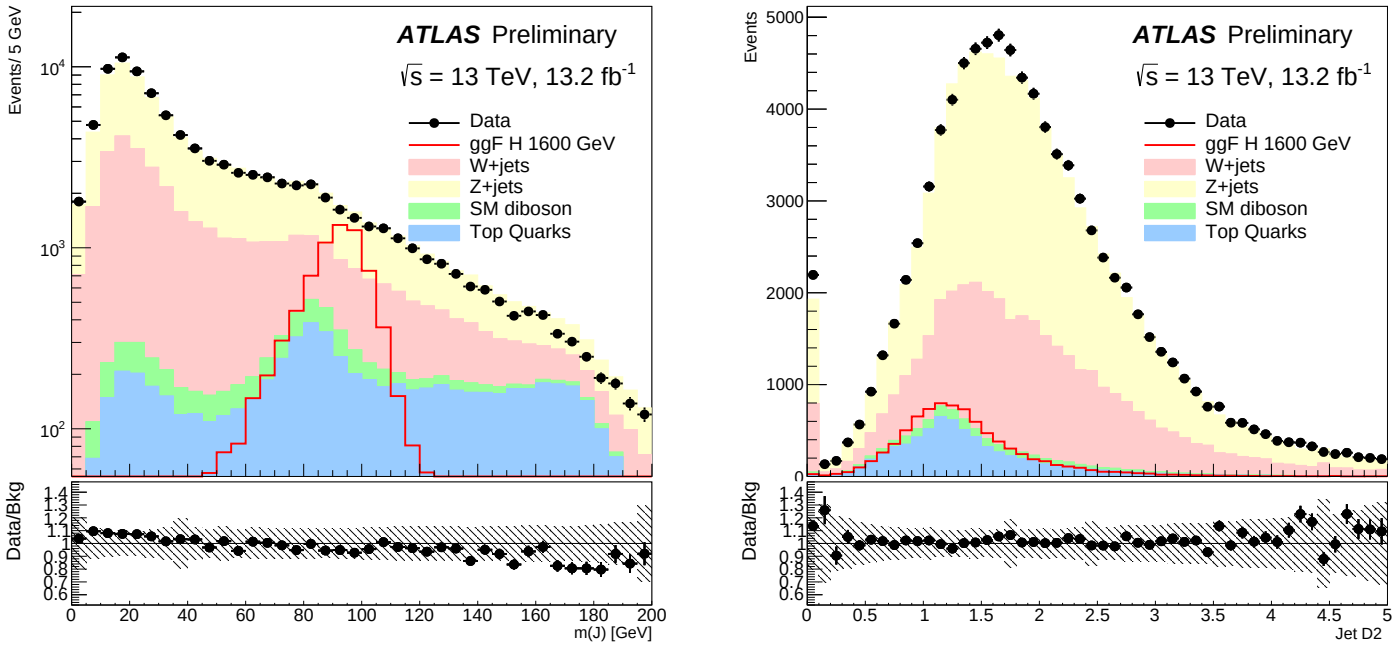

Figure 6.19: The (a) mass and (b) $D_2^{(\beta=1)}$ distribution of the leading large-R jet in the $\nu\nu qq$ channel. The selection excludes $m_{\ell\ell J}$-window and $D_2^{(\beta=1)}$ cuts. The heavy Higgs signal shown is given a $\sigma \times$ BR$(H \rightarrow ZZ)$ value of 1 pb.

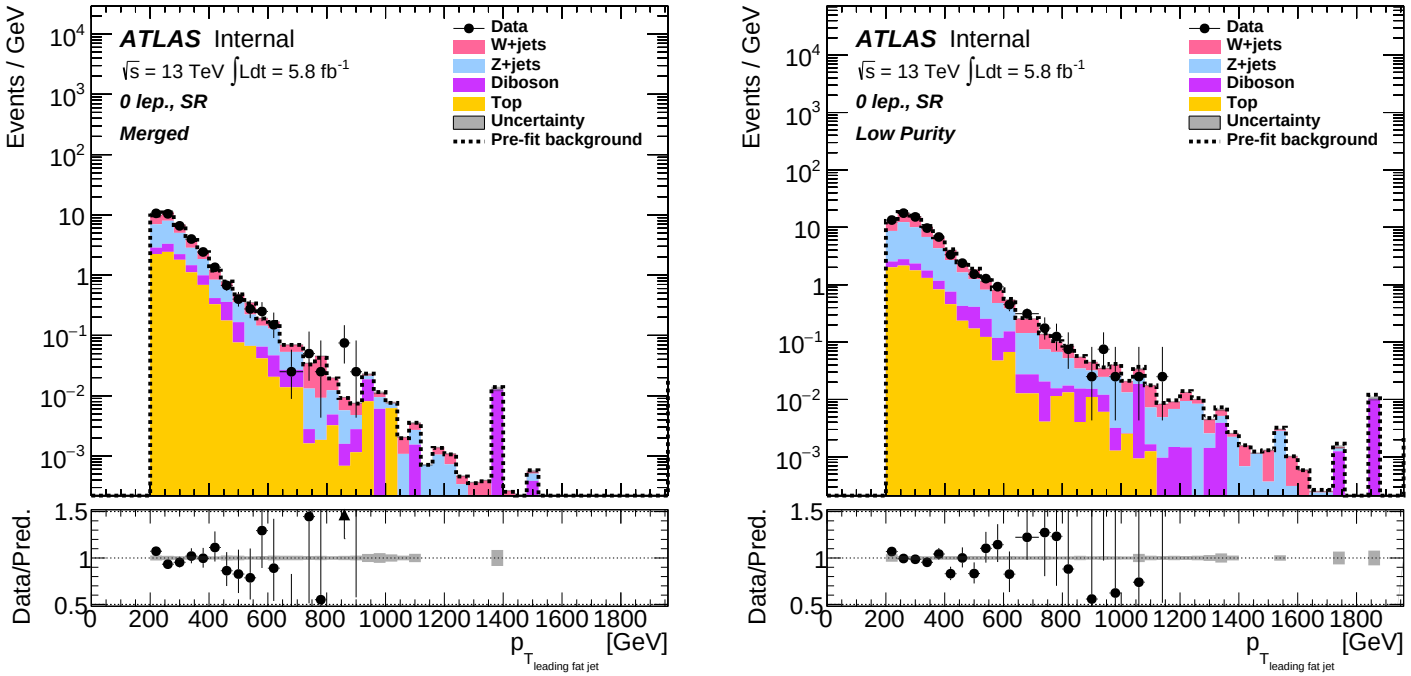

Figure 6.20: Data and MC comparison of the p_{T}-distribution of the leading large-R jets in the $\nu\nu qq$ channel in the (a) high-purity signal region and (b) low-purity signal region. The pre-fit background is shown in the black dashed line. Systematic uncertainties are shown in the gray bands (except MC statistical uncertainty.).

A small linear slope is evident in the data-MC comparison, although it is covered by the systematic uncertainty. Future iterations of the analysis in Run 2 will likely fit the difference explicitly, but it is not necessary to do so at this stage. To confirm the good kinematic modeling of the leading large-R jet, leading large-R jet-p_{T} is shown in Figure 6.20 after the final fit is performed. Systematic errors constrained by the fit are propagated to the p_{T} distribution and shown in the gray band.

The efficiency of the selection for the $H \to ZV \to \nu\nu qq$ signals is shown in Fig. 6.21. The low-purity category helps recover around 10-20% efficiency depending on the mass considered and the boson p_T. The efficiency drop at high mass is due to the degradation of the large R-jet mass resolution.

The three main backgrounds Z+jets, W+jets, and $t\bar{t}$ each have a designated CR, separated by the presence of leptons from the SR. The ZCR requires 2 leptons, the WCR and TopCR both require 1 lepton. A modified version of missing transverse momentum is used by removing muons from the calculation $E^{\mathrm{miss}}_{\mathrm{T,no}\ \mu}$. This definition is used to protect against possible differences resulting from trigger inefficiency; the first level $E^{\mathrm{miss}}_{\mathrm{T}}$ trigger does not include muons since they require the combination of the muon spectrometer and calorimeters which are two separate L1 systems. The selection in the CRs requires $E^{\mathrm{miss}}_{\mathrm{T,no}\ \mu}$> 250 GeV and $p^{\mathrm{miss}}_{\mathrm{T,no}\ \mu}$> 50 GeV, matching the cuts of the SR, which are fully efficient.

The ZCR uses the selection of exactly two muons, with one required to have $p_{\mathrm{T}} >$ 25 GeV. In combination with the $\ell\ell qq$ channel the $\ell\ell qq$ ZCR region can be used, as both regions are found to be modeled well and normalizations agree in the individual channel fits. The invariant mass of the dimuon system is required to be between 66 and 116 GeV. To exclude a possible signal in the $\ell\ell qq$ decay the hadronic $V \to qq$ decay mass window is inverted, 65 GeV $< m_J >$ 116 GeV. There is a control region for each of the high and low-purity regions.

The WCR and TopCRs are constructed from events with exactly one muon passing

the minimum selection criteria. If the event contains at least one b-jet then it is considered to be a $t\bar{t}$ event and enters the TopCR, otherwise it is placed in the WCR. This selection captures the characteristic $t \to W + b$ decay chain. The b-jets are required not to overlap with the large-R jet to ensure they are not a V-decay product. The WCR also is limited to the inversion of the hadronic $V \to qq$ decay mass window, 65 GeV $< m_J >$ 116 GeV. This guarantees the exclusion of signal that also produces diboson resonances in the WZ/WW-channels. Like the ZCR, the WCR and TopCR are separated into the high and low-purity selections based on the $D_2^{(\beta=1)}$ cut on the large-R jet.

Together there are 6 control regions in the $\nu\nu qq$ channel to constrain the normalization of each of the three prominent backgrounds in the SRs.

Event Selection Summary

The event selection for the $\nu\nu qq$ channel is summarized in Table 6.6. There is a very limited cross section for SM backgrounds with naturally high $E_{\mathrm{T}}^{\mathrm{miss}}$. Consequently, the limited number of cuts in the $\nu\nu qq$ channel have been chosen to widely accept the signal. The high-purity region is designed to be 50% efficient when taking into account the $D_2^{(\beta=1)}$ cut and mass window. An additional 10-20% of signal efficiency is recovered from the low-purity signal region. Figure 6.21 shows the efficiency for the heavy Higgs signal in the signal regions of the $\nu\nu qq$ channel. Acceptance is limited in the lower mass range of the searches primarily from the large-R jet minimum criteria and also somewhat by the $E_{\mathrm{T}}^{\mathrm{miss}}$ cut. A fit is made independently from the $\ell\ell qq$ channel to all regions in the $\nu\nu qq$ channel. Table 6.7 shows the predicted background counts for each of the control regions, taking into account the constraining power of the fit in the presence of all DoF provided by the systematic uncertainties. The agreement between data and MC in all background regions of the analysis indicates with some further checks that have been made indicate that there is no unphysical exploitation

Common	
	Criteria
Preselection	Exactly 0 loose leptons with $p_{\mathrm{T}} > 7$ GeV
Merged Regime	
Signal jet	≥ 1 large-R jet Leading large-R jet $p_{\mathrm{T}} > 200$ GeV
$E_{\mathrm{T}}^{\mathrm{miss}}$	$E_{\mathrm{T}}^{\mathrm{miss}} > 250$ GeV
Anti-QCD	$p_{\mathrm{T}}^{\mathrm{miss}} > 30$ GeV $\min(\Delta\Phi(E_{\mathrm{T}}^{\mathrm{miss}},\text{small-R jets})) > 0.4$ $\Delta\Phi(E_{\mathrm{T}}^{\mathrm{miss}},p_{\mathrm{T}}^{\mathrm{miss}}) < 1$
mass window $Z \to q\bar{q}$ $W \to qq'$	 $75 < m_J < 105$ GeV $66 < m_J < 96$ GeV Z/WCR: $50 < m_{jj} < 66$ GeV or $105 < m_{jj} < 150$ GeV
boson tag	$D_2^{(\beta=1)}(Z)$ spin-0 or 2 $D_2^{(\beta=1)}(W)$ spin-1

Table 6.6: Event selection summary for the $\ell\ell qq$ channel.

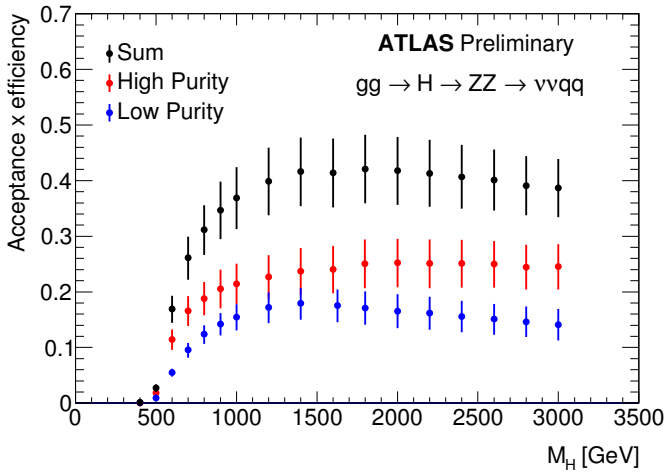

Figure 6.21: Analysis efficiencies of $ZV \to \nu\nu qq$ signals from MC simulation parametrized by signal mass for the spin-0 analysis.

	Z Hi P.	Z Lo P.	W Hi P.	W Lo P.	$t\bar{t}$ Hi P.	$t\bar{t}$ Lo P.
Diboson	21.1 ± 0.9	100 ± 2	88 ± 3	402 ± 8	1.9 ± 0.5	4.9 ± 0.5
Top	9.5 ± 1.3	68 ± 10	1180 ± 100	2600 ± 300	750 ± 30	820 ± 40
Z+jets	880 ± 30	5790 ± 80	115 ± 11	930 ± 20	0.85 ± 0.09	4.2 ± 0.4
W+jets	neg.	neg.	5630 ± 130	38500 ± 400	38 ± 3	139 ± 10
Total	910 ± 30	5960 ± 80	7010 ± 90	42400 ± 200	790 ± 30	970 ± 30
Data	924	5964	7021	42454	798	972

Table 6.7: Best-fit values of the global yields for the Standard Model backgrounds from the background-only ($\mu = 0$) fit, as well as the total number of data candidates in all control regions.

of systematic variations in the fit and the MC model is a good description of the data.

The discriminant used in all control regions is the transverse mass built with the $E^{\text{miss}}_{\text{T,no }\mu}$and the leading large-$R$ jet, analogous to transverse mass constructed in the signal region. Figure 6.22 shows ZCRs used in the $\nu\nu qq$ channel as they are fit in the analysis. Figure 6.23 shows the TopCRs, and Fig. 6.24 shows the WCRs. All control regions are a reasonable fit. Very little disagreement between pre-fit and post-fit MC simulation descriptions of the control regions is observed. In the case of the TopCR there is a notable but small shift in the rate of exponential decay adjusted for in the post-fit distributions. This shift exploits the large modeling systematic uncertainties on $t\bar{t}$ discussed in the following section. It is well within the prior knowledge of the $t\bar{t}$ distribution shape.

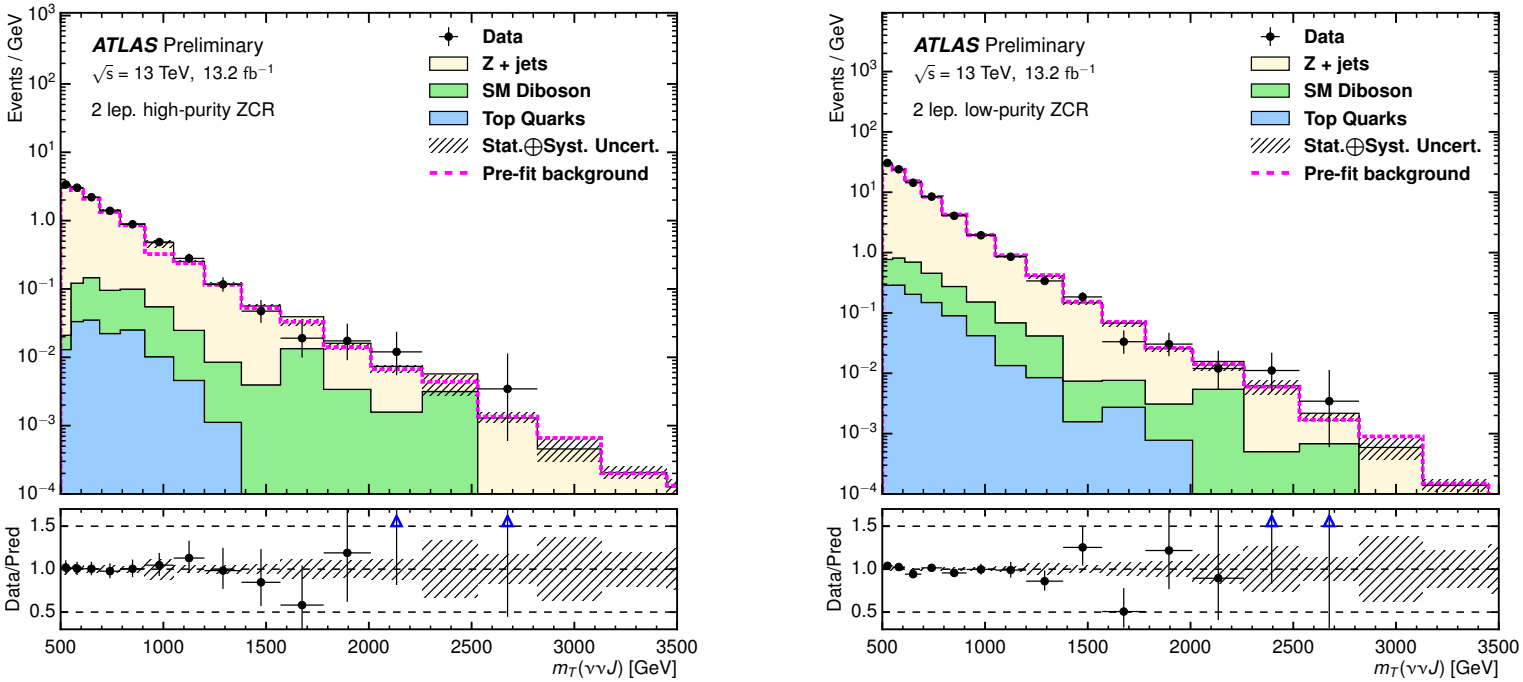

Figure 6.22: Data and MC comparison in the transverse mass distribution $M_T(\nu\nu J)$ in the Z+jets control region of the (a) high-purity and (b) low-purity categories. The ZCR constrains the normalization of Z+jets in signal regions.

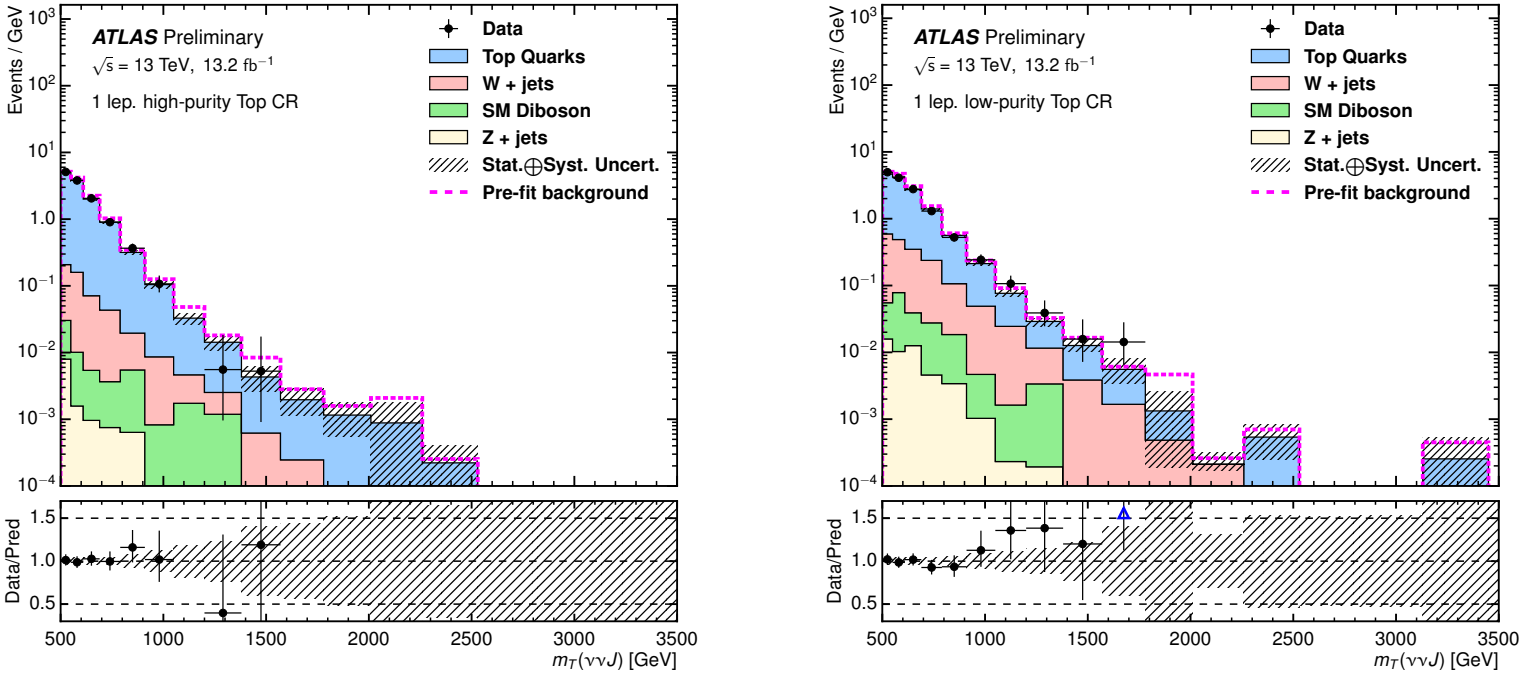

Figure 6.23: Data and MC comparison in the transverse mass distribution $M_T(\nu\nu J)$ in the Top-control region of the (a) high-purity and (b) low-purity categories. The TopCR constrains the normalization of $t\bar{t}$ in signal regions.

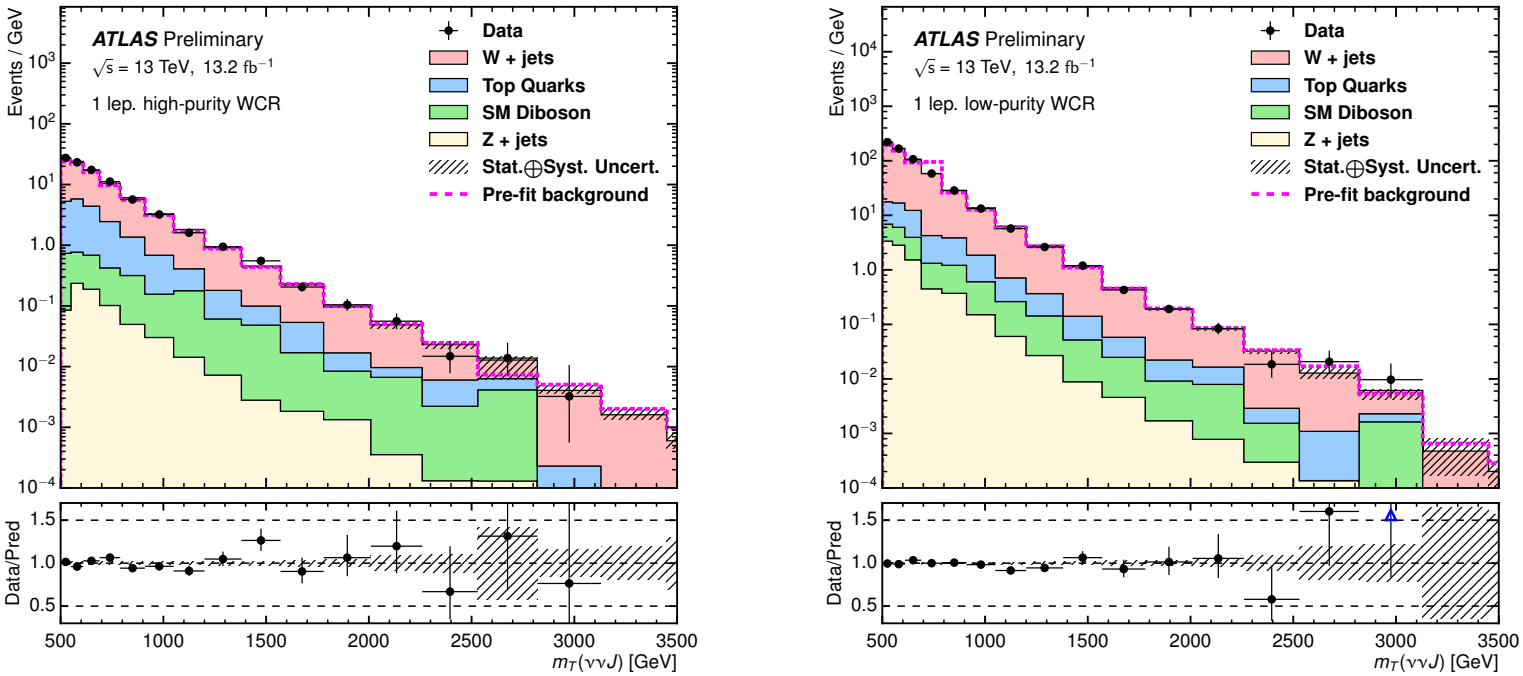

Figure 6.24: Data and MC comparison in the transverse mass distribution $M_T(\nu\nu J)$ in the W+jets control region of the (a) high-purity and (b) low-purity categories. The WCR constrains the normalization of W+jets in signal regions.

6.7 Systematic Uncertainties

Sources of systematic uncertainty affecting the search come from calibration of the detector and the reconstruction of physics objects, modeling and normalization of the backgrounds, and modeling of the signal. Systematic uncertainties entering the analysis are often larger (or less constrained) than they are after the fit is performed to all the regions. This is made explicit in the case of leading background normalizations where no prior constraint has been assumed and the fit to SRs and CRs are responsible for constraining their normalization. The following discussion will reference uncertainties prior to constraint by the final fit to signal and control regions unless otherwise mentioned.

The largest sources of uncertainty entering the $\ell\ell qq$ and $\nu\nu qq$ channels are the modeling uncertainties on the leading V+jets backgrounds and the large-R jet mass and resolution. The derivation of jet uncertainties is treated in Chapter 5. The modeling uncertainty for the Z+jets background in the $\ell\ell qq$ channel is estimated by a data-driven approach measuring data-MC disagreement in the ZCRs and mapping it to the SRs as an uncertainty. In the $\nu\nu qq$ channel MC variations of tunable parameters in the simulation of leading backgrounds are used to provide the modeling uncertainty. Sub-dominant but also of significant impact are uncertainties associated with leptons and background normalizations. Many additional sources enter in a minor way and are included in the analysis. It is worth noting that while small-R jets do not directly enter the $\nu\nu qq$ channel the uncertainties associated with their measurement are propagated into the analysis via the $E_{\mathrm{T}}^{\mathrm{miss}}$ observable.

***Z*+jet modeling uncertainty in the $\ell\ell qq$ channel** The dominance of the Z+jets background in the SRs and ZCRs of the $\ell\ell qq$ channel allows for the use of a simple data-driven technique for providing an estimate of the modeling uncertainty of the Z+jets background in the SRs. For each SR-ZCR pair the ratio of differential

$m_{\ell\ell jj}$ cross sections is taken in MC Z+jets simulation:

$$\alpha_i(m_{\ell\ell jj}) = \frac{\left(\frac{\partial\sigma_i^{\mathrm{SR}}}{\partial m_{\ell\ell jj}}\right)_{\mathrm{MC}}}{\left(\frac{\partial\sigma_i^{\mathrm{CR}}}{\partial m_{\ell\ell jj}}\right)_{\mathrm{MC}}} \tag{6.7}$$

for the ith SR. The α_i ratio is then used to map $\left(\frac{\partial\sigma_i^{CR}}{\partial m_{\ell\ell jj}}\right)_{\mathrm{data}}$ to the SR. The data-driven estimate of the SR is then scaled by the ratio of the distribution of Z+jets to the total MC background distribution for the data-driven estimate of the Z+jets background in the SR. The difference between the MC Z+jets background in the SR and the data-driven estimate is used as the modeling uncertainty.

In practice to remove statistical deviations from affecting the ratio, all distributions involved are completely fit in the peak area and the high mass exponential decay. An up to 9th degree log-polynomial is used to fit the peak region and the decay region is fit with the "dijet function":

$$f(m_{\ell\ell J}) = p_0 \frac{\left[1 - \left(\frac{m_{\ell\ell J}}{\sqrt{s}}\right)\right]^{p_1}}{\left(\frac{m_{\ell\ell J}}{\sqrt{s}}\right)^{p_2 + p_3 \log\left(m_{\ell\ell J}/\sqrt{s}\right)}} \tag{6.8}$$

where $\sqrt{s}$ is the center of mass energy, p_0, p_1, p_2 and p_3 are free parameters, and $m_{\ell\ell J}$ is expressed in GeV. The dijet function is so-called because of its pervasive use in the experimental fitting of the QCD dijet spectrum. It is a heuristic fit in the $\frac{m_{\ell\ell J}}{\sqrt{s}}$ variable with the correct extrapolation to high-mass that incorporates the asymptotic behavior at the center of mass energy of $\sqrt{s} = 13$ TeV.

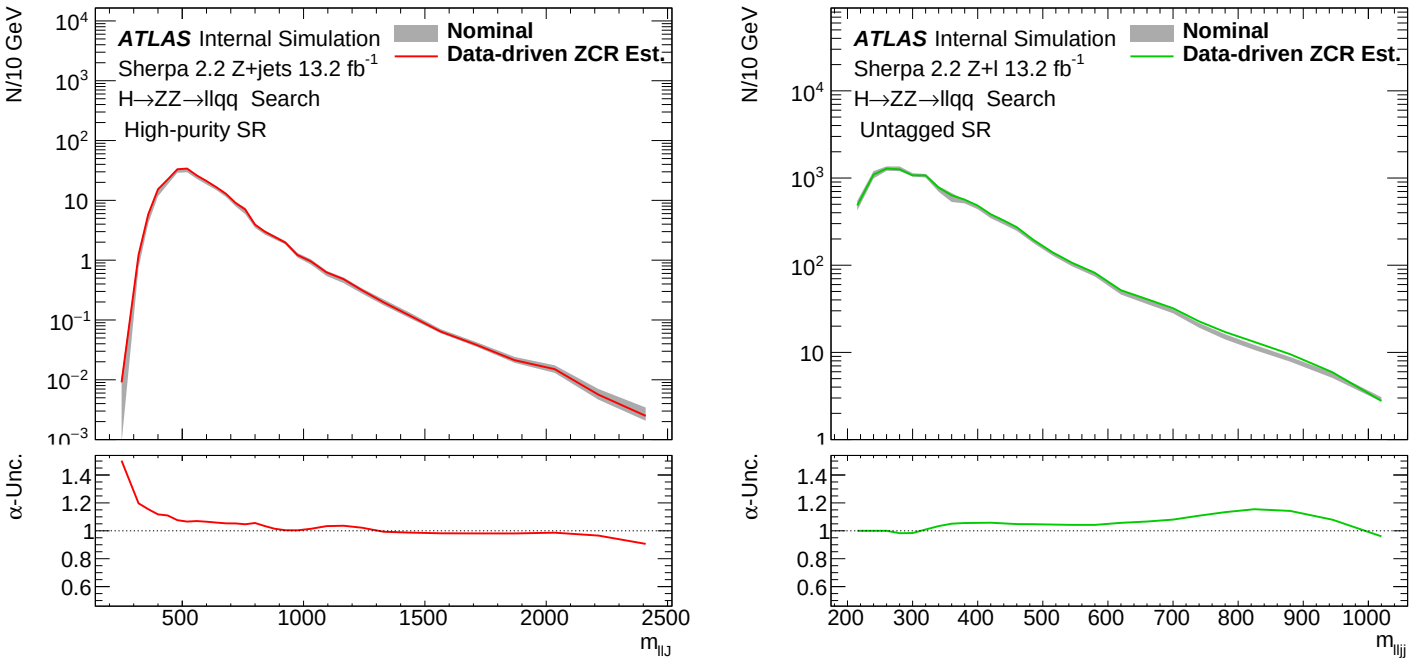

Figure 6.25: The Z+jets background modeling uncertainty applied to the signal regions of the $\ell\ell qq$ channel. The modeling uncertainty is applied to the largest Z+jet flavor slice in the resolved regime. The relative variation for the modeling systematic is shown in the bottom frames for the (a) high-purity SR and (b) untagged SR. Gray bands shown are the nominal MC Z+jets distributions showing the statistical precision of the sample. The modeling uncertainty is derived by mapping the data-MC difference in the control region to the corresponding signal region.

All calculations are then performed on the fits and the modeling uncertainty is added back to the original MC SR to produce the $+1\sigma$ systematic variation. Figure 6.25 shows the comparison of the data-driven estimate in the SR from the α-ratio method to the nominal MC. The difference of the estimate to the nominal sample is taken as the remaining systematic uncertainty on the shape of the $m_{\ell\ell jj}$ distribution attributable to MC modeling of the Z+jets leading background. The down variation is produced by inverting the up variation.

The use of the α-ratio to produce the modeling uncertainty has a few advantages over other techniques where it is applicable. The larger statistics available in the ZCR regions and the fitting procedure produce a systematic variation over the whole range of the SR distribution with little additional noise from the statistical uncertainty. It addresses with a single uncertainty most of the sources of mis-modeling that equally affect SRs and ZCRs, including the ME calculation, normalization and factorization scales, and PDFs. It also has the ability to include uncaptured experimental sources of uncertainty that would affect both ZCR and SRs equally. As a cross check for modeling uncertainty that may affect the ZCRs and SRs differently MadGraph and Sherpa comparisons have been checked for differences in the SRs and ZCRs separately in the same MC study shared in Chapter 4. No differences were observed to be significant.

Background modeling uncertainty in the $\nu\nu qq$ channel

MC variations are used to generate modeling uncertainties in the $\nu\nu qq$ channel for Z+jets, W+jets, and $t\bar{t}$ backgrounds.

W+jets and Z+jets modeling uncertainty

The W+jets and Z+jets samples are produced with Sherpa (see Chapter 4), which uses matrix element matching with a tunable scale parameter in $p_{\perp}$, above which

emissions are produced by matrix element (ME) and below which by parton shower (PS).

CKKW merging scale The multijet merging scale is taken to be 20 GeV nominally and varied up to 30 GeV.

Renormalization scale The renormalization scale on which the running coupling α_a depends is varied by a factor of $\sqrt{2}$.

Factorization scale The factorization scale used for evaluation of the PDFs is varied by a factor $\sqrt{2}$.

QSF resummation scale Varies the resummation scale or the parton shower starting scale by a factor of 2.

These four variations cover uncertainties arising from ME generation, merging, and PS and were made according to recommendations from SHERPA collaborators. To avoid introducing effects from low statistics the difference in the systematic variation and the nominal distribution is fit linearly. The systematic uncertainty after fitting each variation is shown in Fig. 6.26.

$t\bar{t}$ modeling uncertainty

The $t\bar{t}$ samples are particularly susceptible to poor generator modeling due to the complexity of the final state and the atypical selection of phase space for top samples entering these analyses. The nominal $t\bar{t}$ sample has been generated with POWHEG and interfaced with PYTHIA 8 for showering, hadronization, and modeling of the underlying event (UE).

Alternate samples have been produced to cover mis-modeling arising from the models and tunings arising from the generation of the hard scatter, parton showering and the hadronization model, scales used in factorization and renormalization. Three samples have been used to evaluate the sensitivity and introduce the necessary degrees of freedom into the final fit.

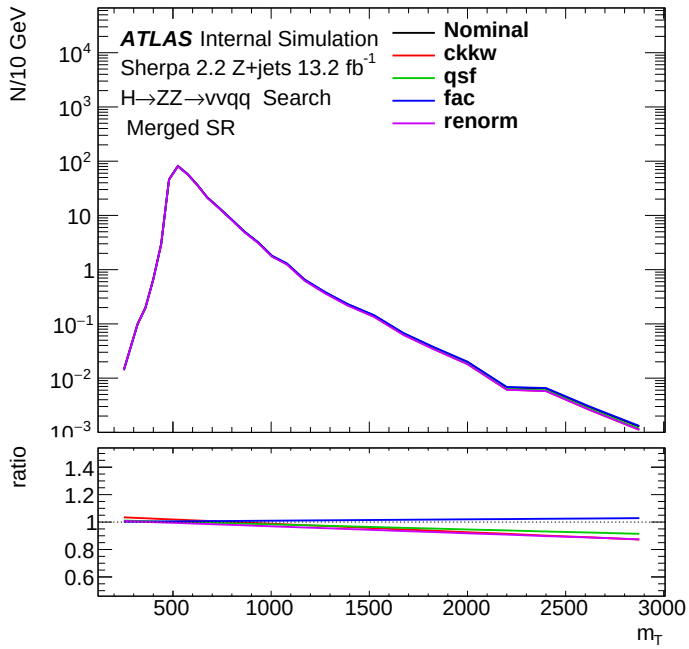

Figure 6.26: Systematic uncertainty associated with the modeling of leading backgrounds. Variations of scales used in the generation of Sherpa 2.2 samples QSF resummation scale, CKKW merging scale, factorization scale, and renormalization scale have similar effects for both W and Z+jets. The latter is shown.

Powheg +Pythia 8 variations Two sets of variations are produced encompassing effects from factor of 2-variations independently applied to the factorization, hadronization scales, and resummation damping factor (a POWHEG parameter controlling ME/PS matching) as well as initial (ISR) and final state radiation (FSR) high and low-tunes. The high and low-tunes are determined by varying $p_\perp$ by factor of 2 in the dependence of the running coupling $\alpha_s(p_\perp)$. Together variation of these parameters sufficiently cover effects regulating high-p_T radiation.

Pythia 8 - Herwig++ Comparison The POWHEG +Herwig++ is generated with the same setup for POWHEG but with PS, hadronization, and UE provided by Herwig++.

Powheg- aMC@NLO Comparison POWHEG and aMC@NLO provide alternate techniques and tuning for the generation of MEs to NLO. The aMC@NLO+Her-

wig++ sample is generated with MadGraph 5 _aMC@NLO and interfaced with Herwig++ for PS, hadronization, and UE modeling.

Normalization is already controlled by the TopCR and so the differences in normalization of the variations do not affect the final fit, only the shape. All modeling variations on W+jets, Z+jets, and $t\bar{t}$ are applied independently on the backgrounds and symmetrically around the nominal distribution.

Large-R Jet Uncertainties

The scales and resolutions of large-R jets are poorly constrained when compared to other objects due to the relatively limited channels in which large-R jets can be balanced against other well-measured particles. The derivations were discussed in Chapter 5. This results in large uncertainties that propagate to the mass discriminants used in the signal regions shown in Fig. 6.27.

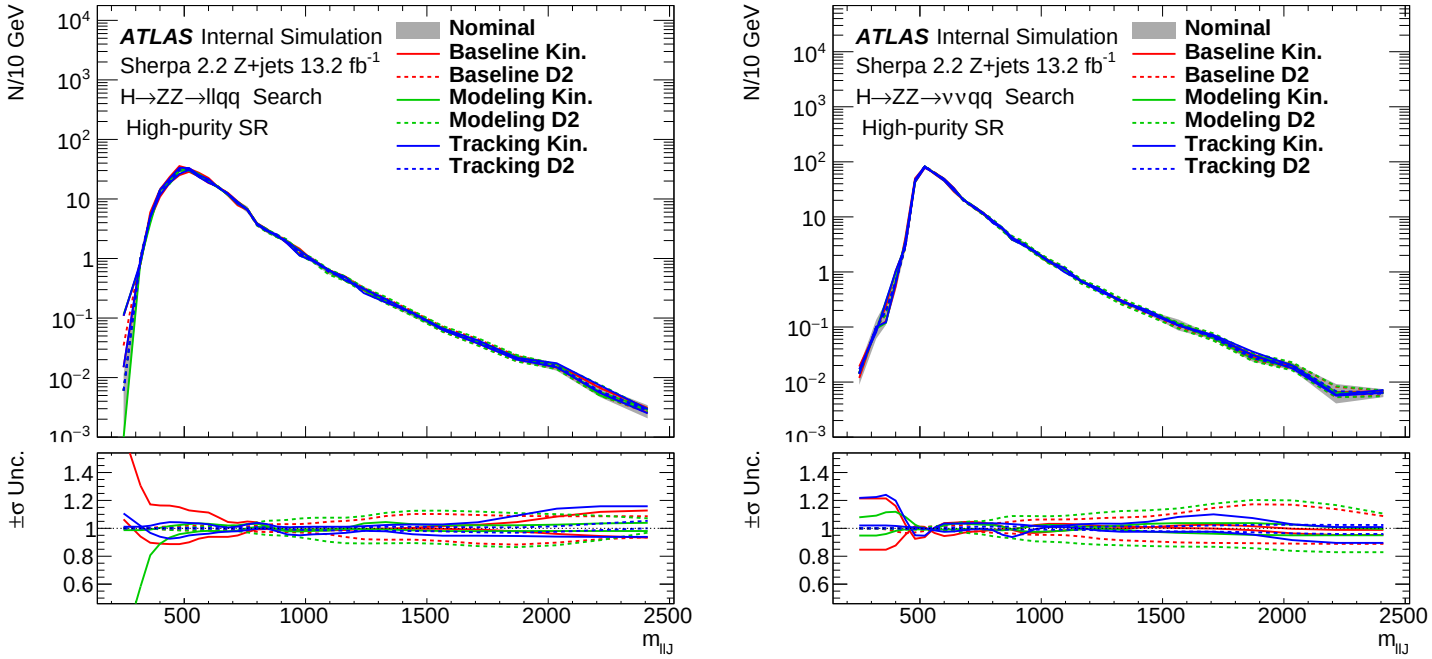

Figure 6.27: Systematic uncertainties associated with large-R jet scales in the high-purity SR of the (a) $\ell\ell qq$ and (c) $\nu\nu qq$ channels. Large-R uncertainties associated with scale are provided to the analyses combining the mass scale and energy scale uncertainties into a single fully-correlated "kinetic" term (solid) along with the $D_2^{(\beta=1)}$ energy correlation ratio scale (dashed).

Other Systematic Uncertainty

Small-R Jets The derivation of jet uncertainties on scale and resolution was outlined in Chapter 5. The dependence of the leading backgrounds on the small-R jet uncertainties on the resolved regime of the $\ell\ell qq$ channel was shown in Fig. 5.13 in Chapter 5 for the strongly reduced description. The jet energy scale in the central region used for the selection of signal jets has an uncertainty of 6% for p_{T} of 25 GeV and rapidly drops to about 1% for jets in the range 100 GeV to 1 TeV. The uncertainty on the jet resolution is under 1% for the same range.

Luminosity Uncertainty on the integrated luminosity is 2.1% for 2015 data set and 3.7% for 2016 data set. The methods used to obtain them were discussed in Chapter 3. The combined luminosity uncertainty for the 13.2 fb^{-1} in 2015+2016 is 2.8%. It is applied to all backgrounds and signal MC equally, and therefore enters the final limit entirely unaltered as it cannot be constrained by the fitting procedure. For the same reason it does not enter the uncertainty bands on the fit to distributions in individual signal and control regions.

Trigger The efficiency of lepton triggers are nearly 100% in the electron channel and 96% in the muon channel. Systematic uncertainties on the efficiency of the electron and muon triggers are evaluated using a tag and probe method [161] and are found to be negligible for these analyses although included in the uncertainties associated with each lepton channel. The $E_{\mathrm{T}}^{\mathrm{miss}}$ trigger efficiency is nearly 100% in the analysis event selection and also enters negligibly into the analysis.

Electrons Systematic uncertainties are derived from tag-and-probe studies with a selection of $Z \to ee$ decays and $J/\psi \to ee$, where one electron is selected on and the other candidate probe is tested to satisfy electron selection criteria [161]. The probe is used to evaluate reconstruction, identification, isolation,

and trigger efficiencies that produce scale factors used to correct MC to data. Uncertainties are evaluated by varying selection in the tag and probe analyses for each study, parametrized by electron E_{T} and η. The combined uncertainty for reconstruction and identification of electrons is about $\sim 1\%$ at 25 GeV and below 0.5% above 30 GeV. The uncertainties for isolation and trigger efficiency are $< 1\%$.

The calibration of electrons undergoes a similar procedure as that of jets [126]. Like the JES, electron energy scale is given an *in situ* correction from data-driven analysis after a MC-based calibration has been used to correct the energy scale. Systematic uncertainties are derived on the correction in an analogous way, benefiting from the narrow $J/\psi \rightarrow ee$ peak in the low-E_{T} region and otherwise using $Z \rightarrow ee$ decays. This results in very low uncertainties associated with electron scale, $\sim 0.1\%$.

Muons The efficiency scale factors correcting data and MC differences are also derived from studies with $Z \rightarrow \mu+\mu-$ in the higher-p_{T} ranges and $J/\psi \rightarrow \mu+\mu-$ in the low-p_{T} range [127, 162]. Uncertainty on muon reconstruction efficiency does not exceed 1% for the range considered, $p_{\mathrm{T}} > 25$ GeV. The uncertainty on isolation is $< 0.5\%$ for the range considered as is the uncertainty on the trigger efficiency. Systematic uncertainty on muons also considers sources related to the matching of the muon track to the primary vertex for which there are cuts on the impact parameters. And finally variations introduced on the inner detector (ID) tracks and muon spectrometer (MS) tracks to cover uncertainty associated with the *in situ* correction to muon resolution are introduced. The muon momentum scale is known to better than 0.1%.

$\boldsymbol{E}_{\mathbf{T}}^{\mathbf{miss}}$ The tracking soft term (TST) scale and resolution in the perpendicular and parallel directions have an uncertainty of about 5% [152, 153]. Uncertainties on the TST can only affect the $\nu\nu qq$ channel.

Flavor Tagging Uncertainties on the tagging efficiency of light, b, and c-jets after undergoing a weak eigenvector reduction similar to that discussed on the JES [163] result together in $\sim 10\%$ uncertainty affecting the $Z + bb$ sample in the tagged category of the ZZ-resonance searches.

Pile-up An uncertainty on the re-weighting of the MC samples by the NPV distribution to match the data set is included.

Signal Uncertainties Uncertainties associated with the PDF used to generate the signals in the analysis are generated by internal error sets in the PDF set and by taking the difference between PDF sets.

For the heavy Higgs signal, 52 internal variations in the CT10 PDF are used. The difference between the CT10 PDF and the the NNPDF30 and MSTW2008NLO is also studied. All uncertainties expressed on the $m_{\ell\ell jj}$ distribution sum in quadrature to about 1%. A scale uncertainty of $\pm 1\%$ for the full range of heavy Higgs mass is used–only the magnitude of the variation affects the narrow resonance.

The Graviton and HVT signal samples use the NNPDF23LO PDF set, which has an ensemble of 100 error PDFs. These variations added in quadrature to uncertainty based on comparison to Cteq6L1 and MSTW2008LO PDF sets suggest the 1% uncertainty applied to heavy Higgs samples is an accurate value for the W' and Graviton samples.

Uncertainty associated with Initial- and final-state gluon radiation (ISR/FSR) modeling is determined from systematic variations in Pythia 8 provided with the tunes used.

For Higgs signal samples, the AZNLO tune is used with Powheg+Pythia. AZNLO provides a set of 2 eigenvector variations. To cover the full range of PS uncertainties and uncertainties related to multiple parton interactions (MPI), the FSR scale is varied up and down by a factor of 2, along with variations of

the MPI cut-off.

Graviton and HVT signal samples use the A14 tune used with MadGraph + Pythia. The A14 tune optimizes 10 parameters corresponding to FSR, ISR and MPI which leads to 10 up and down variations. The ten up/down variations are reduced to the following: one for UE effects, one for jet structure effects, and three to cover aspects related to extra jet production. Again, since uncertainties are applied to narrow resonances, a variation capturing the magnitudes of combining these variations in quadrature is used. A flat uncertainty of 3% for Higgs signals and 5% for Graviton and HVT signals are used.

Summary

The impact of systematic uncertainties on the analysis is certainly not identical to their contribution prior to fitting all the regions. This section introduces groups of systematic uncertainties, and ranks them according to their influence on the constraint of the signal strength in the fit.

Many individual uncertainties undergo eigenvalue reductions or combinations assuming full correlation or no correlation prior to reaching the analyses. Furthermore, they are determined and grouped in various studies of performance resulting correlations of uncertainties, which can be non-trivial in a given analysis. This means that interpreting the impact of a given source of systematic uncertainty often means taking considering uncertainties in a logical group or after correlations have been studied.

To evaluate the impact of various uncertainties independent of the details of the fitting procedure or precise formulation of NPs, groups are identified based on the way they enter the analysis or on the general source. The final constraint on the signal presence is unsurprisingly dominated by the limited quantity of data taken in an early analysis. The amount of simulated MC often enters as a significant source of uncertainty. Care has been taken in analysis design never to allow this to be an

overwhelmingly dominant source of uncertainty, for example in the use of the truth tagging technique in the tagged selections of the $\ell\ell qq$ channel. However, being overly generous in the MC production is not in the budget priorities of ATLAS. Therefore the contribution to total uncertainty from MC statistics is often only just below the sum quadrature of other systematic uncertainty in the final analysis.

The focus here is to understand the greatest contributors to systematic uncertainty beside those mentioned that are purely statistical. The following discussion references the ggF channel of the heavy Higgs analysis. The groups considered by category are:

Jets Uncertainties on jets are in four groups, split between large-R and small-R jets and between all uncertainties on scale and on resolution. For large-R jets that includes the calibrated energy, mass, and $D_2^{(\beta=1)}$.

Leptons Uncertainties are split between muons and electrons, combining all efficiency and scale uncertainties for each.

Background Modeling All background modeling systematics are combined from all categories in each channel.

Background Normalization All free-floating normalizations on backgrounds constrained only by fit to all regions are combined.

Single NPs Luminosity and signal modeling are considered alone. One expects the nominal value entering the analysis to be expressed after the fit at a similar level as a ratio of the total uncertainty for signal modeling because it is only applied to signal. Likewise, the luminosity should be expressed mostly unchanged after the fit since it is applied to all backgrounds and signal.

Evaluating the contribution of a group of uncertainties to the total uncertainty is done by fitting with and without them. The added degrees of freedom from a given set of uncertainties increase the width of the local likelihood minima in the signal magnitude around the best fit value. By subtracting the width in quadrature determined with and without the set of NPs the associated uncertainty is determined taking into

	Unc. on μ,ggF $m_H = 700$GeV
Large-R Jet Resolution	18%
Large-R Jet Scale	13%
Alpha Modeling	9%
Background Normalization	6%
Electrons	6%
Muons	6%

Table 6.8: The dominant uncertainties on the ggF scalar signal hypothesis, $M_H = 700$GeV . The numbers represent the uncertainty relative to the total uncertainty. on the determination of signal cross section, μ.

full account the correlations within the set and within all other uncertainties.

A signal strength of 20 fb is injected into the MC background simulation at a heavy Higgs mass $m_H = 700$ GeV. The leading sources of systematic uncertainty are summarized in Table 6.8 for the $\ell\ell qq$ channel. Dominating the total systematic uncertainty are uncertainties related to large-R jets with background modeling also being a large contributor. At higher signal masses the uncertainty is even more dependent on large-R jet sources and at the lowest mass values in the range, small-R jets contribute significantly. The uncertainty in Table 6.8 is expressed as a fraction of the total uncertainty including data statistics. All systematic sources taken together are only about half the total width. The uncertainty entering the search with 13.2 fb^{-1}of data is therefore dominated by limited statistics and not by systematic sources. The leading source of systematic uncertainty is similarly dominated large-R jet scale and resolution in the $\nu\nu qq$ channel. Modeling is sub-dominant with roughly similar proportions in the final fit uncertainty.

This page intentionally left blank.

Chapter 7

Results

This chapter presents the results for the searches for the heavy Higgs, W', and graviton. Section 7.1 introduces the general approach taken in statistical modeling. Section 7.2 describes the methods used to test the signal hypothesis and set confidence limits. Section 7.3 describes the specific treatment of nuisance parameters and free parameters in the $\ell\ell qq$ and $\nu\nu qq$ channel fits. The limits set on the production cross section times branching ratio for each of the models considered are presented in Secs. 7.4 and 7.5.

A strictly frequentist approach is taken in the statistical interpretation of the data. A model is constructed encapsulating uncertainty from prior measurements and modeled distributions. The observed data is then compared to the distribution of sampling outcomes from the model to understand the significance of the data. The strategy used is inspired from statistical studies at ATLAS in Run 1 involving searches for the SM Higgs that have undergone some of the greatest scrutiny and benefited from abundant manpower and refinement. The statistical combination of several subchannels in these analyses outlined in Chapter 6 is similar to the problem taken up in the combination of independent channels in the search for the SM Higgs [164][1]. The official results of this thesis are presented separately in the $\ell\ell qq$ and $\nu\nu qq$ channels in the form in which they have been made public [150], but both models have been written by the author and combined personally in anticipation of future releases of

[1]Where possible the notation in the following discussion has been matched to this widely read study.

combined results in later Run 2 studies.

7.1 Statistical Model

This analysis combines several sub-channels indexed by c whose event selections are split on the selection of jets. Sub-channels in the $\ell\ell qq$ channel make use the $m_{\ell\ell jj}(m_{\ell\ell J})$ 4(3)-body mass distribution and sub-channels in the $\nu\nu qq$ channel make use of the M_T distribution of signal candidates. The variable x is used in the following general discussion to represent both discriminants and the associated probability density function (PDF) is written $f(x|\alpha)$ with α representing both the theoretical parameters like the signal mass and the nuisance parameters (NP) incorporating systematic uncertainties.

The model desired expresses the probability for obtaining n events in a given selection where the discriminating variable measured in event e is $x_e \in \{x_1, \ldots, x_n\} = \mathcal{X}$. The number of predicted events $\nu = \nu(\alpha)$ is parametrized by α. The Poisson distribution[2] provides the correct distribution associated with counting. Expressed as the probability of repeatedly sampling the PDF, the common expression for the marked Poisson model is obtained,

$$f(\mathcal{X}|\alpha) = \text{Pois}(n|\nu(\alpha)) \prod_{e=1}^{n} f(x_e|\alpha). \tag{7.1}$$

The PDF $f(x|\alpha)$ is the weighted sum of the individual processes taken incoherently, for example as it was shown (MC-sampled) in the control regions with the best fit values and weights applied, Figs. 6.16, 6.17, 6.15, 6.18, 6.22, 6.23, 6.24 in Chapter 6,

$$\nu(\alpha) f(\mathcal{X}|\alpha) = \sum_{k \in \text{processes}} \nu_k(\alpha) f_k(\mathcal{X}|\alpha). \tag{7.2}$$

The fit is made to all sub-channels (all signal and background regions) simultaneously, resulting in a single expression using all available data, $\mathcal{X}_{\text{tot}} = \{\mathcal{X}_1, \ldots, \mathcal{X}_m\}$,

[2] $\text{Pois} = \nu^n e^{-\mu}/n!$

where m is the number of regions/sub-channels in the analysis. One works with the PDF as a whole then,

$$f_{\text{tot}}(\mathcal{X}|\alpha) = \prod_{c=1}^{m} \left[\text{Pois}(n_c|\nu_c(\alpha)) \prod_{e=1}^{n_c} f_c(x_c e|\alpha)\right]. \tag{7.3}$$

Equation 7.3 is interpreted as a likelihood $L(\alpha)$ if $\mathcal{X}$ is given. The the usual maximum log-likelihood is then,

$$-\ln L(\mu) = \nu(\alpha) + \ln n! - \sum_{e=1}^{n} \ln[\nu(\alpha)]. \tag{7.4}$$

The distributions $\mathcal{X}_c$ are binned in these analyses, so Eq. 7.2 can be explicitly stated in terms of individual bins b and their predicted number of events $\nu_b(\alpha)$ ($\nu(\alpha) = \sum_{b\in\text{bins}}^{n} \nu_b(\alpha)$) to provide the clearest understanding of the model implemented,

$$f(\{n_b\}|\alpha) = \text{Pois}(n|\nu(\alpha)) \prod_{b\in\text{bins}} \frac{\nu_b(\alpha)}{\nu(\alpha)} \tag{7.5}$$

The parameter of interest is the signal strength μ which is a scale factor defining the total signal cross section. A $\mu = 0$ indicates there is no presence of signal. The signal PDF is parametrized by the signal mass m_H (or $m_{W'}$ or m_G) and the signal and backgrounds are affected by the set of NPs denoted by θ. The general parameter set entering the analysis is $\alpha = (\mu, m_H, \theta)$.

Auxiliary Measurements

NPs were introduced in Chapter 5 where they were derived from uncertainties entering the *in situ* calibration. They depict any source of uncertainty in the fit including background normalization, reconstruction efficiencies, scales and resolutions, luminosity, and theoretical modeling. A NP communicates an auxiliary measurement of a parameter $\alpha_p \in \theta$ that was formulated as a likelihood fit (or some best fit) to make a measurement, typically on data in ATLAS through calibrations, efficiency, or validation studies,

$$f_{\text{aux}}(\mathcal{X}_{\text{aux}}|\alpha_p, \alpha'). \tag{7.6}$$

Unless the auxiliary measurement is obtained through a control region (able to be identically represented as a sub-channel of the analysis) an estimate of α_p is provided by the auxiliary measurement a_p along with a standard error σ_p resulting in the approximation,

$$f_{\mathrm{p}}(a_p|\alpha_p, \sigma_p), \tag{7.7}$$

known as a constraint term. A Gaussian is typically used to communicate the constraint term to the analysis, $f_{\mathrm{p}}(a_p|\alpha_p, \sigma_p) = \mathrm{gauss}(a_p|\alpha_p, \sigma_p)$. However, this is an unnatural choice for some parameters which are intrinsically positive such as those that are normalization factors and scale uncertainties. In these cases a positive-definite distribution is used to model the constraint term, the log-normal distribution:

$$f_p(a_p|\alpha_p) = \frac{1}{\sqrt{2\pi}a_p \ln(1+\sigma_p/a_p)} \exp\Big[-\frac{\ln^2(a_p/\alpha_p)}{2\ln^2(1+\sigma_p/a_p)}\Big], \tag{7.8}$$

where σ_p/a_p is the relative uncertainty from the observed auxiliary measurement.

Constraint terms are provided to the analysis as up and down variations, $\alpha_p = a_p \pm \sigma_p$, and are in general not symmetric. The binned parametric PDF $f(x|\alpha)$ is formed by using a piecewise exponential function [165] to interpolate between the up and down variations due to the constraint term in each bin. A maximum likelihood fit in the full parameter space can obtain a continuous value from the provision of only an up and down variation to the analysis in this way. The set of NPs constrained by auxiliary measurements are known as global observables $\mathcal{G}$.

Uncertainty associated with limited MC statistics enter as bin-by-bin scale factors labeled γ_{cb}. Also encompassed in this bin-by-bin parameter are uncertainties entering only as bin-to-bin shape uncertainties within a given sub-channel. Luminosity enters as a global constraint term, $G(L_0|\lambda, \sigma_L)$. Unconstrained normalization factors enter as a product ϕ_{ck} parametrized by sub-channel c and process k.

$$\phi_{ck} = \prod_{p\in\mathcal{N}} \phi_p, \tag{7.9}$$

where $\mathcal{N}$ is the set of all unconstrained factors on given sample in given channel. There are also normalization constraints on samples whose normalization has been determined from other studies, η_k. Most importantly are the fully parametrized sample histograms σ_{ckb} built from the nominal samples and interpolation between the full up and down NP variations α_p. The expected number of events in a given bin can be broken down into these components,

$$\nu_{cb}(\phi_c, \alpha_p, \gamma_{cb}) = \sum_{k \in \text{samples}} \lambda \gamma_{cbk} \phi_{ck}(\alpha) \eta_{ck}(\alpha) \sigma_{ckb}. \tag{7.10}$$

The complete description of the fit as the likelihood product over bins is then,

$$f_{\text{tot}}(n_{cb}, a_p | \phi_c, \alpha_p, \gamma_{cb}) = \prod_{c \in \text{sub-channels}} \prod_{b \in \text{bins}} \text{Pois}(n_{cb} | \nu_{cb}) \cdot G(L_0 | \lambda, \sigma_L) \cdot \prod_{p \in \mathcal{S}, -} f_p(a_p | \alpha_p, \sigma_p). \tag{7.11}$$

7.2 Statistical Methods

The following builds the method for calculating p-values and translating them into limits set on signal cross sections. The method for calculating p-values is based on the profile likelihood ratio test statistic. The complete model, Eq. 7.11, is interpreted as a likelihood function by fixing the data set taken,

$$L(\mu, \theta; m_H, \mathcal{X}_{\text{tot}}, \mathcal{G}) = f_{\text{tot}}(\mathcal{X}_{\text{tot}}, \mathcal{G} | \mu, m_H, \theta), \tag{7.12}$$

or in short $L(\mu, \theta)$.

The profile likelihood ratio $\lambda(\mu)$ is defined as the ratio of the maximum likelihood of the fit under two conditions,

$$\lambda(\mu) = \frac{L(\mu, \hat{\hat{\theta}}(\mu))}{L(\hat{\mu}, \hat{\theta})} \tag{7.13}$$

The values $\hat{\mu}$ and $\hat{\theta}$ in the denominator are defined to be those that maximize the likelihood function $L(\mu, \theta)$. The conditional maximum likelihood function $L(\hat{\mu}, \hat{\theta})$

appearing in the numerator is the value of θ that maximizes the likelihood function when μ is fixed. The valid range of interpretation for μ in these searches is only in $\mu \geq 0$ range, but one allows μ to be negative for at least two reasons:

1. Sampling in the background-only case will produce values of $\hat{\mu}$ that are distributed around $\mu = 0$ and therefore in practice one expects to observe this result half the time in a number of independent tests. The scan of the signal mass parameter in these analyses provides these multiple independent tests and one expects the observed confidence limits to fluctuate around the expected limits.
2. p-values larger than 50% have a clear statistical interpretation and provide a confidence interval for μ no matter if $\hat{\mu} < 0$. A deficit with large statistical significance may indicate a need to re-evaluate the modeling of backgrounds.

A value of $\hat{\mu} < 0$ indicates a deficit of expected events, which is not a problem. Enforcing $\hat{\mu} \geq 0$ is only done in the calculation of the likelihood ratio, where the likelihood calculated in the denominator saturates at $\hat{\mu} = 0$, giving,

$$\tilde{\lambda}(\mu) = \begin{cases} \frac{L(\mu, \hat{\hat{\theta}}(\mu))}{L(\hat{\mu}, \hat{\theta})} & \hat{\mu} \geq 0 \\ \frac{L(\mu, \hat{\hat{\theta}}(\mu))}{L(0, \hat{\hat{\theta}}(0))} & \hat{\mu} < 0 \end{cases} \tag{7.14}$$

A test statistic is used to characterize the significance of the hypothesis that signal events produced at a rate μ from the alternate hypothesis that they are produced at different rate μ'. It is defined with the log of the likelihood ratio $\tilde{\lambda}$. An added sign is introduced to retain p-values larger than 50%, giving the definition,

$$\tilde{q}_{\mu} = \begin{cases} -2 \ln \tilde{\lambda} & \hat{\mu} \geq 0 \\ +2 \ln \tilde{\lambda} & \hat{\mu} < 0 \end{cases} \tag{7.15}$$

In practice one varies the free parameter μ with $\mu' = \hat{\mu}$ for $\hat{\mu} \geq 0$ and 0 otherwise.

CLs Technique

Upper limits on the signal presence μ are calculated with the CL_s procedure [166]. CL_s here utilizes the the PDF of the test statistic $f(\tilde{q}_\mu|\mu', m_H, \theta)$ to determine p-values, obtained from the upper tail of the distribution. The p-value based on the observed distribution is sought,

$$p_\mu = \int_{\tilde{q}_{\mu,\mathrm{obs}}}^{\infty} f(\tilde{q}_\mu|\mu, m_H, \hat{\hat{\theta}}(\mu, \mathrm{obs}))d\tilde{q}_\mu. \tag{7.16}$$

The conditional maximum likelihood estimate $\hat{\hat{\theta}}(\mu, \mathrm{pbs})$ is made with observed data. The test statistic $\tilde{q}_\mu$ considers the data $\mathcal{X}$ and global observables $\mathcal{G}$ to be measured quantities that would obtain different values in repetition of the experiment according to the complete model Eq. 7.11. The limit is calculated with the quantity CL_s, defined as the ratio,

$$\mathrm{CL}_s(\mu) = \frac{p_\mu}{1 - p_b}, \tag{7.17}$$

where the p-value p_b is the p-value derived from the background-only hypothesis,

$$p_b = 1 - \int_{\tilde{q}_{\mu,\mathrm{obs}}}^{\infty} f(\tilde{q}_\mu|0, m_H, \hat{\hat{\theta}}(\mu = 0, \mathrm{obs}))d\tilde{q}_\mu. \tag{7.18}$$

The CL_s upper limit on μ is obtained by solving $\mathrm{CL}_s(\mu_{\mathrm{up}}) = 5\%$. A value of $\mu > \mu_{\mathrm{up}}$ is considered to be excluded with 95% confidence by the data.

Expected Limits

The upper-limit determined from data is compared to the median upper limit expected from the background-only hypothesis. The expected upper limit is defined $f(\mu_{\mathrm{up}}|0, m_H, \hat{\hat{\theta}}(\mu = 0, obs))$, so it is dependent on observed data through the constrained NPs assuming $\mu = 0$. The expected limits are expressed with bands representing $\pm 1, 2\sigma$ range implying in multiple retrials the evaluation of the expected limit would be distributed accordingly. The ranges are determined,

$$\int_0^{\mu_{\mathrm{up}} \pm 1\sigma} f(\mu_{up}|0, m_H, \hat{\hat{\theta}}(\mu = 0, \mathrm{obs}))d\mu_{\mathrm{up}} = \Phi(\pm 1), \tag{7.19}$$

where Φ is the normal curve cumulative density function. The mean and variance of the expected limit does not need to be determined by an ensemble of simulated data sets. Rather, a single representative data set referred to as the "Asimov" data set is used to obtain the expected $\hat{\mu}$ and its variance. A formal mathematical justification for use of the Asimov data set can be found here [167]. The Asimov data set obtains exactly the expected number of events in every bin determined by the model with the nominal NPs–this is known as the asymptotic limit with zero fluctuations. The test statistic evaluated on the Asimov data set $\tilde{q}_{\mu,A}$ is enough to determine the upper limits and estimate the variance of $\hat{\mu}$ around the true value μ', $\sigma^2_{\mu'}$. The expected upper limit is determined as,

$$\mathrm{CL}_s = \alpha = 0.05 = \frac{1 - \Phi(\sqrt{\tilde{q}_\mu})}{\Phi(\sqrt{\tilde{q}_{\mu,A}} - \sqrt{\tilde{q}_\mu})} \tag{7.20}$$

The estimate of variance is given by,

$$\sigma_{\mu'} \approx \frac{\mu - \mu'}{\sqrt{\tilde{q}_{\mu,A}}}. \tag{7.21}$$

and the $\pm N\sigma$ expected error bands are,

$$\mu_{\mathrm{up}+N\sigma} = \sigma \cdot (\Phi^{-1}(1 - \alpha\Phi(N)) + N). \tag{7.22}$$

Significance

The significance of an excess expresses the probability of observing a larger $\hat{\mu}$ given the background-only hypothesis,

$$p_0 = \int_{\tilde{q}_{\mu=0,\mathrm{obs}}}^{\infty} f(\tilde{q}_{\mu=0}|0, m_H, \hat{\hat{\theta}}(\mu = 0, \mathrm{obs}))d\tilde{q}_0. \tag{7.23}$$

The two p-values p_0 and p_b differ only in that the value of μ is fixed to 0 in $\tilde{\lambda}(\mu)$ to obtain the significance. This is optimal if the intent is to exclude the background-only hypothesis, as this fixes the numerator of the likelihood ratio to be evaluated given the data with $\hat{\hat{\theta}}(\mu = 0)$.

Look-elsewhere effect

Searches are made with a scan over a large signal mass range where for each signal mass a test is made to determine the significance. The greater number of independent tests made, the larger the chance to observe spuriously a significant result. This should reduce the significance of the find–this is known as the "look elsewhere effect." Values of p_0 that do not take into account the global scope of the search are referred to as *local*. After correction for the look elsewhere effect, the p-value is referred to as *global*. Making this correction is not as simple as considering the number of signal mass points in the search, because the width of the signal is not taken into account.

A procedure is used to estimate the number of independent trials which counts the average number of up crossings of $\tilde{q}_{\mu=0}(m_H)$, the likelihood ratio, at a lower threshold over the search range [168]. The global test statistic is associated with the signal mass value $\hat{m}_H$ obtaining the maximum value of the test statistic in the search in the full range, $\max[\tilde{q}_{\mu=0}(m_H)]$. The average number of up-crossings for two values u and u_0 are related statistically,

$$\langle N_u \rangle = \langle N_{u_0} \rangle e^{-(u-u_0)/2}, \tag{7.24}$$

so an estimate for the number of up-crossings of the high level u can be determined by counting the number at the lower level u_0. This allows the highest local p-value to obtain a factor reducing it to represent the p-value for the global test.

7.3 Implementation

This section outlines the details of the specific implementation of the statistical analysis. Equation 7.11 allows a sophisticated and flexible treatment of NPs in the fit. The organization of the floating normalization parameters in the fit is outlined along with details of the complete list of NPs entering the fit. The statistical method for the smoothing of noisy NPs is discussed, as well as a number of other minor

Region	$\nu\nu qq$ channel	
	Merged	
	high-purity	low-purity
SR	M_T	M_T
ZCR	M_T	M_T
WCR	M_T	M_T
TopCR	M_T	M_T

Table 7.1: Summary of regions entering the binned profile likelihood fit of the $\nu\nu qq$ channel. Regions of the fit are identical in all three searches for the H,W', and G.

treatments to MC binned distributions and NPs to enable an efficient fit. Studies have been extensively performed by the author to validate the choices made in the implementation but are beyond the interest of the reader. The focus here will be to concisely define the fit in its final form.

The statistical treatment in these analyses uses the combined profile likelihood fit to binned discriminants in all categories and regions simultaneously. The $\nu\nu qq$ and $\ell\ell qq$ channels are not combined in this presentation and each channel has a separate fit.

Floating Normalization

All major backgrounds in each of the searches are provided with a designated CR intended to constrain the floating normalization factors ϕ_{ck}.

In the $\nu\nu qq$ channel the structure of the fit is identical in the heavy Higgs, HVT W', and graviton searches. Table 7.1 shows the regions entering the $\nu\nu qq$ fit and the discriminant used in each region.

There are four floating parameters in the fit in the $\nu\nu qq$ channel:

Signal strength μ the parameter of interest, applied to the signal sample is correlated between all regions of the fit.

***Z*+jets norm** Applied to the Z+jets sample, correlated in every region.

Cat.	Region	$llqq$ channel			
		Resolved		Merged	
		untagged	tagged	high-purity	low-purity
ggF	SR	$m_{\ell\ell jj}$	$m_{\ell\ell jj}$	$m_{\ell\ell J}$	$m_{\ell\ell J}$
	ZCR	$m_{\ell\ell jj}$	$m_{\ell\ell jj}$	$m_{\ell\ell J}$	$m_{\ell\ell J}$
	TopCR	—	$m_{\ell\ell jj}$	—	—
VBF	SR	$m_{\ell\ell jj}$		$m_{\ell\ell J}$	$m_{\ell\ell J}$
	ZCR	$m_{\ell\ell jj}$		$m_{\ell\ell J}$	$m_{\ell\ell J}$

Table 7.2: Summary of the regions entering the likelihood fit and the distribution used in each. Rows with "—" indicate that the region is not included in the fit. "SR" stands for the signal regions and "CR" for the control regions.

W+jets norm Applied to the W+jets sample, correlated in every region.

Top norm Applied to the $t\bar{t}$ samples, correlated in every region.

The choice of this scheme was made over another reasonable choice to provide individual normalizations to the high-purity and low-purity regions, which would result in additional three NPs. Agreement in the $D_2^{(\beta=1)}$ variable is found to be extremely good so there is no reason to split the background normalizations between the high and low-purity categories as it turns out. It was tested to ensure that fitting in the case of a split between high and low-purity regions would result in agreement between normalization factors obtained on Z+jets, W+jets, and $t\bar{t}$ samples. They were found to agree well within their respective uncertainties. A single normalization parameter applied to the sample as a whole results in a lower statistical uncertainty in constraining the normalization of the sample.

The regions entering the fit in the $\ell\ell qq$ channel are dependent on the search. The most complex of which is the heavy Higgs search. Table 7.2 shows the regions and discriminants entering the search for the heavy Higgs in the ggF and VBF production channels. The other searches are reductions of the heavy Higgs scheme. There are seven floating normalization parameters in the heavy Higgs search:

Signal strength μ^{ggF} the parameter of interest in setting limits on the ggF pro-

duction, applied to the ggF signal sample in all regions of the analysis including those with VBF-tagged jets.

Signal strength μ^{VBF} the parameter of interest in setting limits on the VBF production, applied to the VBF signal sample in all regions of the analysis including those entering the ggF category of the analysis.

$Z + l$ norm (resolved) factor applied to the $Z + l$ sample to all regions in the resolved regime including regions in the VBF-tagged category.

$Z + b$ norm (resolved) factor applied to the $Z + bb$ sample in all regions in the resolved regime including regions in VBF-tagged category.

Z+jets norm (merged) factor applied to all $Z + jets$ samples in all regions of the merged regime including those with VBF-tagged jets.

Top norm (resolved) factor applied to the $t\bar{t}$ sample in all regions of the resolved regime including the VBF category.

Z*+jets *VBF/ggF ratio Due to the less well-modeled $Z + 4$ jets phase space in the MC simulation, an effect clearly visible in the distributions of the VBF-tag criteria, the VBF-tag cuts have different efficiency in data and MC. The implicit assumption is that the differences in distributions between data and MC of the additional jets on which the VBF-tag cuts are made do not affect notably the two hard central jets entering the signal mass windows and signal discriminant. If this is the case, one additional scale factor applied to all Z+jets samples in all VBF-tagged regions to compensate for the difference in efficiency will suffice. Multiple schemes were tested to check the validity of this assumption and all were found to be in agreement (although some only just). Given the limited MC statistics entering the VBF channels and the large modeling uncertainties applied to the VBF signal regions from the α-ratio a single parameter is found to be optimal even if there is some evidence that it is a slight under-parametrization. The value of the VBF/ggF ratio is not expected to be

consistent with 1.

The resolved analysis keeps track of each of the Z+2 jets products by the flavor of each jet produced in association with the neutral vector boson. The background is dominated in the tagged category by Z produced in association with two b-jets. The background in the untagged category is dominated by Z produced in association with two light-jets. The analysis can constrain tightly the normalization of both these backgrounds from the resolved ZCRs.

The RS graviton search is made only in the ggF channel. There is no identifying of VBF-tag jets and all events passing the signal criteria enter the ggF channels, but it is otherwise identical in structure. There is consequently no VBF/ggF ratio parameter and no μ^{VBF} parameter.

The HVT W' search selects on the hadronic decay of the W boson. Consequently, the tagged and untagged categories of the resolved regime are unified. The $Z+l$ and $Z+b$ normalization factors are replaced with a single Z+jets normalization applied to all regions of the resolved regime. The structure of normalization parameters is otherwise identical to the RS graviton search.

Nuisance parameters with prior constraint

Nuisance parameters constrained by auxiliary measurements entering the analysis belong to three categories: full up/down NPs entering the parametrization of the sample histogram α_p, sample normalization constraints determined by outside measurements η_k, and shape-only parameters affecting the distribution shape within a given region γ_{cb}.

Many of the important systematic uncertainties and their sources were discussed in Chapter 6. Here the NPs will be be summarized as they enter the fit. Some less significant sources are introduced without previous mention–in all cases they have minimal impact. All NPs are expressed in both $\ell\ell qq$ and $\nu\nu qq$ channels except

the modeling uncertainties. Modeling uncertainties enter the fit as a shape-only uncertainties. This is a formality since all are applied to samples that have designated CRs for normalization. Modeling parameters are:

ℓℓqq 7 NPs, applied independently to each of the SRs in the ggF+VBF Higgs analysis. Likewise for the graviton analysis there are 4 NPs, and for the HVT analysis there are 3. All are derived from the data-driven α-ratio technique discussed in Chapter 6.

νννqq 11 NPs, correlated for all regions within a given sample. 3 $t\bar{t}$, 4 W+jets, and 4 Z+jets NPs are derived from generator scale variations and generator-generator comparison.

There are a number of samples that enter minimally into the analysis selections, including single top processes, SM diboson processes, and some $Z+jj$ samples in the $\ell\ell qq$ analysis where they separately enter the fit in the resolved regime. The remaining $Z+jj$ samples that are poorly constrained in the fit are given uncertainties from 12% to 30% based on truth level studies between Sherpa and Alpgen +Pythia. It is not necessary to constrain these further in the analysis due to the similar shape with $Z+ll$, although it should be done in future iterations of the analysis. About 3% of top quark background is from single-top processes. Normalization uncertainties were obtained by varying the renormalization and factorization scales, the strong coupling α_s in showering, and the PDF eigenvectors. This results in 7% uncertainty in the Wt-channel, 4% in the t and s-channels. The SM diboson samples WW, ZW, and ZZ are each given a 6% uncertainty obtained from from various measurements at ATLAS [169] and phenomenological studies [170].

The remaining NPs, discussed in Chapter 6, are the most significant and enter the full histogram parametrization. MC statistical uncertainties are represented as bin-by-bin uncorrelated NPs γ_{cb}. A threshold of 5% is taken on inclusion of the MC statistical uncertainty. This threshold is standard for binned analyses in ATLAS and

is done primarily to reduce unnecessary dimensionality in the fit.

Smoothing

Uncertainties on reconstructed objects are propagated through the analysis in two different ways, either by shifting weights or by shifting kinematic values. For example, uncertainties related to efficiency belong to the former. Scales and resolution belong to the latter. In the latter case statistical uncertainty enters the NP up/down variation in the binned distributions through migration of events in and out of the selection. In many cases the statistical component entering the variation is a dominant component. This effect is unphysical and given the number of NPs entering the fit creates arbitrary DoFs that the fit exploits to match random fluctuations in data.

To overcome this problem, a histogram smoothing procedure is used that merges consecutive bins in the MC templates. Local extrema that are not statistically significant in the up and down variation are merged until they become statistically significant given the MC statistical uncertainties. The resulting shift is applied equally to bins that have been merged. This type of smoothing is applied to some lepton NPs and all the jet NPs.

Signal Interpolation

Signal interpolation is performed to reduce the number of MC signals that must be generated in the scan of a mass range. A method employing the algorithm derived here [171] constructs a binned cumulative density function (CDF) of a signal mass in between the signal masses of two MC generated binned CDFs. The intermediate CDF is constructed through linear interpolation of the values obtained from a constant sampling of $\mathrm{CDF}^{-1}(x)$ for both generated samples. The interpolated normalization of the resulting PDF is obtained by a fit to the integral of the binned histograms. As implemented, the interpolation procedure increases the statistical uncertainty of the

bins of the interpolated sample. This is just perceptible as bumps in the final limits on interpolated samples because the MC signal samples are small, $\sim 10^4$ events and MC uncertainty enters the NPs of the fit.

Blinding

One critical aspect of a proper interpretation of frequentist analyses such as these is to ensure that a fair roll of the die has been made. The method of a blinded search is employed to ensure that the analysis is not manipulated to the observed data. The necessary interpretation of the data as a sampling of a fixed distribution is then no longer a valid one. To combat tuning the analysis to the observed data the signal regions of the analysis are not to be observed until all aspects of the analysis have been fixed. This includes fixing the most mundane details, including precise bin edges for every region and the complete fitting scheme.

When ATLAS is satisfied that the data are understood in the CRs after a background only fit then the signal regions are revealed. At this point the full fit is made and the results of the statistical analysis calculated.

7.4 Results from the $ZV \to \ell\ell qq$ search

This section presents the main results of the searches in this thesis in the $\ell\ell qq$ channel. Searches are made for the heavy Higgs, HVT W', and RS graviton. The search for the heavy Higgs has been made allowing for an unconstrained relative production cross section between the ggF and VBF channels.

In testing the signal hypothesis of ggF H, the VBF H signal becomes a background present in the analysis. There is no prior constraint on the cross section of the heavy VBF H production σ_{VBF} in the search for the heavy Higgs in the ggF category. Luckily it is precisely the purpose of the VBF category signal regions to make this

constraint. The three signal regions (resolved, high-purity, and low-purity) for events with VBF-tagged jets act as control regions for the normalization of the Higgs signal produced in the VBF production channel. While a small but non-negligible fraction of VBF signal events enter the ggF signal regions and vice versa, the analysis constrains the normalization of the signal in the other production channel tightly. The limits have been shown to be independent of the presence of the other signal in the search. The presence of the other production channel in each category of the analysis is constrained to less than 1% that of the intended signal after fit. The searches for the W' and G are made independently in their single production channel.

The results of the background-only fit to the $H \to ZZ$ search suggest an excellent description of data by MC. The normalization factor applied to the Z+jets sample obtains a value of 1.07 ± 0.05 in the merged regime and 1.09 ± 0.06 in the resolved regime. The normalization of $t\bar{t}$ in the resolved regime is 1.06 ± 0.09. These normalizations are obtained from the purest control regions in the analysis. Therefore, the excellent agreement among them centered just above 1. suggests the possibility that the integrated luminosity has been slightly underestimated. It may also be an indication of deviation of the MC k-factors being off by a few percent, although variation would not be correlated between $t\bar{t}$ and Z+jets samples. The normalization factor on the $Z \to bb$ background is found to be 1.00 ± 0.11. It is constrained only by the tagged regions of the analysis. The requirement for 2 b-tags results in limited statistics. This coupled with the significant presence of $t\bar{t}$ and the tagging efficiency uncertainty limit the degree of constraint on this background in the current configuration. The ratio VBF/ggF applied to the Z+jets samples entering the VBF-tagged category settles at 0.83 ± 0.08 in the fit. The tight constraint of this factor is an indicator that ample data are collected in Run 2 at $\sqrt{s} = 13\ TeV$ already to provide a differential cross section (in η, p_{T}) of Z production processes in association with 3, 4 and possibly more jets. Such a study would provide a valuable resource for continuing exotic searches

	Signal regions			
Z+jets	576 ± 22	1230 ± 33	409 ± 18	19900 ± 140
Diboson	49 ± 7	51 ± 5	54 ± 6	670 ± 40
Top quark	4 ± 1	5.9 ± 1.0	131 ± 6	291 ± 28
Total background	629 ± 22	1287 ± 34	594 ± 18	20861 ± 140
Data	606	1270	608	20857
H (400 GeV)	1.6 ± 0.2	4.3 ± 0.7	107 ± 6	626 ± 21
H (700 GeV)	168 ± 4	88.2 ± 2.9	20.0 ± 1.2	71.4 ± 3.3
H (1600 GeV)	35.9 ± 0.8	24.0 ± 0.6	1.00 ± 0.09	1.60 ± 0.08

Table 7.3: Numbers of events predicted from background processes and observed in the data in the four signal regions of the ggF $H \to ZZ \to \ell\ell qq$ search from the background-only fit of both signal and control regions. The numbers of signal events expected from a Higgs boson at 400 GeV, 700 GeV, and 1600 GeV are also shown. The signal yields are calculated assuming $\sigma \times$ BR values of 400 fb at 400 GeV, 100 fb at 700 GeV, and 20 fb at 1600 GeV. The uncertainties combine statistical and systematic contributions. The background uncertainties are posterior to the fit.

and an important constraint for generators.

The modeling uncertainties provided by the α-ratio technique individually to each SR are found to be distributed within $\pm 1\sigma$ of their nominal value. This indicates that shape as well as normalization has been well-modeled in each of the signal regions– one would not be surprised to find the α-ratio NPs pulled to $+1\sigma$ considering their interpretation. They appear to be randomly distributed about 0, four above and three below.

The number of events in the SRs of the ggF category for the fit under the background-only hypothesis is shown in Table 7.3. The level of agreement found in the predicted and observed backgrounds is 1σ. Taken in context with the observed agreement in the CRs, this essentially indicates that modeling of the dijet mass distribution is adequate to the level of accuracy necessary to support the fundamental strategy of using the side-bands of the dijet mass to normalize the Z+jets background in the SR. Uncertainty associated with modeling does enter the dijet mass distribution through jet uncertainties. The distributions of the final discriminant in

the resolved SRs of the ggF category are found in Fig. 7.1. The final discriminants in the SRs of merged regime of the ggF category are in Fig. 7.2. No large deviations from the predicted behavior of the distributions is observed in either the resolved or merged regimes. The largest excess is observed in the untagged category of the resolved regime at mass of approximately 500 GeV. The corresponding maximum in $\tilde{q}_0$ is determined to have a local significance of 2.7σ and a global significance of 1.4σ.

The distribution of the final discriminant in the resolved SR in the VBF category is shown in Fig. 7.4. The merged SRs of the VBF category are shown in Fig. 7.3. The data and MC agree well after the fit and there are no significant excesses. The first bin of Fig. 7.4 has a high pre-fit value–this occurred from being in a transitional p_{T} region of the MC Z+jets description where only a couple MC events were simulated and given very high weights. The associated MC statistical uncertainty. was $\sim 50\%$ before fit and is constrained afterward.

Distributions of the final discriminant in the SRs of the HVT W' search are found in the Appendix. There are no major excesses observed in the data. The data at $m_{\ell\ell J}$ of 1200 are in slight excess (obtaining a global significance of 1.3σ), which was also apparent in the Higgs search although less significant there. The Appendix also includes the fit ZCR distributions in the W' search.

Distributions of the final discriminant in the SRs of the RS graviton search are in the Appendix along with the ZCRs. No major excesses are observed, although several of the same local features are apparent due to the similarity between analyses. The deficit at a mass $m_G = 850$, visible in the merged SRs was only just apparent in the W' and Higgs searches but is rather notable here. Due to the wide mass range scanned in the searches it is not of great concern to see such a feature but warrants attention and quantification. The deficit has a global significance of 2.8σ. With the ongoing collection of data at ATLAS, if it is representative of a real mis-modeling or somehow an interference term it will grow in significance in 2017.

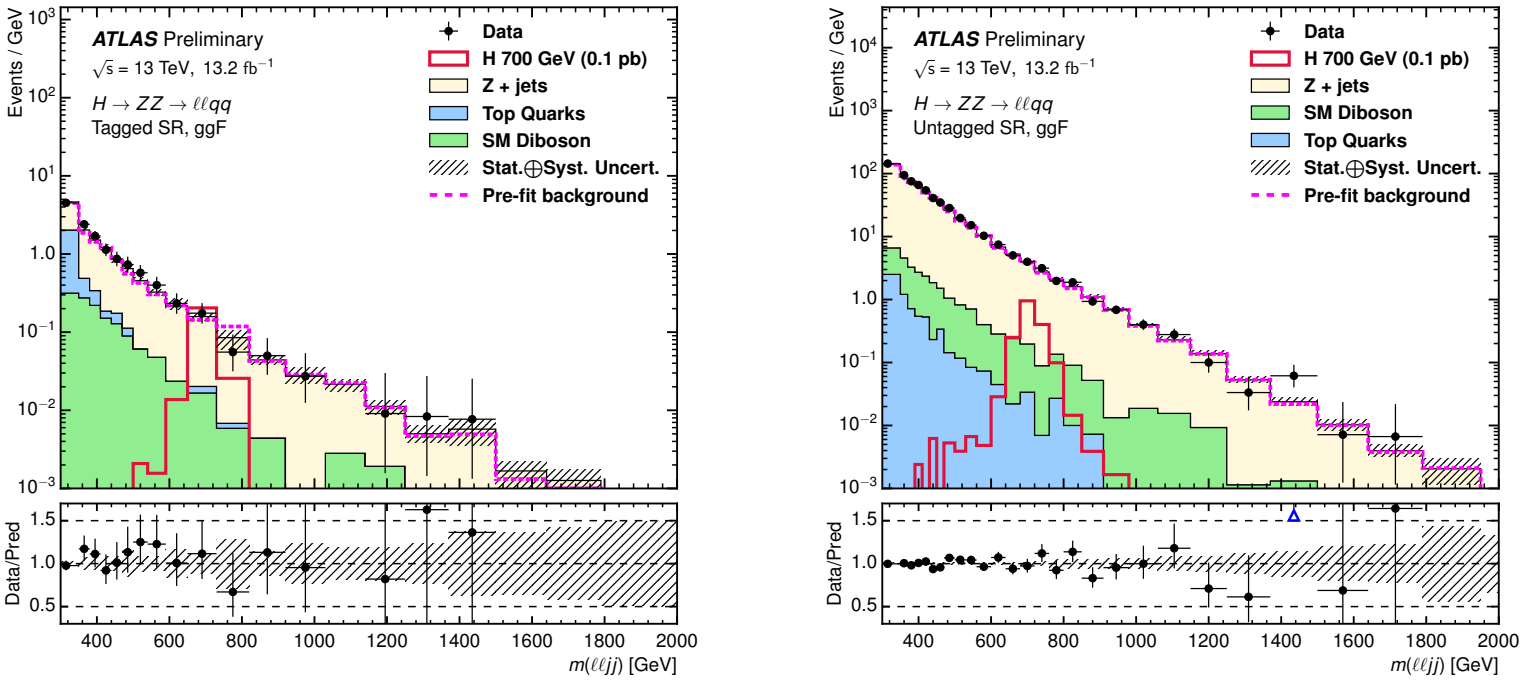

Figure 7.1: Data and MC comparison in the (a) tagged and (b) untagged signal regions in the final discriminant $m_{\ell\ell jj}$ for the ggF $H \to ZZ \to \ell\ell qq$ search. The MC distribution is shown after final fit to all regions under the background-only hypothesis. Uncertainties shown in (diagonal lines) express the $\pm 1\sigma$ width of the posterior likelihood minimum. Signals are shown in (red) with mass $m_H = 700$ GeV and a cross section of $\sigma \times$ BR$(H \to ZZ) = 100$ fb.

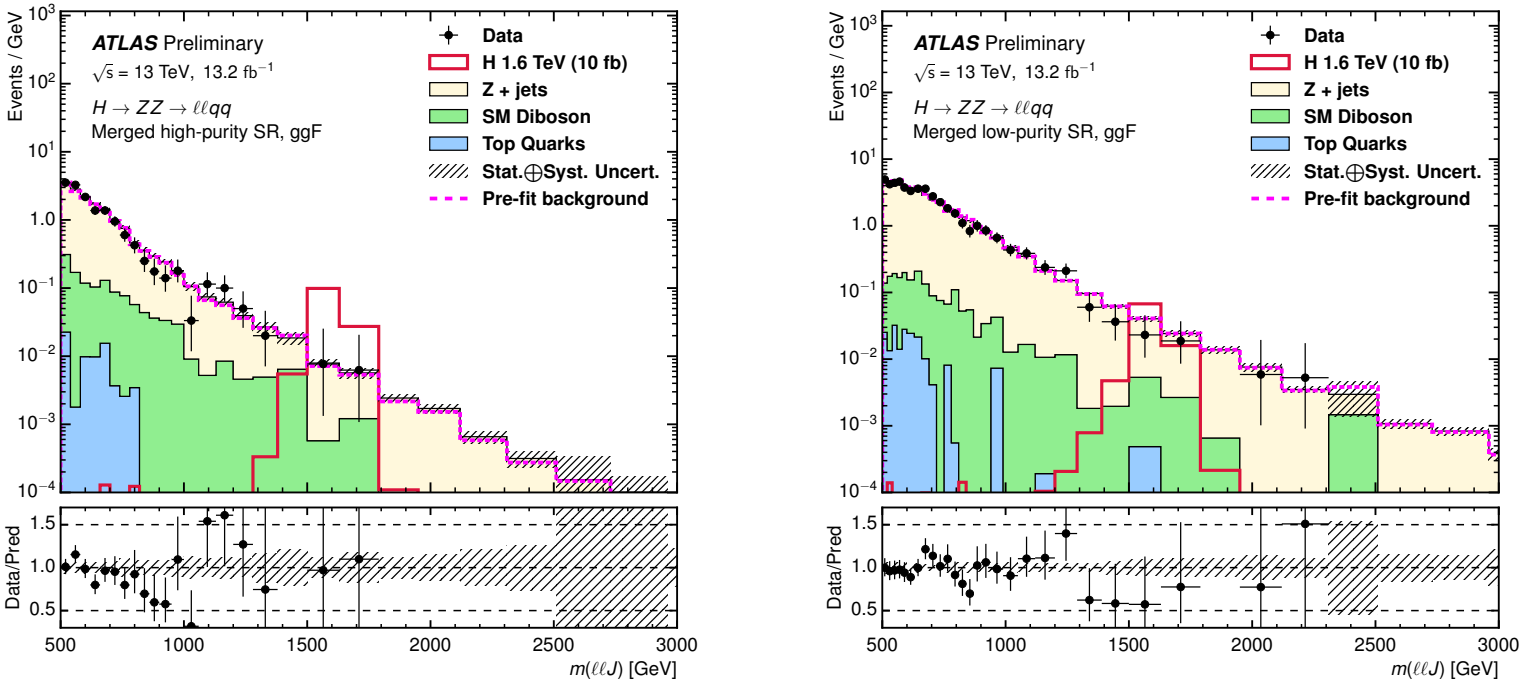

Figure 7.2: Data and MC comparison in the (a) high-purity and (b) low purity signal regions in the final discriminant $m_{\ell\ell J}$ for the ggF $H \to ZZ \to \ell\ell qq$ search. The MC distribution is shown after final fit to all regions under the background-only hypothesis. Uncertainties shown in (diagonal lines) express the $\pm 1\sigma$ width of the posterior likelihood minimum. Signals are shown in (red) with mass $m_H = 1600$ GeV and a cross section of $\sigma \times$ BR$(H \to ZZ) = 10$ fb.

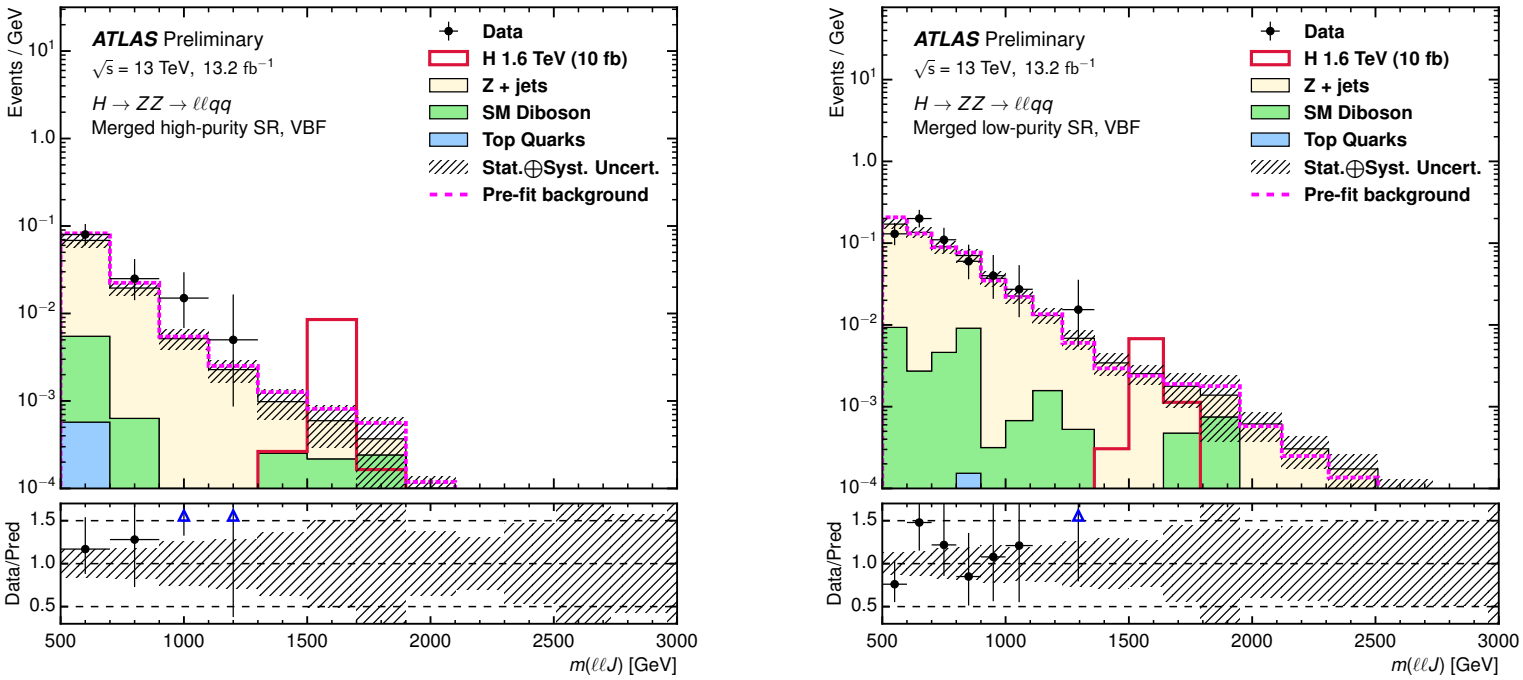

Figure 7.3: Data and MC comparison in the (a) high-purity and (b) low purity signal regions in the final discriminant $m_{\ell\ell J}$ for the VBF $H \to ZZ \to \ell\ell qq$ search. The MC distribution is shown after final fit to all regions under the background-only hypothesis. Uncertainties shown in (diagonal lines) express the $\pm 1\sigma$ width of posterior likelihood minimum. Signals are shown in (red) with mass $m_H = 1600$ GeV and a cross section of $\sigma \times$ BR$(H \to ZZ) = 10$ fb.

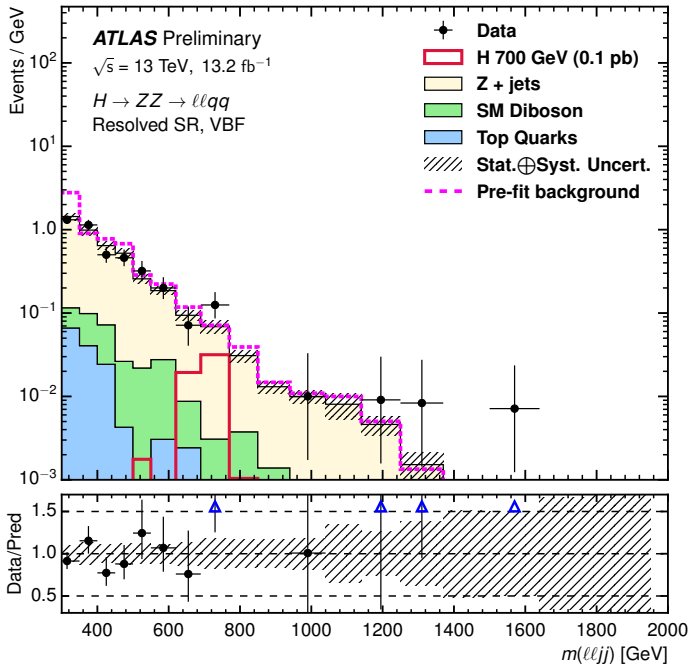

Figure 7.4: Data and MC comparison in the resolved signal region in the final discriminant $m_{\ell\ell jj}$ for the VBF $H \to ZZ \to \ell\ell qq$ search. The MC distribution is shown after final fit to all regions under the background-only hypothesis. Uncertainties shown in (diagonal lines) express the $\pm 1\sigma$ width of the posterior likelihood minimum. Signals are shown in (red) with mass $m_H = 700$ GeV and a cross section of $\sigma \times$ BR$(H \to ZZ) = 100$ fb.

The absence of a clear presence of signal indicates that an interpretation of results should follow with constraint on the production cross sections of the heavy resonances decaying to ZV pairs. Exclusion limits are calculated with the modified frequentist method [172] CL_s using the $\tilde{q}_\mu$ test statistic in the asymptotic approximation [173, 174] as detailed in Sec. 7.2. The observed and expected 95% confidence level (CL) upper limits on $\sigma \times$ BR as functions of the resonance mass are shown in Fig. 7.5 for the Higgs search. Fig. 7.5 shows the upper limit for $\sigma \times$ BR $\to$ZZ on the (a) the ggF production and (b) the VBF production for the narrow width heavy Higgs. The mass range searched is between $300 - 3000$ GeV for $H \to ZZ$ of ggF and VBF processes. The mass range searched for the HVT $W' \to ZW$ and RS graviton $G^* \to ZZ$ signals is from $500 - 5000$ GeV. Fig. 7.6 gives the upper limit for (a) $\sigma \times$ BR $\to$WZ of the

W' and (b) $\sigma \times$ BR $\rightarrow$ZZ for the graviton.

A breakdown of the limits set by each of the SRs in the ggF H analysis is shown in Fig. 7.7. In the low-mass region the limit set is dominated by the untagged category. At $m_H = 600$ GeV the high-purity and untagged categories contribute roughly equally to limit and the range $600 < m_H < 3000$ is dominated by the merged regime. Addition of the low-purity category improves the limit by roughly 10% with slightly more influence at the highest masses. The tagged category improves the resolved limit to a similar degree.

To evaluate the sensitivity of the limit to the theoretical width of the resonance, large width samples were studied. This study was made by the author at an earlier date using only 2015 data [28], but the result is directly applicable to the current study. Figure 7.8 shows the limits set on 3.2 fb^{-1}collected in 2015 for scalar signals with a width of 0,5,10, and 15% the resonance mass. The effect of width on the expected limits should be directly applicable to the current analysis. To summarize, the strength of the limit is reduced about 30% in going from 0 to 5% intrinsic width Γ_H/m_H and 50% for a 15% Γ_H/m_H. This study is not necessary for the $\nu\nu qq$ channel because the width of $\nu\nu qq$ final discriminant M_T is 25-30%.

The observed limit on $\sigma \times$ BR varies from 1.28 (0.6) pb at 300 GeV to 6.2 (5.2) fb at 3000 GeV for ggF (VBF) $H \rightarrow ZZ$, from 1.10 pb at 500 GeV to 13.9 fb at 5000 GeV for HVT $W' \rightarrow ZW$ and from 730 fb at 500 GeV to 6.7 fb at 5000 GeV for RS graviton $G^* \rightarrow ZZ$. These limits are considerably tighter than those of early searches [25, 28]. Theoretical predictions for $\sigma \times$ BR of the HVT $W' \rightarrow ZW$ and RS graviton $G^* \rightarrow ZZ$ are overlaid in Fig. 7.6 (a and b) respectively. The observed (expected) limits exclude the HVT W' lighter than 2225 (2075) GeV and the RS graviton lighter than 1035 (1045) GeV.

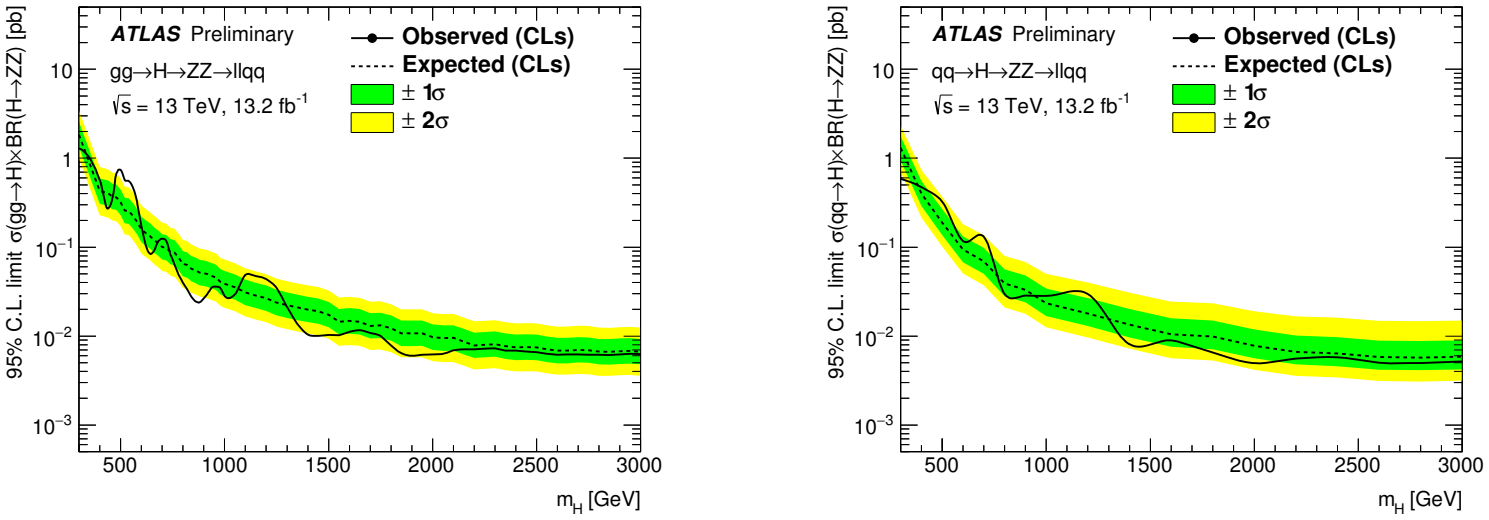

Figure 7.5: Observed and expected 95% CL upper limits on the production cross section of a heavy scalar resonance in the narrow width approximation at $\sqrt{s} = 13$ TeV times its decay branching ratio to ZZ for (a) ggF $H \rightarrow ZZ$ production channel and (b) VBF $H \rightarrow ZZ$ production channel as a function of the resonance mass. Limits are obtained from signal MC samples produced in 100 GeV steps and interpolated in 20 GeV steps in between. The green (inner) and yellow (outer) bands represent $\pm 1\sigma$ and $\pm 2\sigma$ uncertainty on the expected limits.

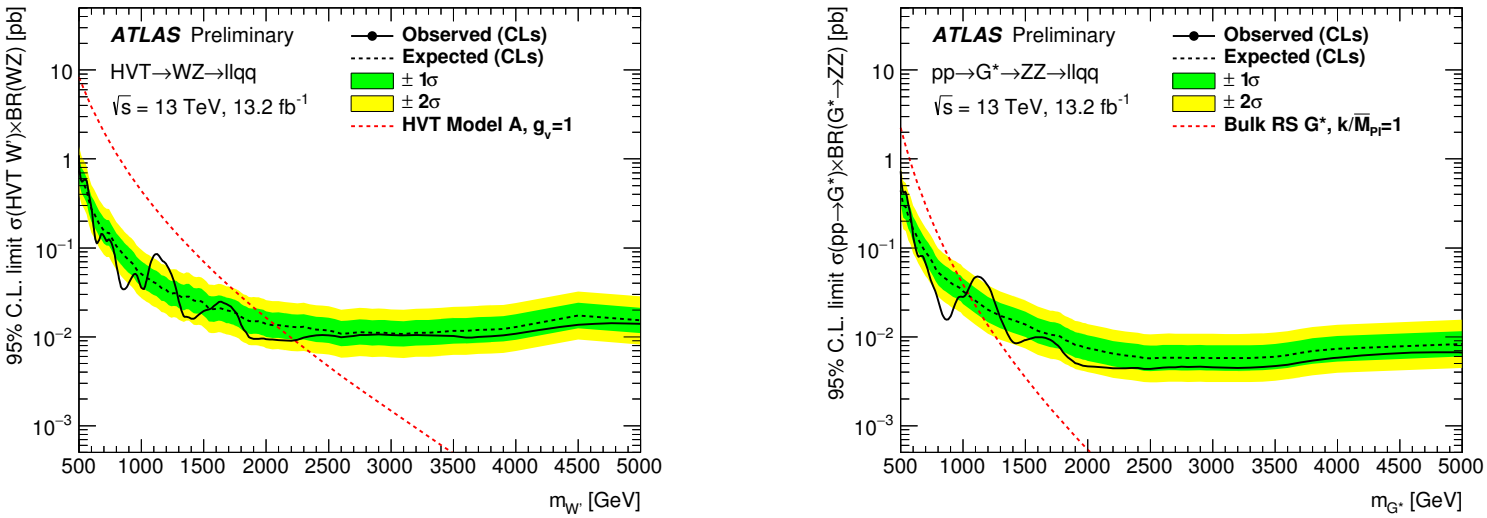

Figure 7.6: Observed and expected 95% CL upper limits on the production cross section of a heavy resonance at $\sqrt{s} = 13$ TeV times its decay branching ratio to VZ for (a) HVT $W' \rightarrow WZ$ and (b) RS graviton $G^* \rightarrow ZZ$ as functions of the resonance mass. Limits are obtained from signal MC samples produced in 100 GeV steps and interpolated in 50 GeV steps in between through 3000 Gin samples separated by 500 GeV above that. The theoretical predictions for $\sigma \times$ BR as functions of resonance mass for the HVT model A W' and the RS graviton with $\kappa/\overline{M}_{\mathrm{Pl}} = 1.0$ are also shown in (a) and (b), respectively. The green (inner) and yellow (outer) bands represent $\pm 1\sigma$ and $\pm 2\sigma$ uncertainty on the expected limits.

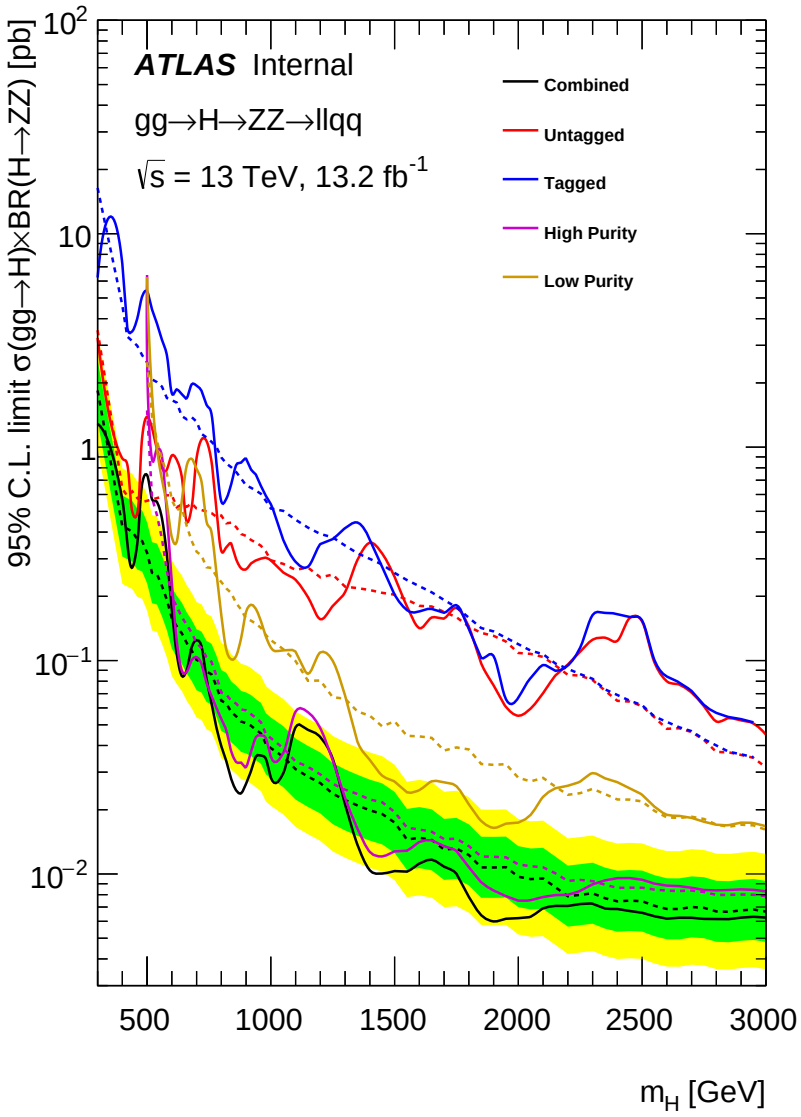

Figure 7.7: Observed and expected 95% CL upper limits on the production cross section of a heavy scalar resonance in the narrow width approximation at $\sqrt{s} = 13$ TeV times its decay branching ratio to ZZ for the ggF $H \rightarrow ZZ$ production channel. Contributions to the limit are separated by SR–expected (dotted) and observed (solid) limits are provided for each category independently.

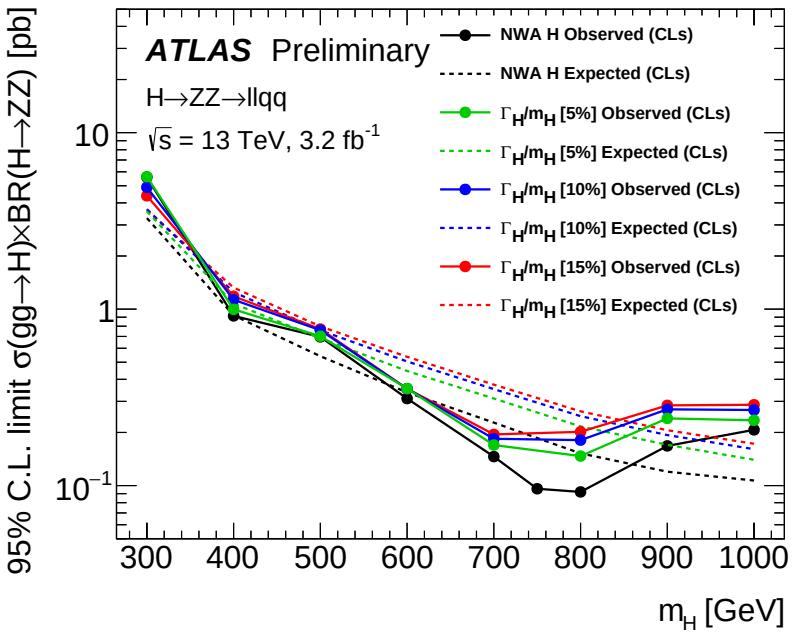

Figure 7.8: From an earlier version of the $\ell\ell qq$ analysis made public with only 2015 data [28]. Observed and expected 95% CL upper limits on the production cross section of a heavy scalar resonance with varying intrinsic signal width from 0-15% of the signal mass at $\sqrt{s} = 13$ TeV times its decay branching ratio to ZZ for the ggF $H \rightarrow ZZ$ production channel.

Process	Merged analysis	
	high-purity	low-purity
Z+jets	1251 ± 56	3130 ± 79
W+jets	881 ± 45	2092 ± 75
Diboson	202 ± 14	227 ± 10
$t\bar{t}$ + single top	557 ± 85	610 ± 100
Total background	2891± 50	6059 ± 76
Data	2859	6044
H (1600 GeV)	63.7 ± 1.9	46.2 ± 1.4

Table 7.4: Numbers of events predicted from background processes and observed in the data in the signal regions of the $\nu\nu qq$ search from the background-only fit of both signal and control regions. The numbers of signal events expected from a Higgs boson at 1600 GeV are also shown. The signal yields are calculated assuming $\sigma \times BR$ values of 20 fb at 1600 GeV. The quoted uncertainties are the combined systematic and statistical uncertainties after the fit. Uncertainties in the normalization of individual backgrounds may be larger than the uncertainty on the total background due to correlations.

7.5 Results from the $ZV \to \nu\nu qq$ search

This section presents the main results of the searches in this thesis in the $\nu\nu qq$ channel. Searches are made for the a heavy Higgs only in the ggF production channel, for the HVT W', and for the RS graviton.

The background-only fit to the $H \to ZZ$ search reveals the excellent agreement between data and MC prior to the application of normalization factors and pull of nuisance parameters as it did in the ggF category of the $\ell\ell qq$ analysis. The normalization factors applied to the Z+jets, W+jets, and $t\bar{t}$ are all found to be in agreement with 1.

The number of events in the SRs for the fit under the background-only hypothesis is shown in Table 7.3. The agreement found in the predicted and observed backgrounds are well within the uncertainty provided by the NPs. The distributions of the final discriminant M_T in the SRs are shown in Fig. 7.9.

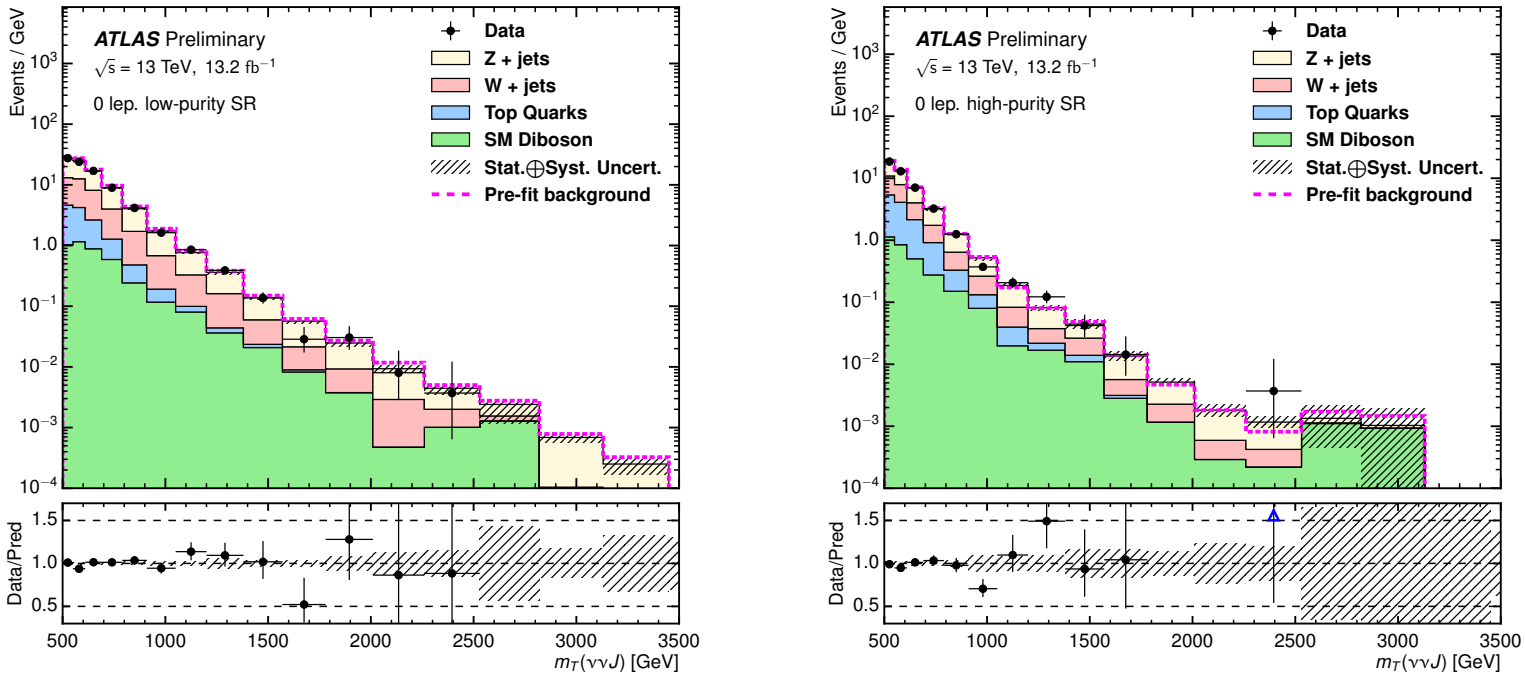

Figure 7.9: Data and MC comparison in the resolved signal region in the transverse mass discriminant M_T for the $ZV \rightarrow \nu\nu qq$ searches. The MC distribution is shown after final fit to all regions under the background-only hypothesis. Uncertainties shown in (diagonal lines) express the $\pm 1\sigma$ width of the posterior likelihood minimum.

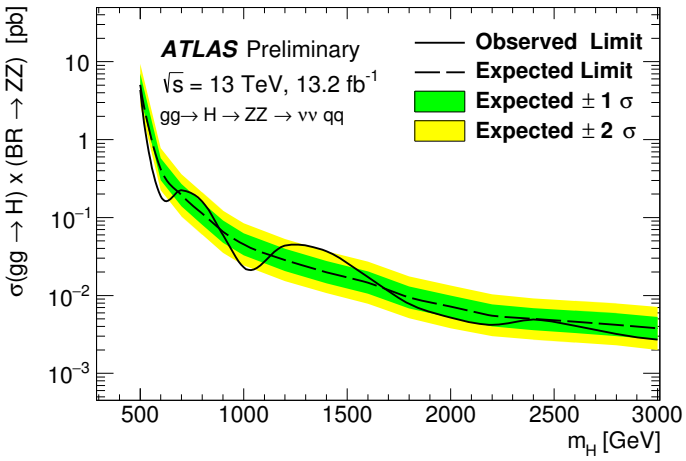

Figure 7.10: Observed and expected 95% CL upper limits on the production cross section of a heavy scalar resonance in the narrow width approximation at $\sqrt{s} =$ 13 TeV times its decay branching ratio to ZZ for the ggF $H \rightarrow ZZ$ production channel as a function of the resonance mass. Limits are obtained from signal MC samples produced in 100 GeV steps. The green (inner) and yellow (outer) bands represent $\pm 1\sigma$ and $\pm 2\sigma$ uncertainty on the expected limits.

There are no large deviations up or down from the predicted behavior of the distribution in either the high or low-purity category. Therefore exclusion limits at the 95% confidence level are set on production cross section $\sigma \times$ BR for the three signals. The observed and expected limits on the production cross-section multiplied by the branching fraction into ZW or ZZ as a function of the resonance mass for the heavy Higgs is shown in Fig. 7.10. The observed and expected limits on the production cross-section multiplied by the branching fraction into ZW for the charged W' in the HVT Model A, and into ZZ for the graviton model as a function of the resonance mass is shown in Fig. 7.11.

The theoretical predictions for the HVT benchmark Model A with coupling constant $g_V = 1$ allow exclusion of $m_{W'} < 2400$ GeV . For the graviton model the corresponding excluded mass is $m_{G^*} < 1100$ GeV.

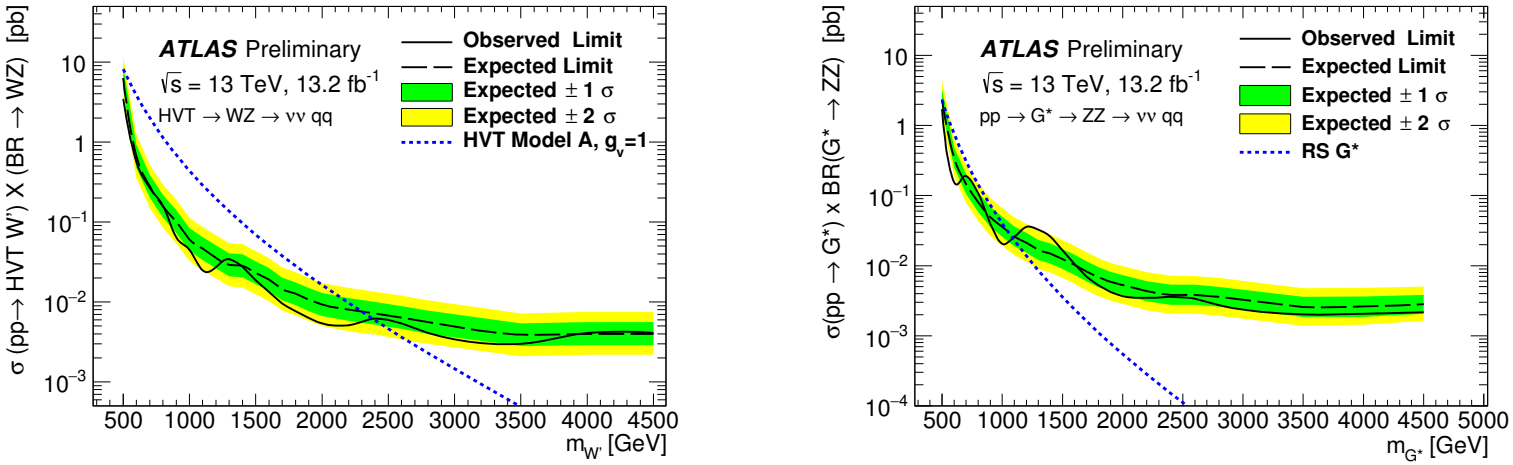

Figure 7.11: Observed and expected 95% CL upper limits on the production cross section of a heavy resonance at $\sqrt{s} = 13$ TeV times its decay branching ratio to VZ for (a) HVT $W' \rightarrow WZ$ and (b) RS graviton $G^* \rightarrow ZZ$ as functions of the resonance mass. Limits are obtained from signal MC samples produced in 100 GeV steps through 3000 GeV in 500 GeV intervals above that. The theoretical predictions for $\sigma \times$ BR as functions of resonance mass for the HVT model A W' and the RS graviton with $\kappa/\overline{M}_{\mathrm{Pl}} = 1.0$ are also shown in (a) and (b), respectively. The green (inner) and yellow (outer) bands represent $\pm 1\sigma$ and $\pm 2\sigma$ uncertainty on the expected limits.

Chapter 8

Conclusion

This thesis presented searches for heavy diboson resonances ZZ or ZW in final states with Z decay to two charged leptons or two neutrinos and W/Z decay to two quarks. The searches use data collected in pp-collisions by the ATLAS detector at LHC in 2015 and 2016, corresponding to a combined integrated luminosity of (13.2 ± 0.4) fb^{-1}.

The LHC was upgraded in the long shutdown from 2012-2015 prior to first collisions at the unprecedented center of mass energy of $\sqrt{s} = 13$ TeV. A focus has been made throughout this thesis to illustrate the evolving nature of the work at ATLAS as Run 2 has progressed. In addition to the main topic of the thesis, the author made substantial contributions to the data acquisition framework for the new insertable B-layer and to the calibration of jets. Chapter 5 outlined the soon-to-be published calibration of jets and the evaluation of their systematic uncertainties in Run 2, a result valuable to the greater ATLAS community.

The analyses made were powerful and preliminary, relying on the increased center of mass energy to set new limits with only a tiny fraction of the data expected to be collected in Run 2 through 2018. The data are found to be consistent with the background-only hypothesis and no evidence for the production of heavy resonances is observed. In the absence of evidence of a signal, upper confidence limits at the 95%-level on the production cross section times branching ratio over a wide range of resonance masses were set for three benchmark models: $H \to ZZ$ in models with an extended Higgs sector, $W' \to ZW$ in model A of a heavy vector triplet model, and for $G^* \to ZZ$ in the context of the bulk Randall-Sundrum model of warped extra

dimensions.

The theoretical predictions for the HVT benchmark Model A with coupling constant $g_V = 1$ allow exclusion of $m_{W'} < 2225$ GeV for the $ZW \to \ell\ell qq$ search, and $m_{W'} < 2400$ GeV for the $ZW \to \nu\nu qq$ search. For the Graviton model the corresponding excluded masses are $m_{G^*} < 1035$ GeV for the $ZZ \to \ell\ell qq$ search, and $m_{G^*} < 1100$ GeV for the $ZZ \to \nu\nu qq$ search.

Bibliography

[1] ATLAS Collaboration, *Observation of a new particle in the search for the Standard Model Higgs boson with the ATLAS detector at the LHC*, Phys. Lett. B **716** (2012) p. 1, arXiv: 1207.7214 [hep-ex].

[2] CMS Collaboration, *Observation of a new boson at a mass of 125 GeV with the CMS experiment at the LHC*, Phys. Lett. B **716** (2012) p. 30, arXiv: 1207.7235 [hep-ex].

[3] F. Englert and R. Brout, *Broken Symmetry and the Mass of Gauge Vector Mesons*, Phys. Rev. Lett. **13** (9 1964) p. 321, URL: http://link.aps.org/doi/10.1103/PhysRevLett.13.321.

[4] P. W. Higgs, *Broken symmetries, massless particles and gauge fields*, Phys. Lett. **12** (1964) p. 132.

[5] T. ATLAS and C. Collaborations, *Measurements of the Higgs boson production and decay rates and constraints on its couplings from a combined ATLAS and CMS analysis of the LHC pp collision data at $\sqrt{s} = 7$ and 8 TeV*, JHEP **08** (2016) p. 045, arXiv: 1606.02266 [hep-ex].

[6] B. P. Abbott et al., *Observation of Gravitational Waves from a Binary Black Hole Merger*, Phys. Rev. Lett. **116** (2016) p. 061102, arXiv: 1602.03837 [gr-qc].

[7] D. Pappadopulo et al., *Heavy Vector Triplets: Bridging Theory and Data*, JHEP **09** (2014) p. 060, arXiv: 1402.4431 [hep-ph].

[8] A. Hill and J. J. van der Bij, *Strongy Interacting Singlet - Doublet Higgs Model*, Phys. Rev. **D36** (1987) p. 3463.

[9] G. C. Branco et al., *Theory and phenomenology of two-Higgs-doublet models*, Phys. Rept. **516** (2012) p. 1, arXiv: 1106.0034 [hep-ph].

[10] G. Altarelli, B. Mele, and M. Ruiz-Altaba,
Searching for New Heavy Vector Bosons in $p\bar{p}$ Colliders,
Z. Phys. **C45** (1989) p. 109, [Erratum: Z. Phys.C47,676(1990)].

[11] J. R. Andersen et al., *Discovering Technicolor*,
Eur. Phys. J. Plus **126** (2011) p. 81, arXiv: 1104.1255 [hep-ph].

[12] S. Catterall et al., *MCRG Minimal Walking Technicolor*,
Phys. Rev. **D85** (2012) p. 094501, arXiv: 1108.3794 [hep-ph].

[13] E. Eichten and K. Lane, *Low-scale technicolor at the Tevatron and LHC*,
Phys. Lett. **B669** (2008) p. 235, arXiv: 0706.2339 [hep-ph].

[14] T. G. Rizzo, "Extended gauge sectors,"
Beyond the standard model 4. Proceedings, 4th International Conference on High-Energy Physics, Tahoe City, USA, December 13-18, 1994, 1994 p. 24,
arXiv: hep-ph/9501261 [hep-ph], URL: http://www-public.slac.stanford.edu/sciDoc/docMeta.aspx?slacPubNumber=SLAC-PUB-6741.

[15] J. C. Pati and A. Salam, *Lepton Number as the Fourth Color*,
Phys. Rev. **D10** (1974) p. 275, [Erratum: Phys. Rev.D11,703(1975)].

[16] H. Fritzsch and P. Minkowski, *Unified interactions of leptons and hadrons*,
Annals of Physics **93** (1975) p. 193 , ISSN: 0003-4916, URL: http://www.sciencedirect.com/science/article/pii/0003491675902110.

[17] H. Davoudiasl, J. L. Hewett, and T. G. Rizzo,
Bulk gauge fields in the Randall-Sundrum model,
Phys. Lett. **B473** (2000) p. 43, arXiv: 9911262 [hep-ph].

[18] L. Randall and R. Sundrum,
A Large mass hierarchy from a small extra dimension,
Phys. Rev. Lett. **83** (1999) p. 3370, arXiv: 9905221 [hep-ph].

[19] T. Kaluza, *Zum Unitaetsproblem der Physik*, Sitzungsberichte der Preussischen Akademie Der Wissenshaften (1921) p. 966,
URL: https://ia801404.us.archive.org/3/items/sitzungsberichte1921preussi/sitzungsberichte1921preussi.pdf.

[20] ATLAS Collaboration, *Search for resonant diboson production in the $\ell\ell q\bar{q}$ final state in pp collisions at $\sqrt{s} = 8$ TeV with the ATLAS detector*,
Eur. Phys. J. **C75** (2015) p. 69, arXiv: 1409.6190 [hep-ex].

[21] ATLAS Collaboration,
Search for an additional, heavy Higgs boson in the $H \to ZZ$ decay channel at $\sqrt{s} = 8$ TeV in pp collision data with the ATLAS detector,
Eur. Phys. J. **C76** (2016) p. 45, arXiv: 1507.05930 [hep-ex].

[22] ATLAS Collaboration,
Search for high-mass diboson resonances with boson-tagged jets in proton-proton collisions at $\sqrt{s} = 8$ TeV with the ATLAS detector,
JHEP **12** (2015) p. 055, arXiv: 1506.00962 [hep-ex].

[23] CMS Collaboration,
Search for massive resonances in dijet systems containing jets tagged as W or Z boson decays in pp collisions at $\sqrt{s} = 8$ TeV, JHEP **08** (2014) p. 173,
arXiv: 1405.1994 [hep-ex].

[24] CMS Collaboration, *Search for a Higgs Boson in the Mass Range from 145 to 1000 GeV Decaying to a Pair of W or Z Bosons*, JHEP **10** (2015) p. 144,
arXiv: 1504.00936 [hep-ex].

[25] ATLAS Collaboration, *Search for diboson resonances in the $\ell\ell qq$ final state in pp collisions at $\sqrt{s} = 13$ TeV with the ATLAS detector*, (2015),
URL: https://cds.cern.ch/record/2114843.

[26] ATLAS Collaboration, *Search for diboson resonances in the $\nu\nu qq$ final state in pp collisions at $\sqrt{s} = 13$ TeV with the ATLAS detector*, (2015),
URL: https://cds.cern.ch/record/2114840.

[27] ATLAS Collaboration, *Searches for heavy diboson resonances in pp collisions at $\sqrt{s} = 13$ TeV with the ATLAS detector*, (2016),
arXiv: 1606.04833 [hep-ex].

[28] ATLAS Collaboration, *Search for ZZ resonances in the $\ell\ell qq$ final state in pp collisions at $\sqrt{s} = 13$ TeV with the ATLAS detector*, (2016),
URL: https://cds.cern.ch/record/2141005.

[29] URL: https://atlas.web.cern.ch/Atlas/GROUPS/PHYSICS/CombinedSummaryPlots/SM/index.html#ATLAS_e_SMSummary_FiducialRatio.

[30] ATLAS Collaboration, *Improved luminosity determination in pp collisions at $\sqrt{s} = 7$ TeV using the ATLAS detector at the LHC*,
Eur. Phys. J. **C73** (2013) p. 2518, arXiv: 1302.4393 [hep-ex].

[31] ATLAS Collaboration, *ATLAS Phase-II Upgrade Scoping Document*, (2015),
URL: http://cds.cern.ch/record/2055248.

[32] K. A. Olive et al., *Review of Particle Physics*,
Chin. Phys. **C38** (2014) p. 090001.

[33] R. P. Feynman, "The behavior of hadron collisions at extreme energies,"
Brown, L.M. (ed.): Selected papers of Richard Feynman 497-518*, 1989.

[34] A. D. Martin et al., *Parton distributions for the LHC*,
Eur. Phys. J. **C63** (2009) p. 189, arXiv: 0901.0002 [hep-ph].

[35] F. J. Hasert et al., *Observation of Neutrino Like Interactions Without Muon Or Electron in the Gargamelle Neutrino Experiment*,
Phys. Lett. **B46** (1973) p. 138.

[36] S. L. Glashow, *Partial Symmetries of Weak Interactions*,
Nucl. Phys. **22** (1961) p. 579.

[37] A. Salam and J. Ward, *Electromagnetic and weak interactions*,
Physics Letters **13** (1964) p. 168 , ISSN: 0031-9163, URL: http://www.sciencedirect.com/science/article/pii/0031916364907115.

[38] S. Weinberg, *A Model of Leptons*, Phys. Rev. Lett. **19** (1967) p. 1264.

[39] G. Arnison et al., *Experimental Observation of Isolated Large Transverse Energy Electrons with Associated Missing Energy at s**(1/2) = 540-GeV*,
Phys. Lett. **B122** (1983) p. 103, [,611(1983)].

[40] G. 't Hooft and M. J. G. Veltman,
Regularization and Renormalization of Gauge Fields,
Nucl. Phys. **B44** (1972) p. 189.

[41] J. Goldstone, A. Salam, and S. Weinberg, *Broken Symmetries*,
Phys. Rev. **127** (1962) p. 965.

[42] M. S. Chanowitz and M. K. Gaillard,
The TeV Physics of Strongly Interacting W's and Z's,
Nucl. Phys. **B261** (1985) p. 379.

[43] V. D. Barger, W.-Y. Keung, and E. Ma,
A Gauge Model With Light W and Z Bosons, Phys. Rev. **D22** (1980) p. 727.

[44] N. Arkani-Hamed, S. Dimopoulos, and G. R. Dvali,
The Hierarchy problem and new dimensions at a millimeter,
Phys. Lett. **B429** (1998) p. 263, arXiv: hep-ph/9803315 [hep-ph].

[45] B. Zwiebach, *A first course in string theory*,
Cambridge University Press, 2006,
ISBN: 0521831431, 9780521831437, 9780511207570, URL: http://www.cambridge.org/uk/catalogue/catalogue.asp?isbn=0521831431.

[46] *LEP design report*, Copies shelved as reports in LEP, PS and SPS libraries,
CERN, 1984, URL: http://cds.cern.ch/record/102083.

[47] ATLAS Collaboration,
The ATLAS Experiment at the CERN Large Hadron Collider,
JINST **3** (2008) S08003.

[48] S. Chatrchyan et al., *The CMS experiment at the CERN LHC*,
JINST **3** (2008) S08004.

[49] A. A. Alves Jr. et al., *The LHCb Detector at the LHC*,
JINST **3** (2008) S08005.

[50] K. Aamodt et al., *The ALICE experiment at the CERN LHC*,
JINST **3** (2008) S08002.

[51] M. Benedikt et al., *LHC Design Report*, CERN, 2004,
URL: http://cds.cern.ch/record/823808.

[52] O. S. Bruning et al., *LHC Design Report Vol.1: The LHC Main Ring*, (2004).

[53] M Bajko et al., "Report of the Task Force on the Incident of 19th September 2008 at the LHC," tech. rep. LHC-PROJECT-Report-1168. CERN-LHC-PROJECT-Report-1168, CERN, 2009,
URL: https://cds.cern.ch/record/1168025.

[54] P. Jenni et al., *ATLAS Forward Detectors for Measurement of Elastic Scattering and Luminosity*, Technical Design Report ATLAS, CERN, 2008,
URL: https://cds.cern.ch/record/1095847.

[55] S van der Meer, *Calibration of the effective beam height in the ISR*, (1968),
URL: https://cds.cern.ch/record/296752.

[56] G. Aad et al., *Improved luminosity determination in pp collisions at sqrt(s) = 7 TeV using the ATLAS detector at the LHC*,
Eur. Phys. J. **C73** (2013) p. 2518, arXiv: 1302.4393 [hep-ex].

[57] M. Aaboud et al., *Luminosity determination in pp collisions at $\sqrt{s}$ = 8 TeV using the ATLAS detector at the LHC*, Eur. Phys. J. **C76** (2016) p. 653,
arXiv: 1608.03953 [hep-ex].

[58] S. Artz et al., *Upgrade of the ATLAS Central Trigger for LHC Run-2*, JINST **10** (2015) p. C02030.

[59] *ATLAS inner detector: Technical Design Report, 1*, Technical Design Report ATLAS, CERN, 1997, URL: https://cds.cern.ch/record/331063.

[60] ATLAS Collaboration, *Fast TracKer (FTK) Technical Design Report*, (2013), ATLAS Fast Tracker Technical Design Report, URL: https://cds.cern.ch/record/1552953.

[61] N. Wermes and G Hallewel, *ATLAS pixel detector: Technical Design Report*, Technical Design Report ATLAS, CERN, 1998, URL: https://cds.cern.ch/record/381263.

[62] G. Aad et al., *ATLAS pixel detector electronics and sensors*, JINST **3** (2008) P07007.

[63] ATLAS Collaboration, *ATLAS Insertable B-Layer Technical Design Report*, ATLAS-TDR-19 (2010), URL: https://cds.cern.ch/record/1291633.

[64] D. Yamaguchi, "Hit occupancy of Pixel detectors with zero bias trigger," tech. rep. ATL-INDET-INT-2016-023, CERN, 2016, URL: https://cds.cern.ch/record/2237564.

[65] E. Abat et al., *The ATLAS Transition Radiation Tracker (TRT) proportional drift tube: Design and performance*, JINST **3** (2008) P02013.

[66] T. Gleisberg and S. Hoeche, *Comix, a new matrix element generator*, JHEP **0812** (2008) p. 039, arXiv: 0808.3674 [hep-ph].

[67] F. Cascioli, P. Maierhofer, and S. Pozzorini, *Scattering Amplitudes with Open Loops*, Phys. Rev. Lett. **108** (2012) p. 111601, arXiv: 1111.5206 [hep-ph].

[68] J. Alwall et al., *MadGraph 5: going beyond*, English, Journal of High Energy Physics **2011**, 128 (2011), URL: http://dx.doi.org/10.1007/JHEP06%282011%29128.

[69] A. Buckley et al., *General-purpose event generators for LHC physics*, Phys.Rept. **504** (2011) p. 145, arXiv: 1101.2599 [hep-ph].

[70] G. Corcella et al., *HERWIG 6: An Event generator for hadron emission reactions with interfering gluons (including supersymmetric processes)*, JHEP **0101** (2001) p. 010, arXiv: hep-ph/0011363 [hep-ph].

[71] B. Andersson et al., *Parton Fragmentation and String Dynamics*, Phys. Rept. **97** (1983) p. 31.

[72] D. Amati and G. Veneziano, *Preconfinement as a Property of Perturbative QCD*, Phys. Lett. **83B** (1979) p. 87.

[73] P. Nason, *A New method for combining NLO QCD with shower Monte Carlo algorithms*, JHEP **0411** (2004) p. 040, arXiv: 0409146 [hep-ph].

[74] S. Frixione, P. Nason, and C. Oleari, *Matching NLO QCD computations with Parton Shower simulations: the POWHEG method*, JHEP **11** (2007) p. 070, arXiv: 0709.2092 [hep-ph].

[75] S. Frixione et al., *The MC@NLO 4.0 Event Generator*, (2010), arXiv: 1010.0819 [hep-ph].

[76] S. Frixione and B. R. Webber, *Matching NLO QCD computations and parton shower simulations*, JHEP **06** (2002) p. 029, arXiv: hep-ph/0204244 [hep-ph].

[77] S. Frixione and B. R. Webber, *The MC@NLO event generator*, (2002), arXiv: hep-ph/0207182 [hep-ph].

[78] S. Catani et al., *QCD matrix elements + parton showers*, JHEP **11** (2001) p. 063, arXiv: hep-ph/0109231 [hep-ph].

[79] L. Lonnblad, *Correcting the color dipole cascade model with fixed order matrix elements*, JHEP **05** (2002) p. 046, arXiv: hep-ph/0112284 [hep-ph].

[80] L. Lonnblad, *ARIADNE version 4: A Program for simulation of QCD cascades implementing the color dipole model*, Comput. Phys. Commun. **71** (1992) p. 15.

[81] P. Z. Skands and D. Wicke, *Non-perturbative QCD effects and the top mass at the Tevatron*, Eur. Phys. J. **C52** (2007) p. 133, arXiv: hep-ph/0703081 [HEP-PH].

[82] T. Gleisberg et al., *Event generation with SHERPA 1.1*, JHEP **0902** (2009) p. 007, arXiv: 0811.4622 [hep-ph].

[83] S. Hoeche et al., *QCD matrix elements + parton showers: The NLO case*, JHEP **04** (2013) p. 027, arXiv: 1207.5030 [hep-ph].

[84] T. Gleisberg and S. Höche, *Comix, a new matrix element generator*, JHEP **0812** (2008) p. 039, arXiv: 0808.3674 [hep-ph].

[85] R. D. Ball et al., *Parton distributions for the LHC Run II*, JHEP **04** (2015) p. 040, arXiv: 1410.8849 [hep-ph].

[86] ATLAS Collaboration, *The ATLAS Simulation Infrastructure*, Eur. Phys. J. C **70** (2010) p. 823, arXiv: 1005.4568 [hep-ex].

[87] S. Agostinelli et al., *GEANT4: A Simulation toolkit*, Nucl.Instrum.Meth. **A506** (2003) p. 250.

[88] S. Alioli et al., *NLO Higgs boson production via gluon fusion matched with shower in POWHEG*, JHEP **04** (2009) p. 002, arXiv: 0812.0578 [hep-ph].

[89] J. Pumplin et al., *New generation of parton distributions with uncertainties from global QCD analysis*, JHEP **0207** (2002) p. 012, arXiv: hep-ph/0201195 [hep-ph].

[90] Sjöstrand, Torbjorn and Mrenna, Stephen and Skands, Peter Z., *PYTHIA 6.4 Physics and Manual*, JHEP **0605** (2006) p. 026, arXiv: 0603175.

[91] ATLAS Collaboration, *Measurement of angular correlations in Drell-Yan lepton pairs to probe Z/γ^* boson transverse momentum at $\sqrt{s} = 7$ TeV with the ATLAS detector*, Phys. Lett. B **720** (2013) p. 32, arXiv: 1211.6899 [hep-ex].

[92] T. Sjostrand, S. Mrenna, and P. Z. Skands, *A Brief Introduction to PYTHIA 8.1*, Comput.Phys.Commun. **178** (2008) p. 852, arXiv: 0710.3820 [hep-ph].

[93] ATLAS Collaboration, *ATLAS Run 1 Pythia8 tunes*, (2014), URL: http://cds.cern.ch/record/1966419.

[94] H.-L. Lai et al., *New parton distributions for collider physics*, Phys. Rev. **D82** (2010) p. 074024, arXiv: 1007.2241 [hep-ph].

[95] C. Anastasiou et al., *High precision QCD at hadron colliders: Electroweak gauge boson rapidity distributions at NNLO*, Phys. Rev. **D69** (2004) p. 094008, arXiv: 0312266 [hep-ph].

[96] P. Z. Skands, *Tuning Monte Carlo Generators: The Perugia Tunes*, Phys. Rev. **D82** (2010) p. 074018, arXiv: 1005.3457 [hep-ph].

[97] M. Czakon, P. Fiedler, and A. Mitov, *Total Top-Quark Pair-Production Cross Section at Hadron Colliders Through $O(\alpha_s^4)$*, Phys. Rev. Lett. **110** (2013) p. 252004, arXiv: 1303.6524 [hep-ph].

[98] M. Czakon and A. Mitov, *NNLO corrections to top pair production at hadron colliders: the quark-gluon reaction*, JHEP **1301** (2013) p. 080, arXiv: 1210.6832 [hep-ph].

[99] M. Czakon and A. Mitov, *NNLO corrections to top-pair production at hadron colliders: the all-fermionic scattering channels*, JHEP **1212** (2012) p. 054, arXiv: 1207.0236 [hep-ph].

[100] P. Baernreuther, M. Czakon, and A. Mitov, *Percent Level Precision Physics at the Tevatron: First Genuine NNLO QCD Corrections to $q\bar{q} \to t\bar{t} + X$*, Phys.Rev.Lett. **109** (2012) p. 132001, arXiv: 1204.5201 [hep-ph].

[101] M. Cacciari et al., *Top-pair production at hadron colliders with next-to-next-to-leading logarithmic soft-gluon resummation*, Phys.Lett. **B710** (2012) p. 612, arXiv: 1111.5869 [hep-ph].

[102] M. Czakon and A. Mitov, *Top++: A Program for the Calculation of the Top-Pair Cross-Section at Hadron Colliders*, Compt/ Phys. Commun. (2014) p. 2930, arXiv: 1112.5675 [hep-ph].

[103] S. Alioli et al., *NLO single-top production matched with shower in POWHEG: s- and t-channel contributions*, JHEP **09** (2009) p. 111, [Erratum: JHEP02,011(2010)], arXiv: 0907.4076 [hep-ph].

[104] E. Re, *Single-top Wt-channel production matched with parton showers using the POWHEG method*, Eur. Phys. J. **C71** (2011) p. 1547, arXiv: 1009.2450 [hep-ph].

[105] N. Kidonakis, *Two-loop soft anomalous dimensions for single top quark associated production with a W^- or H^-*, Phys. Rev. D **82** (2010) p. 054018, arXiv: 1005.4451 [hep-ph].

[106] N. Kidonakis, *NNLL resummation for s-channel single top quark production*, Phys. Rev. D **81** (2010) p. 054028, arXiv: 1001.5034 [hep-ph].

[107] R. Frederix, E. Re, and P. Torrielli, *Single-top t-channel hadroproduction in the four-flavour scheme with POWHEG and aMC@NLO*, JHEP **09** (2012) p. 130, arXiv: 1207.5391 [hep-ph].

[108] J. Alwall et al.,
The automated computation of tree-level and next-to-leading order differential cross sections, and their matching to parton shower simulations,
JHEP **07** (2014) p. 079, arXiv: 1405.0301 [hep-ph].

[109] ATLAS Collaboration, *Monte Carlo Generators for the Production of a W or Z/γ^* Boson in Association with Jets at ATLAS in Run 2*,
ATL-PHYS-PUB-2016-003, 2016,
URL: https://cds.cern.ch/record/2120133.

[110] M. Cacciari, G. P. Salam, and G. Soyez,
The Anti-k(t) jet clustering algorithm, JHEP **04** (2008) p. 063,
arXiv: 0802.1189 [hep-ph].

[111] G. P. S. M. Cacciari and G. Soyez, URL: http://fastjet.fr.

[112] G. P. Salam and G. Soyez,
A Practical Seedless Infrared-Safe Cone jet algorithm,
JHEP **05** (2007) p. 086, arXiv: 0704.0292 [hep-ph].

[113] M. Wobisch and T. Wengler,
"Hadronization corrections to jet cross-sections in deep inelastic scattering,"
Monte Carlo generators for HERA physics. Proceedings, Workshop, Hamburg, Germany, 1998-1999, 1998 p. 270,
arXiv: hep-ph/9907280 [hep-ph], URL: https://inspirehep.net/record/484872/files/arXiv:hep-ph_9907280.pdf.

[114] S. D. Ellis and D. E. Soper,
Successive combination jet algorithm for hadron collisions,
Phys. Rev. **D48** (1993) p. 3160, arXiv: hep-ph/9305266 [hep-ph].

[115] M. Cacciari and G. P. Salam, *Dispelling the N^3 myth for the k_t jet-finder*,
Phys. Lett. **B641** (2006) p. 57, arXiv: hep-ph/0512210 [hep-ph].

[116] Y. L. Dokshitzer et al., *Better jet clustering algorithms*,
JHEP **9708** (1997) p. 001, arXiv: hep-ph/9707323 [hep-ph].

[117] M. Cacciari, G. P. Salam, and G. Soyez, *The Catchment Area of Jets*,
JHEP **0804** (2008) p. 005, arXiv: 0802.1188 [hep-ph].

[118] ATLAS Collaboration, *Topological cell clustering in the ATLAS calorimeters and its performance in LHC Run 1*, (2016), arXiv: 1603.02934 [hep-ex].

[119] S. P. Alkire et al., "An Analysis of the Impact of Pile-up and Topological Clustering Thresholds on Jet and Etmiss Measurement,"

tech. rep. ATL-COM-PHYS-2016-850, CERN, 2016,
URL: https://cds.cern.ch/record/2195807.

[120] P. Speckmayer, T. Carli, and C. W. Fabjan,
"Energy Measurement of Hadrons with the CERN ATLAS Calorimeter,"
Presented on 18 Jun 2008, PhD thesis: Vienna, Tech. U., 2008,
URL: https://cds.cern.ch/record/1112036.

[121] A. Collaboration, *Performance of the electronic readout of the ATLAS liquid argon calorimeters*, Journal of Instrumentation **5** (2010) P09003,
URL: http://stacks.iop.org/1748-0221/5/i=09/a=P09003.

[122] ATLAS Collaboration,
Pile-up subtraction and suppression for jets in ATLAS, (2013),
URL: https://cds.cern.ch/record/1570994.

[123] M. Cacciari and G. P. Salam, *Pileup subtraction using jet areas*,
Phys.Lett. **B659** (2008) p. 119, arXiv: 0707.1378 [hep-ph].

[124] ATLAS Collaboration,
Properties of Jets and Inputs to Jet Reconstruction and Calibration with the ATLAS Detector Using Proton-Proton Collisions at sqrt(s) = 13 TeV,
(2015), URL: https://cds.cern.ch/record/2014750.

[125] ATLAS Collaboration,
Jet energy measurement and its systematic uncertainty in proton-proton collisions at sqrt(s)=7 TeV with the ATLAS detector,
Eur.Phys.J. **C75** (2015) p. 17, arXiv: 1406.0076 [hep-ex].

[126] ATLAS Collaboration, *Electron and photon energy calibration with the ATLAS detector using LHC Run 1 data*, Eur. Phys. J. C **74** (2014) p. 3071,
arXiv: 1407.5063 [hep-ex].

[127] ATLAS Collaboration, *Muon reconstruction performance of the ATLAS detector in proton–proton collision data at* $\sqrt{s} = 13$ *TeV*,
Eur. Phys. J. C **76** (2016) p. 292, arXiv: 1603.05598 [hep-ex].

[128] W. Lukas, "Fast Simulation for ATLAS: Atlfast-II and ISF," 2012,
URL: http://cdsweb.cern.ch/record/1458503/files/ATL-SOFT-PROC-2012-065.pdf.

[129] M. Aaboud et al., *A measurement of the calorimeter response to single hadrons and determination of the jet energy scale uncertainty using LHC Run-1 pp-collision data with the ATLAS detector*,
Eur. Phys. J. **C77** (2017) p. 26, arXiv: 1607.08842 [hep-ex].

[130] ATLAS Collaboration, *Jet Calibration and Systematic Uncertainties for Jets Reconstructed in the ATLAS Detector at $\sqrt{s} = 13$ TeV*, (2015), URL: https://cds.cern.ch/record/2037613.

[131] ATLAS Collaboration, *Jet energy resolution in proton–proton collisions at $\sqrt{s} = 7$ TeV recorded in 2010 with the ATLAS detector*, Eur. Phys. J. C **73** (2013) p. 2306, arXiv: 1210.6210 [hep-ex].

[132] ATLAS Collaboration, *Monte Carlo Calibration and Combination of In-situ Measurements of Jet Energy Scale, Jet Energy Resolution and Jet Mass in ATLAS*, ATLAS-CONF-2015-037, 2015, URL: https://cds.cern.ch/record/2044941.

[133] ATLAS Collaboration, *Jet energy measurement with the ATLAS detector in proton–proton collisions at $\sqrt{s} = 7$ TeV*, Eur. Phys. J. C **73** (2013) p. 2304, arXiv: 1112.6426 [hep-ex].

[134] S Alkire, "Line of Fire Hidden Valley Triggers," tech. rep. ATL-COM-PHYS-2011-844, CERN, 2011, URL: https://cds.cern.ch/record/1366065.

[135] ATLAS Collaboration, *Characterisation and mitigation of beam-induced backgrounds observed in the ATLAS detector during the 2011 proton–proton run*, JINST **8** (2013) P07004, arXiv: 1303.0223 [hep-ex].

[136] ATLAS Collaboration, *Selection of jets produced in 13TeV proton-proton collisions with the ATLAS detector*, (2015), URL: https://cds.cern.ch/record/2037702.

[137] "Tagging and suppression of pileup jets with the ATLAS detector," tech. rep. ATLAS-CONF-2014-018, CERN, 2014, URL: https://cds.cern.ch/record/1700870.

[138] M. Cacciari, G. P. Salam, and G. Soyez, *The Anti-k(t) jet clustering algorithm*, JHEP **04** (2008) p. 063, arXiv: 0802.1189 [hep-ph].

[139] D. Krohn, J. Thaler, and L.-T. Wang, *Jet Trimming*, JHEP **02** (2010) p. 084, arXiv: 0912.1342 [hep-ph].

[140] G. Aad et al., *Identification of boosted, hadronically decaying W bosons and comparisons with ATLAS data taken at $\sqrt{s} = 8$ TeV*, Eur. Phys. J. **C76** (2016) p. 154, arXiv: 1510.05821 [hep-ex].

[141] D. Krohn, J. Thaler, and L.-T. Wang, *Jet Trimming*, JHEP **02** (2010) p. 084, arXiv: 0912.1342 [hep-ph].

[142] S. D. Ellis, C. K. Vermilion, and J. R. Walsh, *Recombination Algorithms and Jet Substructure: Pruning as a Tool for Heavy Particle Searches*, Phys. Rev. **D81** (2010) p. 094023, arXiv: 0912.0033 [hep-ph].

[143] S. D. Ellis, C. K. Vermilion, and J. R. Walsh, *Techniques for improved heavy particle searches with jet substructure*, Phys. Rev. **D80** (2009) p. 051501, arXiv: 0903.5081 [hep-ph].

[144] J. M. Butterworth et al., *Jet substructure as a new Higgs search channel at the LHC*, Phys. Rev. Lett. **100** (2008) p. 242001, arXiv: 0802.2470 [hep-ph].

[145] A. J. Larkoski, I. Moult, and D. Neill, *Analytic Boosted Boson Discrimination*, JHEP **05** (2016) p. 117, arXiv: 1507.03018 [hep-ph].

[146] A. J. Larkoski, I. Moult, and D. Neill, *Power Counting to Better Jet Observables*, JHEP **12** (2014) p. 009, arXiv: 1409.6298 [hep-ph].

[147] ATLAS Collaboration, *Identification of boosted, hadronically-decaying W and Z bosons in $\sqrt{s} = 13$ TeV Monte Carlo Simulations for ATLAS*, (2015), URL: https://cds.cern.ch/record/2041461.

[148] ATLAS Collaboration, *Measurement of large radius jet mass reconstruction performance at $\sqrt{s} = 8$ TeV using the ATLAS detector*, ATLAS-CONF-2016-008, 2016, URL: https://cds.cern.ch/record/2139642.

[149] URL: https://atlas.web.cern.ch/Atlas/GROUPS/PHYSICS/PLOTS/JETM-2016-009/.

[150] ATLAS Collaboration, *Searches for heavy ZZ and ZW resonances in the $\ell\ell qq$ and $\nu\nu qq$ final states in pp collisions at $\sqrt{s} = 13$ TeV with the ATLAS detector*, ATLAS-CONF-2016-082, 2016, URL: https://cds.cern.ch/record/2206275.

[151] ATLAS Collaboration, *Performance of Missing Transverse Momentum Reconstruction in Proton-Proton Collisions at 7 TeV with ATLAS*, Eur. Phys. J. **C72** (2012) p. 1844, arXiv: 1108.5602 [hep-ex].

[152] ATLAS Collaboration,
Performance of missing transverse momentum reconstruction for the ATLAS detector in the first proton-proton collisions at $\sqrt{s} = 13$ *TeV*, (2015),
URL: http://cds.cern.ch/record/2037904.

[153] *Expected performance of missing transverse momentum reconstruction for the ATLAS detector at* $\sqrt{s} = 13$ *TeV*, (2015),
URL: https://cds.cern.ch/record/2037700.

[154] ATLAS Collaboration, *Electron efficiency measurements with the ATLAS detector using the 2012 LHC proton-proton collision data*, (2014),
URL: https://cds.cern.ch/record/1706245.

[155] ATLAS Collaboration,
Muon reconstruction performance in early 13 TeV data, (2015),
URL: https://cds.cern.ch/record/2047831.

[156] ATLAS Collaboration,
Measurement of the muon reconstruction performance of the ATLAS detector using 2011 and 2012 LHC proton-proton collision data,
Eur.Phys.J. **C74** (2014) p. 3130, arXiv: 1407.3935 [hep-ex].

[157] ATLAS Collaboration,
Optimisation of the ATLAS b-tagging performance for the 2016 LHC Run,
ATL-PHYS-PUB-2016-012, 2016,
URL: https://cds.cern.ch/record/2160731.

[158] A. Hocker et al., *TMVA - Toolkit for Multivariate Data Analysis*,
PoS **ACAT** (2007) p. 040, arXiv: physics/0703039 [PHYSICS].

[159] ATLAS Collaboration, *Commissioning of the ATLAS high performance b-tagging algorithms in the 7 TeV collision data*, ATLAS-CONF-2011-102, 2011, URL: https://cds.cern.ch/record/1369219.

[160] G. Piacquadio and C. Weiser,
A new inclusive secondary vertex algorithm for b-jet tagging in ATLAS,
J. Phys. Conf. Ser. **119** (2008) p. 032032.

[161] ATLAS Collaboration, *Electron efficiency measurements with the ATLAS detector using the 2015 LHC proton–proton collision data*,
ATLAS-CONF-2016-024, 2016,
URL: https://cds.cern.ch/record/2157687.

[162] ATLAS Collaboration,
Muon reconstruction performance in early $\sqrt{s} = 13$ *TeV data*,

ATL-PHYS-PUB-2015-037, 2015,
URL: https://cds.cern.ch/record/2047831.

[163] ATLAS Collaboration,
Performance of b-Jet Identification in the ATLAS Experiment,
JINST **11** (2016) P04008, arXiv: 1512.01094 [hep-ex].

[164] ATLAS Collaboration,
Combined search for the Standard Model Higgs boson using up to 4.9 fb^{-1} of pp collision data at $\sqrt{s} = 7$ TeV with the ATLAS detector at the LHC,
Phys. Lett. B **710** (2012) p. 49, arXiv: 1202.1408 [hep-ex].

[165] K. Cranmer et al., *HistFactory: A tool for creating statistical models for use with RooFit and RooStats*, (2012).

[166] A. L. Read, *Presentation of search results: The CL(s) technique*,
J. Phys. **G28** (2002) p. 2693, [,11(2002)].

[167] G. Cowan, K. Cranmer, E. Gross and O. Vitells,
Asymptotic formulae for likelihood-based tests of new physics,
Eur. Phys. J. C **71** (2011) p. 1554, arXiv: 1007.1727 [physics.data-an].

[168] E. Gross and O. Vitells,
Trial factors or the look elsewhere effect in high energy physics,
Eur. Phys. J. **C70** (2010) p. 525, arXiv: 1005.1891 [physics.data-an].

[169] F Bertolucci,
"Measurements of diboson production with the ATLAS detector,"
tech. rep. ATL-PHYS-PROC-2014-012, CERN, 2014,
URL: https://cds.cern.ch/record/1668918.

[170] J. M. Campbell, R. K. Ellis, and C. Williams,
Vector boson pair production at the LHC, JHEP **07** (2011) p. 018,
arXiv: 1105.0020 [hep-ph].

[171] A. L. Read, *Linear interpolation of histograms*,
Nucl. Instrum. Meth. **A425** (1999) p. 357.

[172] A. L. Read, *Presentation of search results: the CL_s technique*,
J. Phys. G **28** (2002) p. 2693.

[173] G. Cowan et al.,
Asymptotic formulae for likelihood-based tests of new physics,
Eur. Phys. J. **C71** (2011) p. 1554, [Erratum: Eur. Phys. J.C73,2501(2013)],
arXiv: 1007.1727 [physics.data-an].

[174] G. Cowan et al.,
Erratum to: Asymptotic formulae for likelihood-based tests of new physics,
Eur. Phys. J. C **73** (2013) p. 1434.

HVT W' Search: signal and control regions

This Appendix presents the fit control regions (Figs. 2 (a), 3) and signal regions (Fig. 2 (b), 4) entering the search for the HVT W' in the $\ell\ell qq$ channel, outlined in Fig. 1.

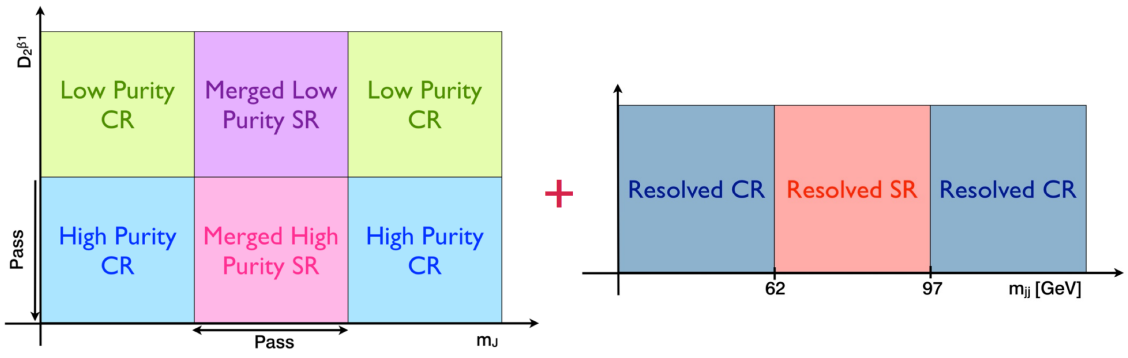

Figure 1: Event categories entering the spin 1 analysis. There are 6 regions in total: the high and low-purity merged signal regions, corresponding high and low-purity Z-control regions, the resolved signal region, and the resolved Z-control regions . There is one resolved top control region.

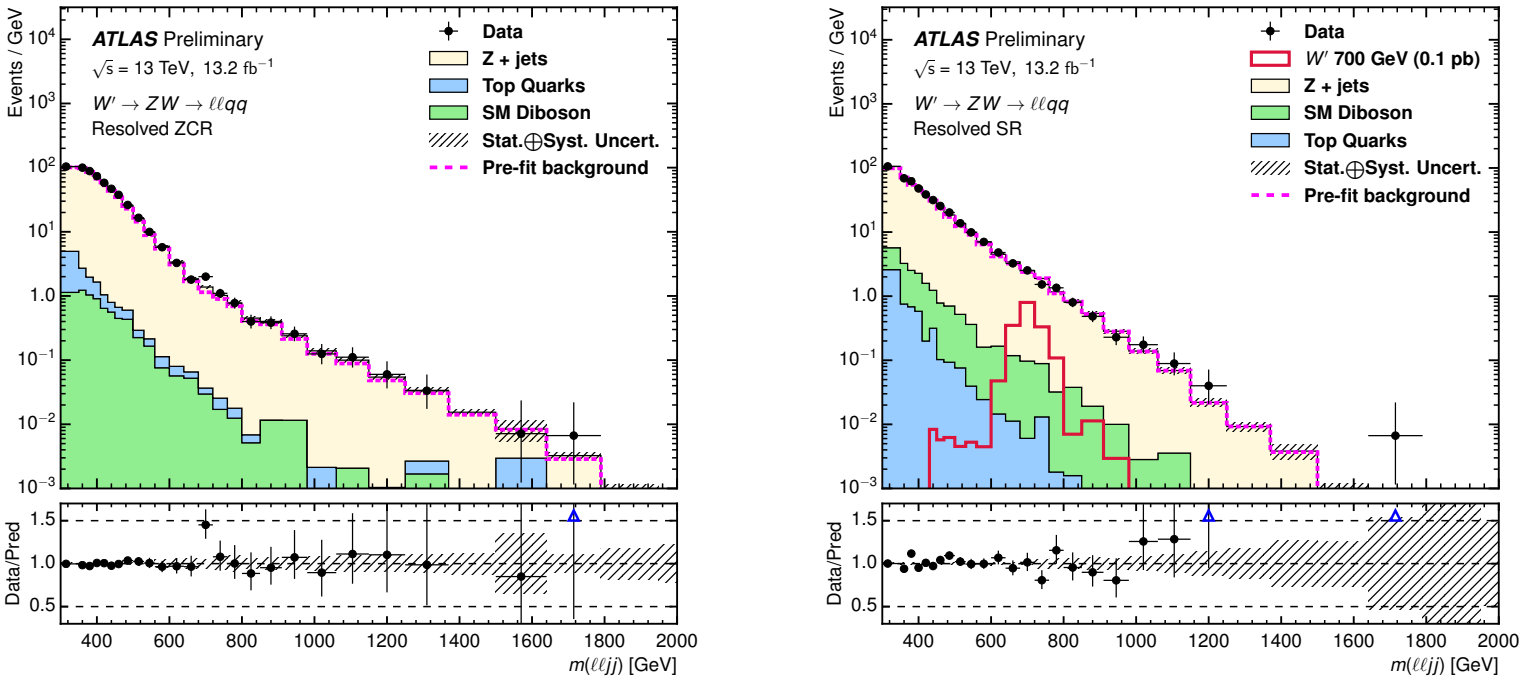

Figure 2: Data and MC comparison in the $m_{\ell\ell jj}$ distribution in the HVT $W' \to ZW \to \ell\ell qq$ search of Z+jets for (a) the control region of the resolved analysis, and (b) the $m_{\ell\ell jj}$ final discriminate of the resolved analysis. The MC distribution is shown after final fit to all regions under the background-only hypothesis. Uncertainties shown in (diagonal lines) express the $\pm 1\sigma$ width of the posterior likelihood minimum. The W' signal (red) is assumed to have a $\sigma \times \mathrm{BR}(W' \to ZW)$ value of 100 fb at 700 GeV.

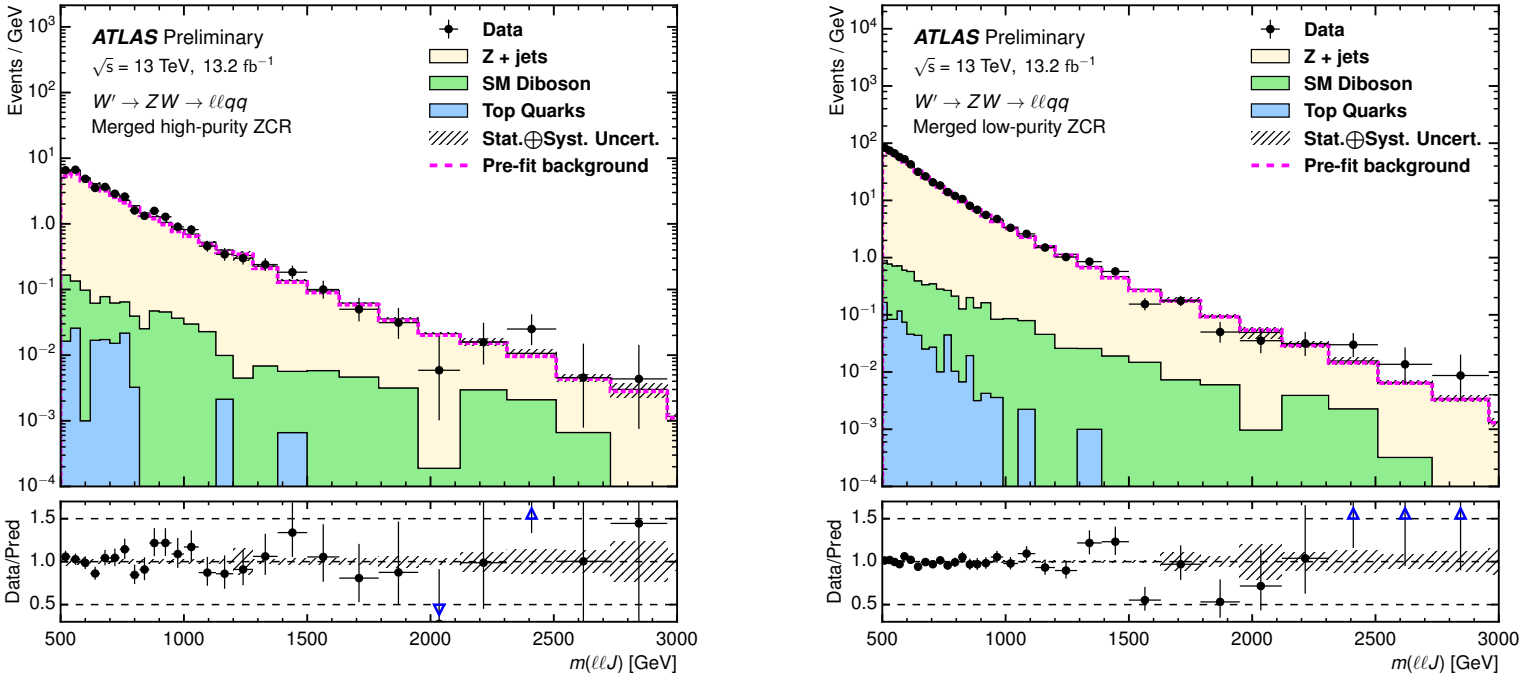

Figure 3: Data and MC comparison in the $m_{\ell\ell J}$distribution in the Z+jets control regions of the HVT $W' \to ZW \to \ell\ell qq$ search for the (a) high-purity region and (b) low-purity regions. The MC distribution is shown after final fit to all regions under the background-only hypothesis. Uncertainties shown in (diagonal lines) express the $\pm 1\sigma$ width of the posterior likelihood minimum.

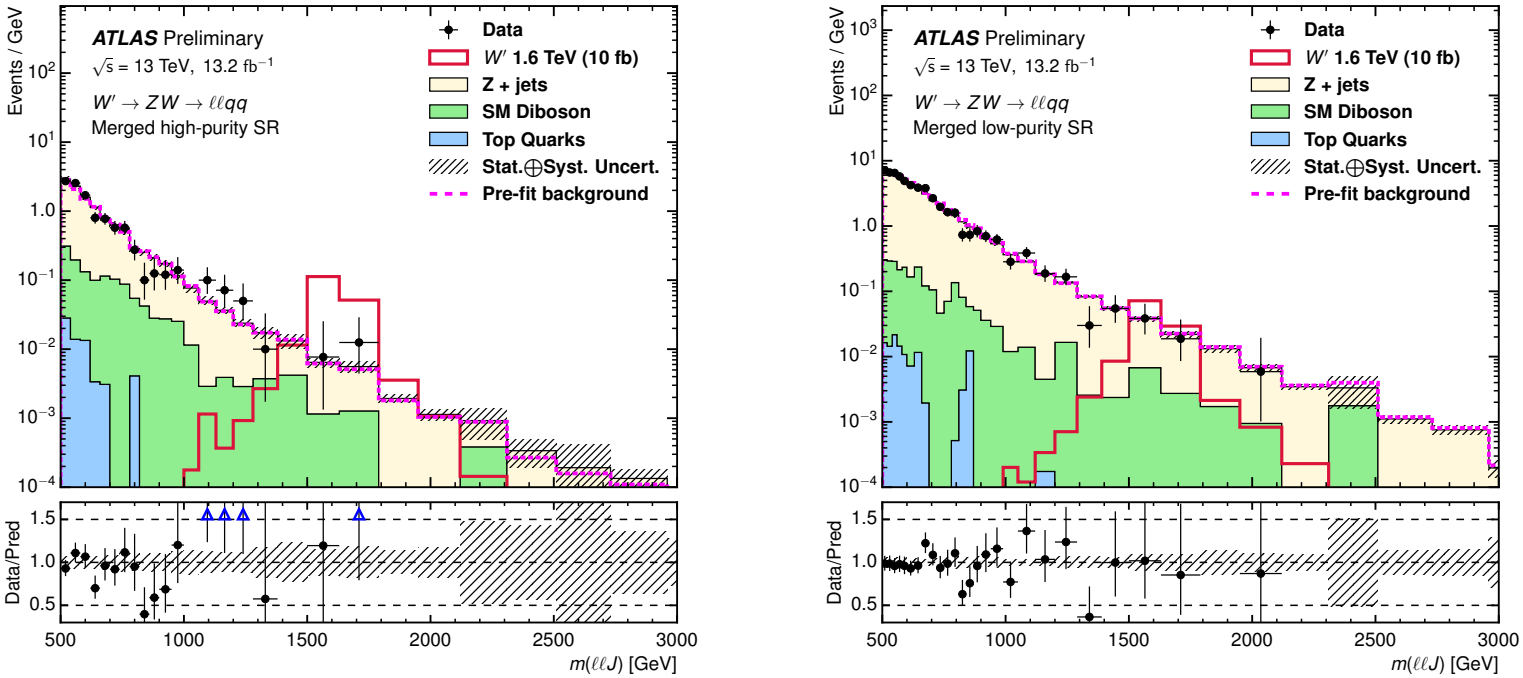

Figure 4: Data and MC comparison in the $m_{\ell\ell J}$distribution of the final discriminants of the HVT $W' \to ZW \to \ell\ell qq$ search for events passing all selections for the $m_{\ell\ell J}$ distributions of the merged analysis for (a) high-purity region and (b) low-purity region. The MC distribution is shown after final fit to all regions under the background-only hypothesis. Uncertainties shown in (diagonal lines) express the $\pm 1\sigma$ width of the posterior likelihood minimum. The W' signal (red) is assumed to have a $\sigma \times \mathrm{BR}(W' \to ZW)$ value of 10 fb at 1600 GeV.

Randall Sundrum Graviton Search: signal and control regions

This Appendix presents the fit control regions (Figs. 6, 8) and signal regions (Fig. 7, 9) entering the search for the RS graviton in the $\ell\ell qq$ channel, outlined in Fig. 5.

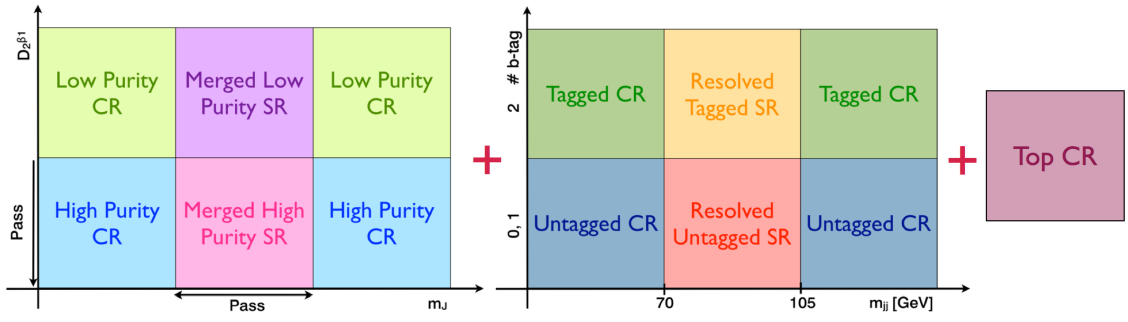

Figure 5: Event categories entering the spin-2 analysis. There are 9 regions in total: the high and low-purity merged signal regions, corresponding high and low-purity Z-control regions, the untagged and tagged resolved signal regions, and the untagged and tagged resolved Z-control regions. Additionally, there is one top control region.

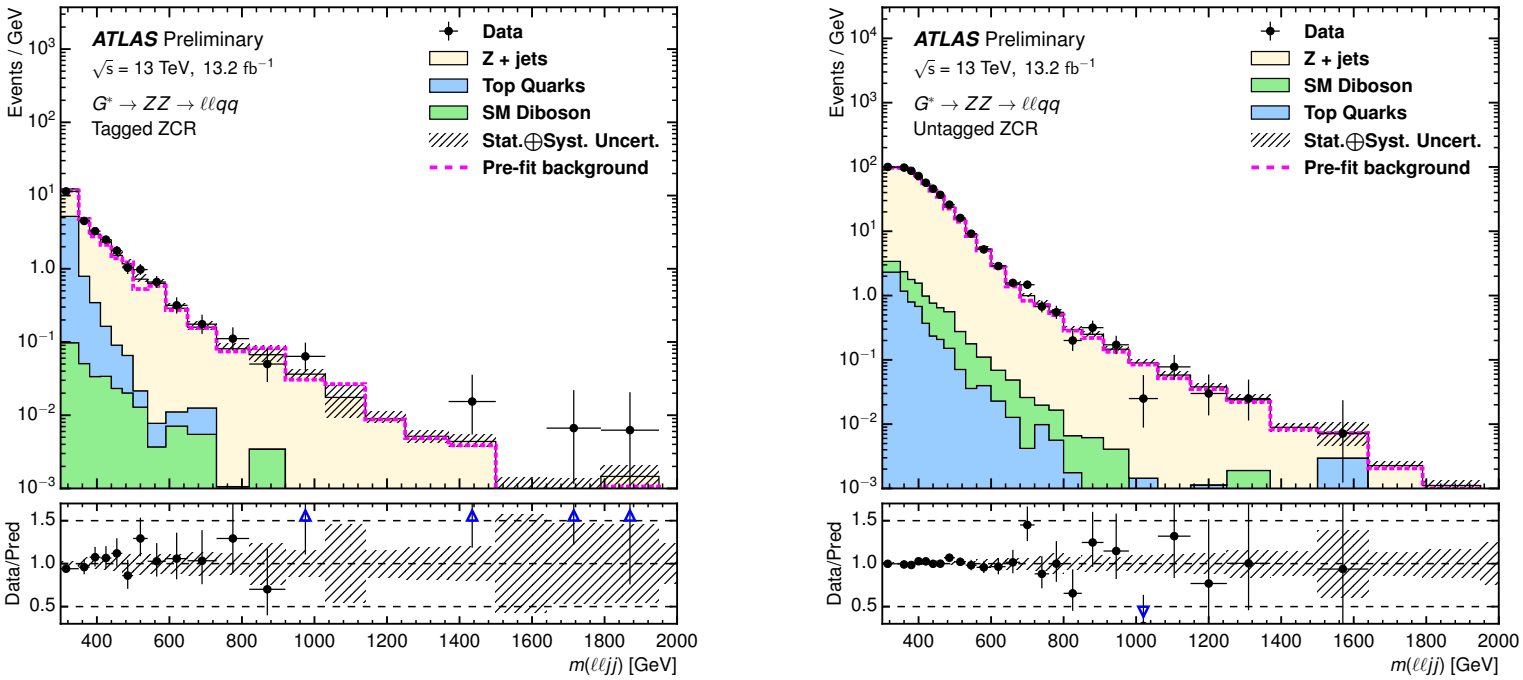

Figure 6: Data and MC comparison in the $m_{\ell\ell jj}$ distribution in the Z+jets control regions of the $G^* \to ZZ \to \ell\ell qq$ search of the resolved analysis for (a) tagged category and (b) untagged categories. The MC distribution is shown after final fit to all regions under the background-only hypothesis. Uncertainties shown in (diagonal lines) express the $\pm 1\sigma$ width of the posterior likelihood minimum.

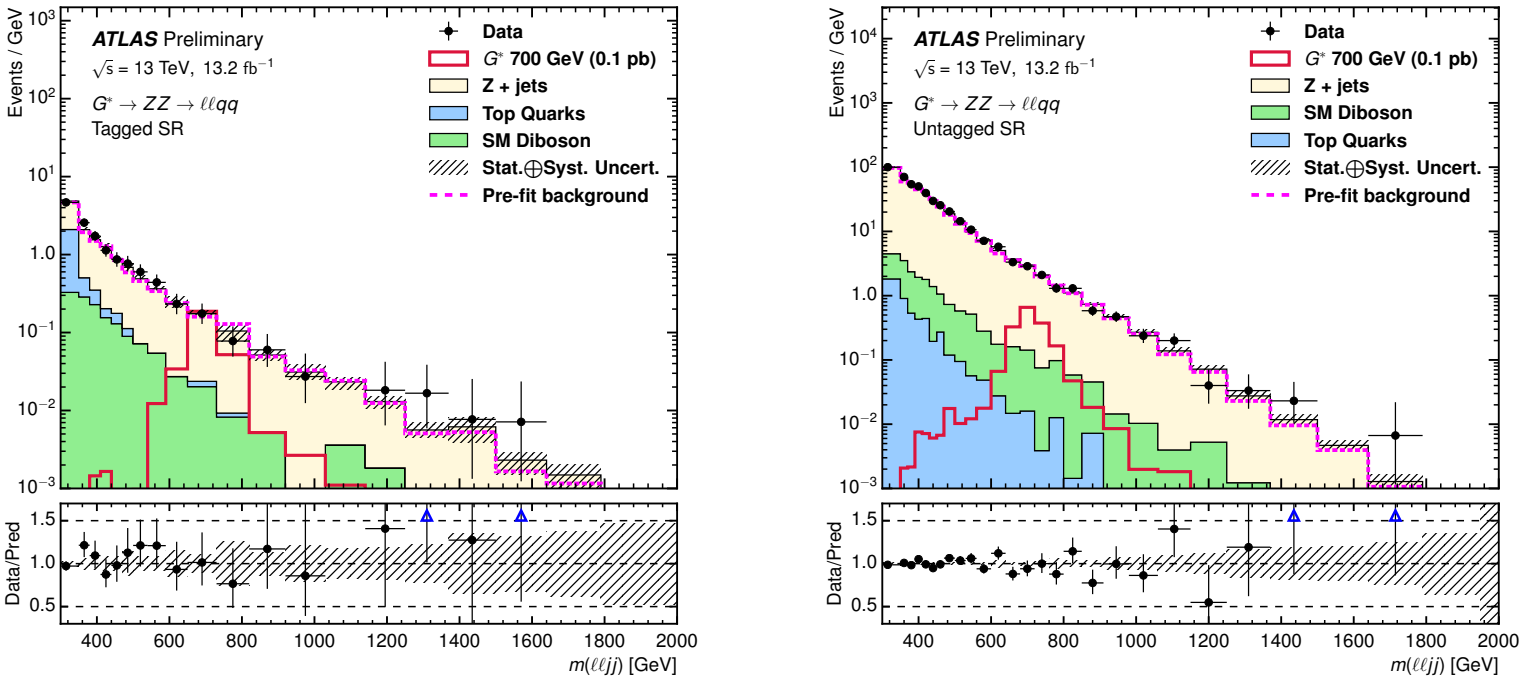

Figure 7: Data and MC comparison in the final $m_{\ell\ell jj}$ discriminant of the $G^* \to ZZ \to \ell\ell qq$ search in the resolved analysis for (a) tagged category and (b) untagged categories. The graviton is shown with a $\sigma \times \mathrm{BR}(G^* \to ZZ)$ value of 100 fb at 700 GeV. The MC distribution is shown after final fit to all regions under the background-only hypothesis. Uncertainties shown in (diagonal lines) express the $\pm 1\sigma$ width of the posterior likelihood minimum.

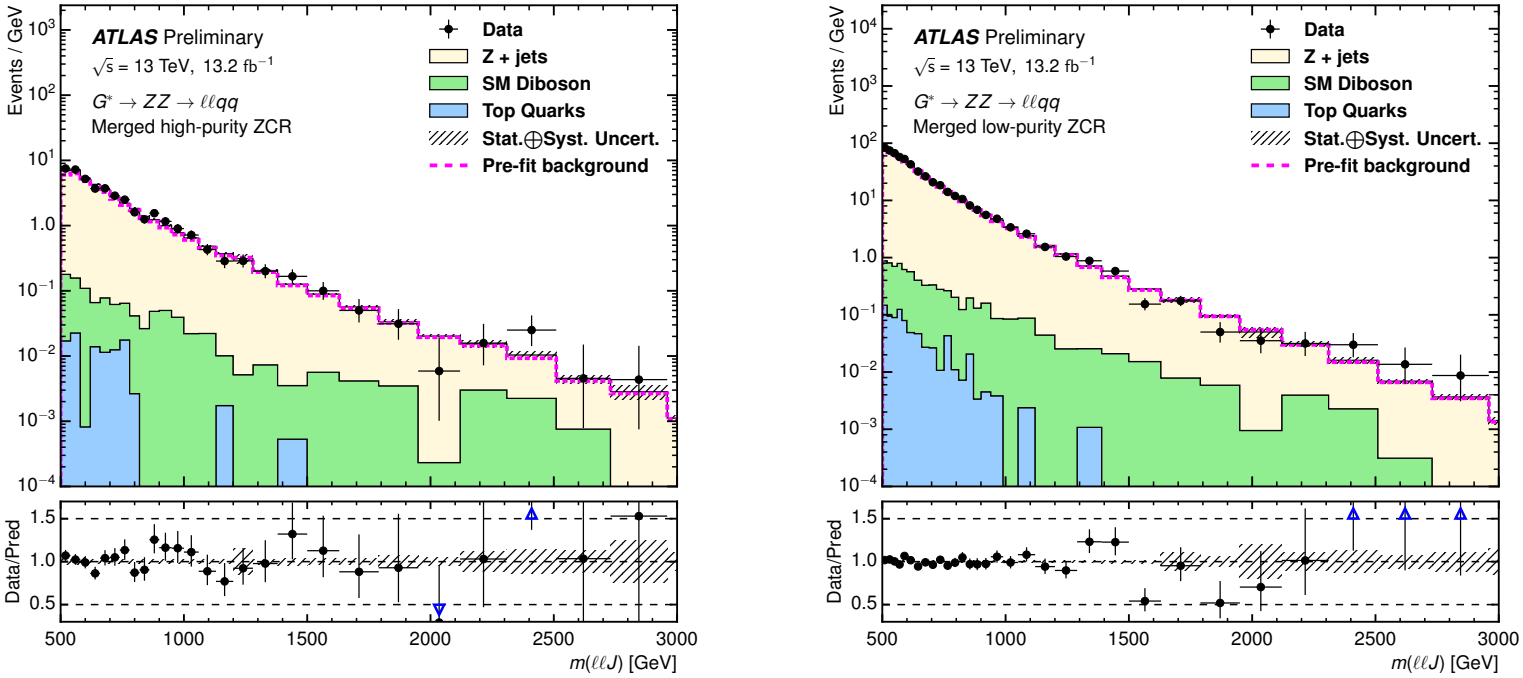

Figure 8: Data and MC comparison in the $m_{\ell\ell J}$ distributions in the merged analysis of the Z+jets control regions for the $G^* \to ZZ \to \ell\ell qq$ search for the (a) high-purity and (b) low-purity regions. The MC distribution is shown after final fit to all regions under the background-only hypothesis. Uncertainties shown in (diagonal lines) express the $\pm 1\sigma$ width of the posterior likelihood minimum.

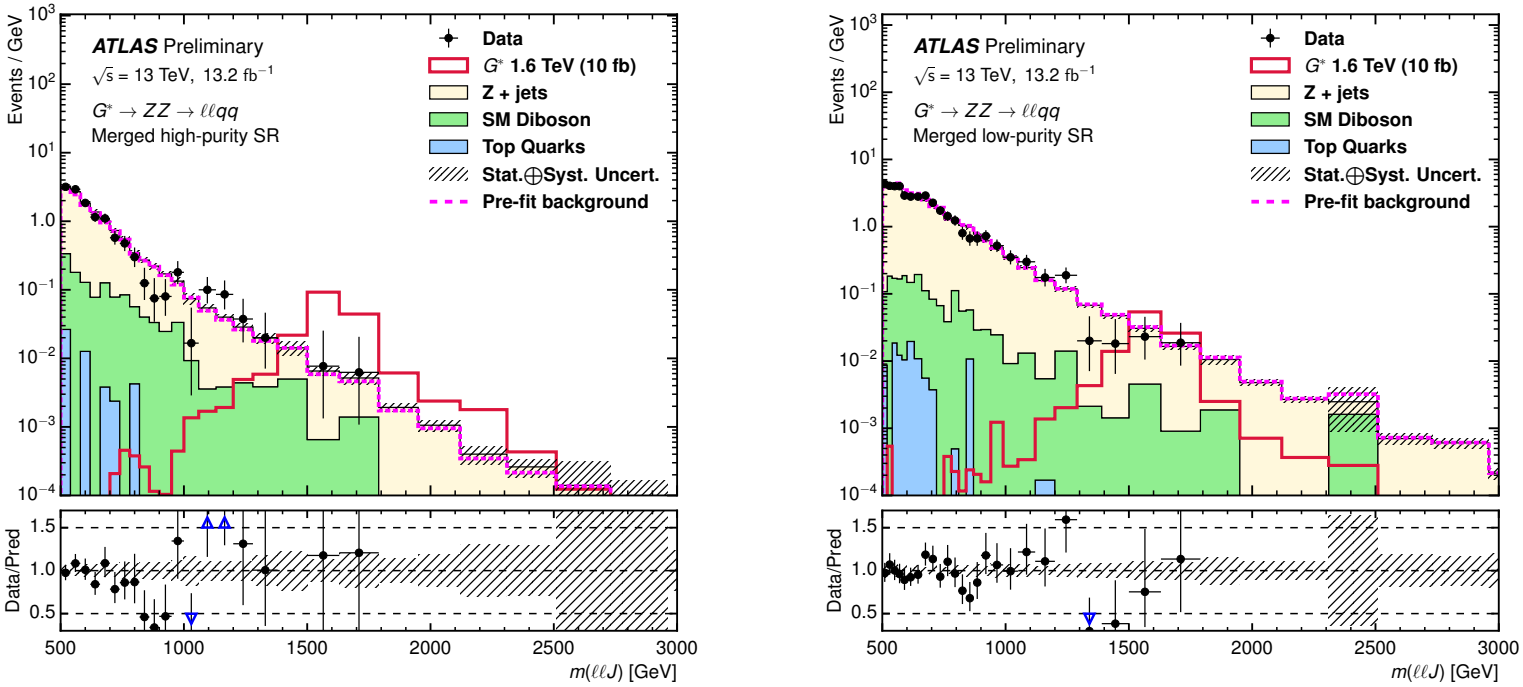

Figure 9: Data and MC comparison in the final $m_{\ell\ell J}$ discriminant of the $G^* \to ZZ \to \ell\ell qq$ search for the merged selection in the (a) high-purity and (b) low-purity regions. The MC distribution is shown after final fit to all regions under the background-only hypothesis. Uncertainties shown in (diagonal lines) express the $\pm 1\sigma$ width of the posterior likelihood minimum. The graviton signal is shown with a $\sigma \times \mathrm{BR}(G^* \to ZZ)$ value of 10 fb at 1600 GeV.